Technische Universität München
Fakultät für Informatik

A Stable and Transparent Framework for Adaptive Shared Control of Robots

Ribin Radhakrishna Balachandran, M.Sc.

Preface

This dissertation is based on research undertaken at the Institute of Robotics and Mechatronics of German Aerospace Center (DLR) in Oberpfaffenhofen, Germany. It took six years (2016-2021) to accumulate the results which are reported in the thesis. This duration, for me, was not just a technical quest, but rather an opportunity to grow into an improved version of myself. Fortunately, I was blessed along the way with great people, for both, technical and emotional support. I take the space here to acknowledge them in detail.

First of all, I would like to express my deepest gratitude to my supervisor Prof. Alin Albu-Schaeffer for his guidance and inspiring discussions throughout the course of this work. After each discussion with him, I came back with a renewed and improved sense of my goals. Not just as a PhD supervisor, his support and guidance as our institute head were immense during the period I could serve as the co-project lead for Kontur-3 space project.

Next, I would like to express my sincere gratitude and appreciation to Dr. Christian Ott, our department head and my mentor. When Jordi (next on the list) left our institute, there was a period when I was aimless ☺. Christian gave me the direction and research support which lead to what I am now. Our monthly update meetings were very fruitful and his critical and objective comments about the subject made me learn and led to most of my publications. Special thanks to Christian for reviewing the thesis is great detail.

Dr. Jordi Artigas: First of all, I thank him for inviting me for the job interview when I made an open job application. Along with Konstantin (next on the list), he gave good feedback about me to Alin, which resulted in my being here now. I was privileged to work with Jordi from the day I started. Among many other things, Jordi was my first mentor who taught me the passivity tools to make robots stable, and was also a brother who gave me life advice to make me emotionally stable ☺!

Dr. Konstantin Kondak: After giving me this job opportunity, Konstantin was a great leader for our flying robots team. I learned a lot from him, mainly his attitude and desire to put all the research work that we do, into practical use. His 'work hard and also enjoy life to the fullest' motto has been a great inspiration to all our teammates. He also bought us really expensive wine to celebrate our results on our official trips ☺!

Dr. Joern Malzahn: Joern was my master thesis supervisor (at TU Dortmund) who introduced me to the robotics research field. He really worked along with me during the

thesis work and had, by himself, even applied for jobs after the thesis completion for me. That thesis is what landed me the job at DLR, and I will be always grateful to him!

Prof. Jee-Hwan Ryu: Through Jordi, I was fortunate to meet and work with Prof. Ryu, which was a turning point in my research life. Prof. Ryu invited me to his lab for a research stay, during which we did the work that was published in my first paper. That collaboration continues even now with him giving me many more research opportunities and productive feedback, and led to many publications reported in this thesis.

I would like to thank my colleagues in the software, electronic and hardware teams, who lay the foundations on which all our research and publications are built. I was fortunate that I had these wonderful colleagues who supported me promptly, when asked for help. Some colleagues played special roles in my journey. Martin Stelzer, Florian Schmidt, Robert Burger and Andreas Stemmer helped me with all the software issues. Stefan Engelhardt, Stefan von Dombrowski, Hansjoerg Maurer, Andreas Biebl and Manuel Santos helped with the network administration stuff. Alexander Beyer, Wieland Bertleff, Martin Heumos and Benedikt Pleintinger fixed the electronic components when we destroyed the robots ☺! When we needed special hardware parts, Bertram Willberg, Harald Wagner, Michael Dreer, Michael Heumos and Tran Van Thuan from the hardware workshop were always happy to help us build them.

I was fortunate to work in multiple projects and teams, which not only supported my research but was an important factor in my social life here. Special thanks to all the colleagues associated with the Kontur 2,3 projects: Cornelia Riecke, Bernhard Weber, Oxana Domsch, Jan Cremer, Michael Steinmetz, Rico Belder, Armin Wedler, Kristin Bussman, Michael Panzirsch, Harsimran Singh and Marek Sierotowicz. Connie was not just a co-project lead, she turned into a sister-like figure for me during all the work we did together.

I thank the colleagues of the flying robots team: Jongseok, Yura, Andre, Minjun, Khizer, Michael, Marco and Konstantin for all the wonderful times we had during the outdoor experiments and project trips!

Special thanks to the OOS-Sim team members: Roberto, Marco, Hrishik, Nassir, Bernhard, Martin, Alessandro and Ria for the interesting demos and project work. Special thanks to Roberto for being really understanding and letting me have some time off from projects to focus on the thesis writing.

A major part of my time was spent for teleoperation experiments, which would not have happened without the support of the TP-Group members: Thomas, Michi, Simran, Andre, Max, Nicolai, Neal and Aaron helped me with theory, software and hardware issues throughout my work here. All the interesting discussions we had helped me learn more about our topics. Thanks to Neal for getting me connected to Prof. Abbink, my second reviewer. Special thanks to Michi for all the passivity-based discussions and experiments that we did together from day 1. I could learn a lot from him. Also, special thanks to Thomas for the support he gave me with English-German translation throughout my stay here and especially for the abstract of this thesis. Special Thanks to Annika for the time spent on the slides.

I thank my students Natalia, Matteo, Jaeseok and Elizabeth for supporting me with the research. I learned a lot while working with you all.

I would like to give special acknowledgments to the next few people!

Abstract

With the advent of high precision sensors, fast computers and artificial intelligence, autonomous robots have been demonstrated to be capable of implementing highly intricate and complicated tasks. Yet, complete autonomy is a goal that we have still not achieved. When perception of the environment cannot be precise, human supervision is desired to give both high level commands using supervised autonomy, as well as direct control using *teleoperation*. Although teleoperation with haptic feedback has proven to be a useful solution to interact with dangerous and remote environments through the robotic *avatars*, performance degradation caused due to communication delays and large effort demanded from the operators are seen as limitations of this approach. To combine the benefits of autonomy and direct teleoperation in a synergistic manner, the paradigm of *shared control* was developed and has been widely researched.

This thesis focuses on a special form of shared control, namely *mixed-initiative*, where the final command to the robot is a weighted sum of the commands from the operator and the autonomous controller. The weights (fixed or adaptive), called authority allocation (AA) factors, decide who has more control authority over the robot. Different research groups use different methods to adapt the AA factors online and the benefits of adaptive mixed-initiative shared control have been well established in terms of task completion success and operator usability. However, stability of the overall shared control framework, with communication time-delays between the operator and the robot, is a field that has not been examined extensively. This thesis looks at the system from a control perspective and develops methods to improve performance and stability in shared control so that the possibilities of its applications can be widened. Firstly, methods to improve the haptic feedback performance of teleoperation are developed. A novel approach for stabilizing arbitrary and user-defined feedback controllers in teleoperation with high and time-varying communication delays is presented. Secondly, methods to stabilize online adaptation of AA factors in multi-agent shared control systems are proposed. All these methods are combined to develop a unified framework for shared control, which can be used in a wide variety of domains by different research groups, focusing on different approaches for haptic shared control and online adaptation of AA factors. The methods are validated on multiple robotic systems and published in several peer-reviewed conferences and journals. To show the real life applicability of the developed methods, they were availed in several projects, both in space and terrestrial domains.

Contents

List of Symbols and Abbreviations

In the thesis, all scalar quantities are described by plain letters (e.g. V_r, F_e). Matrices and vectors are printed in bold (e.g. $\boldsymbol{V_r}$, $\boldsymbol{F_e}$). Subscripts and superscripts will denote the specific quantities. Total derivatives with respect to time t are represented by dots, for example $\dot{x} = \frac{d}{dt}x$, $\ddot{x} = \frac{d^2}{dt^2}x$. The list contains only the quantities which appear at several places in the thesis or are of prominent importance.

List of Symbols

t	Time
k	Discrete-time step
T	Sampling time
u	Input
y	Output
$F, \boldsymbol{F}$	Force, Wrench vector
α_t	Authority allocation factor for teleoperation force
α_a	Authority allocation factor for automatic controller
α_l	Gain of force feedforward gain
α	Scaling factor for force
β	Scaling factor for velocity
$X, \boldsymbol{X}$	Position, Cartesian pose coordinates
$V, \boldsymbol{V}$	Velocity, Cartesian end-effector velocity vector
$\boldsymbol{q}$	Vector of joint angles
$M, \boldsymbol{M}$	Mass, Inertia matrix
$\boldsymbol{C}$	Coriolis/centrifugal matrix
$K_p, \boldsymbol{K}_p$	Coupling stiffness, Cartesian stiffness matrix
$K_d, \boldsymbol{K}_d$	Coupling damping, Cartesian damping matrix
$\boldsymbol{\Lambda}$	Cartesian inertia matrix
$\boldsymbol{\mu}$	Cartesian Coriolis/centrifugal matrix

$D, \boldsymbol{\Gamma}$	Viscous friction, Cartesian viscous damping matrix
Z	Impedance
S	Storage function
E	Energy
P	Power
E^{obs}	Energy observer
E^{diss}	Energy dissipated by passivity controller
R^{PC}	Time varying damping of passivity controller

List of Abbreviations

SC	Shared Control
TP	Teleoperation
ACS	Automatic Control System
AA	Authority Allocation
FAA	Fixed Authority Allocation
AAA	Adaptive Authority Allocation
PCR	Passive Coupling Reference
SAM	Suspended Aerial Manipulator
WVT	Wave Variables Transformation
EFC	Explicit Force Controller
ER	Energy Reflection
USB	Universal Serial Bus
RMSE	Root Mean Square of Errors
OSP	Output Strictly Passive/ Output Strict Passivity
OOS	On Orbit Servicing
HIL	Hardware in the Loop
OOS-Sim	On Orbit Servicing Simulator
FTS	Force Torque Sensor
LWR	Light Weight Robot
TD	Time-Delay
DoF	Degree of freedom
TDPA	Time Domain Passivity Approach
PO	Passivity Observer
PC	Passivity Controller
PD	Proportional-Derivatives
PI	Proportional-Integral

Introduction

"Synergy - the bonus that is achieved when things work together harmoniously."

– Mark Twain

1.1 Motivation

We, as humans, have evolved to be great at using tools. Or, it could be the other way around — we evolved because of our tool-using skills. Though the causality might not be clear, it cannot be denied that, now, we are good at inventing tools and solutions. This has played a crucial role in our long odyssey from the grasslands of Africa to beyond the surface of our planet. However, what is humanly possible is limited by our knowledge, physiology, psychology and of course, basic laws of physics. When it came to *dull, distant, dirty, demanding, distributed* and, most importantly, *dangerous* tasks, we invented a new tool— Robots! With the advent of high-tech sensors, actuators, computational capabilities and artificial intelligence, we have been able to develop robots that help mankind when it comes to the tasks that can take the aforementioned *adjectives*. Robots— the tools that started as crude and mechanically controlled systems, are now one of mankind's greatest scientific marvels. Yet again, what is possible with robots has limits. Complete autonomy in robots is a goal we are yet to achieve. For the time being, humans and robots *working harmoniously helps achieve the best bonus.* The research conducted in this thesis tries to extend and support this *synergy.*

Automatic control systems (ACS) in robots support humans with demanding and dull/ repetitive tasks, if the work objects and environments are well perceived or modeled. Robots can even work round-the-clock getting tasks completed, which reduces the demand from the shrinking manual workforce in many developed nations [For20]. When perception of the environment cannot be precise, their human counterparts, who have better cognitive and decision-making capabilities can support the robots. In supervised-autonomy, humans give high level commands and the robots follow these instructions to the best of their capabilities [CZ01]. If this also fails, the human takes direct control of the robot and this leads us to a different paradigm called *teleoperation.*
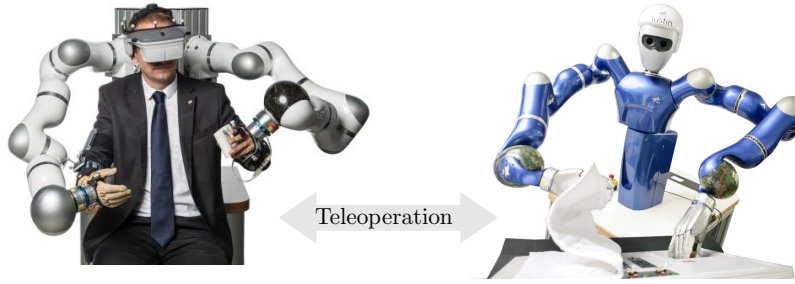
Figure 1.1: Bilateral teleoperation paradigm

Teleoperation was developed to carry out tasks that were mainly dangerous and as the name suggests, *distant* or remote. A human operator, using an input device, controls a remote robot and implements these tasks in the robot's environment. If the forces of interaction between the robot and its environment are sent back to the human operator, it is called bilateral teleoperation or telepresence [HS06], and an input device that allows this is called a haptic device. Through a communication channel, position signals are sent from the haptic device to the remote robot and forces are sent back to the haptic device. A simple bilateral teleoperation set-up is shown in Fig. 1.1. If the robot is distant, the time-delays introduced by the communication channel can make this closed-loop control system unstable and there are several methods developed to still ensure its stability [HS06]. However, ensuring stability comes with a cost— it reduces the system performance. Transparency is a performance criterion in bilateral teleoperation, which measures how well the operator perceives the interaction between the robot and its environment. With an ideally transparent system, the operators feel that they directly interact with the environment or that they are *tele*-present in the remote environment [YY94, Law93].

Yet, having human operators continuously doing remote work through their robotic avatars demands high physical and mental effort from them [AMB12]. This is where shared control paradigm comes into the picture. The basic idea of shared control is this: let the ACS do whatever it is capable of doing safely and accurately. If and only when the ACS fails, the operator comes in and makes corrective measures and actions [I⁺03]. Shared control has proven helpful in task completion and reduction in operator effort. The shared control paradigm is broadly shown in Fig. 1.2.
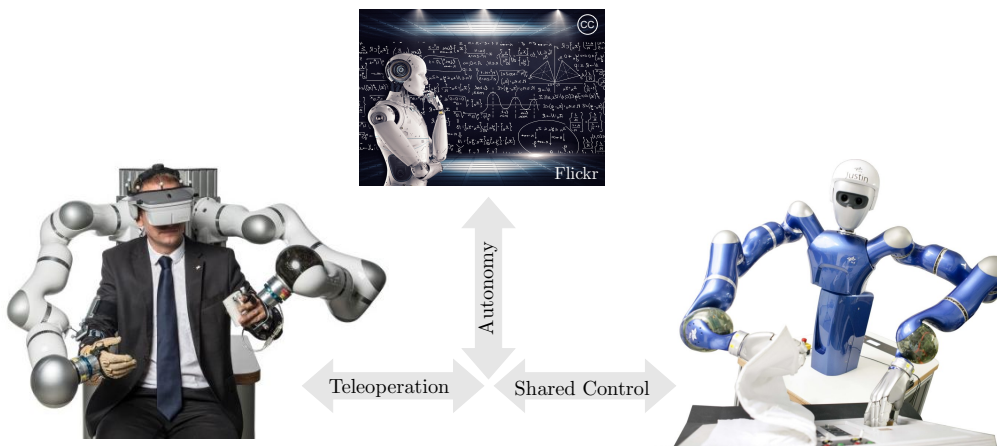
Figure 1.2: Shared control paradigm

Shared control is also classified according to the approach used. In traded control, the operator and robot do tasks in a serial manner (one after the other) and in a mixed-initiative (also called mixed-input) shared control approach, they do it in parallel [Her16, MH17b]. This thesis focuses on the latter, where the final control signal commanded to the robot is a weighted sum of the control signals from the operator and the ACS. As in teleoperation tasks [WAH⁺12], haptic feedback has been shown to improve performance in shared control in several studies [MO04, VOAK⁺13]. Haptic feedback in shared control allows the operator to feel additional forces acting on the remote robot. These additional forces could be from virtual fixtures [Ros93] which restrict the operator from moving the robot into certain areas in its workspace, or they could guide the operator along a specific trajectory to support the robot in reaching a target location [GG05]. Surveys on different shared control approaches can be found in [SCN⁺21, AMB12] and [LMBO18].

In mixed-initiative shared control, the weights called authority allocation (AA) factors, decide who has more control authority over the robot [I⁺03, PR97] and the process of control authority distribution is called arbitration [LMBO18]. The AA factors can be fixed or adaptive during the task execution period. Fixed authority allocation (FAA) enables simpler controller designs. Yet, they need to be tuned a priori based on several factors (like, quality of ACS and operator, traditional human factor issues etc [AMB12]), which makes the optimal choice of these gains really complicated. In some cases, fixed AA gains can even affect the system performance negatively [LPO09], since the operator might have to *fight* against the ACS and the robot might end-up in a local minima, where the two inputs balance each other out. Adaptive authority allocation (AAA), enables necessary online modification of these gains to suit the current requirements in the task implementation phase [Abb06, GWS08, PdV⁺07]. The performance improvements using AA adaptation in terms of task completion rate and reduced operator effort have been well established [MO04, SCN⁺21, AMB12]. In [AMB12], based on a meta-analysis, four guidelines were chosen for the design of haptic shared control systems, namely: *The human*

- **G1**: *should always remain in control, but should be able to experience or initiate smooth shifts between levels of authority,*

- **G2**: *should receive continuous feedback about the automation boundaries and functionality,*

- **G3**: *should continuously interact with the automation, and*

- **G4**: *should benefit from increased performance and/or reduced workload.*

Based on these guidelines, the main motivation for this thesis work is to develop a control framework to support online adaptation of AA factors and give the operator a better perception of the forces of interaction between the robot and its environment. At the same time, transparent haptic guidance is also envisioned, which should allow the operator to continuously interact with and get feedback from the ACS, and smoothly shift control authority between the two agents (operator, and ACS) when necessary. In the next section, the motivation and contributions are made more clear from a control perspective in the context of the available work and the gaps in research where this thesis could support shared control domain.

1.2 Related Work

Teleoperation is a field in robotics that has been in research for several decades. Enforcing stability caused by the non-idealities in the teleoperation system (e.g. time-delay, package loss etc) while increasing the transparency has been analyzed in detail and several methods, both model-based and model-independent, have been developed over the years in these contexts [HS06]. Model-based methods for stability and transparency ([LCS02, CS04]) allow for less conservative behavior compared to passivity-based model-independent methods [HCFS]. On the other hand, passivity-based methods like wave variables [NS97], energy tanks [FSM+11] and time domain passivity control [HR02] make it robust towards errors in system modeling. Although this thesis presents ways to improve transparency while maintaining stability, it should be seen as a means to achieving the main goal, which is the transparent framework for adaptive shared control. Since several others (for example, [Pan18], [Reb15] and [Art14]) cover the topic of transparency, it will not be covered in this section. However, relevant related work will be mentioned in the chapters that present the proposed methods for transparency enhancement.

The main literature surveyed here is for the field of shared control of robots and the effects of AA factors. Fixed AA values have shown to improve performance in sub-task controllers in teleoperated robots [SGFS19, LC11]. Fixed gains have also been applied with demonstrated benefits in space robots [MBDSO21b] and surgical robots [FPBS15, MF16]. Multilateral control, a form of shared control between multiple operators have availed benefits of fixed AA factors [PBA15, Pan18] and multilateral systems have been used in expert-novice training [OGGL06, LPO09].

To make shared control systems more flexible, different research groups follow different approaches to modify the AA factors online, both human-driven and system-driven. As the name suggests, in human-driven systems, the operators in charge of the arbitration process manually distribute the control authority as and when deemed appropriate for corrective intervention. System-driven adaptation is when the system resolves authority allocation between the two control agents, and its timing [Sce96]. Some of the adaptation methods are based on human intention recognition [DS13, KSB12] and probabilistic approaches [Tra15, PJTKLP10]. Closely related to a probabilistic system-driven approach addressed in this thesis, [OGD15] uses the uncertainty of the autonomous controller with an *a priori* noise model. In the field of assisted-driving, [AM10, AMVdH+11] use neuromuscular signals of the driver to smoothly shift the control authority between the two agents and have been shown to improve driving performance [GG05]. Adaptation of AA factors has been used for learning and programming the robots by demonstration [AEK05, ZHC18], and has been also availed in operator training [LHPO09].

Shared control is a field that is versatile due to the possibilities of combining different forms of autonomy and arbitration. The aforementioned list of approaches and applications is not exhaustive and could be easily continued. So, what is the point of further research in this field? The following section will reveal certain gaps in research that this thesis addresses from a control perspective to enable the widened use of haptic shared control in more challenging and real-life scenarios. Furthermore, the thesis covers multiple aspects in haptic shared control and the related works in these aspects will be addressed in the respective chapters.

1.3 Research Gaps

As reported in [SCN⁺21, AMB12, LMBO18], extensive work has been done in the field of haptic shared control and most works present the benefits derived from their methods to support the operator [Rah20]. Even so, from a control perspective, stability of haptic shared control is a field that has not been investigated thoroughly [WL12] and very few publications address the stability issues. This is non-trivial since the dynamics of the human as well as unknown environment characteristics [WL12, LTH14] can affect the stability of the system, which becomes more critical when the AA factors are varied online. This is aggravated by the closed haptic loop, mentioned earlier, which is sensitive towards communication latencies. In [PBA15], we considered multilateral haptic control with delay in the loop for fixed AA factors. But the passivity properties were not analyzed. Later, in [Pan18] and [RHVJ19] the passivity properties of multilateral controllers for fixed AA factors with time-delay in the teleoperation channel were considered and stability was ensured. Energy tanks were applied to preserve passivity of the shared control schemes in [SGFS19] and [SFF⁺18]. Model-based stability methods have been applied in [LTH14, WL12, SRCG06, KHZ11, Nic20], but they do not consider the delay in the teleoperation communication channel. It should be noted that when the distance between the operator and the remote system is not so large (as in medical robots, driving assistance etc), the effects of the communication delay could be neglected. But allowing for larger time-delays in the teleoperation system within the shared control framework, can widen the possibilities of using robotics in fields like on-orbit servicing, tele-surgery and telenavigation of vehicles with haptic feedback. As an example, the AHEAD project spearheaded by the United Nations - World Food Programme and DLR uses the Sherp system (see Fig. 1.3 left) for the transport of humanitarian goods to rough-terrained, flood-prone and dangerous locations, where the use of remote haptic shared control is envisioned to replace human drivers [UWFP20].

Additionally, in spite of the communication delays, providing accurate feedback of forces from both, the environment and the ACS, lets the operator safely implement the tasks, which require high precision in robot positioning and force application. This will come in handy in the fields of tele-surgery [ERER20, MF16] and in-orbit assembly of satellites [WMPH⁺18]. Most of the works in haptic shared control do not focus on the how to combine a transparent teleoperation system with the shared control framework in a stable manner. In general, arbitration in shared control heuristically enforces the unity-sum rule of the AA factors. This means the sum of AA factors is always ensured to be equal to 1, so that when the authority of the ACS increases, the human operator has lower authority, and vice-versa [SCN⁺21, MH17a]. Is this really a necessity? Can the haptic shared control system be stable with arbitrary AA factors, which could make the system more versatile?

Sherp Telenavigation   Tele-surgery   On-Orbit Servicing
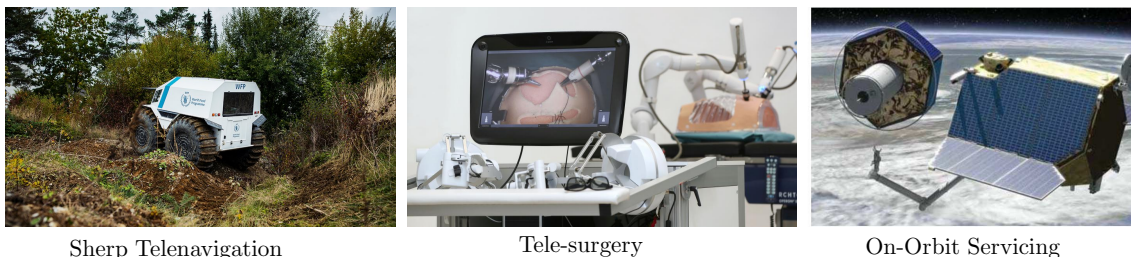
Figure 1.3: Applications of time-delayed haptic shared control

This topic has not been widely addressed in literature and is a major contribution of this thesis among others, which are mentioned in detail in the next section.

To summarize: Extensive work has been done in the field of haptic shared control. The implementation and benefits of haptic shared control in terms of operator usability and task completion have been widely reported. However, to the best of the author's knowledge, there has been no work that ensures stability and transparency of the overall shared control framework considering delays in the teleoperation system and allowing for stable and arbitrary adaptation of AA factors.

1.4 Contribution and Overview

This thesis develops a control framework for mixed-initiative shared control that can be used in a wide variety of domains by multiple research groups, focusing on different approaches for haptic shared control and online adaptation of AA factors in a stable manner. The framework is developed from a control perspective based on the identified research gaps and has the following features, which furthermore supports the guidelines from [AMB12] mentioned in Section 1.1:

1. **Transparency**: The haptic feedback of the shared control framework provides the operator with a good perception of the environment forces and also the forces generated by the ACS, in spite of the delays in the communication channel. This feature supports and enables the guidelines $G2$, $G3$ and $G4$.

2. **Adaptability**: The AA factors are online-adaptable to distribute control authority between the operator and the ACS. It supports any form of AA factor adaptation. This feature in the framework mainly enables guideline $G1$ so that the human can smoothly distribute the authority.

3. **Modularity**: Any form of haptic support (restrictive like virtual fixtures or supportive like trajectory generators) can be used in this framework. The *forces* from the teleoperation system and the autonomous system must be weighted and commanded to the robot.

4. **Stability**: The overall system maintains stability in spite of large and varying time-delays between the operator and the robot, while accommodating fixed or online-adaptable AA factors. The stability methods are robust towards system modeling errors.

Fig. 1.4 shows a schematic of the thesis contribution, which consists of a novel haptic shared control framework integrating teleoperation and autonomy in an adaptive manner with improved transparency, while maintaining overall system stability. In terms of teleoperation transparency, two new methods are presented and a novel stability ensuring approach is developed to stabilize any user-defined feedback controllers in time-delayed teleoperation. In terms of arbitration in shared control, the factors that might lead to system instability are first analyzed and identified. Then, two methods are presented which can remove the effects of these factors which are applicable in different forms of multi-agent robot control. Both contributions, the teleoperation transparency enhancement and adaptive multi-agent control stability, are developed and presented in ways so that different groups working in these fields can avail them.
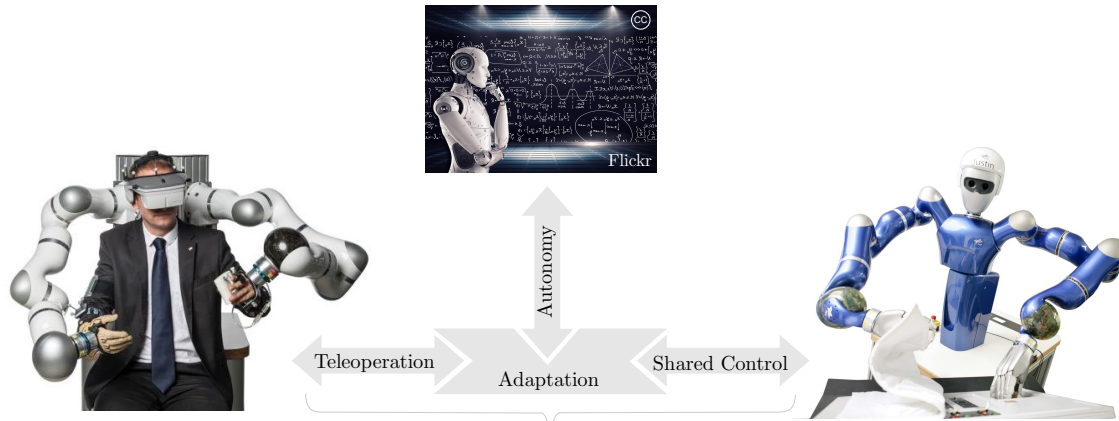
A Stable and Transparent Framework for Adaptive Shared Control of Robots

Figure 1.4: Contribution of this thesis.

The research performed in this thesis has contributed to the theoretical field in addition to being extensively used in practical scenarios and validated with hardware experiments. The methods were applied in several projects and practical applications (like the European Union H2020 project AEROARMS, Kontur-2 space mission for ISS-Ground teleoperation etc).

The structure of the thesis is summarized in Fig. 1.5. Chapter 2 discusses the basic theoretical tools, which this thesis employs. Firstly, the concept of finite-gain stability is explained following which, passivity, a tool that has been extensively used in this work to achieve finite-gain stability of a shared control system, is presented. Later, the widely used definitions and performance indices of transparency are covered.

Chapter 3, then presents two methods to improve transparency of a teleoperation system. To this end, non-linear local force feedback control and explicit force controllers are used. To overcome the limitations imposed by trade-offs between stability and transparency, a new and general stability method, namely, passive reference coupling (PCR), which guarantees stability for any user-defined feedback controller is finally proposed. The PCR approach can be used by different research groups working in teleoperation and it is validated for a practical task that requires precision in both position following and force application.

Chapter 4 addresses adaptive authority allocation in shared control. First, a system-driven adaptive shared control is introduced. Unlike existing methods, this approach smoothly concedes control authority to the human operator based on real sensor measurement noise. The results of a user-study are presented for this approach. The next two sections in this chapter present two methods for a general multi-agent robot control system with varying authority using force and stiffness scaling. The factors that destroy passivity while fixed scaling and adapting the AA factors are identified and then model-independent methods are developed to ensure stability of the control system. Both these methods are validated on real robotic hardware.

Chapter 5 consolidates all the methods from the two previous chapters, where the final framework is presented. The transparent segment of the teleoperation is combined with autonomous controllers in an adaptive shared control form, while maintaining the stability of the entire system including haptic feedback of the forces produced by the ACS. The framework is validated on real hardware, the performance of different methods presented is compared and a discussion on the system behavior is given at the end of this chapter.

Chapter 6 presents the practical applications of the research, where the main projects in space and terrestrial domains that used the methods developed during this thesis work are summarized. Additionally, several secondary contributions were made by the author in other domains of robot control, which resulted in many publications and were availed in several projects. Some of the main secondary contributions are also summarized in this chapter.

Chapter 7 concludes the thesis. The research led to several positive theoretical results practically validated on real hardware and used by several projects. However, detailed analysis helped identify some limitations of these methods which are clearly discussed and presented in the previous chapters. These limitations and learned lessons could lead to further extensions and are mentioned in this concluding chapter.

The research findings reported in this thesis resulted in ten conference and two journal publications, and three patents. These main publications on which this thesis is based are summarized in Table 1.1. Furthermore, seventeen conference and six journal publications have been co-authored, which are related to the control topic but not integrated in this thesis. These are listed in Table 1.2.

To summarize: **The main contributions of this thesis are listed here:**

1. Developed a unified framework for stable and transparent adaptive shared control which is highly modular.

2. Two different approaches (non-linear local force feedback and explicit force control in Chapter 3) are developed to improve force feedback transparency in teleoperation and haptic shared control.

3. Developed a new method to ensure stability of time-delayed teleoperation systems with arbitrary user-defined feedback controllers which can avail existing passivity tools.

4. A novel system-driven method for arbitration is developed, which can be used not only in robotics, but other domains of human-machine interaction.

5. Arbitration is formulated as both force and stiffness scaling problems, the analysis of which would give the reader a better understanding of the system behavior.

6. The theoretical developments from the thesis are validated in multiple robotics systems and availed in several projects.

7. The work in this thesis was published in six conferences and one journal (and one more submitted).

8. The work done during this thesis also supported other researchers, which resulted in sixteen publications (four in journals and twelve on conferences and workshops) as second author.

9. In addition to these first and second author works, twelve other publications were co-authored in leading conferences and journals.

10. Three patents were submitted out of which one is already granted.
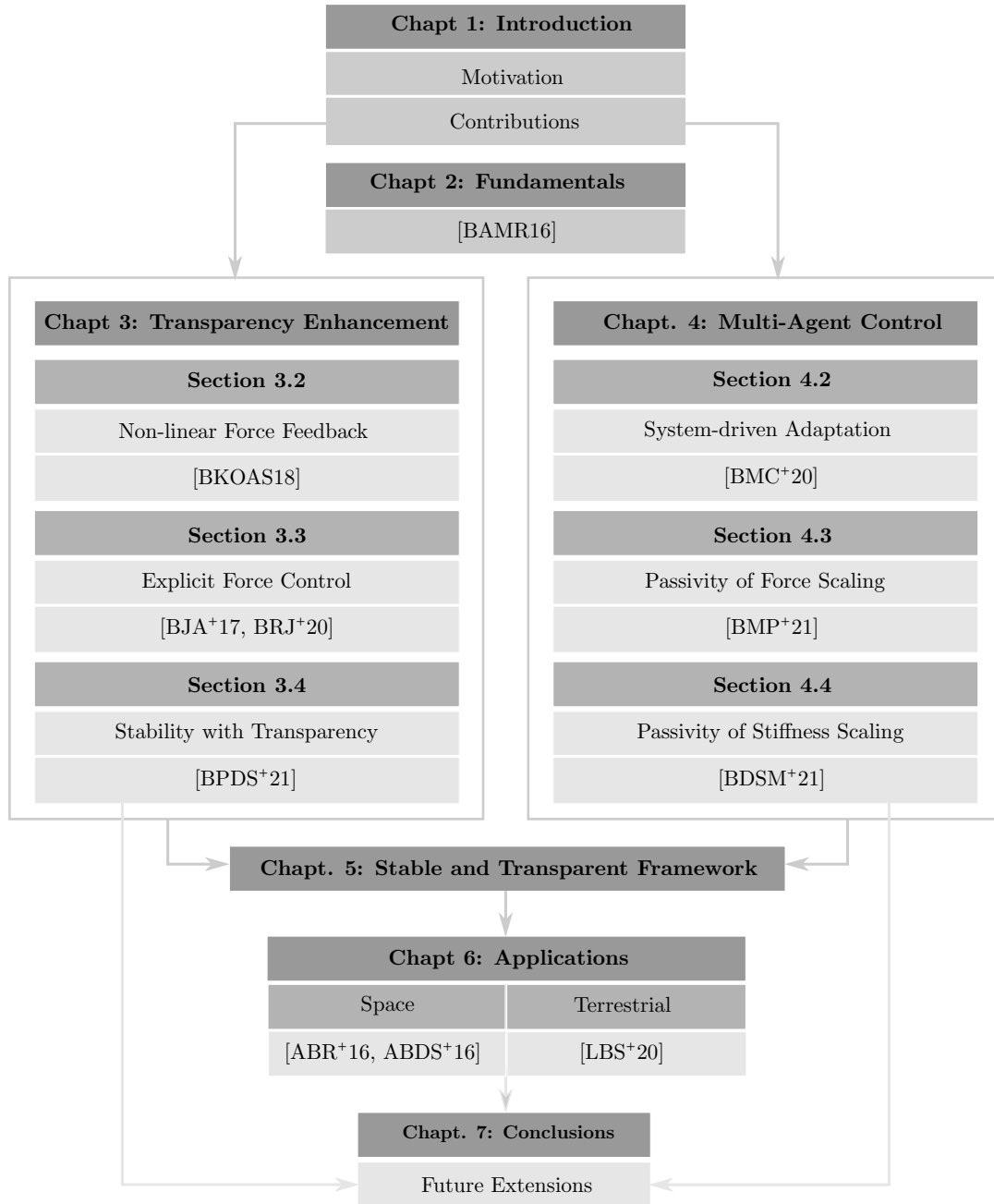
Figure 1.5: Structure of the thesis

Table 1.1: Main publications on which the thesis is based.

Reference	Details
[BMP⁺21] *Conference*	**Balachandran, R.**, Mishra, H., Panzirsch, M., and Ott, C., A Finite-Gain Stable Multi-Agent Robot Control Framework with Adaptive Authority Allocation, International Conference on Robotics and Automation (ICRA), 2021.
[BPDS⁺21] *Journal*	**Balachandran, R.**, Panzirsch, M., De Stefano, M., Singh, H., Ott, C. and Albu-Schaeffer, A., Stabilization of User-Defined Feedback Controllers in Teleoperation With Passive Coupling Reference. IEEE Robotics and Automation Letters, 2021.
[BMC⁺20] *Conference*	**Balachandran, R.**, Mishra, H., Cappelli, M., Weber, B., Secchi, C., Ott, C. and Albu-Schaeffer, A., Adaptive Authority Allocation in Shared Control of Robots Using Bayesian Filters. IEEE ICRA, 2020.
[BRJ⁺20] *Conference*	**Balachandran, R.**, Ryu, J.H., Jorda, M., Ott, C. and Albu-Schaeffer, A., Closing the force loop to enhance transparency in time-delayed teleoperation. IEEE ICRA, 2020.
[BKOAS18] *Conference*	**Balachandran, R.**, Kozlova, N., Ott, C. and Albu-Schaeffer, A., Non-linear local force feedback control for haptic interfaces. IFAC-PapersOnLine, 2018.
[BJA⁺17] *Conference*	**Balachandran, R.**, Jorda, M., Artigas, J., Ryu, J.H. and Khatib, O., Passivity-based stability in explicit force control of robots. IEEE ICRA, 2017.
[BAMR16] *Conference*	**Balachandran, R.**, Artigas, J., Mehmood, U. and Ryu, J.H., Performance comparison of wave variable transformation and time domain passivity approaches for time-delayed teleoperation: Preliminary results. IEEE/RSJ IROS, 2016.
[BDSM⁺21] *Journal - Submitted*	**Balachandran, R.**, De Stefano, M., Mishra, H., Ott, C. and Albu-Schaeffer, A., Passive Arbitration in Adaptive Shared Control of Robots with Variable Force and Stiffness Scaling, Mechatronics, 2021.
[LBS⁺20] *Conference*	Lee, J., **Balachandran, R.**, Sarkisov, Y.S., De Stefano, M., Coelho, A., Shinde, K., Kim, M.J., Triebel, R. and Kondak, K., Visual-inertial telepresence for aerial manipulation. IEEE ICRA 2020
[ABR⁺16] *Conference*	Artigas, J., **Balachandran, R.**, Riecke, C., Stelzer, M., Weber, B., Ryu, J.H. and Albu-Schaeffer, A., Kontur-2: force-feedback teleoperation from the international space station. IEEE ICRA , 2016.
[ABDS⁺16] *Conference*	Artigas, J., **Balachandran, R.**, De Stefano, M., Panzirsch, M., Lampariello, R., Albu-Schaeffer, A., Harder, J. and Letschnik, J., Teleoperation for on-orbit servicing missions through the astra geostationary satellite. IEEE Aerospace Conference, 2016.
[JBRK17] *Conference*	Jorda, M., **Balachandran, R.**, Ryu, J.H. and Khatib, O., Passivity-based stability in explicit force control of robots. IEEE IROS, 2017.
[AB15] *Patent*	Artigas, J. and **Balachandran, R.**, Kontroll-Netzwerk mit einem haptischen Eingabemittel: DE102014004115 B3, 2015.
[BM20] *Patent - Submitted*	**Balachandran, R.** and Mishra, H., Adaptive Authority Allocation in Shared Control based on sensor measurement noise (Submitted), 2020.
[BP21] *Patent - Submitted*	**Balachandran, R.** and Panzirsch, M., Passive Coupling Reference Approach for user-defined feedback stability in haptics and teleoperation (Submitted), 2021.

Table 1.2: Publications of secondary contributions.

Reference	Details
[MBDSO21a] *Journal*	Mishra, H., **Balachandran, R.**, De Stefano, M. and Ott, C., A Compliant Partitioned Shared Control Strategy for an Orbital Robot, IEEE RA-L 2021.
[DSBS19] *Journal*	De Stefano, M., **Balachandran, R.** and Secchi, C., A passivity-based approach for simulating satellite dynamics with robots: Discrete-time integration and time-delay compensationIEEE Transactions on Robotics, 2019.
[PBW⁺18] *Journal*	Panzirsch, M., **Balachandran, R.**, Weber,. B, Ferre, M. and Artigas, J., Haptic augmentation for teleoperation through virtual grasping points. IEEE Transactions on Haptics, 2018
[HBRG⁺18] *Journal*	Henze, B., **Balachandran, R.**, Roa-Garzon, M., Ott, C. and Albu-Schaeffer, A., Passivity analysis and control of humanoid robots on movable ground, RA-L 2018.
[DSMB⁺19] *Journal*	De Stefano, M., Mishra, H., **Balachandran, R.**, Lampariello, R., Ott, C. and Secchi, C., Multi-rate tracking control for a space robot on a controlled satellite: A passivity-based strategy IEEE RA-L, 2019.
[HPS⁺21] *Journal*	Hulin, T., Panzirsch, M., Singh, H., Coelho, A., **Balachandran, R.**, and others, Model-Augmented Haptic Telemanipulation: Concept, Retrospective Overview and Current Use-Cases, Frontiers in Robotics and AI, 2021
[OHF⁺18] *Journal*	Ollero, A. et al The aeroarms project: Aerial robots with advanced manipulation capabilities for inspection and maintenance, IEEE Robotics- Automation Magazine, 2018
[PB19] *Conference*	Panzirsch, M. and **Balachandran, R.**, Time Domain Control for Passive Variable Motion Scaling in Delayed Teleoperation IFAC-PapersOnLine, 2019.
[WBR⁺19] *Conference*	Weber, B., **Balachandran, R.**, Riecke, C., Stulp, F. and Stelzer, M., Tele-operating robots from the international space station: Microgravity effects on performance with force feedback, IEEE IROS 2019.
[KBDS⁺18] *Conference*	Kim, M.,**Balachandran, R.**, De Stefano, M., Kondak, K. and Ott, C., Passive compliance control of aerial manipulators. IEEE IROS, 2018.
[PBA⁺17] *Conference*	Panzirsch, M., **Balachandran, R.**, Artigas, J., Riecke, C., Ferre, M. and Albu-Schaeffer, A., Haptic intention augmentation for cooperative teleoperation, IEEE ICRA 2017.
[DSBG⁺18] *Conference*	De Stefano, M., **Balachandran, R.**, Giordano, A. and Secchi, C., An energy-based approach for the multi-rate control of a manipulator on an actuated base. IEEE ICRA , 2018.
[ABDS⁺16] *Conference*	De Stefano, M., **Balachandran, R.**, Artigas, J. and Secchi, C.,Reproducing physical dynamics with hardware-in-the-loop simulators: A passive and explicit discrete integrator, IEEE ICRA 2017.
[SBE16] *Workshop*	Schmidt, P., **Balachandran, R.** and Artigas, J., Shared control for robotic on-orbit servicing. Robotics: Science and Systems Workshop, 2016.
[PBA15] *Conference*	Panzirsch, M., **Balachandran, R.** and Artigas, J., Cartesian task allocation for cooperative, multilateral teleoperation under time delay, IEEE ICRA 2015.
[CSL⁺21] *Conference*	Coelho, A.,Sarkisov, Y.,Lee, J., **Balachandran, R.**, Franchi, A., Kondak, K. and Ott, C., Hierarchical Control of Redundant Aerial Manipulators with Enhanced Field of View, IEEE International Conference on Unmanned Aircraft Systems (ICUAS) 2021.
[KFG⁺20] *Conference*	Krueger, T., Ferreira, E. and others, Designing and Testing a Robotic Avatar for Space-to-Ground Teleoperation: the Developers Insights, International Astronautical Congress (IAC) 2020.

Table 1.3: Publications of secondary contributions: Continued

Reference	Details
[RWM+20] *Conference*	Riecke, C., Weber, B., Maier, M., Stelzer, M., **Balachandran, R.**, Kondratiev, A. and others, Kontur-3: Human Machine Interfaces for Telenavigation and Manipulation of Robots from ISS, IEEE Aerospace Conference 2020.
[WMPH+18] *Conference*	Weber M., Pereira, A., Hulin, T., Ruf, O., Kugler, S., Giordano, A., **Balachandran, R.** and others, Space Factory 4.0-New processes for the robotic assembly of modular satellites on an in-orbit platform based on Industrie 4.0 approach, IAC 2018.
[CSM+18] *Conference*	Coelho, A., Singh, H., Muskardin, T., **Balachandran, R.** and Kondak, K., Smoother position-drift compensation for time domain passivity approach based teleoperation, IEEE IROS 2018.
[RAB+16] *Conference*	Riecke, C., Artigas, J., **Balachandran, R.** and Bayer, R., Beyer, A. and others, Kontur-2 mission: the DLR force feedback joystick for space telemanipulation from the ISS, IEEE iSAIRAS International Symposium on Artificial Intelligence, Robotics and Automation in Space 2016.
[WSR+16] *Conference*	Weber, B., and Schaetzle, S., Riecke, C., Brunner, B., Tarassenko, S., and Artigas, J., **Balachandran, R.** and Albu-Schaeffer, A., Weight and weightlessness effects on sensorimotor performance during manual tracking, International Conference on Human Haptic Sensing and Touch Enabled Computer Applications 2016.
[ARW+16] *Conference*	Artigas, J., Riecke, C., Weber, B., Stelzer, M., **Balachandran, R.** and others, Force-feedback teleoperation of on-ground robots from the international space station in the frame of the Kontur-2 experiment, International Extreme Robotics Conference 2016.
[SADS+15] *Conference*	Schmidt, P., Artigas, J., De Stefano, M., **Balachandran, R.** and Ott, C., Increasing the Performance of Torque-based Visual Servoing by applying Time Domain Passivity, IFAC-PapersOnLine 2015.

Fundamentals

Chapter 2 briefly reviews the basics that are required for the theoretical investigations in this thesis. As explained in Section 1.1, two main criteria for a good teleoperation system are *stability* and *transparency*. The concept of stability for an input-output system is introduced in Section 2.1. To be more precise, the concept of finite-gain stability is dealt with. Since, passivity of the input-output system is closely related to its finite-gain stability, the concept of passivity is explained in Section 2.1.2 giving more emphasis on *output-strict passivity* and its relation to finite-gain stability. This is followed by some tools and methods used in this thesis to make control systems passive. Second part of this chapter deals with the other performance criterion, *transparency*, which is introduced in Section 2.2 along with existing measures to evaluate and compare transparency of teleoperation systems.

2.1 Stability of Input-Output Systems

In a bilateral teleoperation system, the human operator applies a force to move the haptic device, which in turn is coupled to the remote robot and moves it. The robot interacts with its environment to complete the intended task. The forces produced by the robot-environment interaction directly affect the motion of the robot. Additionally, the motion of the haptic device is indirectly affected by the robot-environment interaction, due to the feedback forces. Therefore, as shown in Fig. 2.1, the bilateral teleoperation system can be formulated as an input-output system, with input as the forces from the operator and the environment, and output as the motion of the haptic device and robot.
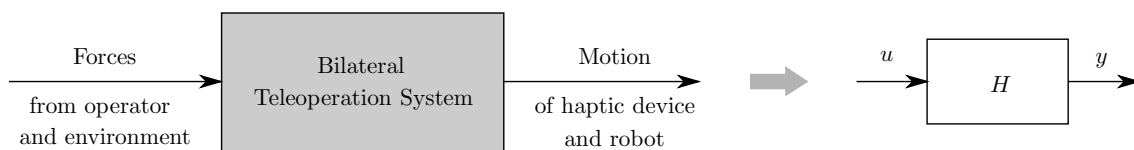

Figure 2.1: Bilateral teleoperation system as an input-output system

A time-invariant input-output system H as shown on the right side of Fig. 2.1, is represented with a non-linear state-space model as:

$$H : \begin{cases} \dot{x} = f(x, u) \\ y = h(x, u) \end{cases} \tag{2.1}$$

with input $u \in \mathbb{R}^m$, output $y \in \mathbb{R}^m$, and state $x \in \mathbb{R}^n$. The function $f : \mathbb{R}^n \times \mathbb{R}^m \to \mathbb{R}^n$ is locally Lipschitz, and $h : \mathbb{R}^n \times \mathbb{R}^m \to \mathbb{R}^m$ is continuous, and $f(0,0) = h(0,0) = 0$. Note that the system has the same number of inputs and outputs here [Kha02].

2.1.1 Input-Output Stability

Now a generally accepted form of stability in input-output systems, namely, finite-gain L_2 stability [Def. 5.1][Kha02], is introduced[1].

Definition 2.1. *(L_2 **Stability**) The dynamical system represented in (2.1) is finite-gain L_2 stable if there exist non-negative constants γ and β such that*

$$\|y_\tau\|_{L_2} \le \gamma \|u_\tau\|_{L_2} + \beta \quad for \ all \quad u_\tau \in L_{2e}^m \quad and \quad \tau \in [0, \infty). \tag{2.2}$$

The term $\bullet_\tau$ is a truncation of $\bullet$, that is:

$$\bullet_\tau (t) = \begin{cases} \bullet(t), & \text{if } 0 \le t \le \tau, \\ 0 & \text{if } t \ge \tau. \end{cases} \tag{2.3}$$

$u_\tau \in L_{2e}^m$ means that the L_2 norm of u_τ is finite. The value γ is called the gain of the system and β is the bias. In other words, the system is finite-gain L_2 stable if the L_2 norm of the output is always bounded by a finite value times L_2 norm of the input, for inputs with bounded L_2 norms.

Example of a finite-gain stable system:

Consider a mass M placed on a surface with viscous friction (damping) D as shown in Fig. 2.2. Let the mass be pushed by a human with a force F_h, as a result of which it moves with a velocity V.
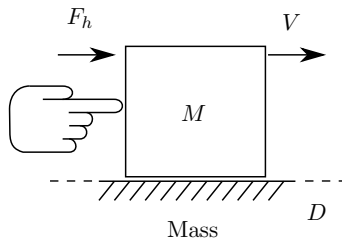

Figure 2.2: Example of a finite-gain stable system.

The equation of motion of the mass is given by:

$$M\dot{V} = F_h - DV. \tag{2.4}$$

---

[1]Note that the definitions only give an overview of the concepts here. For rigorous mathematical descriptions, readers are advised to refer [Kha02]

Here the input to the system is the force F_h and output is its velocity V. If the human continues to apply the force, at some point V will grow so large that the damping force DV will equal the force exerted on it by the human. At this point, the net force acting on the mass becomes zero and the mass will stop accelerating. That is, $F_h - DV = M\dot{V} = 0$, when $F_h = DV$. The velocity of the mass at this point is given by $V = \frac{F_h}{D}$. This means that for the bounded input force F_h, the velocity of the mass is bounded by the value $\frac{F_h}{D}$ and the system is finite-gain L_2 stable with a gain $\frac{1}{D}$.

2.1.2 Passivity

In a teleoperation system, physical energy is exchanged between the different components. The concept of passivity is linked to the dissipative properties of a system, which is closely related to the physical energy [OPNSR13]. Thus passivity is a property that has been used to analyze the energetic behavior of the components and to ensure finite-gain stability of the closed-loop system. The definition of passivity is given in [Def. 6.3][Kha02] and is reported here as follows:

Definition 2.2. *(Passivity) The system represented in (2.1) is passive with respect to input u and output y, if there exists a continuously differentiable, positive semi-definite function $S(x)$ (storage function), such that*

$$\dot{S} \leq u^T y \Leftrightarrow S(x(t)) - S(x(0)) \leq \int_0^t u(\tau)^T y(\tau) d\tau \quad \forall \ t > 0. \tag{2.5}$$

If the storage function chosen is the total energy of the system, the passivity property in (2.5), can be physically interpreted as:

$$\underbrace{S(x(t))}_{\text{Current energy}} \leq \underbrace{S(x(0))}_{\text{Initial energy}} + \underbrace{\int_0^t u(\tau)^T y(\tau) d\tau}_{\text{Energy input/output}}. \tag{2.6}$$

Therefore, if the energy stored in a system at any point of time is less than or equal to the sum of the initial stored energy and the energy transferred to/from the system via the input-output pair (u, y), it is passive. Now a special case of passivity, namely, output-strict passivity is defined in the following.

Definition 2.3. *(Output-strict passivity) The system represented in (2.1) is said to be output-strict passive if there exists a continuously differentiable, positive semi-definite function $S(x)$ (storage function), such that for $\delta > 0$*

$$\dot{S} \leq u^T y - \delta y^T y \Leftrightarrow S(x(t)) - S(x(0)) \leq \int_0^t u(\tau)^T y(\tau) d\tau - \int_0^t \delta y(\tau)^T y(\tau) d\tau. \tag{2.7}$$

As in (2.6), the output-strict passivity (OSP) property in (2.7), can be physically interpreted as:

$$\underbrace{S(x(t))}_{\text{Current energy}} \leq \underbrace{S(x(0))}_{\text{Initial energy}} + \underbrace{\int_0^t u(\tau)^T y(\tau) d\tau}_{\text{Energy input/output}} - \underbrace{\int_0^t \delta y(\tau)^T y(\tau) d\tau}_{\text{Dissipated energy}}, \tag{2.8}$$

where the dissipated energy has to be a positive-definite function of the output of the system. Now that the definitions for finite-gain stability and passivity are introduced, the relation between the two concepts is presented in the next section.

27

Passivity and Finite-Gain Stability

Lemma 1. *If the system represented in (2.1) with $f(0,0) = h(0,0) = 0$, is output-strict passive with $\dot{S} \le u^T y - \delta y^T y$, for some $\delta > 0$, then it is finite-gain L_2 stable and its L_2 gain is less than or equal to $\frac{1}{\delta}$.*

The proof for Lemma 1 can be found in [Lemma 6.5][Kha02]. Here, the single mass example from Fig. 2.2, which was shown to be finite-gain L_2 stable, is used again to illustrate that OSP is a sufficient condition for L_2 stability. To analyze passivity of the mass pushed by the human, consider its kinetic energy as the storage function, that is, $S_m = \frac{MV^2}{2}$. Taking the time derivative of S_m and using (2.4), we get:

$$\dot{S}_m = VM\dot{V} = V(F_h - DV) = VF_h - DV^2, \tag{2.9}$$

which makes the system OSP for the input F_h, and output V. The presence of the damping term D makes the mass (single dynamical system) both OSP and L_2 stable.

Interconnection of Passive Systems

When it comes to multiple dynamical systems interacting energetically with each other, the interconnection properties of passive systems can be used to prove overall passivity. Consider two passive systems H_1 and H_2 as shown in Fig. 2.3.

Parallel Interconnection: When the systems are connected in parallel as in Fig. 2.3a, the input u_1 to H_1 and u_2 to H_2 is the same common input u. The final output y is the sum of the two outputs y_1 and y_2.

Feedback Interconnection: When the systems are connected with a *negative* feedback as in Fig. 2.3b, the input u_1 to H_1 is the difference between the original input e_1 and the output y_2 of H_2. Also, the input u_2 to H_2 is the sum of the original input e_2 and the output y_1 of H_1.

(a) Parallel   (b) Feedback

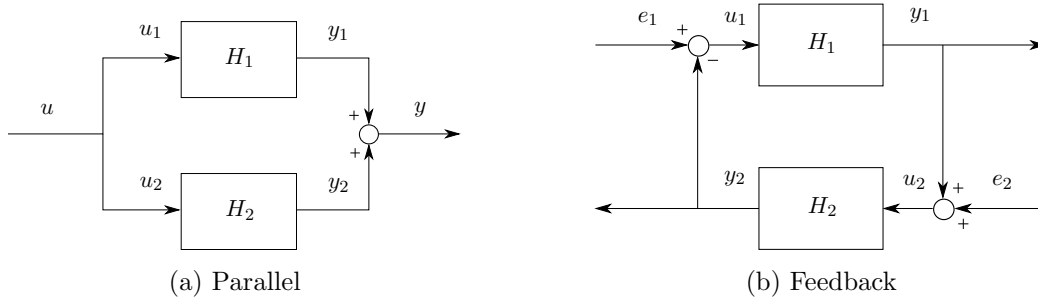Figure 2.3: Interconnection of passive systems

The following lemmas[2] are essential properties of passive systems, which are used extensively in this thesis.

Lemma 2. *Parallel interconnection* *of passive systems results in a passive system.*

Lemma 3. *Feedback interconnection* *of passive systems results in a passive system.*

---

[2]The proofs for Lemma 2 and Lemma 3 can be found in [Kha02].

Finite-Gain Stability of Teleoperation System

To present the passivity tools in the following sections, the mechanical representation of the simplest form of teleoperation— a two-mass, spring-damper coupling system is considered as shown in Fig. 2.4.
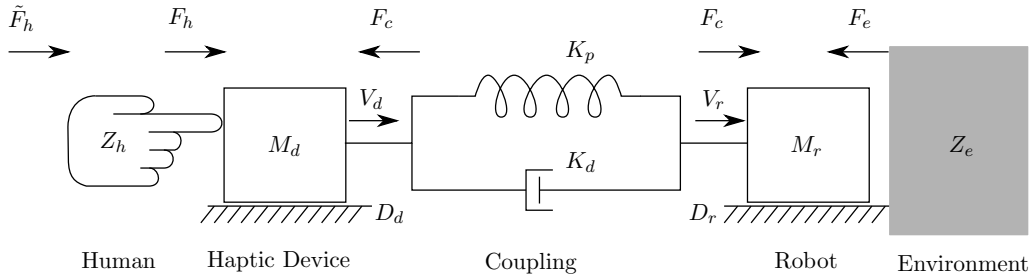

Figure 2.4: Physical representation of a teleoperation system.

A human operator moves a haptic/input device, represented by mass M_d and physical damping D_d applying a force F_h. The force F_h arises due to the exogenous force $\tilde{F}_h$ (say, the force desired by the human's muscles) and the interaction of human impedance Z_h. The haptic device moves with a velocity V_d and is physically connected to a robot, with mass M_r and damping D_r, using a spring-damper coupling with stiffness K_p and damping K_d. The robot moves with a velocity V_r due to the net force applied on it from the coupling F_c and the interaction force F_e due to the environment impedance Z_e. X_d and X_r are the positions of the haptic device and robot, respectively. The input device also receives feedback of the force F_c produced by the coupling. The equations of motion for the masses are:

$$\begin{aligned} M_d \dot{V}_d &= F_h - F_c - D_d V_d, \\ M_r \dot{V}_r &= F_c - F_e - D_r V_r, \end{aligned} \tag{2.10}$$

and the coupling force F_c is given by:

$$F_c = K_p(X_d - X_r) + K_d(V_d - V_r). \tag{2.11}$$

Since this single degree-of-freedom (DoF) representation of a teleoperation system is a multi-body dynamical system, the passive interconnection property from Lemma 3 is used here and the overall passivity of the teleoperation system is shown in Table 2.1. In the first two rows of Table 2.1, passivity of the individual subsystems are shown. For this, the storage functions for the haptic device and the robot are their kinetic energies, S_d and S_r, respectively and for the coupling, the potential energy stored in the spring is chosen as the storage function S_c. The time derivatives of these storage functions show their OSP property as per Def. 2.3.

Since the teleoperation system is a feedback interconnection of these three subsystems, the storage function S_t of the overall system is chosen to be the sum of the individual storage functions as shown in the last row of Table 2.1. The time derivative of S_t shows that the overall teleoperation is still OSP for the inputs $(F_h, -F_e)$ and outputs (V_d, V_r), and is therefore finite-gain L_2 stable as per Lemma 1 and Lemma 3.

Table 2.1: Teleoperation system as an interconnection of passive systems

Device: $u = (F_h, -F_c)$, $y = (V_d, Vd)$	Coupling: $u = (V_d, -V_r)$, $y = (F_c, Fc)$	Robot: $u = (F_c, -F_e)$, $y = (V_r, V_r)$
$S_d = \frac{1}{2} M_d V_d^2$	$S_c = \frac{1}{2} K_p (X_d - X_r)^2$	$S_r = \frac{1}{2} M_r V_r^2$
$\dot{S}_d = V_d M_d \dot{V}_d,$	$\dot{S}_c = K_p (X_d - X_r)(V_d - V_r),$	$\dot{S}_r = V_r M_r \dot{V}_r,$
$\quad = V_d(F_h - F_c - D_d V_d),$	$\quad = [F_c - K_d(V_d - V_r)](V_d - V_r),$	$\quad = V_r(F_c - F_e - D_r V_r),$
$\quad = \underbrace{V_d F_h - V_d F_c - D_d V_d^2}_{\text{OSP}}$	$\quad = \underbrace{V_d F_c - V_r F_c - K_d(V_d - V_r)^2}_{\text{Passive}}$	$\quad = \underbrace{V_r F_c - V_r F_e - D_d V_r^2}_{\text{OSP}}$

Entire Teleoperation System: $u = (F_h, -F_e)$, $y = (V_d, V_r)$
$S_t = S_d + S_c + S_r$ $\dot{S}_t = \dot{S}_d + \dot{S}_c + \dot{S}_r,$ $\quad = V_d F_h - \cancel{V_d F_c} - D_d V_d^2 + \cancel{V_d F_c} - \cancel{V_r F_c} - K_d(V_d - V_r)^2 + \cancel{V_r F_c} - V_r F_e - D_d V_r^2,$ $\quad = \underbrace{V_d F_h - V_r F_e - D_d V_d^2 - D_r V_r^2 - K_d(V_d - V_r)^2}_{\text{OSP}}$

2.1.3 Passivity Tools and Methods

In this section, certain tools used to ensure passivity of components of dynamical systems will be covered. These tools enable us later to apply the passivity properties from Lemma 1 and Lemma 3 on complex physical systems to finally ensure the finite-gain stability.

Power-Correlated Variables and Port-Networks

When dynamical systems interact with each other (as in the teleoperation system from Fig. 2.4), the interactions can be seen as exchange of energy or power. A physical system can be analyzed using a pair of power-correlated dual variables called, flow and effort. These dual variables define a power port and their duality product is power [ARPH11].

Definition 2.4. (Power-Port): *A power-port is represented by a pair of effort ($e \in \mathbb{R}^p$) and flow ($f \in \mathbb{R}^p$) variables, whose product $P = e^T f$ is the power traversing the port.*

Power-ports are very useful in analyzing the energetic behavior of interconnected systems. In a mechanical system, the effort variable is the force applied, and the flow variable is its velocity. From ports connected with each other, the product of the effort and flow variables (force and velocity, respectively) gives the mechanical power, whose integral over time gives the physical energy exchanged between the ports. When multiple subsystems are connected together, the overall system can be represented by combining *1-port*, *2-port* or *n-port* into a **port-network**. Representation of a system in form of a port-network is called a port-network model. Fig. 2.5 shows the representations of a 1-port and a 2-port.

For the 1-port network shown in Fig. 2.5a, the power flow $P_1(t)$ at any time t is computed by $P_1(t) = e_1(t)^T f_1(t)$. Then the total energy $E_{1p}(t)$ exchanged through the port at time t is given by:

$$E_{1p}(t) = \int_0^t e_1(\tau)^T f_1(\tau) d\tau. \tag{2.12}$$

The 2-port network in Fig. 2.5b interacts with the rest of the system through two ports with power correlated variables (e_1, f_1) and (e_2, f_2). A positive value of P_i $(i = 1, 2)$
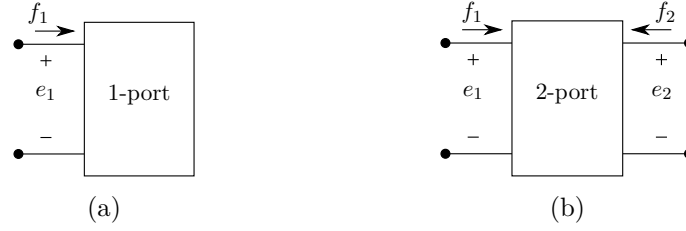
Figure 2.5: 1-port and 2-port networks

implies that power flows into the port and negative value shows that power is drawn out of the port.

$$
\begin{aligned}
P_i^{in} &= e_i^T f_i, \text{ if } e_i^T f_i \geq 0, \\
P_i^{out} &= -e_i^T f_i, \text{ otherwise.}
\end{aligned}
\tag{2.13}
$$

Then, energy flow in and out of the port is $E_i^{\bullet} = \int_0^t P_i^{\bullet}(\tau)d\tau$ with ($\bullet = (in, out)$). So, the total energy exchange between the 2-port and rest of the system is:

$$
\begin{aligned}
E_{2p}(t) &= \int_0^t (e_1(\tau)^T f_1(\tau) + e_2(\tau)^T f_2(\tau))d\tau, \\
&= E_1^{in} - E_1^{out} + E_2^{in} - E_2^{out}.
\end{aligned}
\tag{2.14}
$$

Since E_{1p} and E_{2p} are the energy exchanged with the rest of the system, passivity of the 2-port can be defined here based on the definition of passivity from Def. 2.2 and the energy-based interpretation in (2.6).

Definition 2.5. *(Passivity of 2-port) The 2-port with power correlated variables (e_1, f_1) and (e_2, f_2) is passive if for initial energy $E(0)$ there exists a lower bounded energy function $E(t)$, such that*

$$
E(t) = E(0) + \int_0^t (e_1(\tau)^T f_1(\tau) + e_2(\tau)^T f_2(\tau))d\tau \geq 0, \quad \forall t > 0.
\tag{2.15}
$$

This means that the energy stored in the 2-port has to be non-negative at all times, which is the case with physical energy of a mechanical system. These principles can be used to analyze the energetic behavior and passivity of a system, which will be shown later. To derive the port-network of any interconnected system, a straight-forward method is to use electrical circuits, which will be shown in the following section.

Electrical Circuits for deriving Port-Networks
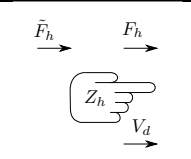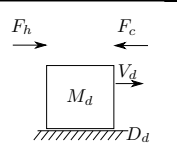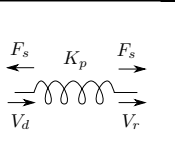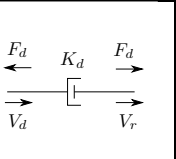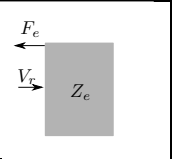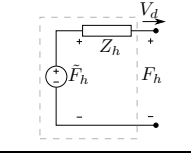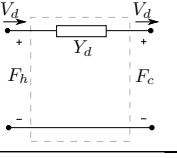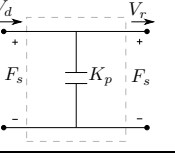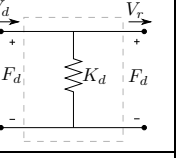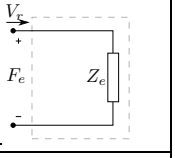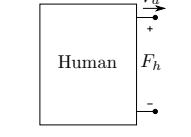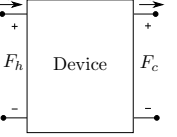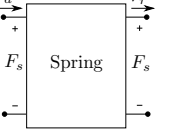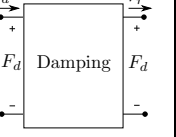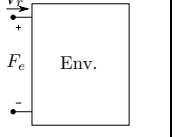
The first step in the derivation of the port-network of a mechanical system is to convert it into its electrical circuit, from which the effort and flow variables of the different ports can be directly identified. In this thesis, the *force-voltage* mechanical-electrical analogy is used to derive the electrical circuit, that is, force applied on/by each component is the voltage in the electrical domain, and the velocity of each component is the current. The variables in both domains for all the entities in the system are shown in Table 2.2.

. The teleoperation system from Fig. 2.4 is used as an example and each of its mechanical components is converted into the electrical domain and is shown in Table 2.3. In a spring-damper coupling, the final force produced $F_c = F_s + F_d$, where F_s and F_d are the forces produced by the spring and damper, respectively.

Table 2.2: Force-Voltage mechanical-electrical conversion table

Mechanical Domain	Electrical Domain
Force	Voltage
Velocity	Current
Mass	Inductance
Damping	Resistance
Stiffness	Elastance
Compliance	Capacitance

Table 2.3: Mechanical, electrical and port-network of teleoperation subsystems

Note that the *human* and the *environment* are represented as 1-ports, since they start and terminate the chain of interconnected subsystems. The other components are 2-ports. Also, while converting the human operator, the exogenous force desired by the human is represented in electrical domain as an *independent* voltage source. The impedances (input: velocity, output: force) of the human and environment are represented by Z_h and Z_e, respectively. The admittance (input: force, output: velocity) of the input device is represented by Y_d. Note that the representation of the robot, with admittance Y_r, is similar to that of the input device (with different flow and effort variables), and has not been shown in the table. The dashed box containing the elements in the electrical circuit, can now be converted directly in the ports with well defined effort and flow variables, as shown in the last row of the table. Now, all components of the teleoperation system are combined into an electrical circuit and later into its port-network as shown in Fig. 2.6.

Dependent sources

If the haptic device and the robot are not physically coupled, as is the case with remote teleoperation, the velocity of the haptic device needs to be measured and transmitted to the robot controller. Similarly for having haptic feedback, the forces from the robot side need to be communicated to the haptic device. When a force or velocity in a dynamical system needs to be measured and transmitted for control purposes, the electrical analogy can avail the so called *dependent sources*. A dependent voltage source produces the desired
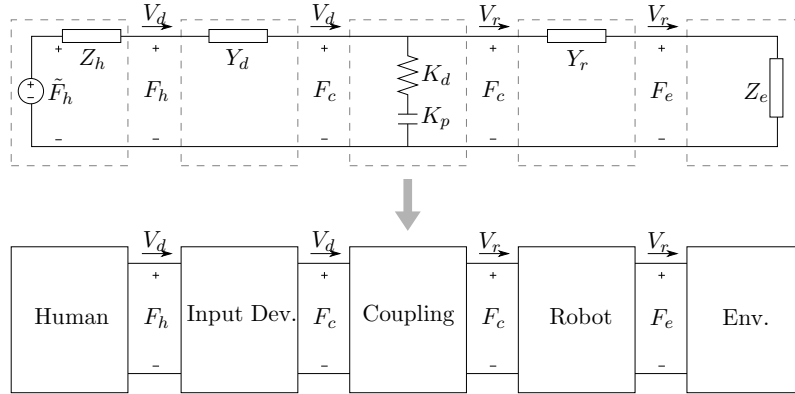
Figure 2.6: Electrical and port representation of the teleoperation system from Fig. 2.4.

voltage across it, irrespective of the current flow. Similarly, a dependent current source can produce the desired current through it, independent of the voltage across it.

To see the practical application of dependent sources, consider the electrical and port network of the teleoperation system in Fig. 2.6. To implement the teleoperation system practically, we will need two systems. One at the operator side, where the input device moves as a result of the human force F_h and the feedback force F_c. On the robot side, the controller gets the transmitted velocity of the haptic device V_d as its desired input. This is shown in Fig. 2.7, where the single electrical circuit in Fig. 2.6 is divided into two circuits and two port-networks. The new port on the operator side 'Receive F_c' uses a dependent voltage source in its electrical analogy. Also, the Port 'Receive V_d' on the robot side uses a dependent current source to give input to the controller. Note that the power on the outputs of the dependent sources are the same, namely $F_c V_d$. This means that the separation of the single circuit to two circuits, in this *particular* case is power preserving, and therefore maintains the passivity properties of the system. If such power preservation and passivity properties cannot be maintained, we can use several methods to enforce passivity, which will be covered in the next section.

Methods for Passivation

In this section, all the tools presented till now will be used to passivate components in a dynamical systems. Three different approaches followed in the research community to passivate systems are discussed here. First, an analytical method is presented to inject damping into the system as soon as the passivity condition is violated. Based on its limitations, the next two methods, namely, Wave Variable Transformation and Time Domain Passivity Approach, will be described.

Method 1: Analytical Damping Injection

In this method, the passivity of the system is analytically checked for, and the terms leading to a certain loss or indefinite guarantee of passivity are canceled off by adding appropriate damping into the system. Consider the single mass example in Fig. 2.2. It was shown in (2.9) that this system is output-strict passive due to the power dissipated by the damping. This was true since the mass was constant. The same system with a time-varying mass, on the other hand, might not be passive. The single DoF system with time-varying mass M' is used as an example here. Again, the kinetic energy of the time-
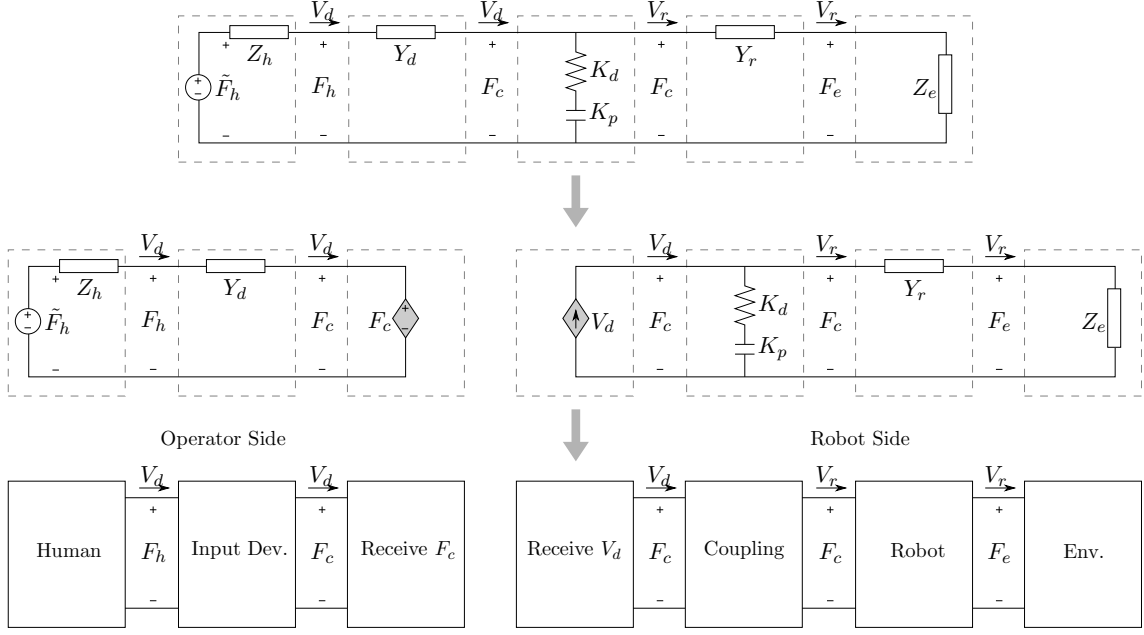
Figure 2.7: Separation of circuits using dependent sources

varying mass is taken as the storage function S'_m to analyze passivity, that is $S'_m = \frac{M'V^2}{2}$. The time derivative gives:

$$\dot{S}'_m = VM'\dot{V} + \frac{\dot{M}'V^2}{2} = VF_h - DV^2 + \underbrace{\frac{\dot{M}'V^2}{2}}_{\text{sign-indefinite}} , \qquad (2.16)$$

The additional sign-indefinite term appearing due to the time-varying nature of mass violates the passivity condition at instances where $\dot{M}'$ is positive. But, if this term can be *observed* and canceled by applying an additional damping term $D_m = \frac{\dot{M}'}{2}$, the system can be passivated again, given by:

$$\dot{S}'_m = VF_h - (D + D_m)V^2 + \frac{\dot{M}'V^2}{2} = VF_h + \left(\frac{\dot{M}'}{2} - D_m - D\right)V^2 = VF_h - DV^2, \ (2.17)$$

which is now output-strict passive for the input F_h and output V.

Limitations: This is an effective approach when the additional sign-indefinite terms in the time-derivation of storage function can be measured or observed, which in many cases is not possible. An example of such a system where the sign-indefinite terms are not directly observable is a communication link with unknown/time-varying delays. In teleoperation systems where the robot is located geographically remote from the human operator, there will be delays in the signals transmitted between the device and the robot and this is a limitation of this analytical method. The port-network of the teleoperation system from Fig. 2.4, with additional delays in the *Comm.* port is shown in Fig. 2.8. $(\bullet')$ is the delayed value of $(\bullet)$.

Method 2: Wave Variable Transformation

Wave Variables Transformation (WVT) is based on scattering parameters and was applied in time-delayed teleoperation in [NS97]. This approach uses a transformation of mechanical
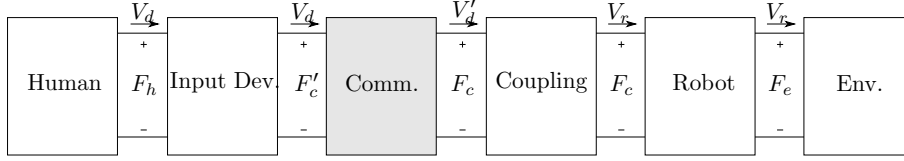
Figure 2.8: Port-network from Fig. 2.6 with communication port.

variables (forces and velocities) into wave variables (forward and backward waves), which are then transmitted through the delayed communication channel. The port-network of the time-delay teleoperation augmented with WVT is shown in Fig. 2.9.
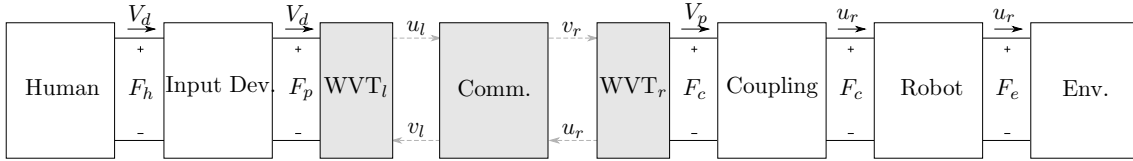
Figure 2.9: Port-network from Fig. 2.8 with WVT.

The new port WVT_l uses the velocity of the haptic device and the approaching wave v_l to derive the forward traveling wave variable u_l, and the passivated force feedback F_p. The signal u_l is delayed across the communication channel and reaches the robot side as v_r, which along with F_c is used by WVT_r to compute the passivated velocity V_p and the forward traveling wave u_r. The transformation equations are:

$$u_l = \sqrt{2b}V_d - v_l, \quad F_p = bV_d - \sqrt{2b}v, \tag{2.18}$$

$$V_p = \frac{F_c + \sqrt{2b}v_r}{b}, \quad u_r = \sqrt{2b}V_p - v_r, \tag{2.19}$$

where b is called the characteristic impedance of the wave. More details on the approach can be found in [NS97].

Limitations: Although WVT is an effective and simple method to passivate teleoperation systems with delays, there are certain limitations to this method [TN04]. The stability of the system is dependent on the characteristic impedance value b. Also the method is not straightforward when the communication channel has time-varying delays or package losses, which are common scenarios in internet-based and space communications links.

Method 3: Time domain Passivity Approach

A method that can handle time-varying delays and package losses in the communication channel is Time Domain Passivity Approach (TDPA). The method was developed for haptic devices [HR02], and was extended to teleoperation [RAP10a]. It has also been used in other fields like satellite dynamic simulation using robots [DSBS19] and humanoid walking robots [HBRG$^+$18], among many others. It uses a passivity observer (PO) which keeps track of the energy flowing through a port. If and when the passivity condition is violated, a passivity controller (PC) applies a time-varying damping to dissipate the extra energy introduced by the port.

To present the approach for a general case, it is applied here for a non-passive 2-port N on the left side in Fig. 2.10. As mentioned earlier, for a non-passive 2-port, TDPA applies time-varying dampers to dissipate extra energy using the POPC concept. Let
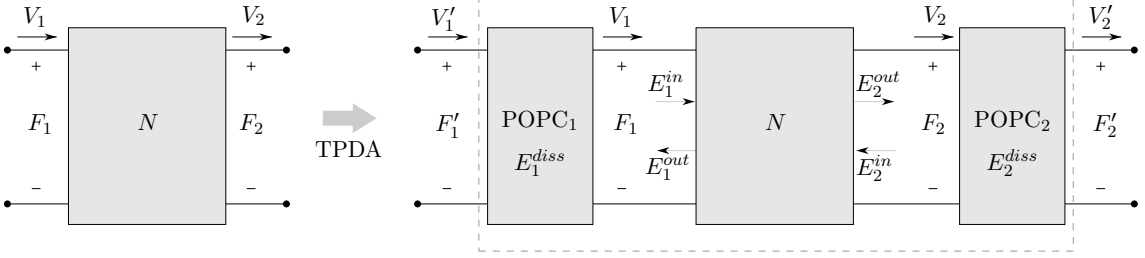
Figure 2.10: Analysis of POPC and Comm. port.

these dampers be denoted by the ports POPC_1 and POPC_2, as shown on the right side in Fig. 2.10 and let the energy dissipated by them be E_1^{diss} and E_2^{diss}, respectively. The objective is to make the feedback interconnection of the three subsystems in the dashed box passive.

The energy transferred to the dashed 2-port, with power correlated variables (V_1', F_1') and (V_2', F_2') at all times is either dissipated by $\text{POPC}_{1,2}$ or is stored in the port N. Therefore, with zero initial energy, the available energy E_D of the dashed port as per (2.14) at the time-step k in discrete time is given by:

$$
\begin{aligned}
E_D(k) \quad = \quad & \sum_0^k \left(V_1'(k)F_1'(k) + V_2'(k)F_2'(k) \right), \\[6pt]
= \quad & \sum_0^k \left(V_1(k)F_1(k) + V_2(k)F_2(k) \right) - E_1^{diss}(k) - E_2^{diss}(k), \\[6pt]
= \quad & E_1^{in}(k) - E_1^{out}(k) + E_2^{in}(k) - E_2^{out}(k) - E_1^{diss}(k) - E_2^{diss}(k), \quad \text{(from (2.14))} \\[6pt]
= \quad & \underbrace{E_2^{in}(k) - E_1^{out}(k) - E_1^{diss}(k)}_{E_1^{obs}(k)} + \underbrace{E_1^{in}(k) - E_2^{out}(k) - E_2^{diss}(k)}_{E_2^{obs}(k)}. \quad (2.20)
\end{aligned}
$$

The condition for passivity of a 2-port from (2.15) requires that $E_D(k) \ge 0, \quad \forall k > 0$. Therefore, if E_1^{obs} and E_2^{obs} in (2.20) are always positive, then the dashed 2-port can be ensured to be passive. This is what the POs on both sides ensure, that is:

$$
\begin{aligned}
\text{PO}_1 \quad &\Rightarrow \quad E_1^{obs}(k) = E_2^{in}(k) - E_1^{out}(k) - E_1^{diss}(k) \ge 0, \\
\text{PO}_2 \quad &\Rightarrow \quad E_2^{obs}(k) = E_1^{in}(k) - E_2^{out}(k) - E_2^{diss}(k) \ge 0. \quad (2.21)
\end{aligned}
$$

In case one of the POs observes a violation of the condition in (2.21), the corresponding PC applies a damping to compensate the negative E^{obs} value. With T_s being the discrete sampling time, the formulae to implement these passivity checks are given in Table 2.4 for impedance causality PC (which is used in this thesis) for POPC_1. Based on the energy of the 1-port in (2.12), the impedance causality PC equations are given in Table 2.5 for a 1-port.

Note that in Table 2.4 and Table 2.5, the dissipated energy for computing the observed energies at time-step k are considered only till time-step $(k-1)$ to avoid algebraic loops. More details on the theory and implementation for 2-port passivity can be found in [RAP10a] along with the admittance causality PC.

Limitations: As mentioned in [RPHH05], energy accumulation in TDPA might lead to short instances of unstable behavior. Also, the high frequency force modification of PC can result in chattering behavior of the hardware.

Table 2.4: Implementation of impedance PC for 2-port

	Impedance type	Elect. Network
PO	$E_1^{obs}(k) = E_2^{in}(k) - E_1^{out}(k) - E_1^{diss}(k-1)$	
$E_1^{diss}(k)$	$T_s \sum_{n=0}^{k} R_1^{PC}(n) V_1(n)^2$	
PC	$R_1^{PC}(k) = \begin{cases} \frac{-E_1^{obs}(k)}{TV_1(k)^2} & \text{if } E_1^{obs}(k) < 0 \\ 0 & \text{else.} \end{cases}$	
$V_1'(k), F_1'(k)$	$V_1(k), F_1(k) - V_1(k) \times R_1^{PC}(k)$	

Table 2.5: Implementation of impedance PC for 1-port

	Impedance type	Elect. Network
PO	$E_1^{obs}(k) = T_s \sum_{n=0}^{k} F_1(n) V_1(n) - E_1^{diss}(k-1)$	
$E_1^{diss}(k)$	$T_s \sum_{n=0}^{k} R_1^{PC}(n) V_1(n)^2$	
PC	$R_1^{PC}(k) = \begin{cases} \frac{-E_1^{obs}(k)}{TV_1(k)^2} & \text{if } E_1^{obs}(k) < 0 \\ 0 & \text{else.} \end{cases}$	
$V_1'(k), F_1'(k)$	$V_1(k), F_1(k) - V_1(k) \times R_1^{PC}(k)$	

2.1.4 Passivity in Teleoperation of Manipulators

For practical applications of teleoperation, the haptic device and the robot are generally multi-DoF systems. Consider the teleoperation described in Section 2.1.2 with spring-damper coupling acting on both the haptic device and the robot. Here the multi-DoF equivalent of the same system is considered.

For an m joint manipulator, a Cartesian task of c DoF leaves $m-c$ redundant DoF (null-space) unconstrained. Consequently, the additional null-space dynamics might affect the primary Cartesian task. The control of such redundant manipulators was considered in [Ott08, /S 4], where the joint dynamics was decomposed into Cartesian and null-space dynamics. A key property of the resulting dynamics was that they were decoupled in inertia, but not in the Coriolis-centrifugal terms. Hence, a feedforward term was used therein to cancel Coriolis couplings and an additional null-space damping control was applied to stabilize the null-space motion. As a consequence, the Cartesian dynamics can be written in a way which aids its independent passivity analysis. In the following, for both the haptic device and the robot, we consider the aforementioned decoupling and the resultant Cartesian dynamics [Ott08, eq.433], which are written as:

$$
\begin{aligned}
\boldsymbol{\Lambda}_d(\boldsymbol{q}_d)\dot{\boldsymbol{V}}_d + \boldsymbol{\mu}_d(\boldsymbol{q}_d, \dot{\boldsymbol{q}}_d)\boldsymbol{V}_d + \boldsymbol{\Gamma}_d \boldsymbol{V}_d &= \boldsymbol{F}_h - \boldsymbol{F}_c, \\
\boldsymbol{\Lambda}_r(\boldsymbol{q}_r)\dot{\boldsymbol{V}}_r + \boldsymbol{\mu}_r(\boldsymbol{q}_r, \dot{\boldsymbol{q}}_r)\boldsymbol{V}_r + \boldsymbol{\Gamma}_r \boldsymbol{V}_r &= \boldsymbol{F}_c - \boldsymbol{F}_e,
\end{aligned}
\tag{2.22}
$$

where for ($\bullet = d$) for the haptic device and ($\bullet = r$) for the robot, $\boldsymbol{\Lambda}_\bullet, \boldsymbol{\mu}_\bullet, \boldsymbol{\Gamma}_\bullet \in \mathbb{R}^{c \times m}$, $c \leq m$, are the matrices of inertia, Coriolis/centrifugal terms and viscous damping[3], respectively with $\boldsymbol{q}_\bullet \in \mathbb{R}^m$ and $\boldsymbol{V}_\bullet \in \mathbb{R}^c$ being the joint-space configuration and the Cartesian end-effector velocity, respectively [Kha87]. The input wrench from the operator is $\boldsymbol{F}_h \in \mathbb{R}^c$.

---

[3]Although viscous damping is not considered in the literature for manipulator dynamics, either inherent viscous friction or additionally introduced viscous damping is considered here to be consistent with the single-DoF analogies presented till now

The external wrench (measured) at the robot's end-effector is $\boldsymbol{F}_e \in \mathbb{R}^c$, and $\boldsymbol{F}_c \in \mathbb{R}^c$ is the coupling wrench given by:

$$\boldsymbol{F}_c = \boldsymbol{K}_p \Delta \boldsymbol{X} + \boldsymbol{K}_d \Delta \boldsymbol{V}, \qquad (2.23)$$

where, $\boldsymbol{K}_p \in \mathbb{R}^{c \times c}$ and $\boldsymbol{K}_d \in \mathbb{R}^{c \times c}$ are the constant positive-definite matrices of the Cartesian stiffness and Cartesian damping of the coupling, respectively. $\Delta \boldsymbol{X} \in \mathbb{R}^c$ and $\Delta \boldsymbol{V} \in \mathbb{R}^c$ are the differences in Cartesian position and Cartesian velocities of the end-effectors, respectively. Note that (2.22) is the multi-DOF equivalent of (2.10).

To analyze the passivity and finite-gain stability for this multi-DoF teleoperation system, consider the storage function S_m, the total energy for the haptic device, the robot and the coupling as the single-DoF S_t in Table 2.1,

$$S_m \;\; = \;\; \frac{1}{2} \boldsymbol{V}_d^T \boldsymbol{\Lambda}_d \boldsymbol{V}_d + \frac{1}{2} \boldsymbol{V}_r^T \boldsymbol{\Lambda}_r \boldsymbol{V}_r + \frac{1}{2} \Delta \boldsymbol{X}^T \boldsymbol{K}_p \Delta \boldsymbol{X}. \qquad (2.24)$$

Taking the time-derivative of S_m, and exploiting the passivity property of Euler-Lagrange systems, i.e, $\boldsymbol{V}_\bullet^T (\dot{\boldsymbol{\Lambda}}_\bullet - 2\boldsymbol{\mu}_\bullet) \boldsymbol{V}_\bullet = 0$ [SSVO10], we obtain the OSP condition, which is the same as for the single-DoF case, as shown here:

$$
\begin{aligned}
\dot{S}_m \;\; = \;\; & \boldsymbol{V}_d^T \Big(\boldsymbol{\Lambda}_d \dot{\boldsymbol{V}}_d - \frac{1}{2} \dot{\boldsymbol{\Lambda}}_d \boldsymbol{V}_d\Big) + \boldsymbol{V}_r^T \Big(\boldsymbol{\Lambda}_r \dot{\boldsymbol{V}}_r - \frac{1}{2} \dot{\boldsymbol{\Lambda}}_r \boldsymbol{V}_r\Big) + \Delta \boldsymbol{V}^T \boldsymbol{K}_p \Delta \boldsymbol{X}, \\
= \;\; & \boldsymbol{V}_d^T \Big(\boldsymbol{F}_h - \boldsymbol{F}_c - \boldsymbol{\mu}_d \boldsymbol{V}_d + \boldsymbol{\Gamma}_d \boldsymbol{V}_d - \frac{1}{2} \dot{\boldsymbol{\Lambda}}_d \boldsymbol{V}_d\Big) \\
+ \;\; & \boldsymbol{V}_r^T \Big(\boldsymbol{F}_c - \boldsymbol{F}_e - \boldsymbol{\mu}_r \boldsymbol{V}_r + \boldsymbol{\Gamma}_r \boldsymbol{V}_r - \frac{1}{2} \dot{\boldsymbol{\Lambda}}_r \boldsymbol{V}_r\Big) \\
+ \;\; & \Delta \boldsymbol{V}^T (\boldsymbol{F}_c - \boldsymbol{K}_d \Delta \boldsymbol{V}), \\
= \;\; & \boldsymbol{V}_d^T \boldsymbol{F}_h - \boldsymbol{V}_r^T \boldsymbol{F}_e - \Delta \boldsymbol{V}^T \boldsymbol{K}_d \Delta \boldsymbol{V} - \boldsymbol{V}_d^T \boldsymbol{\Gamma}_d \boldsymbol{V}_d - \boldsymbol{V}_r^T \boldsymbol{\Gamma}_r \boldsymbol{V}_r, \\
= \;\; & \sum_{i=1}^{c} (V_{di} F_{hi} - V_{ri} F_{ei} - K_{di} \Delta V_i^2 - \Gamma_{di} V_d^2 - \Gamma_r V_{ri}^2) \qquad (2.25)
\end{aligned}
$$

which makes the system OSP and finite-gain stable for inputs $(\boldsymbol{F}_h, -\boldsymbol{F}_e)$ and outputs $(\boldsymbol{V}_d, \boldsymbol{V}_r)$, and is equivalent to c single-DOF systems as in Table 2.1. Therefore, by applying the passivity ensuring conditions in every Cartesian DoF separately, the overall passivity of the manipulator can be ensured, which is followed in the rest of the thesis.

2.2 Transparency

After stability, transparency is an important performance criterion for a bilateral teleoperation system. Ideal transparency can be defined as: the operator feels as if he/she is manipulating the remote environment directly, without feeling the coupled robotic systems. This section gives some basics about transparency, starting from requirements for an ideally transparent system and existing measures to evaluate transparency based on these requirements. Finally, a comparison of some widely used teleoperation architectures is presented, which is necessary for the research done in this thesis.

2.2.1 Ideal Responses
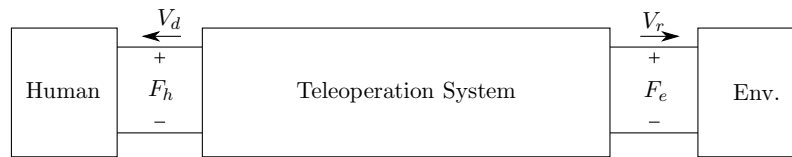
Figure 2.11: Human and environment interacting with teleoperation system

A reduced representation of the port network from Fig. 2.8 has been shown in Fig. 2.11. Note that the 2-port named *Teleoperation System* encompasses the different subsystems, namely, the haptic device, communication channels, the controller and the remote robot. This simplification of the model shows the power correlated variables for the interaction of the teleoperation system with the human operator, (F_h, V_d) and for the robot-environment interaction, (F_e, V_r), which is consistent with Fig. 2.8. Note that the exogenous force input given by the human operator $\tilde{F}_h$ is within the 1-port, *Human*. If the human operator should perceive a feeling of directly interacting with the remote environment, naturally, the controlled robot should duplicate the motion of the operator in a precise manner. Also the operator should feel the exact forces of interactions between the robot and the environment. The following conditions, analytically describe and combine these two requirements, [YY94, Law93].

- **Ideal Response 1:** The position responses X_d and X_r, by the operator's exogenous input $\tilde{F}_h$ are identical, whatever the environment object dynamics is. This means:

$$X_d = X_r. \tag{2.26}$$

- **Ideal Response 2:** The force responses F_h and F_e, by the operator's exogenous input $\tilde{F}_h$ are identical, whatever the environment object dynamics is. This means:

$$F_h = F_e. \tag{2.27}$$

- **Ideal Response 3:** Both the position responses X_d and X_r, and the force responses F_h and F_e, by the operator's exogenous input $\tilde{F}_h$ are identical, respectively, whatever the environment object dynamics is. This means:

$$
\begin{aligned}
X_d &= X_r, \\
F_h &= F_e
\end{aligned}
\tag{2.28}
$$

- **Ideal Response 4:** [Law93] states that the impedance perceived by (or transmitted to) the human and the environment are equal. This means:

$$Z_t = Z_e, \text{ that is:}$$
$$\frac{F_h}{V_d} = \frac{F_e}{V_r}. \tag{2.29}$$

2.2.2 Transparency Measures

The position tracking and force tracking performances can be quantitatively evaluated by finding the errors, $(X_d - X_r)$ and $(F_h - F_e)$. All these variables can be directly measured using position and force sensors in the hardware set-up. For comparing impedances, a common approach is to evaluate the linearized model of the teleoperation system in terms of transfer functions in the frequency domain. Some of the common performance criteria in frequency domain are the performance index of maneuverability, [YY94] and effective impedance [CSO14]. The mathematical equations of these performance indices are mentioned here:

1. **Position tracking** $|X_d - X_r|$: This metric expresses how well the robot follows the positions of the haptic device. The absolute value of the error between the positions are computed for all times and can be represented in terms of the root mean square value. Naturally, the error should be 0 for an ideally transparent system.

2. **Force tracking** $|F_h - F_e|$: This metric expresses how well the forces from the robot-environment interactions are conveyed back to the operator. The absolute value of the error between the forces are computed at all times and can be represented in terms of the root mean square value. Similar to the position tracking, the force errors should be zero for an ideally transparent system.

3. **Performance index of maneuverability** J_p, J_f: In frequency domain, the following transfer functions are defined:

$$G_{mp}(s) = \frac{X_d(s)}{\tilde{F}_h(s)}, \quad G_{sp}(s) = \frac{X_r(s)}{\tilde{F}_h(s)}, \quad G_{mf}(s) = \frac{F_h(s)}{\tilde{F}_h(s)}, \quad G_{sf}(s) = \frac{F_e(s)}{\tilde{F}_h(s)}. \tag{2.30}$$

Then the indices J_p for position tracking and J_f for force tracking is evaluated for all the frequencies as:

$$J_p = \int_0^{\omega_{max}} |G_{mp}(j\omega) - G_{sp}(j\omega)| \left| \frac{1}{1 + j\omega T_1} \right| d\omega,$$
$$J_f = \int_0^{\omega_{max}} |G_{mf}(j\omega) - G_{sf}(j\omega)| \left| \frac{1}{1 + j\omega T_1} \right| d\omega, \tag{2.31}$$

where ω_{max} is the maximum frequency of the manipulation bandwidth of the operator and T_1 is the time constant of first-order-lag which puts higher weight on the low frequency region than the high frequency region. If J_p and J_f indices are smaller, the system performance is better [YY94].

4. **Effective Impedances** Z_{eff}: This index is also computed in the frequency domain for some parameters that human operator can perceive mechanically. The forces F_h

is measured using a force sensor at the interface between the operator and the haptic device and the velocity V_d is measured using encoders in the haptic device. Over the frequency range of operation, the effective (perceived) impedance $Z_{eff}(j\omega)$ is identified as:

$$
\begin{aligned}
Z_{eff}(j\omega) &= \frac{F_h(j\omega)}{V_d(j\omega)}, \\
K_{eff}(\omega) &= \omega \operatorname{Im}^- Z_{eff}(j\omega), \quad \theta \in [-180°, \ 0°], \\
D_{eff}(\omega) &= \operatorname{Re}^+ Z_{eff}(j\omega), \quad \theta \in [-90°, \ 90°], \\
M_{eff}(\omega) &= \omega^{-1} \operatorname{Im}^+ Z_{eff}(j\omega), \quad \theta \in [0°, \ 180°],
\end{aligned}
\tag{2.32}
$$

where $K_{eff}(\omega), D_{eff}(\omega)$ and $M_{eff}(\omega)$ are the components of the effective impedance namely, effective stiffness, damping and mass respectively and $\theta = \angle Z(j\omega)$ and Im^-, Re^+ and Im^+ are the negated imaginary, real and imaginary parts of the complex variable that is Z_{eff}, respectively [CSO14].

2.2.3 Transparency Comparison

One of the major difficulties in evaluating the performance of force-feedback systems is the fact that the human operator is part of the closed loop system. The forces sensed at the task space are processed and transmitted to the operator, who in turn generates a reaction that depends on his or her intentions. Although well defined, system transparency remains as an abstract concept which mixes system performance with human perception, i.e. a transparent system is not seen nor felt by the human, which is indeed, the definition of an ideal transparent system [BAMR16]. It is therefore necessary to segment the various aspects that intervene in this quality assessment of force-feedback systems in order to create a proper metric. In this section, the most common architectures used in teleoperation community are briefly presented. Later, a transparency comparison study is implemented based on two underlying ideas:

1. To evaluate the performance of the force-feedback system in terms of elements that the human brain can process (mechanical parameters) and how it varies with input frequency, while

2. excluding the human operator from the analysis.

The perceived stiffness K_{eff} from (2.32) is evaluated for three different teleoperation architectures, which are stabilized using the two stability approaches: Wave Variables Transformations (from Section 2.1.3) and Time Domain Passivity Approach (from Section 2.1.3). Basic description of teleoperation architectures and the results of the comparative study are presented here. More details can be found in [BAMR16].

Bilateral Teleoperation Architectures

The architecture of a teleoperation system is defined by the physical variables conveyed between the haptic device and the remote robot. For example, in a unilateral teleoperation system, only the position from the haptic device is sent to the robot side. A position controller locally on the robot side, commands forces to the robot to match its position to the desired position of the haptic device. For a bilateral teleoperation system, forces are

sent back to the haptic device from the robot side and the conceptual block diagrams of commonly used architectures are shown in Fig. 2.12, which are:

1. 2-channel position-computed force $(P - F_c)$ [NS97] in Fig. 2.12a,

2. 2-channel position-measured force $(P - F_e)$ [PHA$^+$16] in Fig. 2.12b,

3. 3-channel position-force $(P - F_c, F_e)$ [TN05] in Fig. 2.12c,

4. 4-channel position, measured force-position, measured force $(P, F_h - P, F_e)$ [Law93] in Fig. 2.12d.

(a) $P - F_c$ (b) $P - F_e$ (c) $P - F_c, F_e$ (d) $P, F_h - P, F_e$
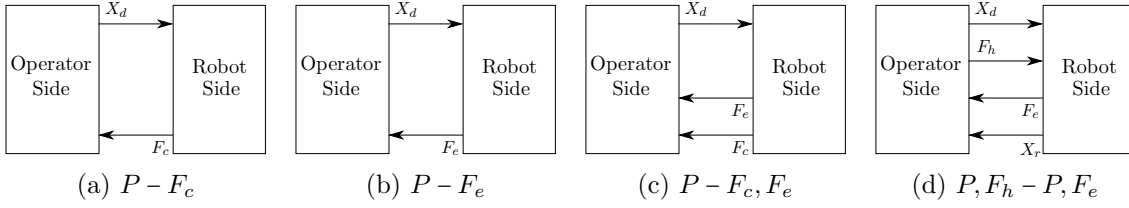
Figure 2.12: Common architectures in bilateral teleoperation

Comparative Study

For the transparency comparison study, five approaches are selected: 1) W2: 2-channel $(P - F_c)$ stabilized by WVT, 2) T2: 2-channel $(P - F_c)$ stabilized by TDPA, 3) W3: 3-channel $(P - F_c, F_e)$ stabilized by WVT, 4) T3: 3-channel $(P - F_c, F_e)$ stabilized by TDPA and 5) T4: 2-channel $(P, F_h - P, F_e)$ stabilized by TDPA with the following error indices:

1. **Effective Stiffness Error:** The effective stiffness K_{eff} from (2.32) is computed at the haptic device side. The error index for effective stiffness ΔK_E between $K_{eff}(\omega)$ and the real environment stiffness (K_e):

$$\Delta K_E = \int_{\omega_1}^{\omega_2} \beta_K(\omega) \left| K_e - K_{eff}(\omega) \right| d\omega, \tag{2.33}$$

where $[\omega_1, \ \omega_2]$ is the range of frequency under consideration and $\beta_K(\omega)$ is a frequency dependent gain assigned to give more weight to desired frequencies of operation. Here, this weight was given a constant value of unity.

2. **Position Tracking Error**: The magnitude of the transfer function of the position error and the input position is calculated as:

$$P_E(s) = \frac{\tilde{X}_d(s) - X_r(s)}{X_d(s)}, \tag{2.34}$$

where $\tilde{X}_d$, X_d, X_r are the delayed haptic device position, actual haptic device and robot positions, respectively. The error index for tracking ΔP_E, which is the deviation of P_E from the desired value of 0, in the same range of frequency is calculated as:

$$\Delta P_E = \int_{\omega_1}^{\omega_2} \beta_P(\omega) |P_E(\omega)| d\omega, \tag{2.35}$$

where again, $\beta_P(\omega)$ is a frequency dependent weight as explained in (2.33). A constant value of unity has been assigned here in this study.

Figure 2.13: Experimental setup of the teleoperation system including the linear actuator and the environmental impedance

3. **Combined Error**: new index, Normalized Error and Weighted (N_{ew}) is proposed and evaluated here which is calculated as the weighted sum of the normalized values of the 2 previous error indices, that is:

$$N_{ew} = \alpha_K \Delta K'_E + \alpha_P \Delta P'_E, \tag{2.36}$$

where $\Delta K'_E$ and $\Delta P'_E$ are the unity-based normalized values of ΔK_E and ΔP_E and the weights $[\alpha_K, \alpha_P]$ satisfy the condition $\alpha_K + \alpha_P = 1$ with $\alpha_K, \alpha_P \geq 0$. The selection of the $[\alpha_K, \alpha_P]$ is task specific. For example, if a teleoperation task requires more precision for position tracking, $\alpha_P > \alpha_K$ and vice-versa. An equal value of 0.5 has been allocated to α_P and α_K in this study. The performance of the time-delayed bilateral controller can be evaluated from the value of N_{ew} index: the lower the value, the better will be the performance and the ideal value is 0.

Experiments

Experiments were performed using two PHANToM Premium 1.5 devices, which run at a sampling rate of 1 kHz, with communication delay being simulated in software. Fig. 2.13 shows the dual PHANToM teleoperation setup. As explained earlier, in order to remove the human operator out of the loop and to ensure identical input to haptic device for all the control architectures, a one-degree of freedom linear actuator with pre-programmed trajectories was used. ATI Nano force-torque sensors were used as end effectors on device and robot devices. In order to vary the environmental impedance, different masses and varying number of elastic bands were attached to remote robot force sensor. In each of the experiments, the haptic device was excited with a pre-programmed, white noise motion input using the linear actuator for 90 seconds and all the system variables were logged. The effective impedance at the device side was computed using the `tfestimate()` function in Matlab which calculates the transfer function as the quotient of the cross power spectral density of the input signal V_d and the output signal F_h, and the power spectral density of V_d. Later the effective stiffness was calculated as shown in (2.32). The same method was followed for the tracking error.

Results of Transparency Comparison

Teleoperation experiments with all the aforementioned architectures were repeated for 5 values of round-trip delay: $D0 = 0ms$, $D1 = 20ms$, $D2 = 40ms$, $D3 = 100ms$ and $D4 = 200ms$. Five different environmental stiffnesses selected are $K0 = 0\ N/mm$, $K1 = 0.06\ N/mm$, $K2 = 0.12\ N/mm$, $K3 = 0.16\ N/mm$ and K4 is the situation with robot mechanically clamped. The methods with the least values in stiffness, position tracking and combined error are shown in Fig. 2.14.

2.2.4 Discussion

As can be inferred from Fig. 2.14, TDPA produces least errors in most scenarios. Detailed explanations for the behavior can be found in [BAMR16]. Based on the theory presented in Section 2.1.3 and the results from the transparency comparison study, the thesis will start with TDPA as the main tool for making the subsystems of the shared control framework passive. This is mainly due to three reasons:

1. TDPA is a model-free method for ensuring passivity. This makes it robust against modeling errors. All the variables required for the implementation of TDPA, namely velocities and forces, can be measured in the system.

2. TDPA produced the least errors and therefore, the best performance in the comparison study, the reasons for which are explained in detail [BAMR16].

3. TDPA can handle time-varying communication delays and package losses, which are common in internet-based and space communication links, which are the most practically relevant ones in this thesis.

(a) Stiffness comparison of 2-channel architectures

(b) Stiffness comparison of 3-channel architectures

(c) Stiffness comparison of all architectures

(d) Position comparison of 2-channel architectures

(e) Position comparison of 3-channel architectures

(f) Position comparison of all architectures

(g) Combined error comparison of 2-channel architectures

(h) Combined error comparison of 3-channel architectures

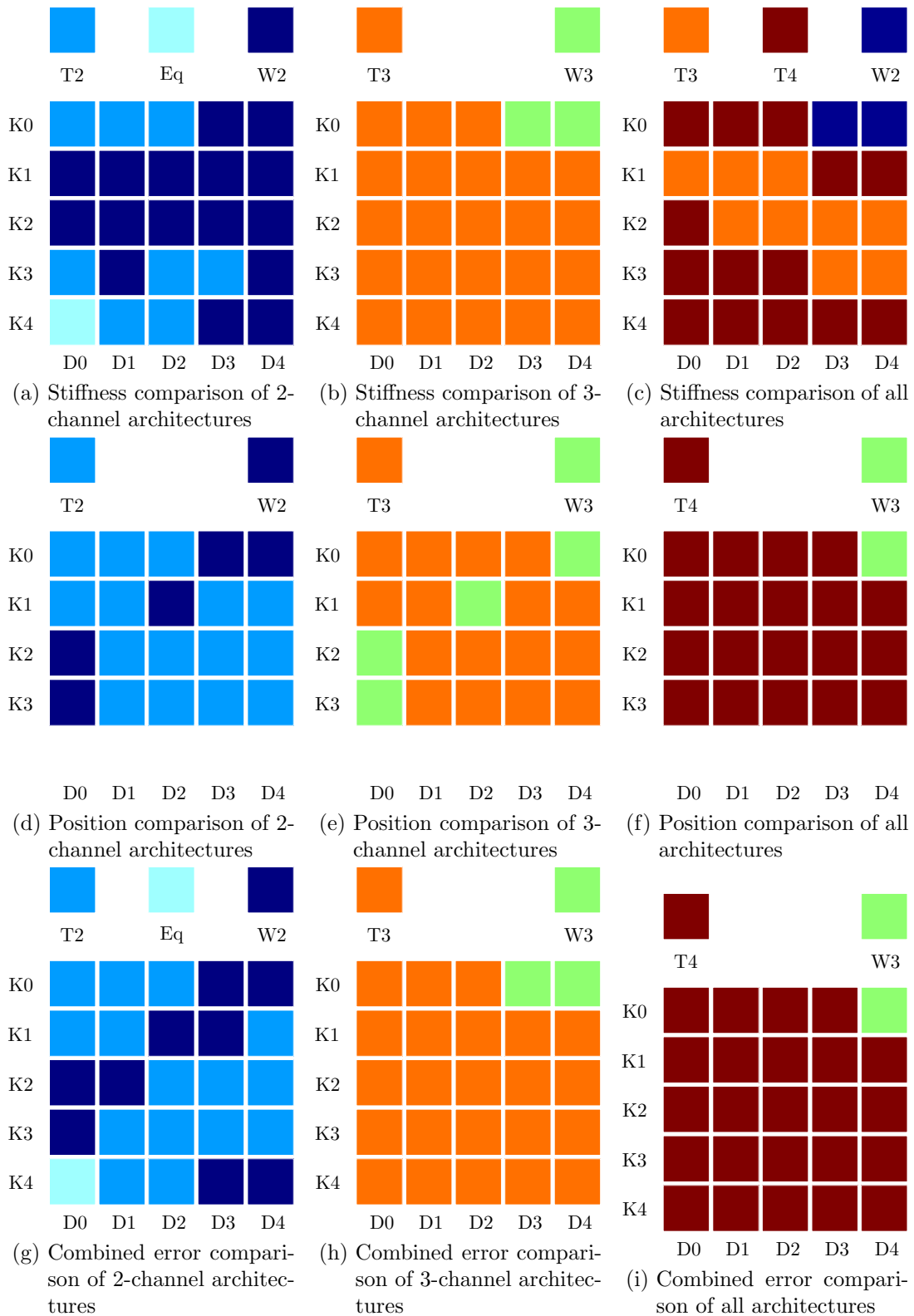(i) Combined error comparison of all architectures

Figure 2.14: These matrices show the methods with the least errors for the 5 different stiffnesses and the 5 different delays.

2.3 Summary

The content in this chapter played two important roles for the description of the research done during this thesis work.

First, it gave a short review of theoretical tools that will be used in this research, in terms of stability and transparency. The relationship between passivity and stability is crucial and passivity will be used to stabilize the frameworks developed later on. The 2-port networks will be used to present the shared control framework as a modular and versatile system, applicable in many scenarios. TDPA and analytical damping injections presented in Section 2.1.3 will be used to make the subsystems of the overall shared control framework passive.

Second, the transparency comparison of the bilateral teleoperation architectures is used for the selection of the passivity methods and architectures for the research in this thesis. Time domain passivity approach will be the main passivity tool used for the transparency enhancement methods presented in the next chapter.

CHAPTER 3

Transparency Enhancement in Teleoperation

3.1 Introduction

As the first step towards the final goal of this thesis, namely, *a stable and transparent framework for adaptive shared control*, this chapter presents two methods to improve the transparency of the *teleoperation part* of the shared control framework. As mentioned in Section 1.2, transparency enhancement in teleoperation, while maintaining system stability is a field that has been researched for decades [HS06] and different haptic devices have been developed, which inherently by design improve the operator's haptic perception. Light-weight haptic devices like sigma.7 [THH+11] from Force Dimension, Virtuose from Haption and the Kontur space joystick (to mention a few) have been shown to provide excellent haptic experience to the operator [Sag19]. Some of the light-weight haptic devices are shown in Fig. 3.1.

Figure 3.1: Light-weight haptic devices

However, the limited workspace and force feedback range of these devices led to the development of robotic manipulator-based haptic devices. They provide more natural human arm workspace and much larger force feedback range. Two widely used, manipulator-based devices are shown in Fig. 3.2. DLR-HUG in Fig. 3.2a is a bi-manual robotic facility comprised of KUKA Light Weight Robots (LWR) transformed as haptic devices and provides intuitive telemanipulation capabilities to the operator [HHK+11]. On the other hand, due to the massive structure and inherent physical damping, these devices demand higher physical effort from the operator, especially while telemanipulating similarly massive remote

robots [Sag19]. The dynamics of these large haptic devices also affect the operator's ability to differentiate between free motion and contact phases of the remote robot, reducing transparency of the teleoperation system.

There are several methods to improve the position synchronization of the teleoperation system[Sea20, CO14, PS21]. This chapter focuses mainly on enhancing the force transparency while using these large haptic devices. However, the proposed methods are also applicable to light-weight haptic devices like sigma.7 used in tele-surgery, where the fine interactions between the surgical robot and the human tissue should be perceived by the surgeon with best possible quality [THH$^+$11].

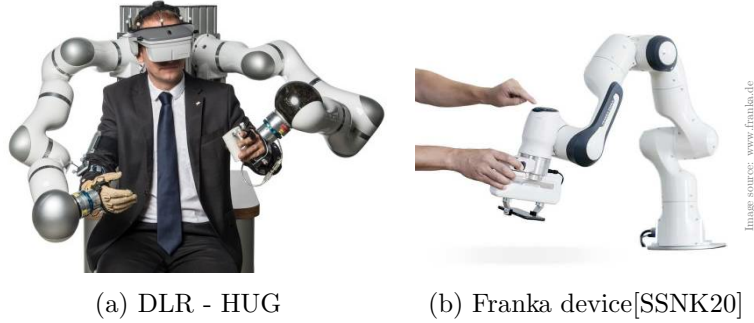(a) DLR - HUG   (b) Franka device[SSNK20]

Figure 3.2: Manipulator-based haptic devices

In Section 3.2, the first method is presented, where a non-linear gain is applied to the feedforward forces at the operator side. Hardware experiments validate the improvements in transparency promised by this method. The limitations are identified and discussed which encourages the second method in Section 3.3, which is to apply an explicit force controller at the operator side to match the forces felt by the operator to the interaction forces measured at the robot's end-effector. Both the proposed methods are local force controllers, which play two vital roles:

1. reduce the perceived inertia to lower the total effort demanded from the operator and

2. improve the quality of the feedback of the robot-environment interaction.

Stability of these controllers are ensured using passivity-based methods. Finally, a novel stabilization method is described in Section 3.4 to ensure stability of any user-defined feedback controllers in teleoperation systems using existing passivity-based tools. Along with the summary, the future scope of this thesis has been mentioned based on the limitations of the final stabilization method. The logical flow of the chapter is presented in Fig. 3.3 to give an overview to the reader.
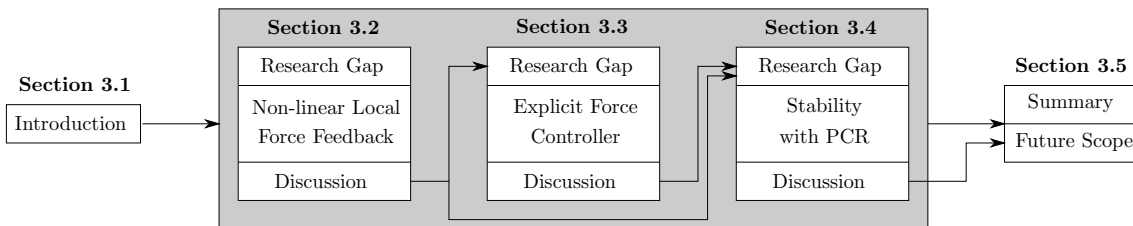

Figure 3.3: Overview of Chapter 3

3.2 Non-linear Local Force Feedback

In this section a time-varying gain for the local force feedback is proposed which shows better performance compared to conventional methods that use only constant gains. The gain is modified based on the measured forces from the remote robot-environment interaction, which is a simple and heuristic approach to improve the transparency of the system. Later, the stability of the system is ensured using two methods:

1. Model-based damping injection,

2. Model-independent damping injection using TDPA

Hardware experiments validate the benefits of this approach. This section is based on the work published by the author in [BKOAS18].

3.2.1 Research Gap and Objectives

Related Work

Local force feedback control has been widely used in bilateral controllers to improve the transparency of the haptic system and it was introduced in [HZS99], [HZS02] and [IK12]. In these works, it has been analytically and experimentally shown that ideal transparency can be achieved only under negligible time-delays in the communication channel. Constant force feedback gain has been used in [KTTK98] to improve the manipulation dexterity while working in different scale worlds. The method in [Col93] alters the impedance of the task and also changes the device dynamics as in [AS08]. A local force feedback scheme has been used in [UB] to compensate gravitational forces. It has also been successfully applied to decrease the perceived inertia of the device in [THH+11] and [GRS09]. In [GRS09], it is shown that only low gains for local force feedback ensures stability of the system. All the aforementioned works apply constant gains for local force feedback, which has limitations, especially in teleoperation systems with large communication time-delays. The concept of local force feedback gains and its limitations are presented in the following section.

Local force feedback control

The signal-flow diagram of a general 4-channel teleoperation system with local force feedback [HZS99] is shown in Fig. 3.4. The measured force of the operator-haptic device interaction, F_h, is amplified with a gain α_l and is applied to the haptic device as a feedback force. The amplified human force on the haptic side then becomes:

$$\hat{F}_h = F_h + \alpha_l F_h. \tag{3.37}$$

One of the conditions for perfect transparency for a non-delayed teleoperation system with 4-channel architecture with local force feedback, as mentioned in [HZS99], states that the force feedback gains should satisfy:

$$C_2 \quad = \quad 1 + \alpha_l, \tag{3.38}$$

where C_2 is the feedback gain of the measured forces from the remote robot side. The network representation of the reduced model of the haptic device interacting with the human and the controller is shown in Fig. 3.5. The port named 'Gain' introduces a gain $G = 1 + \alpha_l$ to the human force F_h. The port 'Ctrl. Port' is the entire teleoperation system,
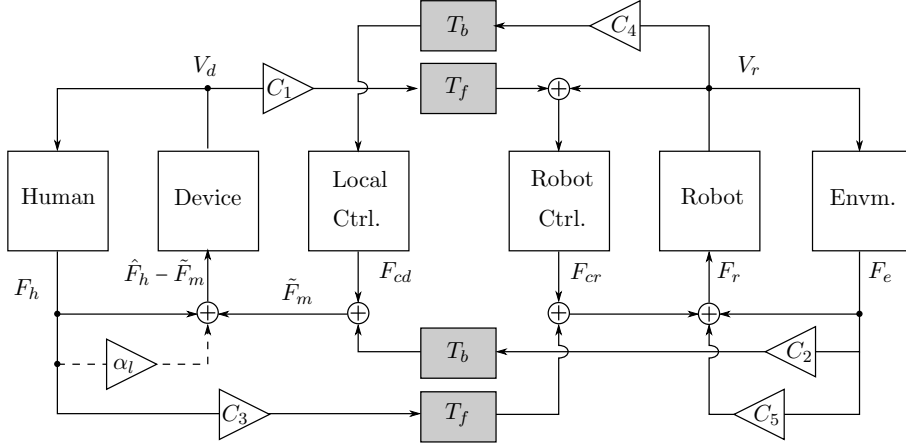
Figure 3.4: Signal-flow diagram of 4-channel bilateral controller.

which gives force feedback to the haptic device. The operator with the local force feedback gain interacts with the haptic device through the power-port $< \hat{F}_h, V_d >$ and the controller port interacts with the haptic device with $< \tilde{F}_m, V_d >$.
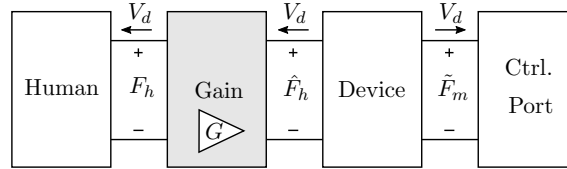

Figure 3.5: Teleoperation system with a local force feedback gain.

Problem Description

As it is pointed out in [HZS99], perfect transparency cannot be achieved and the system gets unstable with high values of the measured remote robot force feedback gain C_2. Although the effects of time-delay can be removed using passivity-based tools like wave-variables [NS91] or TDPA [ABR+16], the gain margins are limited as explained in [PHA+16]. This is presented in the following experiments.

Teleoperation experiments with a 4-channel bilateral controller for the LWR-based haptic device were conducted with local force feedback, with gains satisfying the condition in (3.38) with and without time-delay. The haptic device is moved by a human operator trying to follow a desired trajectory (blue dashed line, X_h). The position and force signals of the haptic device are commanded to a virtual mass of $2\ Kg$, which simulates the remote robot and collides with a virtual wall of stiffness $1200\ N/m$. The local force feedback gain for the haptic device is $\alpha_l\ = 1.4$ and the environmental force feedback gain is 2.4 (C_2, which satisfies (3.38)). The corresponding positions X_h, X_d, X_r, being the desired position trajectory given to the operator, position of the haptic device, and virtual robot device, respectively and measured forces of the operator and remote robot are shown in Fig. 3.6. It can be seen that the forces of the robot (red) while in contact with the virtual wall (the black line denoted by X_w) are perceived by the human (blue) with high transparency. The high level of transparency is indicated by the matching of the measured forces from the robot's end-effector and the haptic devices interaction point

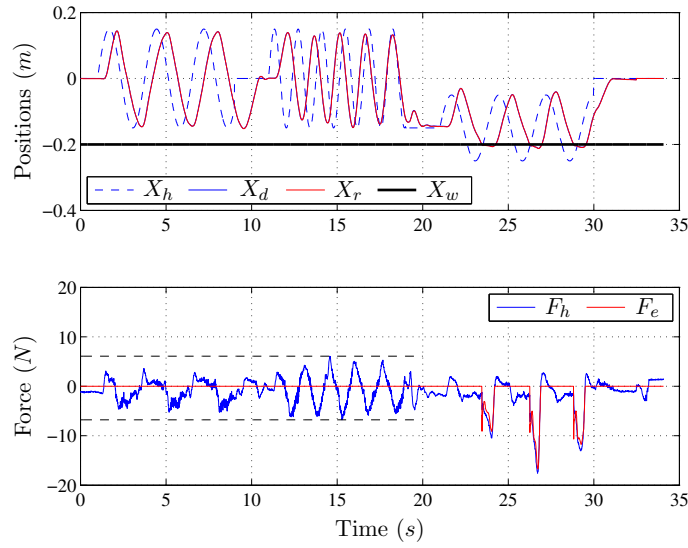with the operator. This is in accordance with Ideal Response 2 for transparency presented in Section 2.2.1.

Figure 3.6: Positions and forces of the devices with local force feedback control, without delay, α_l=1.4 and C_2=2.4. Note that positions X_m and X_s are almost identical that it is hard to differentiate them.
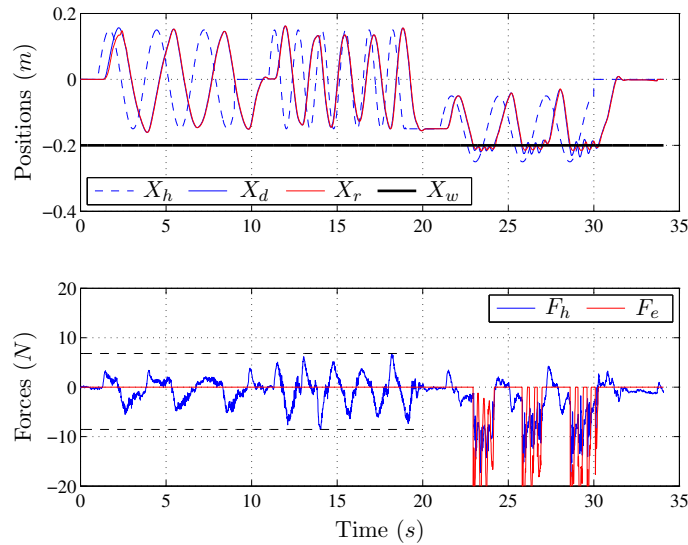
Figure 3.7: Positions and forces of the devices with local force feedback and with a round-trip delay of 30 ms, α_l=1.4 and C_2=2.4. It can be seen that the contacts get highly unstable.

However, it can be seen in Fig. 3.7 that the contact with the virtual wall makes the system highly unstable with a round-trip delay of 30 ms for the same measured force feedback gain C_2 = 2.4. So, for teleoperation systems with time-delay, the feedback gain of the environmental forces has to be reduced considerably (for example, C_2 = 1.0), while α_l is still 1.4, thus violating (3.38). In the next experiment, the controller gains are tuned to make teleoperation system stable using TDPA as explained in [ABR+16]. Fig. 3.8 shows

the teleoperation system with 30 ms round-trip delay and without local force feedback. It can be seen that although the human operator needs to apply high forces on the haptic device during free motion of the remote robot, the contacts are perceived well at the haptic side. Now compare this with Fig. 3.9, which shows the results of the same system applying a local force feedback with constant gain. It can be seen that the human needs to apply lower forces during free motion. But the force perceived by the operator is reduced significantly when the remote robot makes contacts with the wall, which can be seen from the low force values at the human side as compared to the remote robot forces.
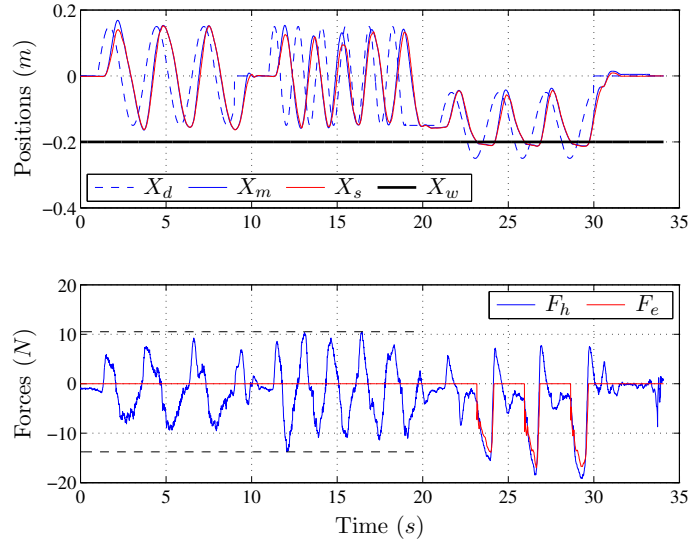
Figure 3.8: Positions and forces of the devices without local force feedback, a round-trip delay of 30 ms, C_2 =1.0. Note the high F_h values in free motion, but better force tracking during contacts.
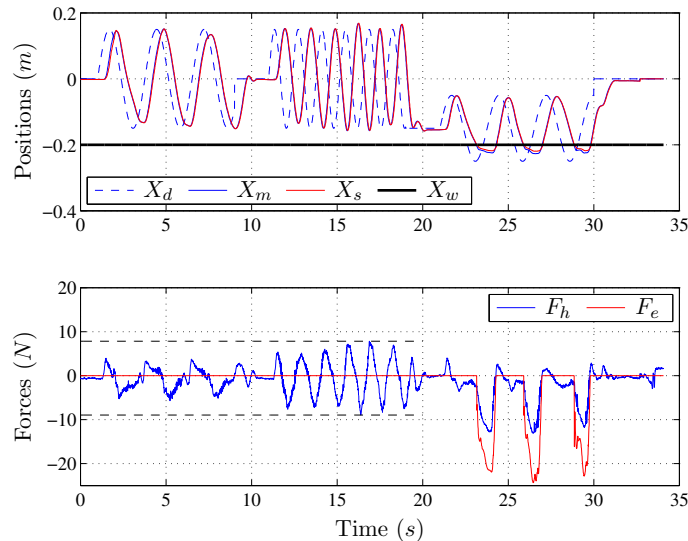

Figure 3.9: Positions and forces of devices with constant local force feedback gain α_l=1.4, with round-trip delay of 30 ms and C_2 =1.0

To summarize: With constant local force feedback gain for time-delayed teleoperation,

the free motion transparency is increased. However, during contacts, when the feedback force is felt by the human, the force sensor measures it and feeds it to the local feedback controller, which supports the human to push against the wall. This consequently reduces the contact force perception.

Objective

The goal of this section is to design a local force feedback controller at the haptic device to increase the transparency of the teleoperation system with delays, such that the inertia of the haptic device is reduced in free motion, and to improve the feedback quality of the contact forces.

3.2.2 Proposed Method

The previous section presented the benefits of local force feedback controller with constant gain during free motion and its limitations during contacts. Here, instead of having a constant gain, a varying gain $\alpha_l(t)$ is introduced to improve system transparency. If the gain is reduced/removed when the robot makes a contact with its environment, the benefit of local force feedback during free motion can be availed and also the limitation during contact situations can be avoided. The proposed method is to reduce α_l gain with respect to the measured force of the robot-environment interaction.

Non-linear Gain Variation

In order to modify the gain of the local force feedback controller, the measured environmental forces F_e are sent to the haptic device side and the gain $\alpha_l(F'_e(t))$, where F'_e is the delayed measured force, is varied such that it has a high value during free motion (when $F'_e \approx 0$) and has a low value when the remote robot interacts with its environment. Any gain variation function that results in high gain values during free remote robot motion and low gain values when the remote robot interacts with the environment can be chosen for this. Two such *purely heuristic functions* of F'_e are illustrated in Fig. 3.10. The left-side plot shows a linear variation with α_l^{max} being the maximum value achieved by the gain and F_e^{max} is chosen to be the expected upper bound for $|F'_e|$, which could be the force limited by the actuator capability, for example. The right-side plot shows logistic curve where k_s is the steepness of the curve, F_{e0} is the $|F'_e|$ value of the sigmoid's midpoint and therefore, α_l^{max} is twice the gain when $F'_e = F_{e0}$. The modified network of the teleoperation system with time varying local force feedback gain is shown in Fig. 3.11. In this work the logistic variation of the local force feedback gain is considered and tested with hardware experiments. So, the gain varies as follows:

$$\alpha_l(F'_e) = \frac{\alpha_l^{max}}{1 + e^{k_s(|F'_e| - F_{e0})}}. \tag{3.39}$$

Passivity

In this section, the passivity properties of the system are discussed. The factors destroying passivity are identified and two methods are presented to ensure passivity of the system, namely, damping injection with energy-function and with TDPA. Both methods ensure passivity of the system for any gain, independent of the variation function. The stability issue related to time-delay has already been treated and the 4-channel bilateral controller
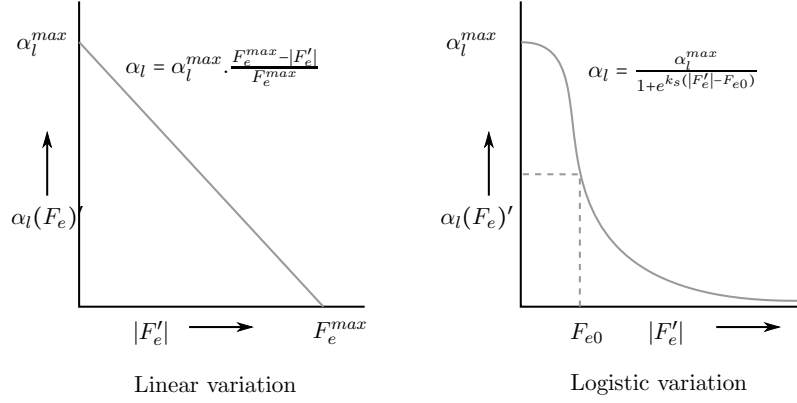
Figure 3.10: Variation of the gain α_l with the measured force signal F_e'. The left-side plot shows a linear variation and the right-side plot shows a logistic variation.
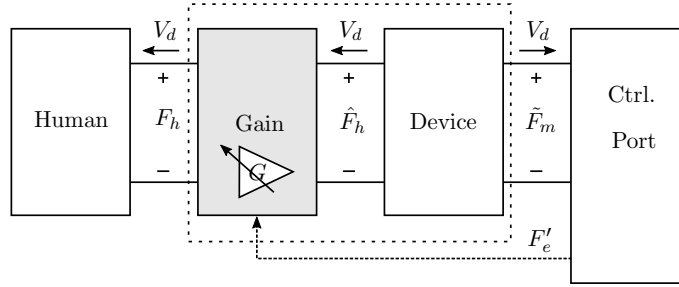

Figure 3.11: The reduced model of the teleoperation system with a varying local force feedback gain. It should be noted that F_e' signal is shown here to represent that the gain network is modified with respect to the delayed measured force signal received from the remote robot side.

has been stabilized using time domain passivity approach explained in [ABR$^+$16]. This means that in Fig. 3.11, the 1-port network of 'Ctrl. Port', which comprises of the communication channel, haptic device, robot controller, remote robot and the environment are already passivated.

Consider the port 'Gain' in Fig. 3.11. The power input from the human side is $F_h V_d$ and the power output to the haptic device is $\hat{F}_h V_d$, since only the force is amplified for the same velocity value. Clearly, this is a purely active system (unlike a power-preserving electrical transformer which amplifies voltage at its output and simultaneously reduces the current and vice-versa). The active power P_{active} can be calculated by:

$$P_{active} = \hat{F}_h V_d - F_h V_d = \alpha_l F_h V_d \quad \text{if } F_h V_d > 0. \tag{3.40}$$

The system can be made passive if at every point of time, this active power P_{active} can be dissipated. For this, a simple method is to add a virtual damping γ (as shown in Fig. 3.12) in this port which dissipates the exact amount of power, namely, $\alpha_l F_h V_d$. For the velocity V_d of the haptic device, the power dissipated by the damping γ is γV_d^2. Therefore, the value of damping that is needed to dissipate the active power due to the force amplification is:

$$\gamma = \frac{\alpha_l F_h V_d}{V_d^2} = \frac{\alpha_l F_h}{V_d} \quad \text{if } F_h V_d > 0. \tag{3.41}$$
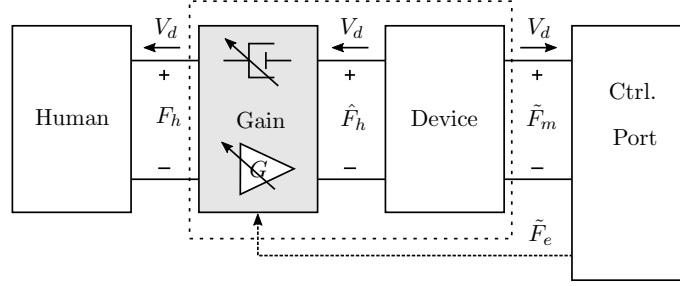
Figure 3.12: The reduced model of the teleoperation system with a varying local force feedback gain and a variable damping.

This method has a limitation. The benefit introduced by the local force feedback could be canceled out by the additional damping. All haptic devices have some physical damping or friction (although in some devices, it is very low). Because of the friction, the haptic device considered alone is already a dissipative system as shown in Table 2.1. In this work, this inherent dissipative nature of the haptic device is exploited to reduce the additional damping γ needed to passivate the gain port. For this, the combined port of the haptic device and the gain is considered to analyze passivity. This combined port is shown inside the dotted rectangle in Fig. 3.12.

1. Passivity by Damping Injection: Model-Based Analysis

The equation of motion of a 1-DoF haptic device with inertia M, viscous friction D, local force feedback gain α_l and additional damping γ is:

$$
\begin{aligned}
M\dot{V}_d &= \hat{F}_h - \tilde{F}_m - (D+\gamma)V_d, \\
&= (1+\alpha_l)F_h - \tilde{F}_m - (D+\gamma)V_d,
\end{aligned} \tag{3.42}
$$

with $\alpha_l, D, \gamma, \geq 0$. The term $(1+\alpha_l)$ is now replaced by $\frac{M}{\tilde{M}}$ where $\tilde{M}$ is the apparent inertia felt by the operator with the application of the force gain α_l. So (3.42) can be rewritten as:

$$
\tilde{M}\dot{V}_d = F_h - \frac{\tilde{M}}{M}\tilde{F}_m - \frac{\tilde{M}}{M}(D+\gamma)V_d, \tag{3.43}
$$

which means that when the operator applies a force F_h, the apparent inertia, viscous friction, force feedback, and damping felt by the user are $\tilde{M}$, $\frac{\tilde{M}}{M}D$, $\frac{\tilde{M}}{M}\tilde{F}_m$, $\frac{\tilde{M}}{M}\gamma$, respectively. Let us now consider the total energy as the storage function S_l of the haptic device with apparent inertia $\tilde{M}$ and the energy change (power) $\dot{S}_l$ is then calculated as:

$$
\begin{aligned}
S &= \frac{1}{2}\tilde{M}V_d^2, \\
\dot{S}_l &= V_d\tilde{M}\dot{V}_d + \frac{1}{2}\dot{\tilde{M}}V_d^2, \\
&= V_d(F_h - \frac{\tilde{M}}{M}\tilde{F}_m - \frac{\tilde{M}}{M}(D+\gamma)V_d) + \frac{1}{2}\dot{\tilde{M}}V_d^2, \\
&= V_dF_h - \frac{\tilde{M}}{M}V_d\tilde{F}_m - (\frac{\tilde{M}}{M}D + \frac{\tilde{M}}{M}\gamma - \frac{1}{2}\dot{\tilde{M}})V_d^2.
\end{aligned}
$$

So, the *perceived* 2-port of the apparent inertia with input $(F_h, \frac{\tilde{M}}{M}\tilde{F}_m)$ and output (V_d, V_d) is passive if:

$$\frac{\tilde{M}}{M}D + \frac{\tilde{M}}{M}\gamma - \frac{1}{2}\dot{\tilde{M}} \geq 0. \tag{3.44}$$

Since $\frac{M}{\tilde{M}} = (1 + \alpha_l)$, the additional damping required to passivate the port can be calculated to be:

$$\gamma \geq -\frac{M\dot{\alpha}_l}{2(1 + \alpha_l)} - D. \tag{3.45}$$

With the additional damping γ computed as per (3.45), the system is passive as per Def. 2.2. It has to be noted that during the reduction of α_l, when the contact is made, $\dot{\alpha}_l$ is negative and it does not destroy the passivity of the system. In this case, the damping of the haptic device makes the system output-strict passive and therefore, finite-gain stable. The limitation of the method happens during the increase in α_l, when the contact is removed. During this period, the additional damping injected into the system depends on the physical damping of the haptic device. If the physical damping is not considered to ensure OSP and finite-gain stability, too much damping has to be introduced, which disturbs the motion produced by the operator.

In order to find the required value of γ to passivate the port, the exact values of the inertia and friction have to be identified to apply (3.45). This means that the additional damping γ required to passivate the port is subject to inaccuracies in the system modeling.

2. Passivity by Damping Injection: Model-independent TDPA

The issue with model dependency can be avoided if the actual power correlated variables of the combined port of force gain block and the haptic device (the dotted box in Fig. 3.12) can be measured. By doing this, we can passivate this port by using TDPA. In classical TDPA, as presented in Section 2.1.3, the PO observes the energy of the system and the PC is a time varying damping to dissipate energy if ever the PO observes an activity [ABR+16]. Here, the damping value γ is modified with respect to the observed energy. Although this method is very effective, the energy accumulation problem in TDPA is widely accepted as a drawback in systems where there could be phases of passivity (which happens in the system under consideration due to the physical friction) [KH01]. In order to avoid the energy accumulation issue which could make the system unstable, in this work, power-based TDPA is considered for the port. This port is passive at every time step if the power leaving the port is always limited by the power entering it. The observed power (difference between input and output power) is given by:

$$P_{obs} = F_h V_d - \tilde{F}_m V_d. \tag{3.46}$$

This observed power has to be greater than 0 at all times. If not, it means that the power output of the system is greater than input power, which leads to activity at that time step. The power dissipated by a damping element γ in the system with velocity V_d is γV_d^2. In order to satisfy passivity condition, an impedance-type PC (force modifying type) is added, namely the damping γ if P_{obs} becomes negative at any point:

$$\gamma = \begin{cases} -P_{obs}/V_d^2 & \text{if } P_{obs} < 0 \\ 0 & \text{else.} \end{cases} \tag{3.47}$$

Note that, the power observed by the PO is affected by the velocity of the haptic device V_d, which is in fact affected by the physical damping of the system. This method based on TDPA gives benefit to the proposed method only if there is physical friction in the haptic device. Similar to the model-based damping injection in method 1, the POPC method is also limited by the available friction of the haptic device.

3.2.3 Experiments and Results

Similar experiments described in Section 3.2.1 were conducted on the LWR-based haptic device equipped with a force torque sensor at the end-effector. For the time-varying gain approach proposed in this work, the logistic variation of Fig. 3.10 with $\alpha = \frac{\alpha^{max}}{1+e^{k(|\tilde{F}_e|-F_{e0})}}$ with α^{max}=1.4, k =1 and $F_{e0} = 10 \ N$ was selected. The desired trajectory has 3 parts: a low frequency (0.36 Hz) free robot motion, a higher frequency (0.72 Hz) free robot motion and a low frequency motion where the virtual robot hits the virtual wall. The test was first done without passivity checks and then with damping injection using the two proposed methods. The resulting positions and forces are shown in Fig. 3.13, Fig. 3.14 and Fig. 3.15, respectively.
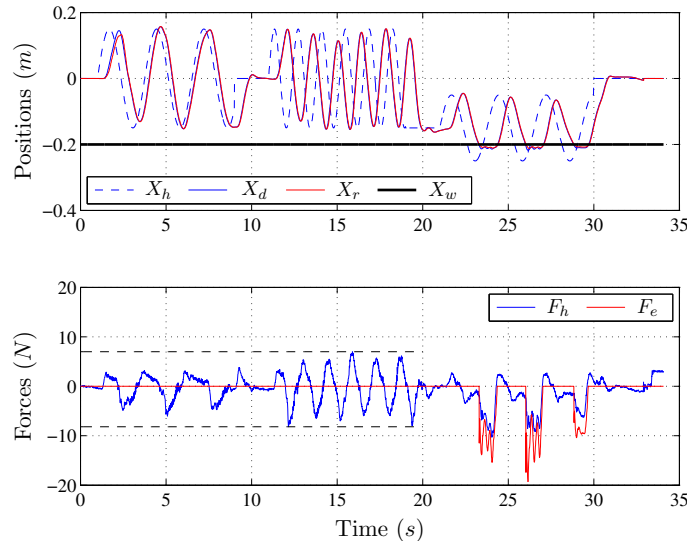

Figure 3.13: Proposed approach and without passivity checks.

3.2.4 Discussion

As desired, the proposed method reduces the perceived force during free motion and also enhances transparency during contacts. This behavior can be seen in Fig. 3.14 and Fig. 3.15, with the proposed methods. On the other hand, the unstable contacts without the passivity checks presented in Section 3.2.2 can be clearly seen in Fig. 3.13.

In order to evaluate the performance improvement of the proposed methods, the root mean square error (RMSE) between the measured environment force F_e and the force felt by the operator, F_h is calculated for the different approaches and are displayed in Fig. 3.16 in a normalized form. As it can be seen, without local force feedforward (NO FF), the error during free motion is higher since the operator feels the high inertia and damping of the haptic device. But during contacts, the error value is low since there is
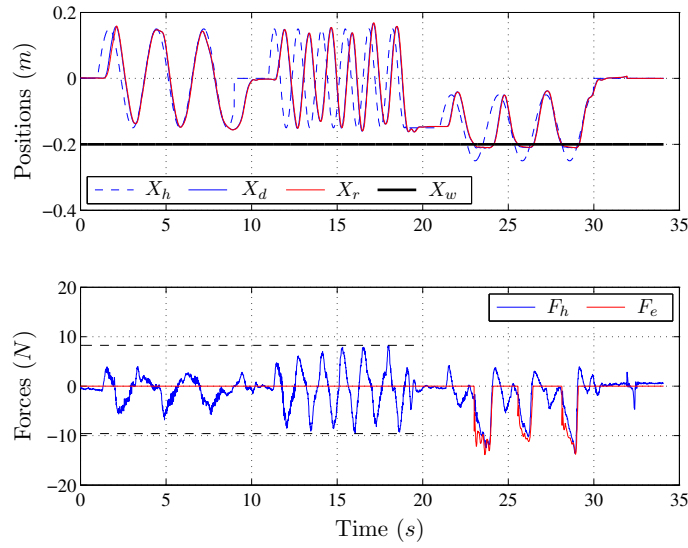
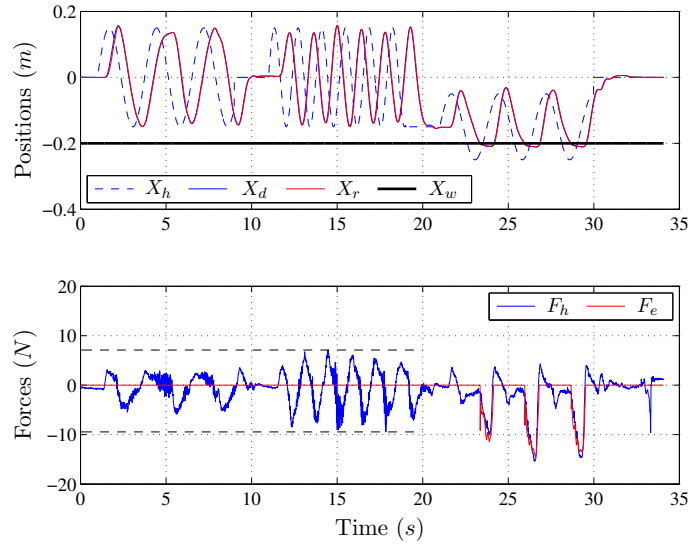Figure 3.14: Proposed approach with model-based damping injection.

Figure 3.15: Proposed approach passivated using TDPA.

no local feedforward and therefore, the operator perceives the remote robot environment with higher transparency. As expected, with the introduction of a constant gain for the local force feedforward, the perceived inertia and damping of the haptic device are highly reduced and the RMSE value is lower. Since the constant gain reduces the environment forces perceived by the human, the RMSE during contact motion is higher. The proposed methods (with damping injection and TDPA) improve the performance of the system in both free motion and during contacts as shown by low RMSE values. These plots validate the effectiveness of the proposed methods and clearly show that the benefits of both the earlier approaches (high transparency during contacts from 'No FF' and low inertia and damping during free motion from constant α) can be availed for a better teleoperation performance. Still the proposed method has certain limitations, which are mentioned in the following section.
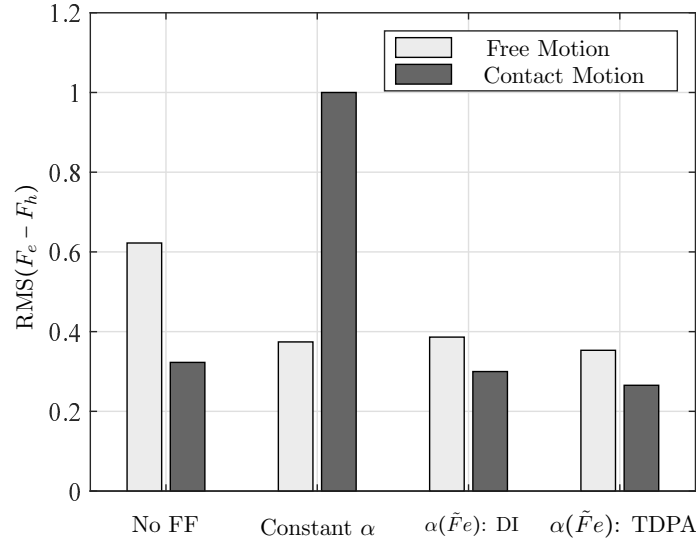
Figure 3.16: Bar plots of normalised root mean square errors of the forces F_e and F_h values for values for all the methods.

Limitations

The limitations of each of the approaches are presented in numbered format in order to refer them at later points in the thesis. The limitations of the methods proposed in this section are:

Limitation 3.2.1:
Model-based damping injection method for stability is highly dependent on the identification of the system parameters like inertia and damping.

Limitation 3.2.2:
TDPA-based approach introduces high frequency force modification (it is slightly seen in Fig. 3.15), which can be disturbing to the operator. This effect can be removed by using low-pass passive force filters [RAP10a], which are inherently passive and therefore, will not disrupt the passivity of the system.

Limitation 3.2.3:
As mentioned in Section 3.2.2, the improvement brought to the force tracking performance with both the approaches is limited by the physical damping present in the hardware of the haptic device. This is a huge limitation. In the next section, it will be shown how this limitation can be overcome using an explicit force controller instead of a feedforward force at the haptic device side.

Objective Achievement

As the position and force plots in Section 3.2.3 and the bar plots in Fig. 3.16 clearly indicate, the transparency of the time-delayed teleoperation system was enhanced during free motion as well as contact situations. In spite of the aforementioned limitations, the results show that the objective for this section presented in Section 3.2.1 has been achieved with the proposed method.

3.3 Explicit Force Control in Teleoperation

The benefits of the variable local force feedforward controller was explained in Section 3.2. The improvement in force tracking was presented there, but it was limited by the physical damping available in the hardware (limitation 3.2.3). Recently, explicit force control approaches for robotic manipulators have been proposed in [BJA⁺17] and [JBRK17], which were stabilized using TDPA. This chapter exploits the explicit force controller aiming to improve the transparency of teleoperation systems. The main contributions of this section can be summarized as follows:

1. Propose a new teleoperation architecture by formulating explicit force controller locally at the haptic device side to reduce the effects of limitation 3.2.3.

2. Ensure passivity of the proposed teleoperation architecture using TDPA, in order to avoid the effects of system modeling uncertainties (limitation 3.2.1).

First, the proposed concept is introduced with a signal flow diagram after which the equivalent electrical circuit representation is presented. This is finally used to employ TDPA to stabilize the system. To illustrate the performance enhancement, the proposed approach is compared to the widely used 4-channel architecture [RS15, ABR⁺16] for time-delays varying from 0 ms to 600 ms. The section is based on the work published by the author in [BRJ⁺20]

3.3.1 Research Gap and Objectives

Related Work

Although there have been large number of works to improve the force tracking performance in bilateral teleoperation, most of the bilateral control architectures send the forces at the remote robot to the haptic device only as feedback without explicitly using this for control. The reason for this could be traced back to the difficulty of ensuring stability of the explicit force control even in general robotic manipulators[SV12, ES86]. Therefore, applying explicit force controllers in teleoperation systems has not been researched significantly. In [ARS⁺15] and [PK06], remote robot forces are used to improve the system transparency and in [TSMO18], disturbance observers were used to compensate time-delays. There has been no work that uses TDPA to passivate the explicit force controllers used in teleoperation systems. This makes the system passivity robust against model uncertainties.

Problem Description

To present the problem and the proposed method, the 2-channel bilateral controller with position-measured force $(P - F_e)$ architecture [ARPH11] is taken as an example, whose signal flow diagram is shown in Fig. 3.17. Unlike in the 4-channel architecture introduced in Fig. 3.4, only the velocity of the haptic device V_d is sent to the robot. The force of interaction F_e, between the remote robot and the environment is measured using a force-torque sensor (FTS) and is sent to the haptic device for force feedback. Note that V'_d and F'_e are the delayed values of V_d and F_e, respectively.

The 2-channel teleoperation controller is applied on a system composed of an LWR-based haptic device and LWR remote robot. The test is conducted with a round-trip delay of 200 ms and the resulting positions and forces are shown in Fig. 3.18. On the top plot, X_d and X_r are the positions of the haptic device and robot, respectively and the
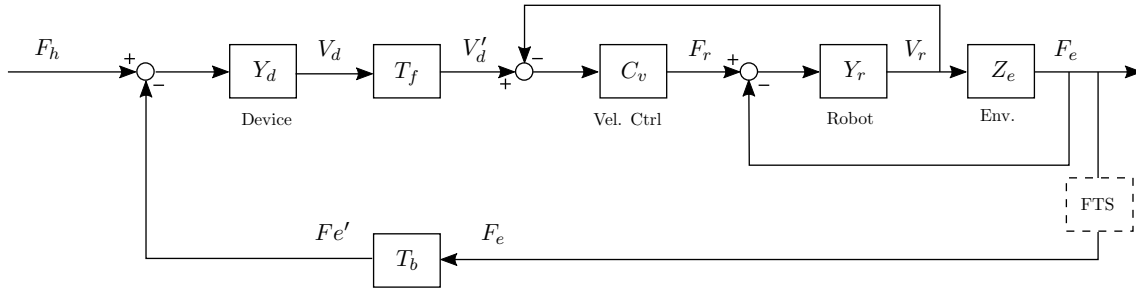
Figure 3.17: Signal flow diagram of the teleoperation system with 2-channel position-measured force architecture.

robot makes contacts with a stiff wall at X_w. Forces measured at the human-haptic device interface F_h and at the robot-environment interface F_e in the vertical direction are shown on the bottom plot. Similar to Fig. 3.8 in Section 3.2.1, the problem is clearly outlined in Fig. 3.18, namely, the operator has to apply significantly large forces even during free motion of the remote robot. This is typically attributed to the large inertia and damping of the LWR-based haptic device.
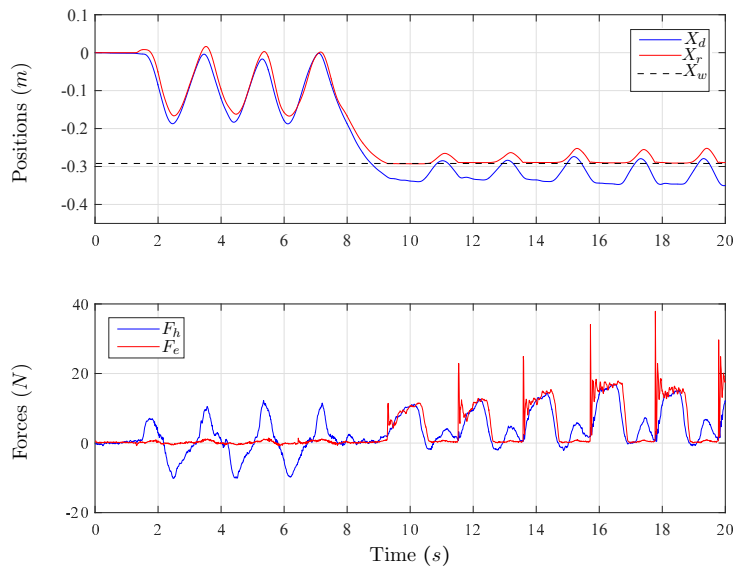

Figure 3.18: Position and forces with the conventional 2-channel $P - F_e$ bilateral controller. Note that even in free motion, the operator feels high forces due to the intrinsic inertia and damping of the haptic device.

Now, an explicit force controller is introduced at the haptic device side, the signal flow diagram of which is shown in Fig. 3.19. The force F_e measured at the robot side using the FTS delayed by the communication block T_b becomes the desired value F_e' of the explicit force controller C_f. At the interface between the operator and the haptic device, another FTS measures the human force F_h and is the measured force for the force controller. In order to generalize, the force controller can produce a PID action on the force error $F_{er} = F_e' - F_h$ such that the output force F_c is given by:

$$F_c(t) = K_{if} \int_0^t F_{er}(\tau)d\tau + K_{df}\dot{F}_{er}(t) + K_{pf}F_{er}(t), \tag{3.48}$$

with K_{pf}, K_{if} and K_{df} being the proportional, integral and the derivative gains, respectively of the force controller.
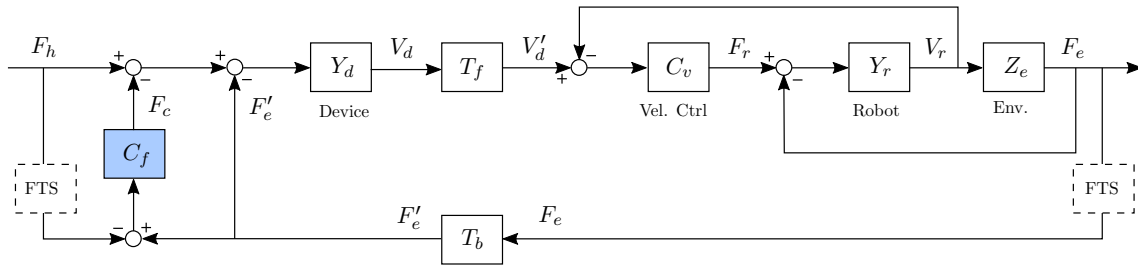

Figure 3.19: Signal flow diagram of the teleoperation system with explicit force controller.

Similar teleoperation experiments are conducted with the explicit force control architecture and the results are presented in Fig. 3.20. If we compare the performance of $P - F_e$ architecture in Fig. 3.18 to the one in Fig. 3.20, we can see that during free motion, the force controller significantly reduces the force perceived by the operator. But, during contacts, the teleoperation system with explicit force controller becomes highly unstable.
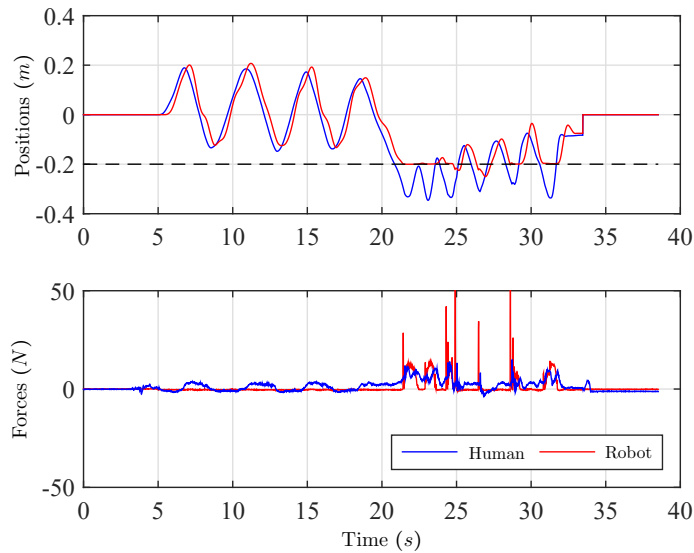
Figure 3.20: Positions and forces with EFC. It can be seen that the system goes unstable during contacts with rigid environments.

To summarize: For time-delayed teleoperation, although explicit force controllers at the haptic device side can improve the free motion force tracking, it might make the system unstable during contacts in the presence of time-delays in the communication channel.

Objective

The goal of this work is to design a stable explicit force controller at the haptic device to increase the transparency of the teleoperation system with delays, such that the inertia of the haptic device is reduced in free motion, and to improve the feedback quality of the contact forces. The stability of the explicit force controller should be independent of the physical damping, which was Limitation 3.2.3 of the method proposed in Section 3.2. To address Limitation 3.2.1, the stability method has to be model-independent.

3.3.2 Proposed Method

This section shows a method to ensure stability of the teleoperation system with explicit force controller by employing TDPA. The most challenging aspect associated with the design procedure is the representation of the overall system with electrical circuit for clearly identifying the energy flow within the system. The controller design procedure is explained sequentially in four steps.

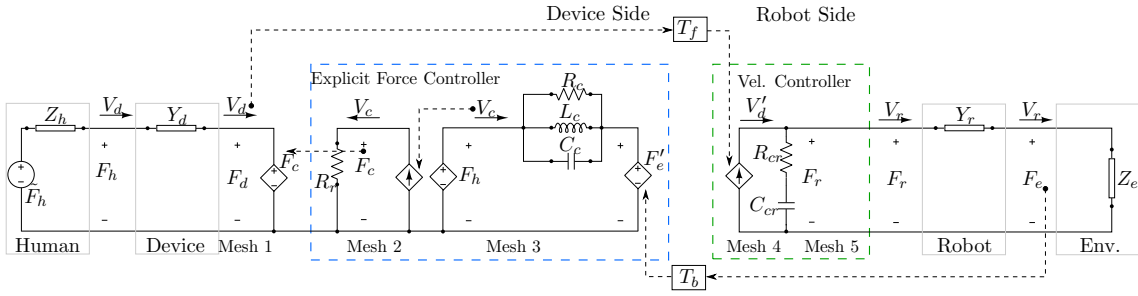### Step 1: Electrical circuit from signal-flow diagram

Figure 3.21: Step 1: Network representation of the time-delayed teleoperation system with explicit force controller at the haptic device side.

As a first step to apply TDPA, it is essential to convert the signal-flow diagram in Fig. 3.19 into an electrical circuit representation. The electrical-mechanical analogy is used here and the impedances of the human (Z_h) and the environment (Z_e) are represented as electrical impedances, admittance of the haptic device and robot are Y_d and Y_r, respectively as shown in Fig. 3.21. Meshes 1-3 correspond to the haptic device side and meshes 4-5 to the robot side of the teleoperation system. The velocity controller (C_v) at the robot side is represented with the resistance R_{cr} and capacitance C_{cr}, corresponding to the proportional and integral gains of the controller, respectively. The robot controller C_v produces a voltage F_r to minimize the error between the currents V'_d, the delayed current flowing through the haptic device impedance and V_r, the current through the robot impedance. F_e is the voltage that is generated across the environment impedance due to the robot current flowing through it.

At the haptic device side, to the explicit force controller (meshes 2-3 in the Blue dashed box), the delayed measured voltage F'_e is commanded as the desired value. The voltage measured across the human impedance F_h is made to match this desired value (F'_e) using the PID explicit force controller. The current in the PID controller (mesh 3) V_c is the sum of the currents flowing through the three parallel elements: R_c is the resistance corresponding to the proportional gain, L_c is the inductance corresponding to the integral gain, and C_c is the capacitance for the derivative gain presented in (3.48). This means, in Laplace domain:

$$V_c(s) \quad = (F'_e(s) - F_h(s))(\tfrac{1}{R_c} + \tfrac{1}{L_c s} + sC_c). \tag{3.49}$$

Mesh 2 is a trans-impedance network which converts current V_c to a voltage F_c across the resistance R_r.

$$F_c(s) = R_r V_c(s) = (F'_e(s) - F_h(s))(\frac{R_r}{R_c} + \frac{R_r}{L_c s} + sC_cR_r). \tag{3.50}$$

In Laplace domain, force controller in (3.48) can be written as:

$$F_c(s) = F_{er}(s)\left(\frac{K_{if}}{s} + sK_{df} + K_{pf}\right). \tag{3.51}$$

Comparing (3.50) with (3.51),

$$K_{pf} = \frac{R_r}{R_c}, \quad K_{if} = \frac{R_r}{L_c}, \quad K_{df} = C_c R_r. \tag{3.52}$$

Now, without any other voltage sources, the voltage F_d applied to the haptic device impedance in mesh 1 (additional to the voltage from the human operator) is F_c. The reason for deriving the electrical circuit of the teleoperation system, although not straight forward, will be clarified in the following steps.

Step 2: Ensure Passivity of Explicit Force Controller

Network representation makes energy flow clear, and can be used to identify potentially active components making the system unstable. The explicit force controller itself can be potentially active. Moreover, the explicit force controller contains delayed effort source, F_e, which makes it difficult to design the TDPA in parallel at the same layer. Therefore, we need to design TDPA sequentially, first for explicit force controller and later for delayed effort source. In our application, the one-port of the force controller is identified directly from the circuit (blue dashed box in Fig. 3.21) and is isolated in Fig. 3.22.
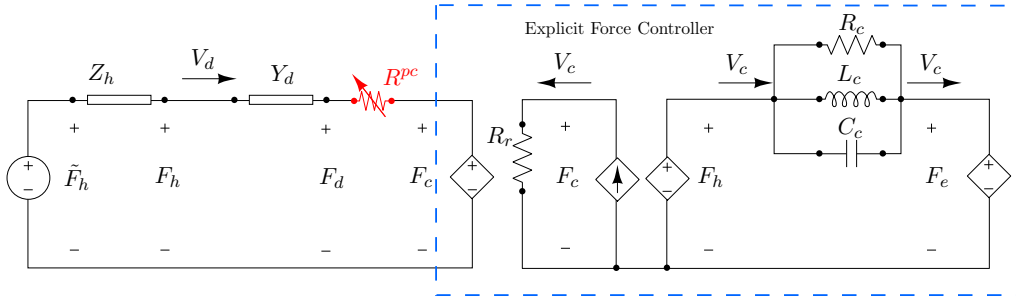
Figure 3.22: Step 2: Ensuring passivity of the explicit force controller (without delay) using TDPA.

For a 1-port network with power conjugated variables F_c and V_d, and with zero initial stored energy $E(0) = 0$, passivity condition, is given by:

$$\int_0^t F_c(\tau)V_d(\tau)d\tau \geq 0, \forall t \geq 0. \tag{3.53}$$

By designing a passivity observer (PO) and passivity controller (PC) and given in Table 2.5, we can ensure the passivity of the explicit force controller. For the given explicit force controller represented as the 1-port in Fig. 3.22, the energy observed by the PO is given for the time-step k by:

$$E^{obs}(k) = T_s \sum_{n=0}^{k} F_c(k)V_d(k) - T_s \sum_{n=0}^{k-1} R^{PC}(n)V_d(n)^2, \tag{3.54}$$

where R^{pc} is the time-varying resistance (the PC) introduced in the system if, at any time, the E^{obs} becomes negative [HR02]. With T_s being the sampling time, R^{pc} is calculated by

the following condition:

$$R^{pc}(k) = \begin{cases} -E^{obs}(k)/T_s V_d(k)^2 & \text{if } E^{obs}(k) < 0 \\ 0 & \text{else.} \end{cases} \tag{3.55}$$

The force commanded to the haptic device from the explicit force controller is modified as:

$$F_d(k) = F_c(k) - V_d(k)R^{pc}(k). \tag{3.56}$$

The resulting resistance R^{pc} is marked in Red in the circuit as shown in Fig. 3.22.

Step 3: Augment the bilateral controller with the passive explicit force controller

Once the passivity of the explicit force controller is ensured with TDPA, we can augment this with the rest of the 2-channel position-measured force bilateral controller [ARPH11]. To this end, the force F_d produced by the passivated explicit force controller is added with the feedback of the measured force F_e and is commanded to the haptic device. The circuit diagram of the resulting architecture is shown in Fig. 3.23. It should be noted that in Fig. 3.23, only the haptic device side of the bilateral controller is shown since this is where the explicit force controller, the object of interest in this work, is located. The remote robot side of the system is passivated exactly as explained in [ARPH11]. High-frequency force modification is widely accepted as a practical limitation of TDPA. To this end, a mass-spring-damper (MSD) filter with sufficiently high damping (making it passive) is introduced in the system as shown within the Green dashed box in Fig. 3.23. Note that, now, the power conjugated variables for the one-port of the force controller are F_c and V_f, where V_f is the velocity of the filter mass. This variable, V_f, should be used in (3.54), (3.55) and (3.56) instead of V_d.
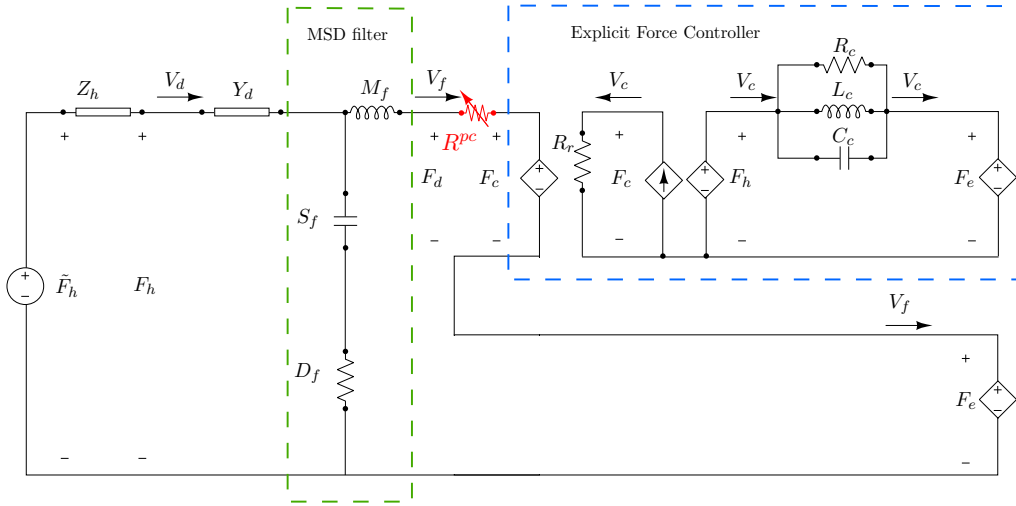

Figure 3.23: Step 3: Operator side of the position-measured force architecture augmented with the explicit force controller and the MSD filter.

Step 4: Make the augmented bilateral controller passive in presence of delays

The communication delays can be addressed by shifting the measured voltage sources to their non-delayed locations and introducing the time-delay power networks (TDPN,

[ARPH11]) in the system as shown in Fig. 3.24. In short, TDPN is a 2-port that introduces delay for the power-correlated variables of the ports on both sides and enables POPC as applied on a normal 2-port as explained in Table 2.4. The 2-port TDPN and the corresponding POPC combination compensate for the activity introduced by the communication delays between the haptic device and remote robot sides by ensuring that the energy coming out of the TDPN (for example, in $TDPN_1$, E_{out1} due to the non-delayed force controller current V_c and the delayed measured voltage F_e') is always less than or equal to the energy entering the TDPN (E_{in1} due to the non-delayed measured voltage F_e delayed force controller velocity V_c'). The PO for $TDPN_1$ with power conjugated variables (F_e, V_c') on the remote robot side, and (F_e', V_c) on the haptic device side is designed as:

$$E^{obs1}(k) = E^{in1}(k) - E^{out1}(k) - T_s \sum_{n=0}^{k} R_{pc1}(n-1)V_c(n-1)^2 T, \qquad (3.57)$$

and later, R_{pc1} is the PC introduced in the system if at any time, the E_{obs1} value becomes less than 0:

$$R_{pc1}(k) = \begin{cases} -E^{obs1}(k)/T_s V_c(k)^2 & \text{if } E_{obs1}(k) < 0 \\ 0 & \text{else.} \end{cases} \qquad (3.58)$$

The same procedure is followed for $TDPN_2$ with the corresponding power conjugated variable pairs : (F_e, V_f') at the remote robot side port and (F_e', V_f) at the haptic device side port. More details on TDPNs and the corresponding PO+PCs can be found in [ARPH11].
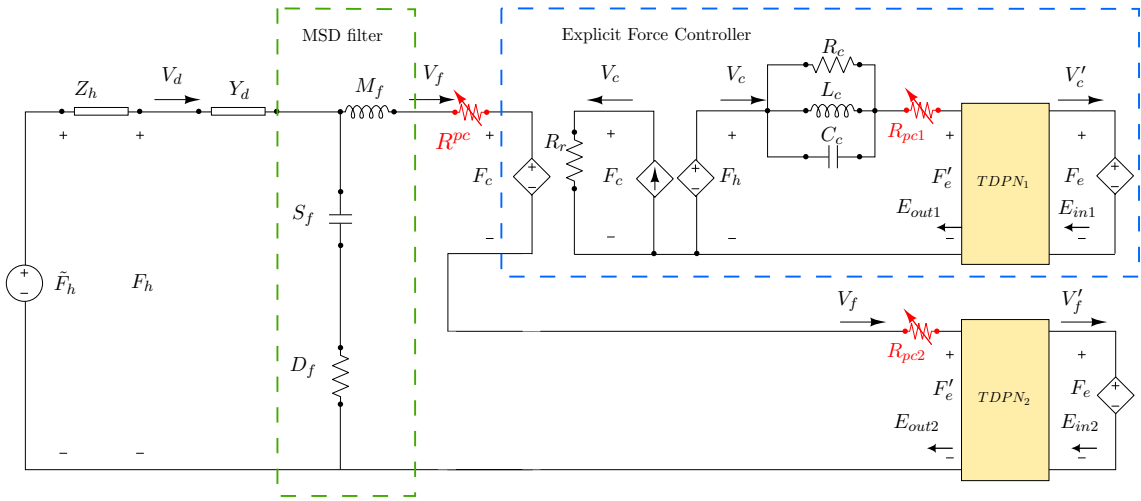
Figure 3.24: Step 4: Electrical diagram of the position-measured force architecture with time-delays, augmented with explicit force controller.

3.3.3 Experiments and Results

Teleoperation experiments similar to the ones presented in Section 3.3.1 were conducted with the explicit force controller stabilized by the proposed method and the results are presented in Fig. 3.25.

To compare the performance of the system with the explicit force controller and the conventional 4-channel architecture, the teleoperation experiments with 10 rounds each of

Figure 3.25: Positions and forces with EFC and 200 ms delay. It can be seen that the system is stable during contacts with rigid environments.

free motions and contacts were conducted for 6 different time-delays for both the bilateral controllers. The delay values chosen were 0 ms, 30 ms, 100 ms, 200 ms, 400 ms and 600 ms. Although the proposed method can handle 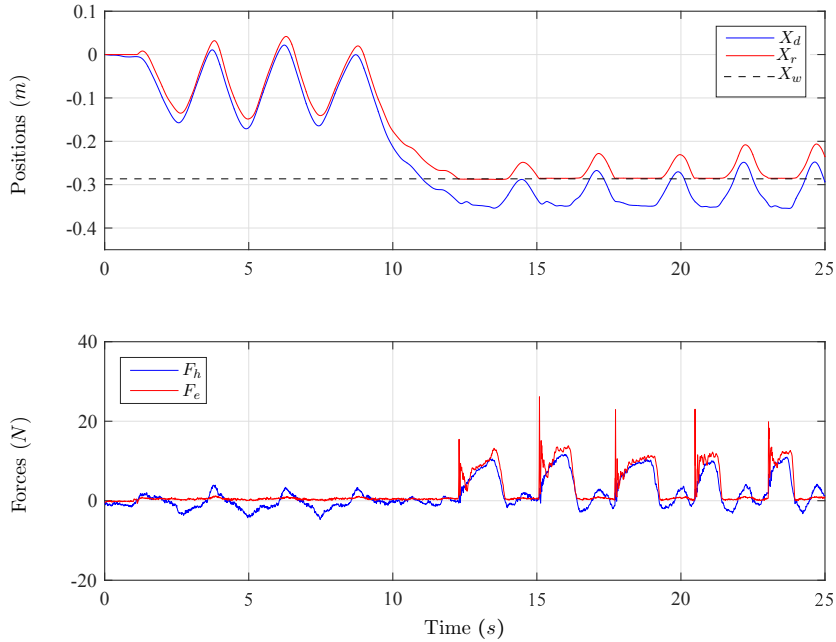time-varying communication delays, only constant time-delay was used in order to identify the tendency of force error as the time-delay increases. The root mean square errors (RMSE) between F_e and F_h were calculated for all the delays whose normalized values are illustrated in Fig. 3.26. The percentage reduction in RMSE due to the explicit force controller for each delay is shown in the bar graphs.

3.3.4 Discussion

It can be seen in Fig. 3.25 that compared to Fig. 3.18 in Section 3.3.1, the force tracking has significantly improved in both free motion, as well as during contacts with the proposed force controller.

As evident from Fig. 3.26, during free motion, in all cases of delay, the force felt by the operator was significantly reduced with the explicit force controller. This implies that the force controller reduces the perceived inertia of the haptic device during free motion and also increases the contact stiffness perception for the operator since the force differences between free motion and contacts are more distinguishable. Also, the bar plots in Fig. 3.26 clearly indicate that the transparency of the time-delayed teleoperation system was enhanced during contact situations. As described in Section 3.3.2, the TDPA used for passivating the force controller needs only measurable quantities in the system, which makes it a model-independent method. Also, the force matching behavior of the force controller is independent of the physical damping of the haptic device.
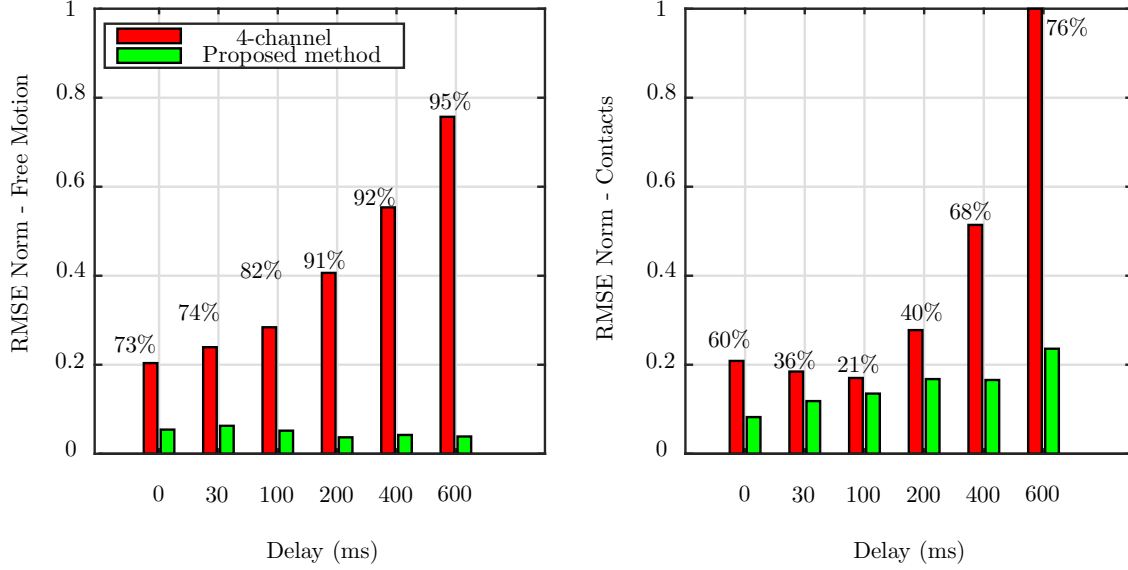
Figure 3.26: Comparison with conventional 4-channel controller.

Limitations

The following limitations were identified during the development of the method and the experiments:

Limitation 3.3.1:
During contact experiments, the error increased with and without the explicit force controller. The reason for the increase in force errors, even with the explicit force controller, is that the feedback gain for F_e (C_2 as explained in Section 3.2) has to be reduced with increasing delay since the PCs get highly noisy in order to remove the activity introduced by the delay. This noise in the PC affects the force loop which could make the system *vibratory*, if the delays are really high.

Limitation 3.3.2:
The energy-based TDPA used in this section leads to periods of instability because of the energy-accumulation problem of 1-port TDPA as described in Step 1 of the passivation procedure in Section 3.3.2. Due to this, the force controller gains had to be reduced.

Objective Achievement

Transparency of the time-delayed teleoperation system was enhanced during free motion as well as contact situations. Since the stability ensuring method using TDPA was independent of the haptic device's friction, the effects of Limitation 3.2.3 was reduced. TDPA is also a model-independent approach which takes care of Limitation 3.2.1.

However, due to the aforementioned limitations (reduction of force controller gains during large delays and energy accumulation of TDPA), the objective of this section mentioned in Section 3.3.1 is ***achieved only partially***. A solution is presented in the next section to solve the effects of these issues and also remove the limitations presented in these two sections.

3.4 Stability with Transparency Enhancement

The methods proposed in the previous sections significantly improved the force tracking performance of the teleoperation system. Still the limitations identified in Section 3.3 were pointed out as:

1. With the model-independent damping injection strategies using TDPA, feedback gain for the robot force has to be reduced with increasing delay since the PCs get highly noisy in order to remove the activity introduced by the delay. This noise from the PC affects the force loop which could make the system *vibratory*. This was mentioned in Limitation 3.3.1.

2. The energy accumulation problem in TDPA leads to short periods of instability as mentioned in Limitation 3.3.2.

In order to reduce the effect of these limitations, a general method to stabilize any user-defined feedback controller is presented in this section. The method is validated by teleoperation experiments with severe communication and contact scenarios. The work was published by the author in [BPDS$^+$21]

3.4.1 Research Gap and Objectives

Related Work

The standard position-computed force $P - F_c$ and position-position $P - P$ architectures have been modified and stabilized using multiple approaches. Some of the methods are wave variables (WV) [NS97], scattering formalism [LCS02], energy-tank approach [FSM$^+$11], passive set-position modulation [LH10] and the time domain passivity approach (TDPA, [RAP10b]). However, if the feedback controller is non-standard, ensuring stability might be difficult, although not impossible. In this section, a passive coupling reference approach (PCR) to stabilize non-standard and user-defined feedback controllers using force limitation is presented. Related to this work, force limitation has been applied in [KBR14, MCD17, LL09, PHA$^+$16, HLL$^+$18]. In [PHA$^+$16] the feedback forces for only the position-measured force architecture are limited to the passive coupling force. In contrast, here a simple framework to stabilize any feedback control architecture is presented. [LL09] and [HLL$^+$18] are developed only for virtual environments and haptics. Unlike in [KBR14] and [MCD17], the proposed method does not need identification of system parameters (for example, friction).

Problem Description

To ensure stability for non-standard feedback controllers with model-based methods [CS04, JSK$^+$18], significant amounts of time might be required to find the right Lyapunov function [NBO11, Li98, HL11]. For model-free methods like TDPA, which gained attention due to its intrinsic robustness against variable delays and modularity [Pea13], finding the correct port network might not be straightforward [BRJ$^+$20].

To summarize: Proving stability for certain user-defined feedback controllers independent of delay and environments is difficult, which limits the freedom of the controller designer to extract the best performance of the available hardware.

Objective

The objective of this section is to design a simple and effective framework to stabilize user-defined feedback controllers in teleoperation systems (with high and time-varying delays) in order to reduce the effects of (i) Limitation 3.2.1: modeling errors, (ii) Limitation 3.3.1: PC noise issues and (iii) Limitation 3.3.2: energy accumulation of TDPA.

3.4.2 Proposed Method

Let us start with a very simple, single degree-of-freedom (DoF) representation of a teleoperation system shown Section 2.1.2. To ease the reading and explanation, it is repeated here with the physical representation of the teleoperation system in Fig. 2.4 . A human operator moves a haptic device (represented by mass M_d and physical damping D_d) applying a force F_h, which arises due to the exogenous force $\tilde{F}_h$ and the interaction of human impedance Z_h with the haptic device, which moves with a velocity V_d. The haptic device is physically connected to a robot (with mass M_r and damping D_r) using a spring-damper coupling (with stiffness K_p and damping K_d). The robot moves due to the net force applied on it from the coupling F_c and the interaction force F_e due to the environment impedance Z_e. X_d and X_r are the positions of the device and robot, respectively.
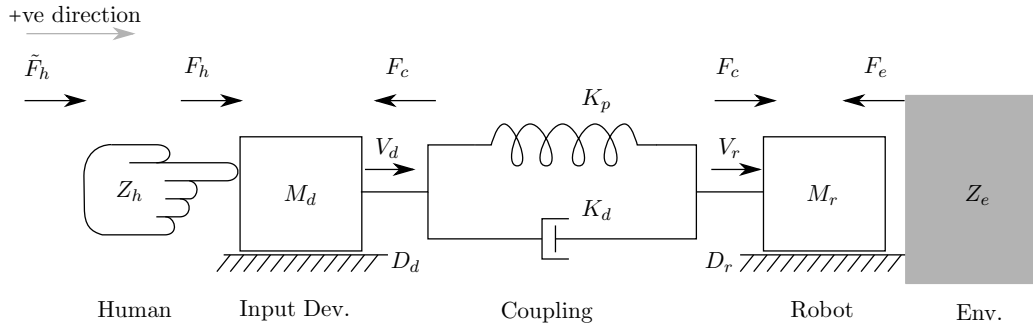

Figure 3.27: Single DoF, physical representation of a teleoperation system.

If the operator pushes the haptic device to the right (positive direction as indicated), the equations of motion for the masses are:

$$M_d\dot{V}_d = F_h - F_c - D_dV_d, \text{ and } M_r\dot{V}_r = F_c - F_e - D_rV_r, \tag{3.59}$$

and the coupling force F_c is computed as:

$$F_c = K_p(X_d - X_r) + K_d(V_d - V_r). \tag{3.60}$$

Consider the sum of kinetic energies of the masses and the potential energy of the spring as a storage function S_{F_c} given by:

$$S_{F_c} = \frac{1}{2}M_dV_d^2 + \frac{1}{2}M_rV_r^2 + \frac{1}{2}K_p(X_d - X_r)^2. \tag{3.61}$$

Taking the time derivative of the storage function S_{F_c}, and using (3.59) and (3.60) we get,

$$\begin{aligned} \dot{S}_{F_c} &= M_dV_d\dot{V}_d + M_rV_r\dot{V}_r + K_p(X_d - X_r)(V_d - V_r), \\ &= V_d(F_h - F_c - D_dV_d) + V_r(F_c - F_e - D_rV_r) \\ &+ (F_c - K_d(V_d - V_r))(V_d - V_r), \\ &= V_dF_h - V_rF_e - D_dV_d^2 - D_rV_r^2 - K_d(V_d - V_r)^2, \end{aligned} \tag{3.62}$$

which is output strictly passive (OSP) for the inputs $(F_h, -F_e)$ and outputs (V_d, V_r) and is therefore finite-gain L_2 stable as per Lemma 1, as already presented in Section 2.1.2.

As in Section 2.1.3, the electrical network representation (and the port representation) of the teleoperation system from Fig. 3.27 is shown in Fig. 3.28, with force $\equiv$ voltage analogy. The mass and damping of the haptic device and robot have been represented by admittances Y_d and Y_r, respectively. In the bottom diagram of Fig. 3.28, dependent voltage (force) and current (velocity) sources represent the same system in the top diagram, although there are two separate circuits. As explained in Section 2.1.3, the port (F_c, V_d) on the haptic device and (F_c, V_d) on the robot side makes the circuit separation lossless, and maintains the passivity of the overall system.

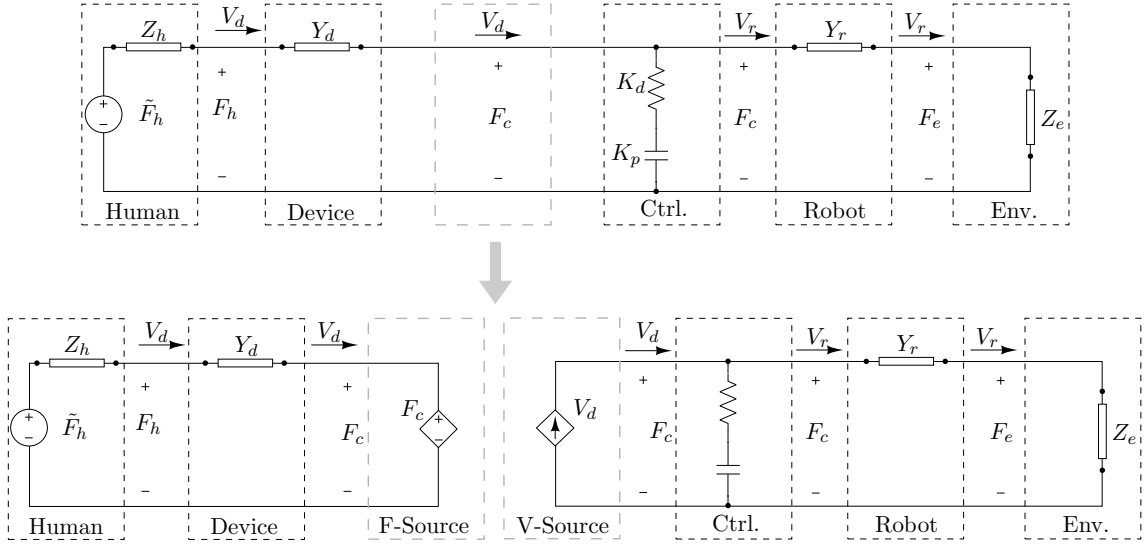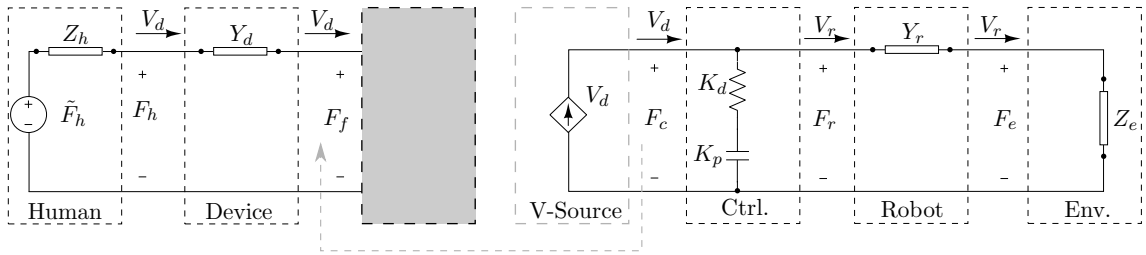Figure 3.28: Separated circuits with dependent force and velocity sources.

Figure 3.29: Separated circuits with dependent force and velocity sources and feedback circuit as a *Gray-box*.

Consider instead, that the force from the dependent source (the *Gray-box* in Fig. 3.29) is F_f. The equation of motion of the haptic device in (3.59) has to be modified as:

$$M_d \dot{V}_d = F_h - F_f - D_d V_d, \tag{3.63}$$

For a storage function S_{F_f} similar to S_{F_c} as in (3.61), the time derivative will result in:

$$
\begin{aligned}
\dot{S}_{F_f} &= M_d V_d \dot{V}_d + M_r V_r \dot{V}_r + K_p (X_d - X_r)(V_d - V_r), \\
&= V_d(F_h - F_f - D_d V_d) + V_r(F_c - F_e - D_r V_r) \\
&+ (F_c - K_d(V_d - V_r))(V_d - V_r), \\
&= V_d F_h - V_r F_e - D_d V_d^2 - D_r V_r^2 - K_d(V_d - V_r)^2 \\
&+ V_d(F_c - F_f).
\end{aligned}
\tag{3.64}
$$

The system is still output strict passive if,

$$
V_d(F_c - F_f) \leq 0
\tag{3.65}
$$

Note that this condition was derived for the case when the operator is pushing the haptic device to the right (positive direction), that is $F_h > 0$. The power exchanged between the operator and the haptic device is $F_h V_d$. In order to evaluate the passivity condition in (3.65) in terms of power interaction between the operator to the overall system, (3.65) is multiplied with the positive value of F_h, which results in:

$$
F_h V_d(F_c - F_f) \leq 0.
\tag{3.66}
$$

This leads to the conditions:

$$
\begin{aligned}
F_c &\leq F_f & \text{if } F_h V_d > 0, \\
F_c &\geq F_f & \text{if } F_h V_d < 0.
\end{aligned}
\tag{3.67}
$$

If the operator pulls the haptic device to the left (negative direction), the equations of motion of the masses and the coupling forces will be modified as:

$$
M_d \dot{V}_d = F_f - F_h - D_d V_d, \quad M_r \dot{V}_r = F_e - F_c - D_r V_r, \quad \text{and} \quad F_c = -K_p(X_d - X_r) - K_d(V_d - V_r),
\tag{3.68}
$$

which lead to the same condition in (3.67). Let us evaluate these conditions physically. Irrespective of the direction of force application, if the human force F_h and velocity V_d are co-aligned, F_f can be greater than F_c. On the other hand, when they are not co-aligned, if F_f is limited by the controller force F_c, the system is strictly output passive and again, finite-gain L_2 stable. The co-alignment of F_h and V_d is checked by the power $(F_h V_d)$ flow between the operator and the haptic device. In other words, if the human is driving the system (power flow from operator to system), we can let F_f be greater than F_c. But we do not let the system drive the haptic device (power flow to the human) with a force more than F_c. Therefore, the passive coupling referenced output force F_{pcr} is given by:

$$
F_{pcr} =
\begin{cases}
F_f & \text{if } F_f > F_c \text{ and } F_h V_d > 0, \\
F_c & \text{if } F_c > F_f \text{ and } F_h V_d > 0, \\
F_f & \text{if } F_c > F_f \text{ and } F_h V_d < 0, \\
F_c & \text{if } F_c \leq F_f \text{ and } F_h V_d < 0.
\end{cases}
\tag{3.69}
$$

To implement (3.69), the forces at the operator-haptic device interaction need to be measured using a FTS. In the absence of a sensor, these forces can either be observed as a disturbance [DLM05] or the power flow from the haptic device to the teleoperation system ($F_f V_d$, instead of $F_h V_d$) can be used to ensure passivity of the system with (3.69).

F

Application to Feedback Architectures

The passive coupling reference method allows for the stabilization of any feedback controller in the Gray-box in the Fig. 3.29 architecture. Let us now apply it in different feedback architectures for bilateral controllers, starting with simple systems, without delay which will lead to the explanation for the delayed case.

Position - Measured Force ($P - F_e$)

As the simplest example, let us consider a position-measured force architecture proposed in [PHA$^+$16] implemented with the PCR approach. Here, the dependent force (voltage) source F_e is plugged into the Gray-box in Fig. 3.29 and is shown in Fig. 3.30. In this case, the feedback force $F_f = F_e$ is limited as in (3.69) which makes the system finite-gain L_2 stable.
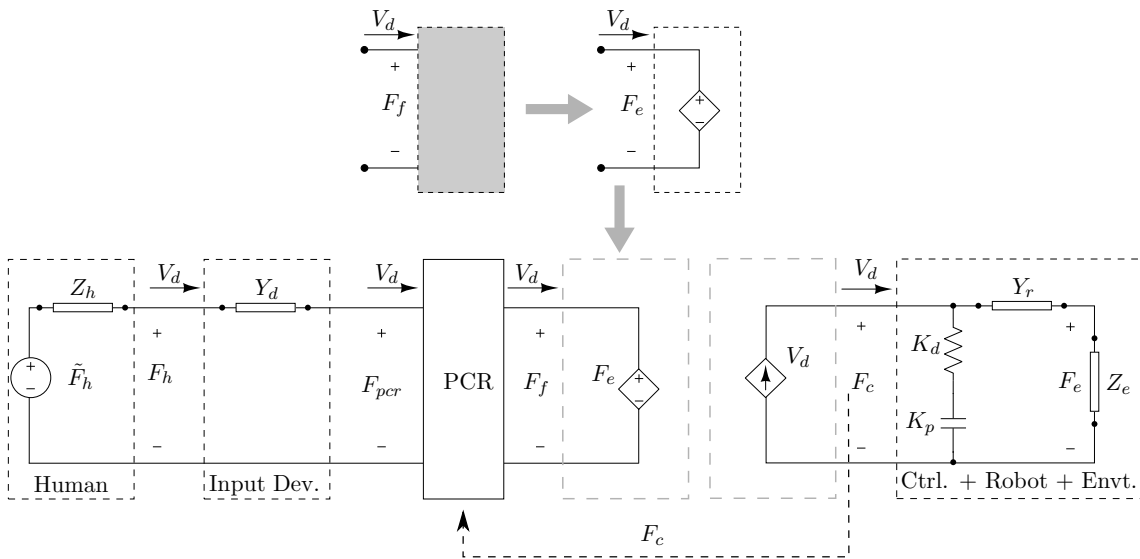

Figure 3.30: Position-measured force feedback with PCR.
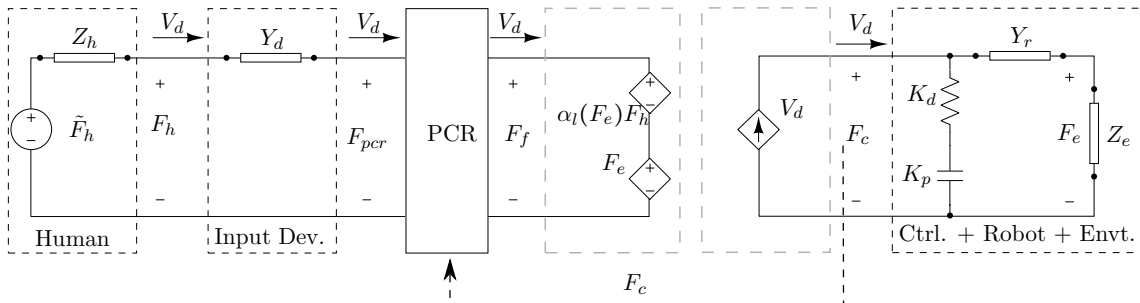
Non-linear Force Feedforward Gain: Section 3.2

Figure 3.31: Non-linear force feedforward method from Section 3.2.

The non-linear gain for the local force feedback from Section 3.2 can be stabilized using PCR. Along with the pure F_e force source in Fig. 3.30, the non-linear feedback of the F_h

is added in the feedback controller forces as shown in Fig. 3.31. Now, to implement PCR and make the system stable, we have $F_f = \alpha_l(F_e)F_h + F_e$ and can then apply the conditions in (3.69).

Explicit Force Controller Feedback ($P-EFC$: Section 3.3)

As the last example, the explicit force controller from Section 3.3 is stabilized with PCR. The electrical representation is shown in Fig. 3.32. The dashed box represents the EFC and the feedback force F_f used for the PCR condition in (3.69). In this case, $F_f = F_{fc} + F_e$, where

$$F_{fc} = \frac{R_r}{R_c}(F_e - F_h) + \int \frac{R_r}{L_c}(F_e - F_h)dt + C_c R_r(\dot{F}_e - \dot{F}_h) \qquad (3.70)$$

is the force produced by the force controller, with $\frac{R_r}{R_c}$, $\frac{R_r}{L_c}$ and $C_c R_r$ being the proportional, integral and derivative terms of the EFC. Please refer [BRJ+20] for detailed explanations.
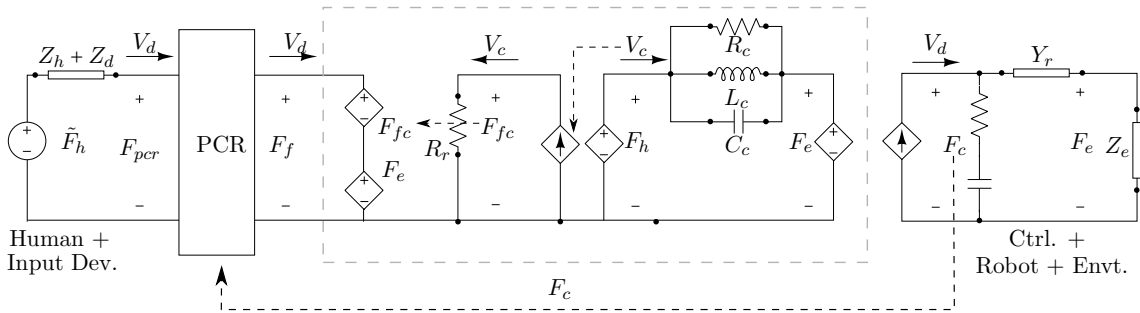
Figure 3.32: Explicit force controller feedback with PCR.

Teleoperation with Delays
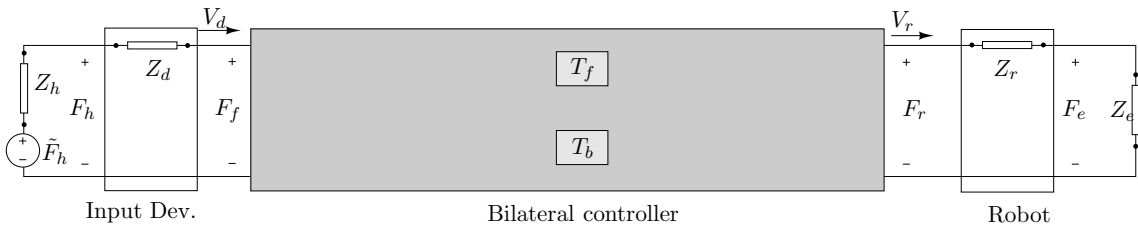
Figure 3.33: Port representation of teleoperation system with delay.

Teleoperation system with delay will now be stabilized using PCR. As shown in Fig. 3.33, the haptic device and the robot are coupled with a bilateral controller with delays T_f and T_b in the forward and feedback channels respectively. It includes the velocity/position controller which applies a force F_r to make the robot follow the haptic device, as well as the force F_f, the feedback to the operator. It is represented as a Gray-box since there are several bilateral controller architectures that use different stability approaches applied in the research community.

The equations of motion for the haptic device and the robot are as in (3.63), with force F_r commanded to the robot. Taking the kinetic energies of the haptic device and robot

as storage functions $S_d = \frac{M_d V_d^2}{2}$ and $S_r = \frac{M_r V_r^2}{2}$, respectively, we get their time derivatives as:

$$
\begin{aligned}
\dot{S}_d &= V_d F_h - V_d F_f - D_d V_d^2, \\
\dot{S}_r &= V_r F_r - V_r F_e - D_r V_r^2.
\end{aligned}
\tag{3.71}
$$

Eq. (3.71) proves that the device is output strict passive for inputs $(F_h, -F_f)$ and outputs (V_d, V_d), and that the robot is output strict passive for inputs $(F_r, -F_e)$ and outputs (V_r, V_r). Note that the negative sign for F_e is because it is an opposing force (or a negative feedback from the environment).

The inputs to the bilateral controller 2-port in Fig. 3.33 are the device and robot velocities V_d and $-V_r$, respectively and it produces the output F_r to move the robot and F_f as the feedback to the haptic device. As long as the bilateral controller 2-port is passive with respect to the input $(V_d, -V_r)$ and output (F_f, F_r), we can prove the overall passivity of the combined system. Any of the methods mentioned in Section 3.4.1 can be used to passivate the bilateral controller, the examples of WV [NS97], TDPA-based $P - P$ architecture [ARP10], and TDPA-based $P - F_c$ architecture [Pea19] are shown in Fig. 3.34.
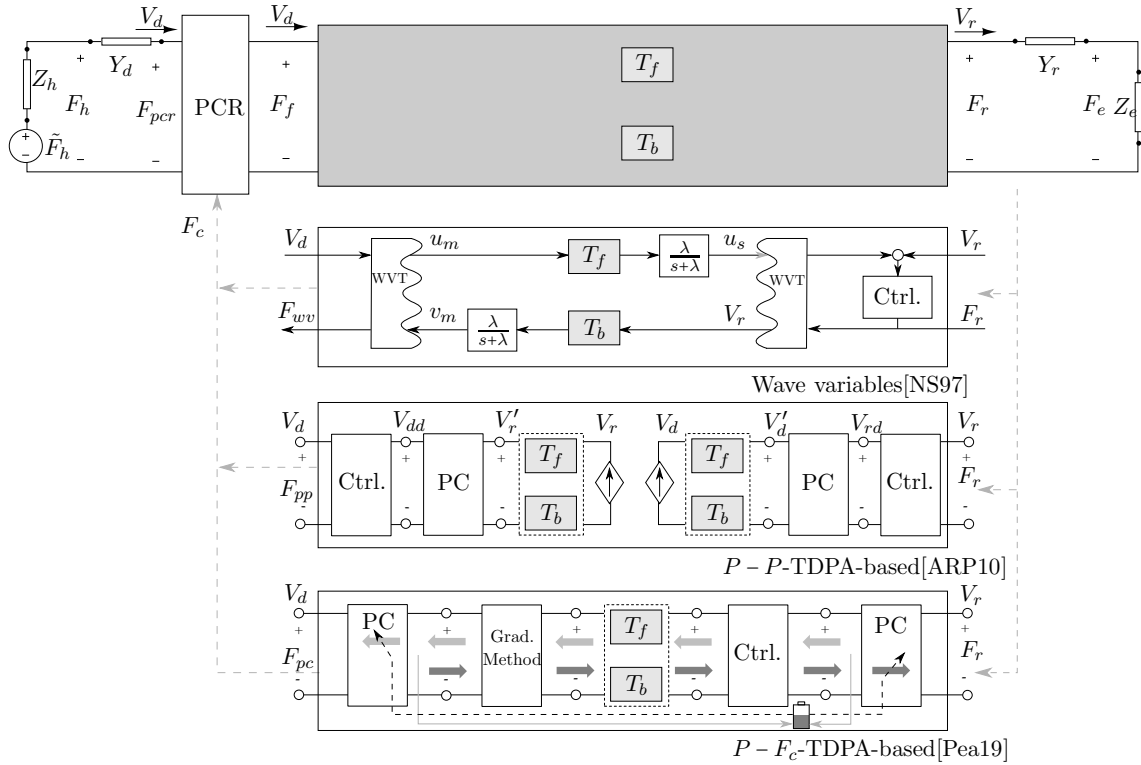
Figure 3.34: Passivating the bilateral controller using existing approaches.

In the block with the wave variable approach, the wave variable transformation (WVT) on either side of the delays transform power conjugated variables (velocities and forces) into wave variables, which are then transmitted between the haptic device and the robot as explained in Section 2.1.3. The noisy behaviors of the wave variables are reduced using filters with cut-off frequency λ which are the blocks containing $\frac{\lambda}{s+\lambda}$. On the other hand, in the TDPA-ER method [Pea19], the gradient method [Sea19] reduces the effect of passivity controllers dissipating excess energies which could make the $P - F_c$ architecture non-passive due to time-delays. For the $P - P$ architecture, the velocities of the devices

are exchanged across the communication channels and are modified at each side by the PCs before commanding them to the individual local controllers [ARP10].

If the feedback force of the Gray-box, F_f is limited by a *passive* force F_c, say, $F_c = F_{wv}$ if we use wave variables, $F_c = F_{pc}$ with TDPA-based $P - Fc$ or $F_c = F_{pp}$ for TDPA-based $P - P$, satisfying the conditions from (3.69), we can ensure the passivity of the bilateral controller of the Gray-box with any arbitrary feedback controller. Let us assume that one of these methods makes the 2-port system passive with inputs $(V_d, -V_r)$ and outputs (F_c, F_r). Then, there exists a storage function S_{bc} such that $\dot{S}_{bc} \leq V_d F_c - V_r F_r$.

Taking the storage function for the combined teleoperation system $S_{tp} = S_d + S_{bc} + S_r$, and using (3.71) and (3.65), we get,

$$
\begin{aligned}
\dot{S}_{tp} &\leq V_d F_h - V_d F_f + V_d F_c - V_r F_r + V_r F_r - V_r F_e \\
&- D_d V_d^2 - D_r V_r^2 \\
&\leq V_d F_h - V_r F_e - D_d V_d^2 - D_r V_r^2,
\end{aligned}
\tag{3.72}
$$

which is OSP for the input $(F_h, -F_e)$ and output (V_d, V_r) and is thus L_2 stable.

To illustrate an implementation example, the explicit force controller at the haptic device in a teleoperation system with time-delay is stabilized with PCR using the TDPA-ER method from [Pea19] as presented in Fig. 3.35. It has to be noted that V_d' and F_e' are the delayed velocity and the measured environment force, respectively and the PCR in (3.69) is applied with $F_f = F_{fc} + F_e'$ and $F_c = F_{pc}$.
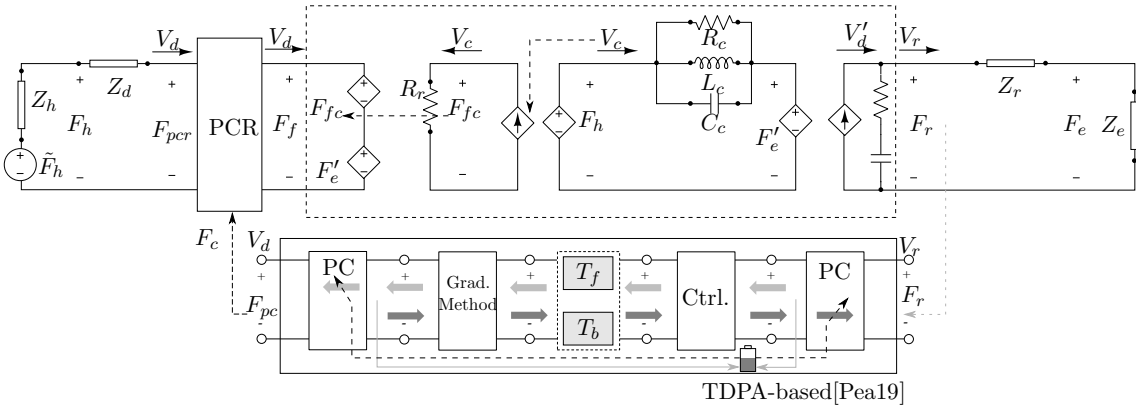

Figure 3.35: Passivating the system with EFC using TDPA-ER from [Pea19].

Extension to Multi-DoF Manipulators

As explained in Section 2.1.4, for the multi-DoF LWR-based haptic device (with number of joints $m = 7$ and Cartesian DoF $c = 6$, compensated for gravity), the Cartesian dynamics and control equation is given by:

$$
\begin{aligned}
\boldsymbol{\Lambda}_d(\boldsymbol{q}_d)\dot{\boldsymbol{V}}_d + \boldsymbol{\mu}_d(\boldsymbol{q}_d, \dot{\boldsymbol{q}}_d)\boldsymbol{V}_d + \boldsymbol{\Gamma}_d \boldsymbol{V}_d &= \boldsymbol{F}_h - \boldsymbol{F}_f, \\
\boldsymbol{\Lambda}_r(\boldsymbol{q}_r)\dot{\boldsymbol{V}}_r + \boldsymbol{\mu}_r(\boldsymbol{q}_r, \dot{\boldsymbol{q}}_r)\boldsymbol{V}_r + \boldsymbol{\Gamma}_r \boldsymbol{V}_r &= \boldsymbol{F}_r - \boldsymbol{F}_e,
\end{aligned}
$$

where $\boldsymbol{\Lambda}_{d,r} \in \mathbb{R}^{6\times6}$, $\boldsymbol{\mu}_{d,r} \in \mathbb{R}^{6\times6}$ and $\boldsymbol{\Gamma}_{d,r} \in \mathbb{R}^{6\times6}$ are the inertia, Coriolis/centrifugal and viscous damping (of the manipulators) matrices, respectively with $\boldsymbol{q}_{d,r} \in \mathbb{R}^7$ and $\boldsymbol{V}_{d,r} \in \mathbb{R}^6$ being the joint space configuration and the end-effector velocity, respectively. These terms are represented for the haptic device by $(\bullet_d)$ and robot by $(\bullet_r)$. $\boldsymbol{F}_h \in \mathbb{R}^6$ and $\boldsymbol{F}_e \in \mathbb{R}^6$ are

the measured wrenches at the end effectors of the haptic device and robot, respectively. $\boldsymbol{F}_r \in \mathbb{R}^6$, the forces commanded to the robot as well as the feedback forces to the haptic device $\boldsymbol{F}_f \in \mathbb{R}^6$, are different for different architectures. We choose the storage function,

$$S_{\boldsymbol{F}_f} = \frac{1}{2}\boldsymbol{V}_d^T \boldsymbol{\Lambda}_d \boldsymbol{V}_d + \frac{1}{2}\boldsymbol{V}_r^T \boldsymbol{\Lambda}_r \boldsymbol{V}_r + \frac{1}{2}\Delta \boldsymbol{X}^T \boldsymbol{K}_p \Delta \boldsymbol{X},$$

where $\boldsymbol{K}_p \in \mathbb{R}^{6\times6}$ is the constant positive matrix of Cartesian stiffness and $\Delta \boldsymbol{X}$ being the end-effectors' position error. Finding the time derivative of $S_{\boldsymbol{F}_f}$, and with passivity property of Euler-Lagrange systems, i.e, $\boldsymbol{V}_{d,r}^T (\dot{\boldsymbol{\Lambda}}_{d,r} - 2\boldsymbol{\mu}_{d,r})\boldsymbol{V}_{d,r} = 0$ [SSVO10], we come to the output strict passivity conditions in (3.65), namely, $\boldsymbol{V}_d^T(\boldsymbol{F}_c - \boldsymbol{F}_f) \le 0$ due to the physical damping considered. As explained in Section 2.1.4, component-wise pairing of the wrenches and the velocities is implemented with $\boldsymbol{V}_{d,i}(\boldsymbol{F}_{c,i} - \boldsymbol{F}_{f,i}) \le 0$, where $(\bullet_i)$ is the ith component of $(\bullet)$, which is a sufficient condition for OSP [DSAS16].

3.4.3 Experiments and Results

Three different architectures ($P - F_c, P - F_e$ and $P - EFC$), three different delays and three different environment stiffnesses are considered for the LWR-LWR teleoperation experiments as in Fig. 3.36. The position- computed force architecture method ($P - F_c$) provides the force used for PCR force limitation.
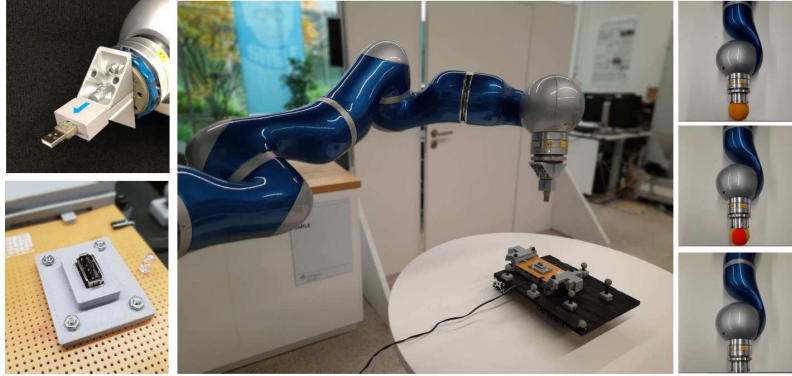

Figure 3.36: Robot (center), USB task board (left) and increasing stiffnesses (Right)

Teleoperation experiments are conducted with each of these three architectures for three different contact delays ($0\ ms$, $200\ ms$ and $600\ ms$) and for three different environment stiffnesses (low, medium and high, see Fig. 3.36). For the controller, proportional gains of $\boldsymbol{K}_{pt} = diag[300, 300, 300]\ N/m$ and $\boldsymbol{K}_{pr} = diag[20, 20, 20]\ Nm/rad$ were chosen for translations and rotations, respectively. The damping gains were $\boldsymbol{K}_{dt} = diag[20, 20, 20]\ Ns/m$ and $\boldsymbol{K}_{dr} = diag[2, 2, 2]\ Nms/rad$ for translations and rotations, respectively.

Comparison Experiments: The position following of the robot and the force tracking at the haptic device for the $200\ ms$ delay, high stiffness are shown in Fig. 3.38. The RMSE of the force errors for all the delays, stiffnesses and methods are summarized in Fig. 3.39a and Fig. 3.39b

Validation Task: A standard USB insertion task which needs precision in both position tracking and force application (see Fig. 3.36) was tested. The delay is varying with mean delay $600\ ms$ with $5\ ms$ variance (to show feasibility in space teleoperation [ABDS+16]).

The results are shown in Fig. 3.39c which validates that, in spite of the high variation in delay, the task was completed successfully.

3.4.4 Discussion

Stability: Stability of all feedback architectures has been ensured by PCR, for the considered delays and contact stiffnesses. Just as an example, compare Fig. 3.20, with Fig. 3.38c, which was conducted for identical conditions (200 ms delay and highest stiffness) to see the benefit of the method. The instability caused by the explicit force controller in Fig. 3.20 is completely removed by the PCR method.

Transparency: It has to be noted that PCR is only a stability tool. The improvement in transparency is due to the particular feedback controller used in the teleoperation system, for example the $P - EFC$ which tries to match the forces felt by the operator with the environment forces. The effect on free motion and contact transparency are discussed in detail as follows and in Fig. 3.37.

Free motion transparency: As it can be seen from Fig. 3.38a, during free motion, $P - F_c$ architecture presents significant forces to the operator due to the high inertia of the haptic device and its coupling with the robot. With $P - F_e$ architecture, the forces are lower since the coupling and robot inertia do not affect the feedback. The forces felt in this case are only due to the inertia of the haptic device. With $P - EFC$ architecture, the forces have been significantly reduced. As it can be seen in Fig. 3.39a, this trend is displayed in all cases. $P - EFC$ with PCR increases the transparency during free motion.

Contact transparency: During contacts, PCR does not produce a significant improvement in transparency. The transparency is almost the same as can be seen in Fig. 3.39b. The reason for this can be observed in Fig. 3.37, where we focus on single contacts for all the methods. During the motion into the wall (light Gray-box in all the plots), the force tracking is good. But while coming out of the wall (dark Gray-box) both $P - F_e$ and $P - EFC$ methods have a force profile almost similar to the $P - F_c$ method since the forces in all cases are limited by $P - F_c$ architecture. Note that force feedback performance was better with the TDPA-based approach from Section 3.3 as presented in Fig. 3.25. This is a limitation of the PCR method. In spite of this limitation, as the operators make contact with the environment, an important factor that affect their perception is the difference between free motion forces and the contact forces. If the transition is larger, the better is ~~the perception~~ [PHK+06]. Now, compare the Green boxes Fig. 3.37 in all cases. Just before and after the contact, $P - F_c$ method produces forces that are high so that the
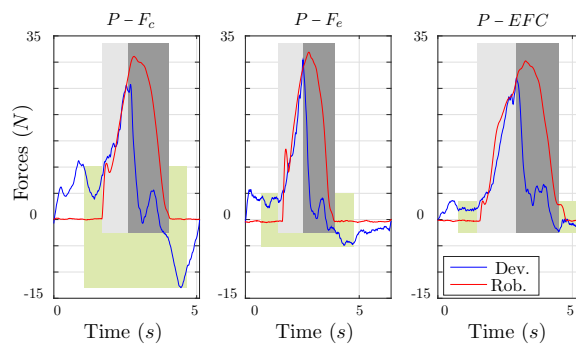

Figure 3.37: Comparison of single contacts for all the methods for 200 ms delay and medium stiffness.

contact perception is lower. The performance is better for $P - F_e$. $P - EFC$ with the explicit force controller proposed in this thesis offers the best contact perception.

It should be noted that although we applied a $P - F_c$ architecture passivated using TDPA-ER (improved with the gradient method to reduce PC noise) in this section, the proposed PCR approach is versatile so that any other method mentioned in Section 3.4.1 could be applied as well.

Limitations

The following limitation was identified during the experiments and evaluation of the results:

Limitation 3.4.1:
Although PCR ensure stability, the saturation of feedback controller force to the coupling force, which as a result also reduces contact transparency, can be seen as a limitation of the proposed method.

Objective Achievement

All the plots show stable behavior of the transparency enhancement method. Although practical limitations were identified during experiments, this section presented a framework to stabilize user-defined feedback controllers in teleoperation systems (with high and time-varying delays) to reduce the effects of (i) modeling errors, (ii) energy accumulation and (iii) PC noise issues of TDPA, which were mentioned as objectives in Section 3.4.1. The TDPA-ER method chosen for the underlying passive $P - F_c$ architecture is free of energy accumulation issues. The versatility of the PCR algorithm makes it possible also to use other methods like wave variables, which are also free of the energy accumulation issue.

3.5 Summary

This section introduced and explained two methods to improve the transparency of the teleoperation part of the shared control framework. Section 3.2 presented a novel nonlinear gain for the force feedforward controller while Section 3.3 improved the transparency by exploiting explicit force controllers locally at the haptic device. The two methods were stabilized using model-based and model-independent passivity tools. The limitations of the passivity tools used in these two sections were addressed in Section 3.4, where a general framework to stabilize any user-defined feedback controllers using passive coupling reference was developed. Hardware experiments with varying time-delays and contact stiffnesses validated the benefits of the methods and led way to the discussions of their limitations. Five of the limitations identified in Section 3.2 and Section 3.3 were addressed within the chapter. The final section based on PCR introduced a new limitation based on the experiment results. This is Limitation 3.4.1, which mentioned that the force feedback performance of PCR during contacts is limited by the underlying passivity tool used. This limitation could lead to future research like development of a stable method, which has high feedback quality during contacts. The next chapter develops the second *part* of the adaptive shared control framework, namely, stability in multi-agent robot control with adaptive authority allocation.
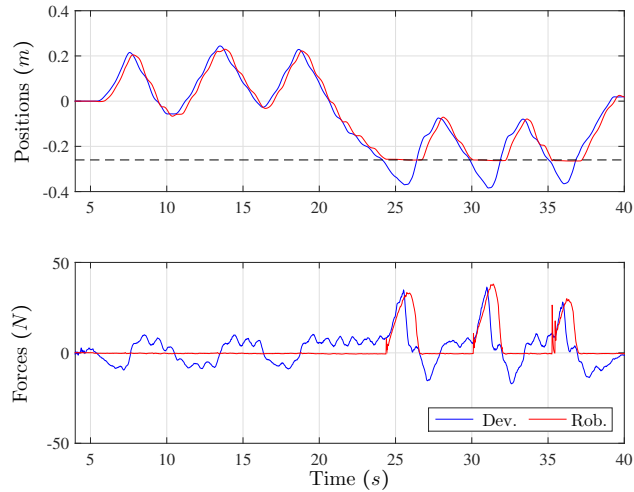
(a) $P - F_c$, High Stiffness
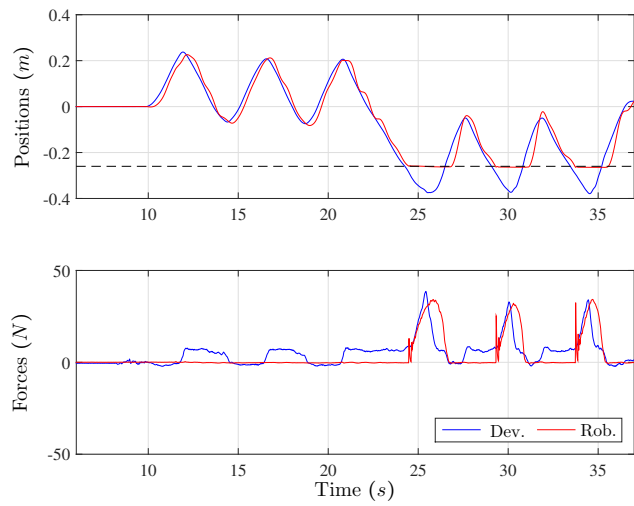
(b) $P - F_e$, High Stiffness

(c) $P - EFC$, High Stiffness

Figure 3.38: Positions and forces with 200 ms constant delay for high stiffness.

(a) Free motion

(b) Contacts
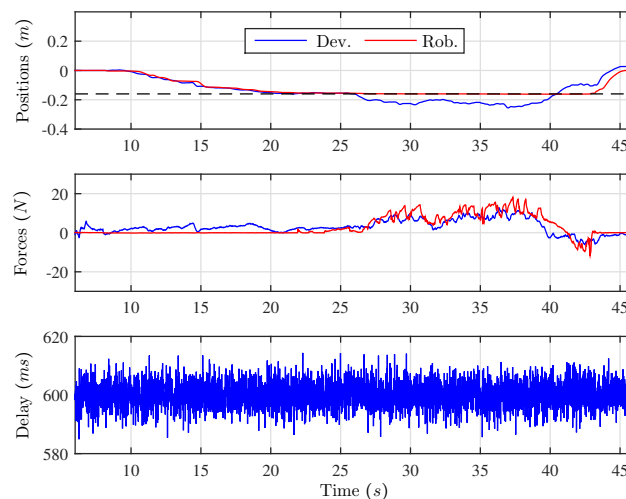
(c) USB insertion task

Figure 3.39: RMSE of Forces during (a): free motion and (b): contacts. (c): Positions, forces and time-varying delay for the USB task.

Multi-Agent Adaptive Shared Control

4.1 Introduction

In Chapter 3, a stable and transparent system was developed, which enabled versatile and modular teleoperation architectures. This chapter will address the second part of the shared control framework, namely, stability of a system, where multiple agents command forces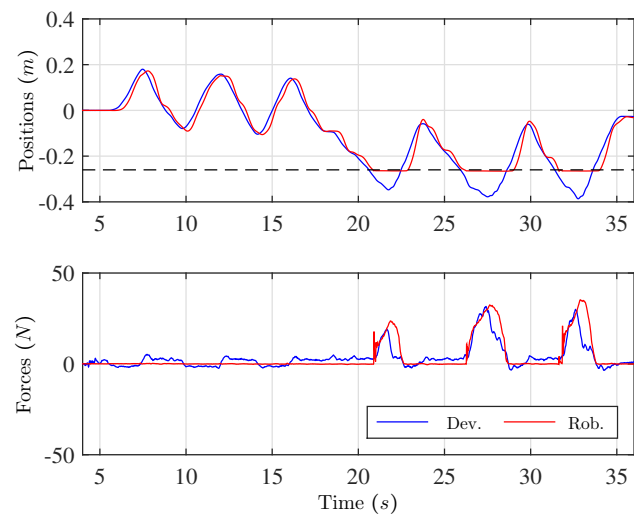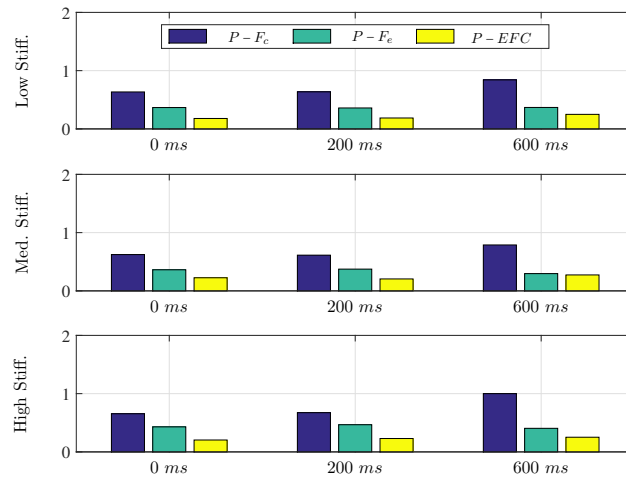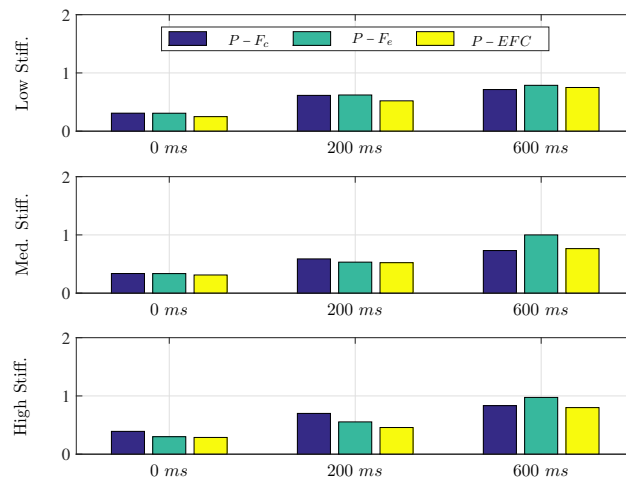 to the robot with varying authority allocation factors. In Section 4.2, the idea of unity-sum arbitration is explained and a novel system-driven authority allocation method is developed for the arbitration process. A user-study analyzes the benefits and limitations of this approach. Later, an analytical method is presented in Section 4.3 to ensure passivity of a multi-agent control framework with adaptive authority allocation. The arbitration is implemented by applying scaling on the forces. Later, Section 4.4 presents a new method for multi-agent adaptive control using varying stiffnesses. Section 4.5 summarizes the chapter with some insights into future research developments enabled by this work. The logical flow of the chapter is presented in Fig. 4.1 to give an overview to the reader.

Figure 4.1: Overview of Chapter 4

4.2 System-Driven Adaptive Shared Control

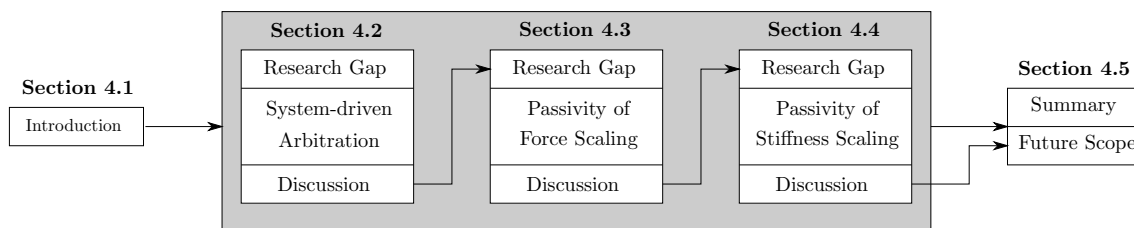As explained in Section 1.1, different research groups have developed several methods to adapt the AA factors online for mixed-initiative shared control. Some of them are human-driven, that is, the operator decides the arbitration process. On the other hand, in a system-driven arbitration process, the system resolves AA between different control agents and its timing [Sce96]. In this section, a novel system-driven approach is proposed, which adaptively allocates authority. The results from a user-study evaluation validates the benefits of the proposed method. This work is published by the author in [BMC⁺20].

4.2.1 Research Gap and Objectives

Related Work

In most system-driven arbitration approaches, the authority is distributed between the operator and the ACS in pre-defined manner. It could be using human intention recognition [DS13, KSB12] and probabilistic approaches [Tra15, PJTKLP10], with fixed process and measurement noise models. In this section, a novel system-driven arbitration approach is developed which modifies the AA factors based on real sensor measurement degradation. In [OGD15], related to the method proposed in the section, the trajectory commanded to the robot is a weighted sum of the trajectories generated by the ACS and commanded by the human. However, AA is based on the uncertainty of the autonomous controller using an *a priori* noise model.

Problem Description

A priori noise models are applicable only in the case where the noise characteristics of the sensor remain consistent. However, for many robotics application, this assumption is rarely guaranteed, for example, in vision-based perception. Using noise models defined a priori might result in modeling errors in case of time-varying noise characteristics and the robot will not react to the changes in the real environment adequately. For example, if the camera measurements degrade significantly due to the robot's ego motion (occlusions to the top camera as shown in Fig. 4.2) or in close proximity of the target, the ACS will not be able to complete the desired task. During such events, the system should allocate more authority to the operator based on its low confidence of target pose estimation. There has been no prior research work in the field of mixed-initiative shared control that addresses system-driven adaptation which depends on real measurement noise.
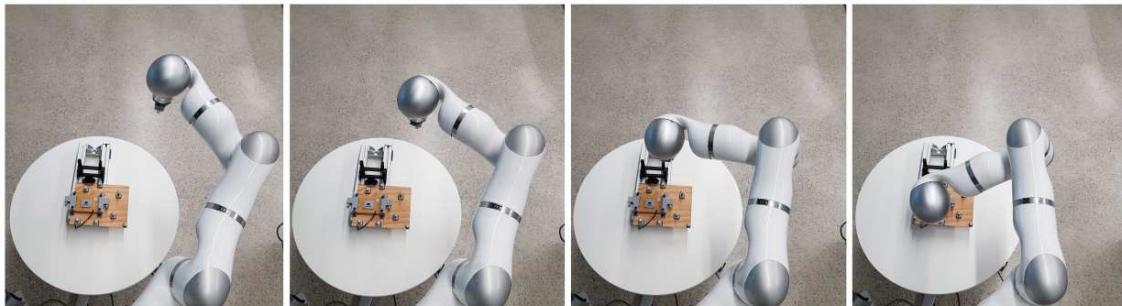

Figure 4.2: Example of a high precision industrial task during which the camera view is occluded by the robotic arm itself (right-most).

Objective

In many of the works in mixed-initiative shared control, the AA factors α_t and α_a for teleoperation and ACS, respectively, heuristically assume the unity-sum condition for arbitration [SCN+21, MH17a]. The following gives the mathematical definition of the unity-sum arbitration process.

Definition 4.1. *(Unity-sum Arbitration) A mixed-initiative shared control system with authority allocation factors α_t and α_a for teleoperation and ACS, respectively, is said to have unity-sum arbitration if*

$$F_r = \alpha_t F_t + \alpha_a F_a, \quad \alpha_t, \alpha_a \in [0,1] \; and \; \alpha_t + \alpha_a = 1, \tag{4.73}$$

where F_t and F_a are the forces produced by the teleoperation system and ACS, respectively and F_r is the final control force commanded to the robot .

The objective of this section is to decrease α_a when measurement degradation occurs and as a result of (4.73), increase $\alpha_t = 1 - \alpha_a$ according to the unity-sum arbitration as per Def. 4.1.

4.2.2 Proposed Method

The ACS is described in the beginning, followed by the limitations of vision-based ACS and Kalman filters with fixed measurement noise model. To reduce these limitations, Adaptive Extended Kalman filters are used to achieve the objective.

Automatic Control System

Consider a robot, represented by a mass M_r placed on a surface with viscous damping D_r, as shown in Fig. 4.3a with reference frame $\{E\}$ attached to it. The ACS is a spring-damper coupling, which regulates the position X_r of the robot to a desired target frame $\{T\}$ which is at a distance X, both measured from a fixed inertial frame $\{I\}$. The robot moves with a velocity V_r due to the forces acting on it by the ACS F_a and damping, that is:

$$\begin{aligned} M_r V_r &= F_a - D_r V_r, \\ F_a &= K_{pa}(X - X_r) - K_{da}V_r, \end{aligned} \tag{4.74}$$

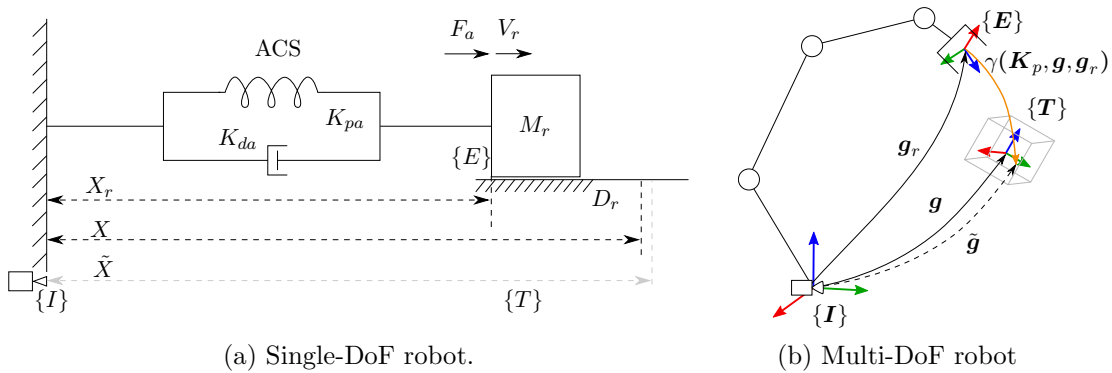
(a) Single-DoF robot.   (b) Multi-DoF robot

Figure 4.3: Representations of controlled robots

where K_{pa} and K_{da} are the stiffness and damping coefficients of the ACS. With a camera placed at the inertial frame, a vision-based feedback system provides a noisy measure of X, denoted as $\tilde{X}$, which is dashed in Gray in Fig. 4.3a. The ACS force produced with such a system is written as, $F_a = K_{pa}(\tilde{X} - X_r) - K_{da}V_r$. This shows that the stiffness term gets affected by the degraded measurements and hence makes the ACS vulnerable to it. This error term might lead to task failure, and more significantly, even increase likelihood of collisions with the environment.

The concept is now expanded for a multi-DoF manipulator. For a multi-DoF, m-joint (revolute) redundant manipulator arm, the task of the ACS is to regulate the end-effector pose, $\boldsymbol{g}_r \equiv (\boldsymbol{p}_r, \boldsymbol{\theta}_r) \in SE(3)$ where, $\boldsymbol{p}_r \in \mathbb{R}^3$ is the translational vector and $\theta_r \in \mathbb{Q}$ is the quaternion parameterization of the rotation, and $\mathbb{Q} \equiv \{\boldsymbol{\theta} \in \mathbb{R}^4 | \; \|\boldsymbol{\theta}\| = 1\}$. The regulation is performed about a Cartesian setpoint $\boldsymbol{g} \equiv (\boldsymbol{p}, \theta) \in SE(3)$ as shown in Fig. 4.3b. The end-effector pose, $\boldsymbol{g}_r(\boldsymbol{q}_r)$, is the forward kinematics map of its joint configuration $\boldsymbol{q}_r \in \mathbb{R}^m$, whose time derivative is written as, $\boldsymbol{V}_r = \boldsymbol{J}(\boldsymbol{q})\dot{\boldsymbol{q}} \in \mathbb{R}^6$, where $\boldsymbol{V}_r$ is the end-effector body velocity and $\boldsymbol{J}(\boldsymbol{q})$ is the corresponding Jacobian map. A vision-based feedback system provides a noisy measure of $\boldsymbol{g}$ as $\tilde{\boldsymbol{g}} \equiv (\tilde{\boldsymbol{p}}, \tilde{\boldsymbol{\theta}})$, which is dashed in Fig. 4.3b. The ACS is implemented as a passivity-based Cartesian PD controller. As presented in Section 2.1.4, the Cartesian dynamics and control equations can be written as,

$$\begin{aligned} \boldsymbol{\Lambda}_r(\boldsymbol{q}_r)\dot{\boldsymbol{V}}_r + \boldsymbol{\mu}_r(\boldsymbol{q}_r, \dot{\boldsymbol{q}}_r)\boldsymbol{V}_r + \boldsymbol{\Gamma}_r(\boldsymbol{q}_r, \dot{\boldsymbol{q}}_r)\boldsymbol{V}_r \; &= \; \boldsymbol{F}_a, \\ &= \; \boldsymbol{K}_p\Delta\boldsymbol{X} + \boldsymbol{K}_d\Delta\boldsymbol{V}, \end{aligned} \qquad (4.75)$$

where $\boldsymbol{\Lambda}_r$, $\boldsymbol{\mu}$, $\boldsymbol{\Gamma}$ and $\boldsymbol{F}_a$ refer to the matrices of Cartesian inertia and Coriolis/centrifugal terms, viscous damping, and Cartesian control forces, respectively, and joint torques are commanded to robot as, $\boldsymbol{\tau} = \boldsymbol{J}(\boldsymbol{q})^T \boldsymbol{F}_a$ (see [Mur17, §5.4]). $\boldsymbol{K}_p$ and $\boldsymbol{K}_d$ are diagonal and positive matrices for Cartesian stiffness and damping, respectively, and $\Delta\boldsymbol{X}$ and $\Delta\boldsymbol{V}$ are Cartesian position and rotation errors between $\tilde{\boldsymbol{g}}$ and $\boldsymbol{g}_r$.

Uncertainty in ACS

In this subsection, the dynamic model for a static setpoint frame $\{\boldsymbol{T}\}$ (see Fig. 4.3b) is provided and the significance of an adaptive Bayesian filter [Sär13, ch. 2] is outlined. For the sake of completeness, first a simple zero-acceleration stochastic process model for $\{\boldsymbol{T}\}$ is described, whose state is, $\boldsymbol{x} = \begin{bmatrix} \boldsymbol{p}^T & \boldsymbol{v}^T & \boldsymbol{\theta}^T & \boldsymbol{\omega}^T \end{bmatrix}^T \in \mathbb{R}^3 \times \mathbb{R}^3 \times \mathbb{Q} \times \mathbb{R}^3$. The dynamic model and the output function are written as,

$$\dot{\boldsymbol{x}} = \boldsymbol{f}(\boldsymbol{x}) = \begin{bmatrix} \boldsymbol{v} \\ \boldsymbol{\nu}_v \\ \frac{1}{2}\boldsymbol{\omega} \otimes \boldsymbol{\theta} \\ \boldsymbol{\nu}_\omega \end{bmatrix}, \; \boldsymbol{y} = \boldsymbol{h}(\boldsymbol{x}) = \begin{bmatrix} \tilde{\boldsymbol{p}} \\ \tilde{\boldsymbol{\theta}} \end{bmatrix}, \qquad (4.76)$$

where the velocities $\boldsymbol{v}$ and $\boldsymbol{\omega}$ are the inertial linear and body angular velocities respectively, and $\otimes$ is the quaternion multiplication operator. The process noise in (4.76) is $\boldsymbol{\nu} = \begin{bmatrix} \boldsymbol{\nu}_v^T & \boldsymbol{\nu}_\omega^T \end{bmatrix}^T \in \mathbb{R}^6$ and $\boldsymbol{Q} = \mathbb{E}(\boldsymbol{\nu}\boldsymbol{\nu}^T)$ is the process covariance, where $\mathbb{E}(\bullet)$ is the stochastic expectation of the argument. The measurement noise model is $\tilde{\boldsymbol{p}} = \boldsymbol{p} + \boldsymbol{\mu}_p$ and $\tilde{\boldsymbol{\theta}} = \begin{bmatrix} \boldsymbol{\mu}_\theta \\ 1 \end{bmatrix} \otimes \boldsymbol{\theta}$, $\boldsymbol{\mu} = \begin{bmatrix} \boldsymbol{\mu}_p^T & \boldsymbol{\mu}_\theta^T \end{bmatrix}^T \in \mathbb{R}^6$, with measurement noise covariance $\boldsymbol{R} = \mathbb{E}(\boldsymbol{\mu}\boldsymbol{\mu}^T)$.

For Bayesian filtering, (4.76) is used as the stochastic model to provide a filtered pose $\hat{\boldsymbol{g}} \equiv (\hat{\boldsymbol{p}}, \hat{\boldsymbol{\theta}})$ corresponding to the state $\boldsymbol{g}$.

A full quaternion representation of $\boldsymbol{\theta}$ is not admissible in the Bayesian filtering framework due to the unity constraint and results in covariance degeneracy [LEM82]. As a result, an unconstrained 3-parameter $\boldsymbol{a} \in \mathbb{R}^3$ is used for the quaternion representation such that $\mathbb{E}(\boldsymbol{a}) = 0_{3,1}$. So, simply by replacing $\boldsymbol{\theta}$ with $\boldsymbol{a}$, we obtain a modified state $\boldsymbol{X} = \begin{bmatrix} \boldsymbol{p^T} & \boldsymbol{v^T} & \boldsymbol{a^T} & \boldsymbol{\omega^T} \end{bmatrix}^T$, using which we obtain a state error $\delta\boldsymbol{X} = (\boldsymbol{X} - \hat{\boldsymbol{X}})$, whose state covariance is given by $\boldsymbol{P} = \mathbb{E}(\delta\boldsymbol{X}(\boldsymbol{x})\delta\boldsymbol{X}(\boldsymbol{x})^T)$.

In the classical Bayesian pose estimation problem, a priori knowledge of uncertainties in measurement noise ($\boldsymbol{R}$) and process noise ($\boldsymbol{Q}$) is assumed and if the assumption holds, the automatic controller is fully capable of performing the task by simply using the filtered pose $\hat{\boldsymbol{g}}$. However, in some practical cases, while the physical model uncertainty ($\boldsymbol{Q}$) is well known, the measurement uncertainty ($\boldsymbol{R}$) for a vision-based system, especially in cases of occlusion and high contrast, is time-varying. This means that there is a time-varying uncertainty in the setpoint pose ($\boldsymbol{g}$) about which the ACS regulates. This negatively affects $\hat{\boldsymbol{g}}$ and will cause ACS errors as pointed out in Section 4.2.2.

In the common class of Bayesian filters, for example, in the extended Kalman filter (EKF), the time-evolution of $\boldsymbol{P}$ is independent of real measurements and hence the change in state uncertainty due to such measurement degradation is not reflected. To address this issue, adaptive filtering techniques [Meh70, SH13, SN17] are employed here, which use measurement data ($\tilde{X}_t$) to adapt the measurement noise uncertainty ($\boldsymbol{R}$). Here, the adaptation is performed using a similar method as in [SN17] for the time t as follows:

$$\boldsymbol{R}(t) = \eta\boldsymbol{R}(t - T_s) + (1 - \eta)(\boldsymbol{\epsilon}(t)\boldsymbol{\epsilon}(t)^T + \boldsymbol{H}\boldsymbol{P}^-(t)\boldsymbol{H}(t)^T), \qquad (4.77)$$

where $\eta \in (0,1)$ is a forgetting factor and $\boldsymbol{\epsilon}(t) = \boldsymbol{y} - \boldsymbol{h}(\hat{\boldsymbol{x}})$ is the measurement residual obtained after the measurement update [SN17]. $\boldsymbol{H}(t)$ is the Jacobian matrix of the measurement function at time t. $\boldsymbol{P}^-$ is the covariance matrix just before the measurement update. Note that T_s is the sampling period.

By adapting $\boldsymbol{R}$ online in this way, the state covariance matrix $\boldsymbol{P}$, which depends on $\boldsymbol{R}$, gives a reliable uncertainty metric of the regulation state $\boldsymbol{x}$. Here, without any loss of generality, the *covariance matching* adaptive EKF for state estimation is used for experimental evaluation, although any of the other methods, including a particle filter [Sär13, ch. 7], may be employed as well.

Proposed Arbitration with $P(t)$

The adaptive Bayesian filter is implemented to map its uncertainty measure to the time-varying gain, α_a, to scale down the ACS forces (in the case of measurement degradation) and to transfer authority to the human operator who completes the task. To this end, the authority of the human operator α_t, is derived from the time-varying covariance $\boldsymbol{P}(t)$ of the adaptive Bayesian filter as:

$$\alpha_t(t) = \begin{cases} \frac{\xi(\boldsymbol{P}(t)) - \xi(\boldsymbol{P}_{low})}{\xi(\boldsymbol{P}_{high}) - \xi(\boldsymbol{P}_{low})} & \text{if } \xi(\boldsymbol{P}_{low}) \leq \xi(\boldsymbol{P}(t)) \leq \xi(\boldsymbol{P}_{high}) \\ 0 & \text{if } \xi(\boldsymbol{P}(t)) < \xi(\boldsymbol{P}_{low}) \\ 1 & \text{if } \xi(\boldsymbol{P}(t)) > \xi(\boldsymbol{P}_{high}), \end{cases} \qquad (4.78)$$

where $\xi(\bullet) = \log(\text{trace}(\bullet))$. $\boldsymbol{P}_{low}$ and $\boldsymbol{P}_{high}$ correspond to the state covariance matrices for good and consistently degraded measurements respectively, which are *a priori* identified for the estimation system in hand as follows. Before beginning the task execution, the adaptive Bayesian filter is allowed to converge, which provides a reliable estimate of $\boldsymbol{P}_{low}$,

whereas an upper bound $\boldsymbol{P}_{high}$ is obtained by performing the task using ACS and noting $\boldsymbol{P}(t)$ when it fails due to consistently degraded measurements. With the unity-sum arbitration law from (4.73), the gain for the ACS forces is then modified as $\alpha_a(t) = 1 - \alpha_t(t)$. In summary, when ACS gets degraded measurements, the value of α_t increases and the authority is accordingly shifted to the human operator.

Proposed Shared Control Architecture

For the teleoperation part of the proposed shared control framework, the conventional 4-channel architecture bilateral controller [Law93] is used as shown in Fig. 4.4.
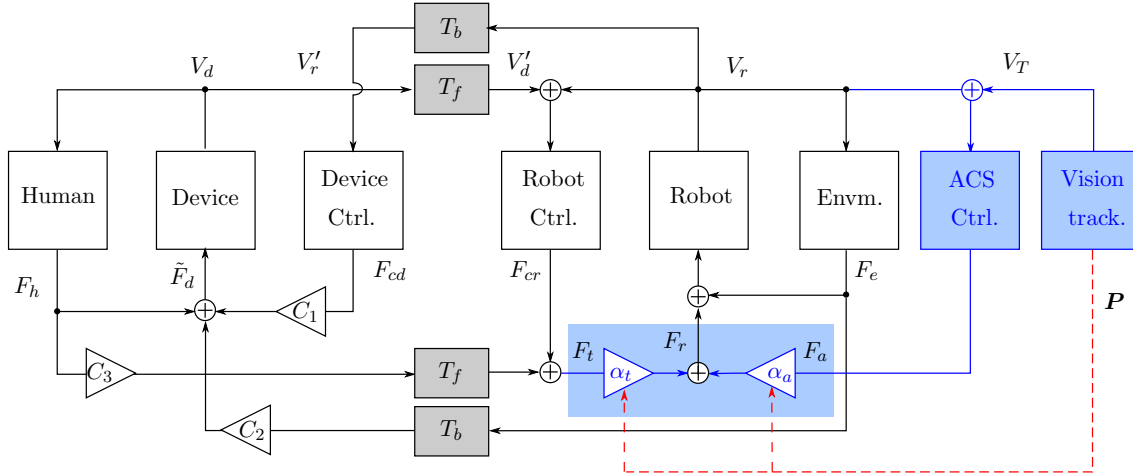

Figure 4.4: Signal-flow diagram of the proposed shared control framework.

The contribution (denoted in Blue and Red in Fig. 4.4)) of the work is the enhancement of the aforementioned teleoperation system by adding the ACS which is based on visual tracking to form the shared control system. V_T is the velocity of the target commanded to ACS (0 in this case since the target is fixed). $\boldsymbol{P}$ refers to the state covariance defined in Section 4.2.2. As can be seen, the commanded force to the robot, F_r, is the weighted sum of teleoperation force F_t and ACS force F_a as per (4.73).

4.2.3 Experiments and Results

A shared control station was set up to validate the feasibility of the proposed method. A KUKA light-weight-robot (LWR) haptic device and an LWR remote robot were employed to complete two tasks. The first task T_1 was to insert the USB male port (fixed on the remote robot end-effector) into a USB female port that was fixed on the work table as shown in Fig. 4.5. Once T_1 was complete (which was signaled by a Green LED bulb on the work-object), the male USB port had to be ejected. The second task T_2 was to move to the other end of the work table and to insert the same USB male port at the remote robot end-effector into the set-up with a larger insertion point (to simulate a tool changer). Both tasks, T_1 and T_2, were executed sequentially with pure teleoperation (TO) and also with the proposed shared control (SC). In both cases, a round-trip delay of $200ms$ was simulated between the haptic device and the remote robot.

The operator station was composed of the haptic device, a monitor with webcam views of the work environment of the remote robot, a graphical user interface (GUI) to visualize the current AA factor α_t. To further assist the operator, a vibro-tactile feedback was
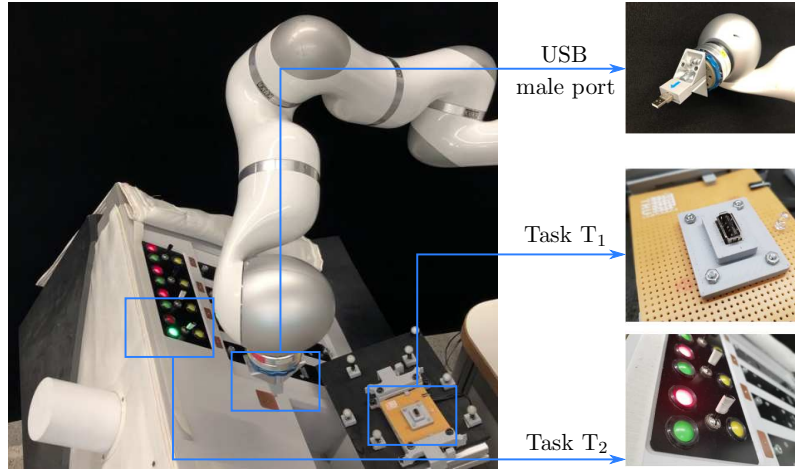
Figure 4.5: Experiment set-up with LWR and task board

provided whenever the authority (α_t) crossed the 0.5 value. In SC, the pose of the USB female port ($\{\boldsymbol{T}\}$) was tracked by a vision-based tracker. The ACS moved the remote robot from its initial position to T_1 target point and the haptic device also followed the remote robot (due to the position coupling of the 4-channel bilateral controller). As the remote robot end-effector approached T_1 target point, the view on the tracked target was occluded by the remote robot itself (see Fig. 4.2). This led to the deterioration of measurements from the tracking system, and resulted in a shift in authority from ACS to the human operator due to the increase in α_t, as explained in Section 4.2.2. The human operator completed the final insertion of the USB male port and then moved towards T_2 target point. As soon as the remote robot moved away and the occlusion was removed, the vision-based tracker started providing good measurements and the covariance of the adaptive EKF reduced and consequently, α_t did so. As a result, the ACS regained control and helped the human operator approach T_2 target point.

In Fig. 4.6, the top plot represents the desired $\boldsymbol{p} = \begin{bmatrix} p_x & p_y & p_z \end{bmatrix}^T$ and actual values $\boldsymbol{p}_r = \begin{bmatrix} p_{rx} & p_{ry} & p_{rz} \end{bmatrix}^T$ of the remote robot tool center point, which shows agreement between the two, and demonstrates convergence of SC. The second plot shows the position of the target measured by the vision-based tracker. For clarity, *only $\tilde{p}_x$ is shown*, which highlights the measurement degradation between $11s - 27s$ The third plot shows the variation in $\xi(\boldsymbol{P}(t))$ with measurement degradation in the same period, which demonstrates the effectiveness of the adaptive EKF. The fourth plot shows the consequent variation of α_t as per (4.78). It can be seen that when the measurements are degraded, α_t increases and when the measurements are nominal after (T_1), α_t decreases. This validates the adaptive SC approach proposed in the section.

User study analysis

To verify the effectiveness of the proposed shared control approach (if it really assists a human operator) in executing tasks that require high precision (USB insertion), a user study was conducted.
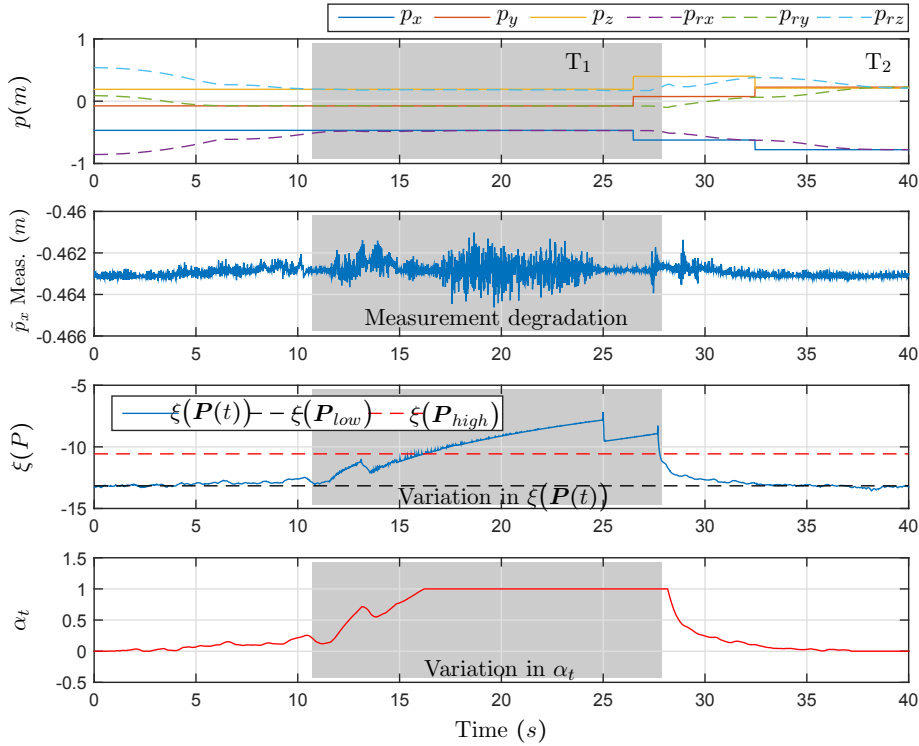
Figure 4.6: Variation in α_t with variation in measurement noise

Method and Experimental Design

Sample N = 14 male employees of DLR with an average age of 27.93 years (SD= 5.6 years, Range: 22-43 years) participated in the present study after having signed an informed consent form. All the participants had to complete T1, and then T2 as mentioned in Section 4.2.3. A within-subject design was applied, namely, each subject completed both TO and SC modes subsequently, with the order of modes counterbalanced across the participants. There were two trials with both modes, resulting in two experimental schemes: 1. TO-SC-TO-SC; 2. SC-TO-SC-TO. After having completed a demographic questionnaire, the subjects were briefly introduced into the concepts of TO and SC. The tasks described in Section 4.2.3 were explained to them and a training with duration of 5 minutes was conducted to complete the tasks both in the TO and SC modes. After the training, the actual experimental trials started. After completing a task, subjects were administered a brief questionnaire with one item measuring the overall workload (*Please rate your overall workload during the last task*, adapted from the OWS scale [VT87], and one item measuring physical demands (*How physically demanding was the last task*, adapted from the NASA-TLX scale [HS88]. Both items were rated on a 20-point bipolar scale ranging from very low to very high. After having finished the entire experiment, a final questionnaire with several items on situation awareness during the SC mode was filled out by participants (in the 8-point Likert-like response format ranging from *does not apply at all* to *completely applies*).

Data Analysis and Results

The repeated measure analysis of variance (rmANOVA) with Conditions (TO vs. SC) and Trial (1 vs. 2) as within factors was conducted on completion time, mean forces, mean

torques, the workload as well as physical demand ratings. Descriptive data (mean M and standard deviation SD) were calculated for the ratings in the final query.

Based on the objective and subjective data analyzed during the study, the following results were obtained:

Completion time: RmANOVA revealed a non-significant trend for Condition ($F(1, 13)$ = 2.9, p = 0.11), namely, completion times tended to be shorter with SC (M = 64.4s) compared with TO (M = 77.3s). Furthermore, Trial reached significance ($F(1, 13)$ = 11.1, $p <$ 0.01), indicating a learning effect from trials 1 to 2.

Mean forces and torques: Regarding mean forces, neither Control ($F(1, 13)$ = 0.03) nor Trial ($F(1, 13)$ = 0.14) reached significance. Yet, a significant Control main effect was found in rmANOVA on mean torques ($F(1, 13)$ = 10.7, $p < .01$), i.e. the average torques were significantly lower with SC (M= 0.059) compared to TO (M = 0.072).

Subjective Ratings: RmANOVA yielded a significant Control ($F(1, 13)$ = 11.6, $p <$ 0.01) and Trial main effect ($F(1, 13)$ = 6.57, $p < 0.05$) on overall workload ratings. Subject ratings were significantly higher during TO (M= 9.43) compared with SC (M = 5.32) and the workload was indicated to be lower in the 2. trial (trial 1: 8.25, trial 2: 6.50). Regarding physical demand, only a Control main effect was evident ($F(1, 13)$ = 12.1, $p <$ 0.01), with significantly lower ratings for SC (M = 4.96; TO: M= 9.04).

Situational awareness: Ratings of the final questionnaire on situation awareness (SA) during SC indicated that subjects mainly felt to be aware of the positions and actions of the robots (M = 6.43; SD =1.16), felt capable of anticipating robot actions (M =6.0; SD =1.75), and were mainly aware of the degree of control they had (M =6.29; SD =1.94). Moreover, they rated the vibro-tactile feedback as being helpful to maintain SA (M =6.36; SD =2.13). Only the ratings whether the GUI was helpful with regard to SA reached rather moderate approval (M =4.64; SD =1.99).

4.2.4 Discussion

The insertion of the USB port using TO with delay is a task that requires high accuracy in both position, orientation and force application. The objective evaluation indicates that the physical effort has been reduced while implementing the task in the SC mode. The improvement has been mainly achieved in terms of the amount of torque input (18% reduction with SC) from the operator since the ACS already places the end-effector USB port in the right orientation before the human operator gets control. He needs to complete only the final insertion, which is not the case in pure teleoperation where he has to execute the task from beginning. The subjective evaluation shows significant reduction in the physical (45.13%) and overall workload (43.58%) of the participants during the task execution. This can be explained by the fact that in SC mode the participant was relieved of most of the work and had to intervene only when the autonomous system could not complete the task. Overall, despite the short training time, the results indicate a reduction in the completion time (16.7%), torque input from the participant and workload, both physical and overall, with the SC approach.

Limitations

Limitation 4.2.1:
Although it was generally reported by the participants and was verified in the subjective and objective analysis that the SC scheme reduced the overall workload of the operators, 3

out of 14 participants mentioned that an option for human intervention was missing when α_t was very low, and they could not override the ACS commanded robot motion. This is a limitation of the proposed system-driven adaptation method with unity-sum condition.

Limitation 4.2.2:
The stability for the shared control framework was not analyzed in this work.

In order to address Limitation 4.2.1 and to allow arbitrary modification of $\alpha_t \in [0, 1]$ and $\alpha_a \in [0, 1]$, without satisfying the condition $\alpha_t + \alpha_a = 1$, the passivity properties of the system will be analyzed in the next section, which also addresses Limitation 4.2.2. If the arbitration process can be implemented without satisfying the unity-sum condition, the AA factor for the human operator α_t can be modified or even given a constant value of 1, so that the operator can make corrective measured as and when required. This also enables *guideline* **G1** from [AMB12] mentioned in Section 1.1.

Objective Achievement

The objective to design a system-driven arbitration algorithm which modifies the AA factors based on real sensor measurement degradation and satisfying unity-sum arbitration, has been achieved. The stability for a mixed-initiative shared control system will be analyzed in the following sections for independent AA factor modification.

4.3 Multi-Agent Adaptive Control: Force Scaling

Section 4.2 presented a novel method to allocate authority between the operator and the ACS in the shared control framework. Still, the stability or passivity properties of the system were not analyzed. Ensuring stability in a system, where forces are scaled without appropriate scaling of velocity, is not trivial. Also, if the unity-sum condition for the AA factors α_t and α_a, that is, $\alpha_t, \alpha_a \in [0, 1]$ and $\alpha_t + \alpha_a = 1$ is not enforced, there will be more freedom for arbitration. This section presents an analytical method for guaranteeing passivity of a mixed-initiative shared control system, which is generalized into a multi-agent robot control framework with adaptive authority allocation without enforcing the unity-sum condition. Later, in Chapter 5, the passive components will be combined to ensure finite-gain stability of the overall system. The work in this section is published by the author in [BMP$^+$21].

4.3.1 Research Gap and Objectives

Related Work

In the robot control community, the idea of multi-agent control is implemented by exploiting the superposition of impedances [Hog85, BS98, PRW11] for a torque-controlled robot. Specifically, the superposition principle guarantees that the combination of different agents with impedance causality can be implemented by summing up the individual control forces. The idea is largely applied to resolve redundancy in Degrees-of-Freedom (DoF) of a robot through a hierarchy of prioritized tasks [DO20, PRW11].
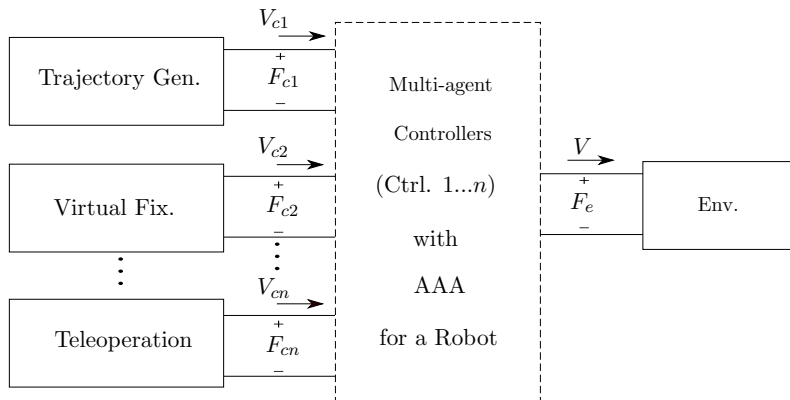

Figure 4.7: A modular framework to interface multi-agent controllers with Adaptive Authority Allocation (AAA) for a robot.

There is also growing interest for multi-agent control topology in the shared control domain [LK07, EK09, BMC$^+$20, LBS$^+$20, WMPH$^+$18] and multi-lateral control [PBA15, LS13, PBA$^+$17]. An example of multi-agent control is shown in Fig. 4.7, where the agents are teleoperator, a trajectory generator and a virtual fixture. This represents an example of mixed-initiative and where each agent provides a desired velocity to its controller and allocation of authority needs to be designed in a stable manner.

A preliminary dynamics-based approach for a mixed-initiative system was proposed in [EK09], wherein the AA factors alternatively modulated the commanded forces. However, the conditions of stability were not analyzed. For time-delayed teleoperation with variable

force and velocity scaling, passivity was ensured in [PB19] using TDPA, however, we considered only a single controller.

Problem Description

Consider a physical system of a 1-DoF robot of mass M (on a surface with damping D) representing a robot, being controlled by two impedance controllers (Ctrl. i, $i = 1, 2$), parameterized as (K_{pi}, K_{di}), which are the spring and damping gains respectively. Note that, the notion of superposition on impedances means that the net force is a sum of both controllers as shown in Fig. 4.8. V_{ci} is the desired velocity commanded to the Ctrl. i which produces forces F_{ci}. The mass moves with a velocity V due to the net forces from these controllers and the force F_e due to its interaction with the environment with impedance Z_e. The same system in its port-network representation [VV65] is shown in Fig. 4.9.
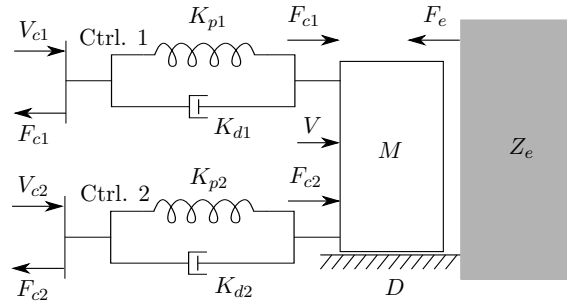

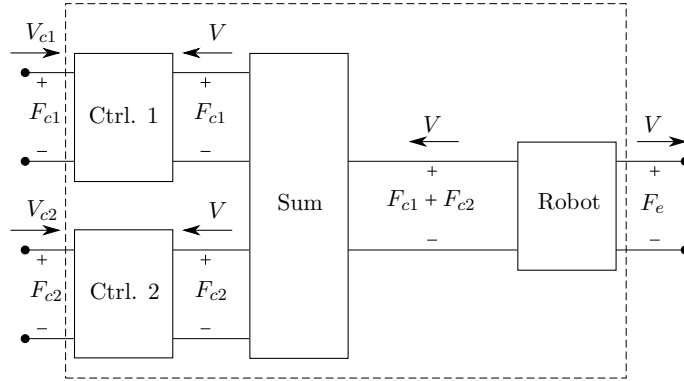Figure 4.8: Physical representation of a 1-DoF robot moved by two controllers.

Figure 4.9: Port-network representation of a 1-DoF robot moved by two controllers.

The equations of motion of the robot and the controller forces are:

$$
\begin{aligned}
M\dot{V} &= F_{c1} + F_{c2} - F_e - DV, \\
F_{c1} &= K_{p1}(X_{c1} - X) + K_{d1}(V_{c1} - V), \\
F_{c2} &= K_{p2}(X_{c2} - X) + K_{d2}(V_{c2} - V),
\end{aligned}
\tag{4.79}
$$

where X is the position of the robot and X_{ci} are the positions commanded to the two controllers. To analyze the passivity of this system, consider the storage function,

$$
S_s = \frac{1}{2}MV^2 + \frac{1}{2}K_{p1}(X_{c1} - X)^2 + \frac{1}{2}K_{p2}(X_{c2} - X)^2,
$$

which is its total physical energy. Taking the time derivative of the storage function S_s, and using (4.79) we get,

$$
\begin{aligned}
\dot{S}_s &= VM\dot{V} + K_{p1}(X_{c1} - X)(V_{c1} - V) + K_{p2}(X_{c2} - X)(V_{c2} - V) \\
&= V_{c1}F_{c1} + V_{c2}F_{c2} - VF_e - DV^2 \\
&\quad - K_{d1}(V_{c1} - V)^2 - K_{d2}(V_{c2} - V)^2,
\end{aligned}
\tag{4.80}
$$

which is passive for the input $u = (V_{c1}, V_{c2}, -F_e)$ and output $y = (F_{c1}, F_{c2}, V)$ with storage function S_s (2.5).
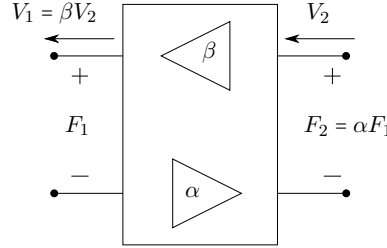

Figure 4.10: Power scaling represented as a 2-port network

Now, consider a scaling 2-port as shown in Fig. 4.10, where the force at the left port F_1 is scaled by a variable gain $\alpha(t)$ and is the output at the right port, i.e. $F_2 = \alpha F_1$. Similarly, the velocity V_2 at the right port is scaled by a variable gain $\beta(t)$ and is output at the left port[1], i.e. $V_1 = \beta V_2$. This scaling 2-port is added in the system in Fig. 4.9 for each controller to enable a mixed-initiative control structure as shown in Fig. 4.11. The final force F_m commanded to the robot is the weighted sum of the two controller forces, i.e. $F_m = \alpha_1 F_{c1} + \alpha_2 F_{c2}$. At the same time, the velocities are scaled with the variable gains β_1 and β_2 as shown in Fig. 4.11.
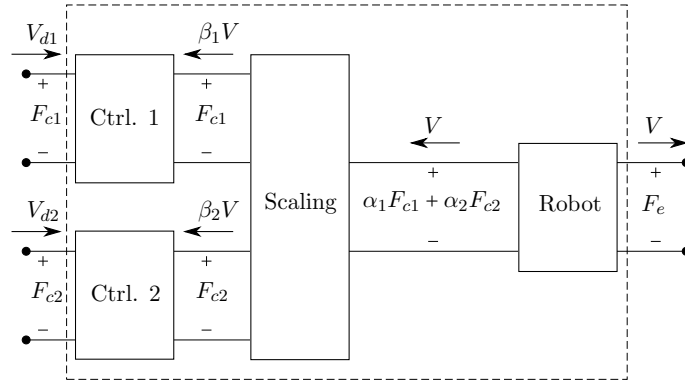

Figure 4.11: Port-network representation of a 1-DoF robot moved by two controllers with scaling.

The same approach as above is followed to analyze passivity of the system with scaling. The modified equations of robot motion and the controller forces are now:

$$
\begin{aligned}
M\dot{V} &= \alpha_1 F_{c1} + \alpha_2 F_{c2} - F_e - DV, \\
F_{c1} &= K_{p1}(X_{c1} - \beta_1 X) + K_{d1}(V_{c1} - \beta_1 V), \\
F_{c2} &= K_{p2}(X_{c2} - \beta_2 X) + K_{d2}(V_{c2} - \beta_2 V).
\end{aligned}
\tag{4.81}
$$

---

[1]For ease of reading, time dependency of the gains will be not written explicitly from now on.

Consider the new storage function S_{SC} (total physical energy), where

$$S_{sc} = \frac{1}{2}MV^2 + \frac{1}{2}K_{p1}(X_{c1} - \beta_1 X)^2 + \frac{1}{2}K_{p2}(X_{c2} - \beta_2 X)^2.$$

Taking the time derivative of the storage function S_{sc}, and using (4.81) we get,

$$\begin{aligned}
\dot{S}_{sc} = &\ V_{c1}F_{c1} + V_{c2}F_{c2} - VF_e - DV^2 \\
&- K_{d1}(V_{c1} - \beta_1 V)^2 - K_{d2}(V_{c2} - \beta_2 V)^2 \\
&+ (\alpha_1 - \beta_1)F_{c1}V - \dot{\beta}_1 X K_{p1}(X_{c1} - \beta_1 X) \\
&+ (\alpha_2 - \beta_2)F_{c2}V - \dot{\beta}_2 X K_{p2}(X_{c2} - \beta_2 X),
\end{aligned} \tag{4.82}$$

which is not passive due to the additional sign-indefinite terms appearing due to the scaling terms (see (2.5)). Note that for constant gains with $\alpha_i = \beta_i$, the scaling is equivalent to an ideal electrical transformer or a mechanical gear/lever arm, both of them being passive as shown in (4.80). This passive behavior is violated with the addition of scaling. A two-agent controlled robot is simulated with and without scaling and the results are shown in Fig. 4.12. The forces and velocities are not scaled in Fig. 4.12a. X_{c1} and X_{c2} are the commanded positions from the two agents and X is the resulting position of the robot, which makes contacts with a wall at X_w. The second plot shows the unity gains for the forces and velocities, while the last plot shows the passive behavior with $P_s \leq 0$, where $P_s = \dot{S}_s - u^T y$ from (4.80). With the addition of force scaling, the passivity of the system is disrupted, which is shown by the positive values of $P_{sc} = \dot{S}_{sc} - u^T y$ in Fig. 4.12b highlighted in the Red dashed box.

To summarize: Without scaling (in Fig. 4.9), the multi-agent controller robot is passive. But when scaling is added in the system (constant or varying) as in Fig. 4.11, the passivity condition is violated.

Objective

The objective of this section is to design a model-independent passive architecture for multi-agent robot control with mixed-initiative approach. The AA factors should be independently adaptable (without enforcing the unity-sum arbitration condition). The approach has to be modular so that it can be applied to a variety of scenarios.

4.3.2 Proposed Method

An analytical method to inject damping to passivate the system is presented here. In (4.82), the sign-indefinite terms $(\alpha_i - \beta_i)F_{ci}V - \dot{\beta}_i X K_{pi}(X_{di} - \beta_i X)$ are independent of the time derivative of the force scaling factors ($\dot{\alpha}_i$) (for $i = 1, 2$). In mixed-initiative shared control, the robot is finally controlled by the weighted sum of the forces produced by the different controllers based on the authorities allocated to them. So, only the variation of the force gains α_i are considered and the velocity scaling factors are given values $\beta_i = 1$.
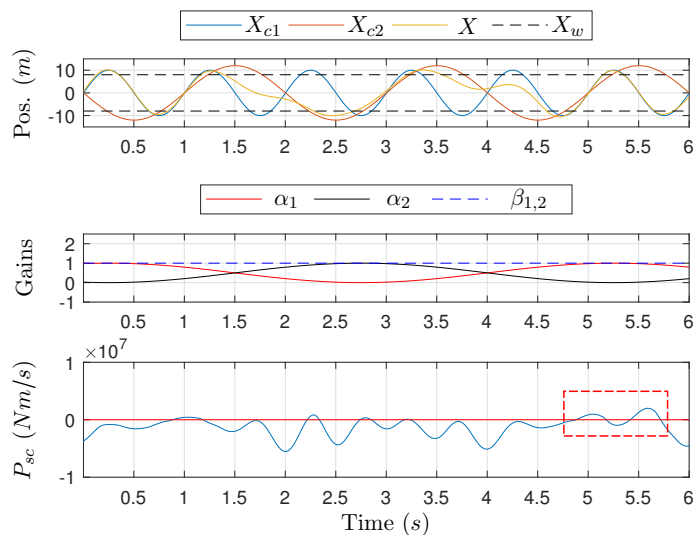
Passivity of a single controller with scaling

First, the scaling 2-port shown in Fig. 4.10 is added to a single-agent robot control as shown in Fig. 4.13. with the scaling port and unity velocity scaling ($\beta = 1$), the equations for the robot motion and the controller are:

$$\begin{aligned}
M\dot{V} &= \alpha F_c - F_e - DV, \\
F_c &= K_p(X_c - X) + K_d(V_c - V).
\end{aligned} \tag{4.83}$$
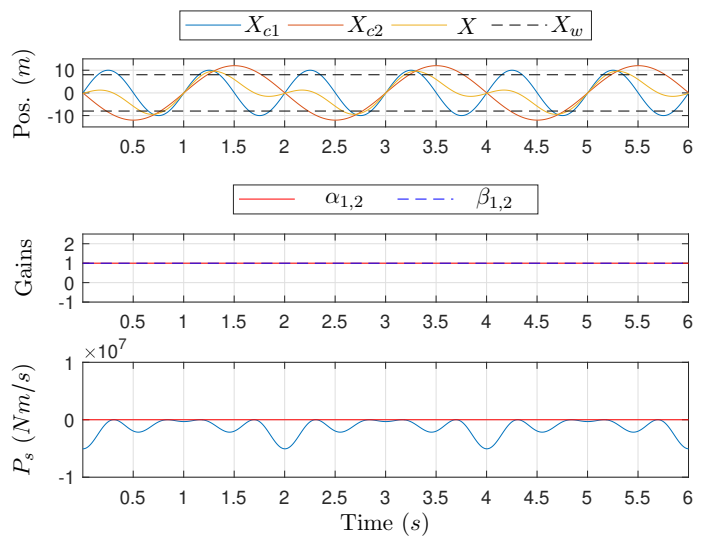
(a) $\alpha_1 = \alpha_2 = \beta_1 = \beta_2 = 1$. Passivity shown by $P_s = \dot{S}_s - u^T y \leq 0$

(b) $\alpha_1 = \text{varying}, \alpha_2 = 1 - \alpha_1$, $\beta_{1,2} = 1$. Not passive as $P_{sc} = \dot{S}_s - u^T y \nleq 0$

Figure 4.12: Passivity and activity for different scaling. X_w is the position of the environment.

To evaluate passivity of this single-agent controlled robot, the total energy is taken as the storage function S_{os} similar to (4.82) and the time derivative of the storage function is calculated:

$$
\begin{aligned}
S_{os} &= \frac{1}{2}MV^2 + \frac{1}{2}K_p(X_c - X)^2, \\
\dot{S}_{os} &= V_d F_c - V F_e - DV^2 - K_d(V_c - V)^2 + (\alpha - 1)F_c V.
\end{aligned}
$$

This system is passive for the inputs $(V_c, -F_e)$ and outputs (F_c, V) if $P_s = (\alpha - 1)F_c V \leq 0$. A new damping element D_s is added such that the additional power flowing from the robot
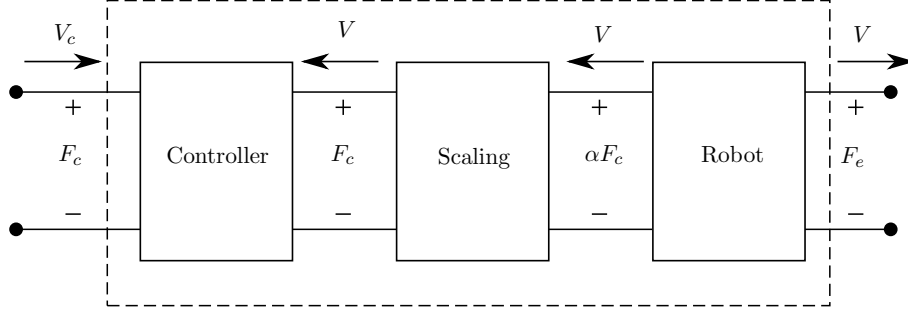
Figure 4.13: Single-agent controlled robot with force scaling

to the controller is dissipated. The value of D_s is computed by:

$$\frac{1}{D_s} = \begin{cases} \frac{P_s}{F_c^2} & \text{if } P_s > 0, \\ 0 & \text{else,} \end{cases} \tag{4.84}$$

The value of $\frac{1}{D_s} = 0$ in electrical representation means an open circuit and in mechanical systems means a pure loss-less connection. This damping element is added to the system and is presented in Fig. 4.14. Note that the velocity entering the controller, denoted as V_n, has to be modified accordingly, and is given by,

$$V_n = V - \frac{F_c}{D_s}. \tag{4.85}$$

Therefore, with this additional damping, the controller does not *see* the real velocity of the robot V. It sees only the modified velocity V_n as per (4.85). This will lead to position drift and is a limitation of this method although the approach ensures system passivity. A solution to reduce the effects of this limitation will be presented in the next section.
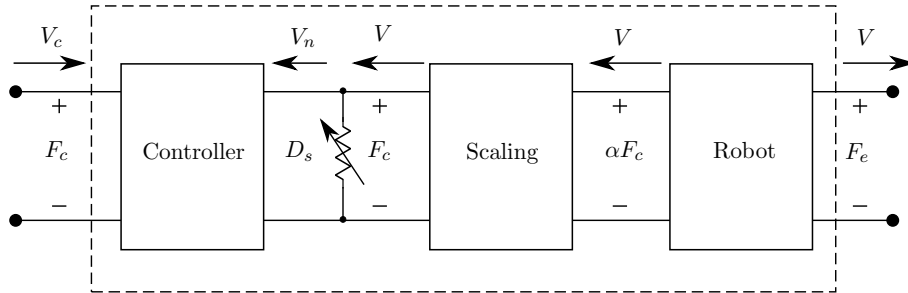

Figure 4.14: Controlled robot with scaling and damping for passivity

Passivity of a multi-agent control with AAA

A multi-agent robot control architecture is now designed by combining n single-agent systems (which are individually passive) from Fig. 4.14 and the weighted sum of the forces from all the individual controllers, $F_{aa} = \alpha_1 F_{c1} + .. + \alpha_n F_{cn}$ is commanded to the robot by the adaptive authority allocation port (AAA) as shown in Fig. 4.15. The equation of motion of the robot, as a result is:

$$M\dot{V} = F_{aa} - F_e - DV. \tag{4.86}$$

Considering the velocity V_{ni} for the controllers due to the additional damping D_{si}, and taking the total energy of this system S_{aa} which is given by:

$$S_{aa} = \frac{MV^2}{2} + \sum_{i=1}^{n} \frac{K_{pi}(X_{ci} - X_{ni})^2}{2}, \tag{4.87}$$

the time derivative of S_{aa} can be finally derived to be:

$$\dot{S}_{aa} = \sum_{i=1}^{n} V_{ci}F_{ci} - VF_e - DV^2, \tag{4.88}$$

which is passive with inputs $(V_{c1..n}, -F_e)$ and outputs $(F_{c1..n}, V)$. This can be seen in the simulation result shown in Fig. 4.16, for similar conditions presented in Fig. 4.12 in Section 4.3.1. As it can be seen in the bottom plot, the proposed method makes the two-agent robot control with varying AA factors passive with $P_{aa} = \dot{S}_{aa} - \sum_{1}^{n} V_{ci}F_{ci} - VF_e \le 0$.
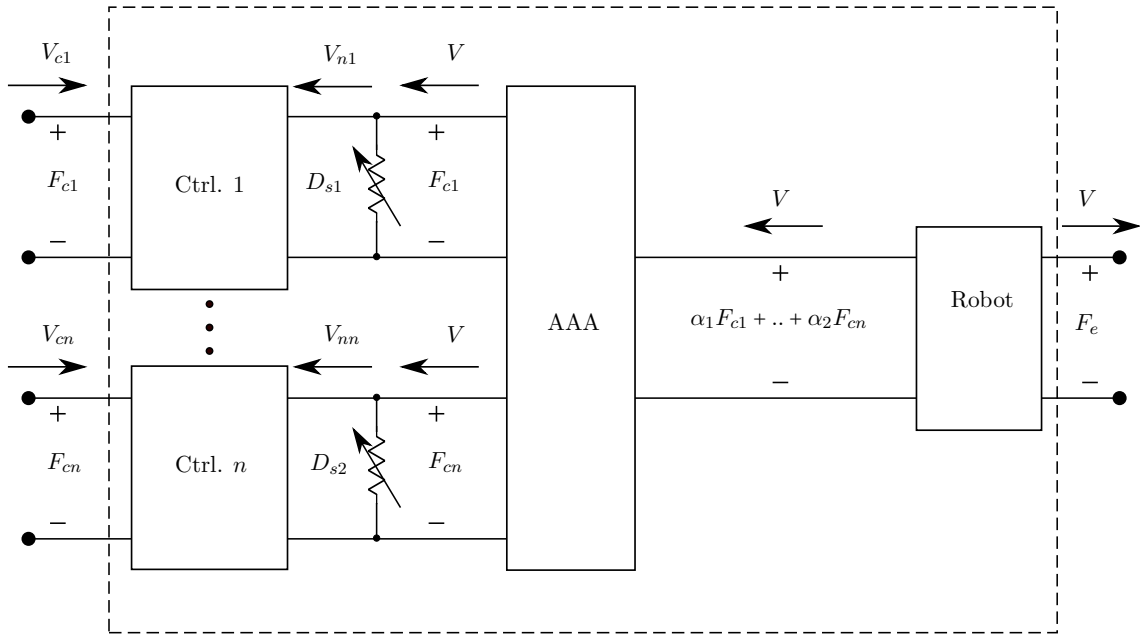

Figure 4.15: Multi-agent robot control with varying AA factors ensured passive.

Extension to multiple-DoF manipulators

As described in (2.22), for a m-joint manipulator, the gravity-compensated Cartesian dynamics is:

$$\boldsymbol{\Lambda}(\boldsymbol{q})\dot{\boldsymbol{V}} + \boldsymbol{\mu}(\boldsymbol{q}, \dot{\boldsymbol{q}})\boldsymbol{V} + \boldsymbol{\Gamma}\boldsymbol{V} = \boldsymbol{F}_{aa} - \boldsymbol{F}_e,$$

where $\boldsymbol{\Lambda}, \boldsymbol{\mu}, \boldsymbol{\Gamma} \in \mathbb{R}^{c \times c}$, are the matrices of inertia, Coriolis/centrifugal terms and viscous damping, respectively with $\boldsymbol{q} \in \mathbb{R}^m$ and $\boldsymbol{V} \in \mathbb{R}^c$ being the joint-space configuration and the end-effector velocity, respectively. The external wrench (measured) at the manipulator's end-effector is $\boldsymbol{F}_e \in \mathbb{R}^c$, and $\boldsymbol{F}_{aa} \in \mathbb{R}^c$ is the coupling wrench, which is the weighted sum of the wrenches from different controllers. Note that the AA factors α can be scalar values,
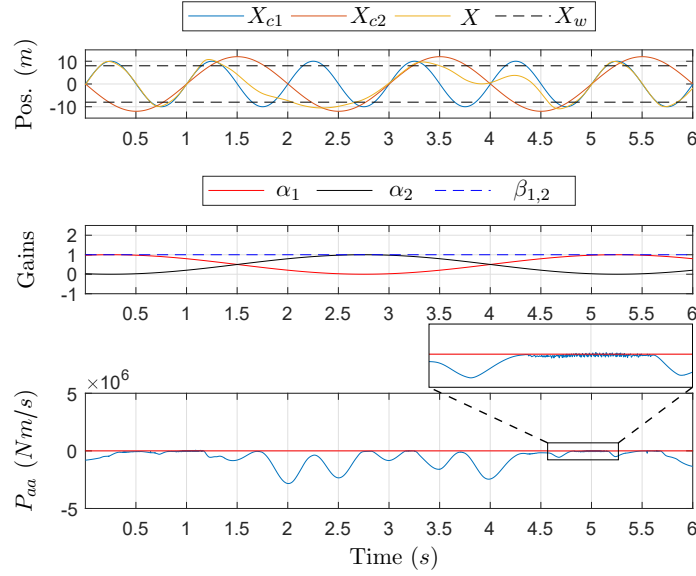
Figure 4.16: Simulation: Positions and power for the system in Fig. 4.15. $\alpha_1 =$ varying, $\alpha_2 = 1 - \alpha_1$, $\beta_{1,2} = 1$

which scale the magnitudes of the wrenches, respectively, or might be generalized as $c \times c$ matrices for finer AA in each DoF. Choosing the storage function as the total energy as in (4.87) for the robot and the n controllers,

$$S_R \;=\; \frac{1}{2}\boldsymbol{V}^T\boldsymbol{\Lambda}\boldsymbol{V} + \sum_{i=1}^{n}\frac{1}{2}\Delta\boldsymbol{X}_i^T\boldsymbol{K}_{pi}\Delta\boldsymbol{X}_i,$$

where $\boldsymbol{K}_{pi}, \in \mathbb{R}^{c\times c}$ is the constant positive-definite matrix of the Cartesian stiffness and $\Delta\boldsymbol{X}_i$ are the pose errors for the end-effector. Taking the time-derivative of S_R, and exploiting the passivity property of Euler-Lagrange systems, i.e, $\boldsymbol{V}^T(\dot{\boldsymbol{\Lambda}} - 2\boldsymbol{\mu})\boldsymbol{V} = 0$, we obtain the passivity conditions, which are the same as in (4.88) for the 1-DoF case as explained in Section 2.1.4. Therefore, by ensuring passivity of the c Cartesian DoFs separately, the passivity of the manipulator controlled by multiple agents can be ensured.

4.3.3 Experiments and Results

The multi-agent control framework was validated on an LWR and the results are presented in Fig. 4.17. Two end-effector controllers were used to command the LWR to move on circular trajectories in the Cartesian YZ plane. The first controller had a desired circular trajectory with 20 cm diameter and frequency 1 rad/s. The second controller had the same diameter for the circle, but with a frequency of 2.7 rad/s. For the controllers, proportional gains of $\boldsymbol{K}_{pt} = diag[1500, 1500, 1500]$ N/m and $\boldsymbol{K}_{pr} = diag[20, 20, 20]$ Nm/rad were chosen for translations and rotations, respectively. The damping gains were $\boldsymbol{K}_{dt} = diag[10, 10, 10]$ Ns/m and $\boldsymbol{K}_{dr} = diag[1, 1, 1]$ Nms/rad for translations and rotations, respectively. The robot made contacts with a compliant physical wall placed at 10 cm. The desired trajectories and the robot position are shown in the top row of Fig. 4.17. The wrenches produced by the two controllers were summed up with varying gains α_1 and α_2 (middle row). The experimental validation of passivity is shown in the last row where it can be seen that passivity is violated without the proposed method, that is, $P_{aa} \nleq 0$. On
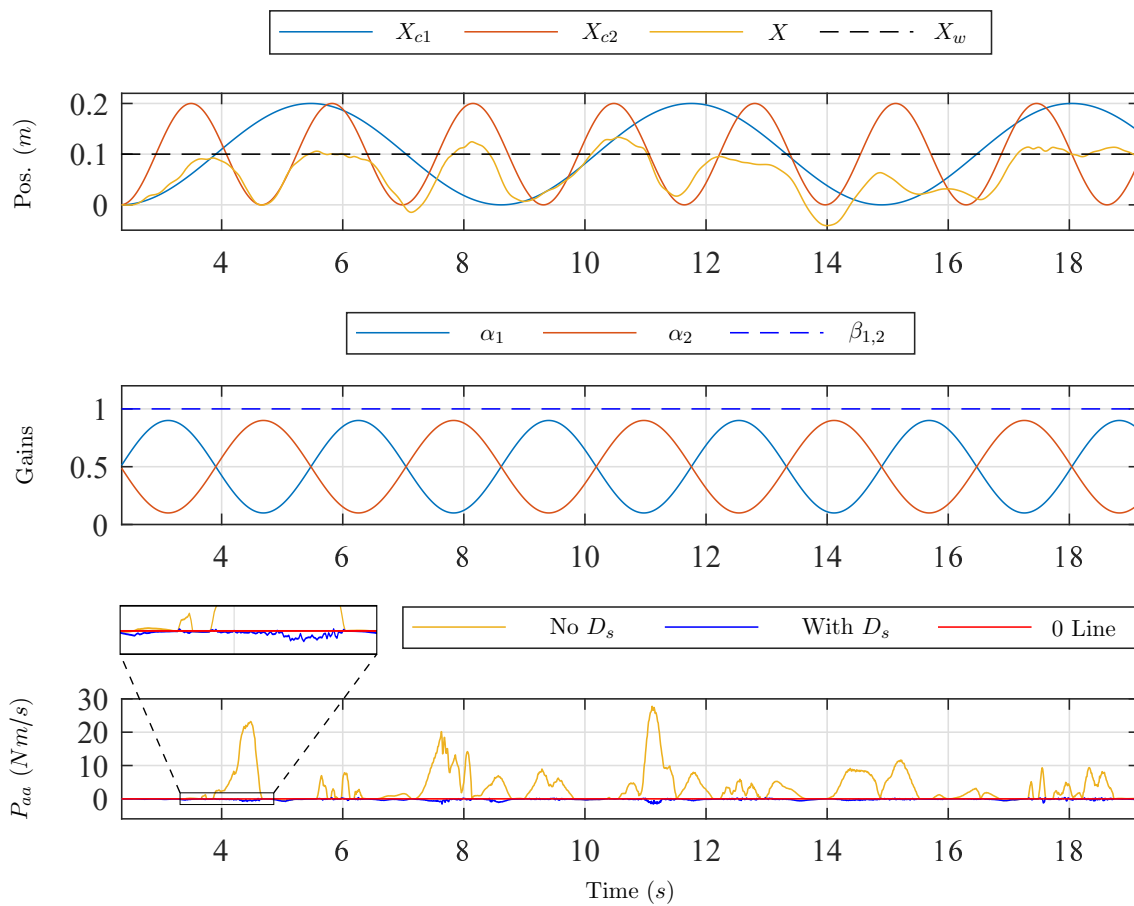
Figure 4.17: Hardware experiments: Positions and power, α_1 = varying, $\alpha_2 = 1 - \alpha_1$, $\beta_{1,2} = 1$

the other hand, with the proposed method, passivity is ensured, as was also shown for simulations in Fig. 4.16.

4.3.4 Discussion

The multi-agent controller with adaptive authority allocation was ensured to be passive as shown by the simulation and hardware experiments. The multi-agent controlled robot is represented as an n-port, which makes the system highly modular and more agents can be added by adding new ports. This modularity of the multi-agent robot control system enables it application in different robot control domains. This is very useful for this thesis and this modularity will be used in the adaptive shared control framework in Chapter 5. Another benefit derived from this section is that the generally used unity-sum condition for the AA factors need not be enforced for a shared controlled system to be passive as it was generalized in this section. This gives more freedom for arbitration, which allows different research groups to apply their allocation algorithms within this framework. As mentioned after (4.85), the additional damping required to ensure passivity of the scaling port introduces position drifts in the system, which will affect the system behavior. There exist methods to remove position drifts that arise due to additional damping developed for admittance type POPC architectures [CSM+18]. Although these methods can be used to reduce the effects the position drifts, this work mainly focuses on analyzing the pure system behavior with force scaling (compared to stiffness scaling in the next chapter).

Reducing position drifts due to scaling of forces will be considered in future work.

Limitations

Limitation 4.3.1:
The proposed method that uses a scaling port and additional damping to ensure its passivity introduces position drifts in the system.

Objective Achievement

The objective of ensuring passivity for a general multi-agent robot control system has been achieved. The passivity conditions are valid for independent adaptation of AA factors, which obviates the need for the unity-sum arbitration condition. The representation of the multi-agent control system as an n-port network provides a modular nature that allows different agents to be connected to the framework.

4.4 Multi-Agent Adaptive Control: Stiffness Scaling

Although the analytical damping injection proposed in Section 4.3 for adaptive scaling of forces of multiple controllers ensures passivity of the system, it leads to position drifts. In this section a different view is taken on the same multi-agent control problem, whereby the controller stiffness is modified, rather than using force scaling. The passivity properties of such a system is analyzed and a gain-gradient limitation method is proposed to ensure passivity. A comparison on the performance of both force scaling and stiffness scaling approaches is performed using hardware experiments. Discussions present the benefits and limitations of this method. Based on these passivity properties, Chapter 5 avails these methods to form the adaptive shared control framework.

4.4.1 Research Gap and Objectives

Related Work

Adaptive controllers have been used since long to vary impedance and admittance of robotic manipulators. The stability and passivity properties for human-robot interaction with variable admittance was published in [FTLS$^+$19]. In [CSG93], a Cartesian variable impedance control was proposed and [FSF13] proposed a variable stiffness controller whose passivity was ensured using energy tanks. Non-linear adaptive controllers for rehabilitation tasks was proposed in [OP14]. This concept was extended to teleoperation systems, where the stiffness of the controller was adapted online and proposed the concept of tele-impedance [ATB12]. The gains of multiple tasks was varied in [MRP$^+$21] and the stability was ensured using energy tanks. Although the concept of varying stiffness has been applied in many robotics domains, to the best of the author's knowledge, it has not been applied in mixed-initiative shared control for adaptive authority allocation.

Problem Description

In Section 4.3, the adaptive multi-agent system was formulated using multiple controllers, whose forces were scaled and added before commanding to the robot. The passivity disruption caused due to force scaling without appropriate velocity scaling was solved by introducing additional damping into the system, as summarized in Fig. 4.15. It is evident that the controllers do not receive the real velocity of the robot V. Due to the additional damping D_{sn}, there is a *leakage of velocity* and the controllers receive velocities V_{nn}. This means that the controller integrates the velocity V_{nn} and produces forces F_{cn} to track V_{nn} to the desired velocity V_{cn}. This will lead to a position drift and affect the system performance if the force scaling of a controller is reduced to a very low value and then increased to a higher value to give higher control authority to the controller.

The mechanical equivalent of the damping D_{sn} from Fig. 4.14 added in parallel to the controller is shown in Fig. 4.18. As explained, the spring-damper coupling does not perceive the real velocity V (and the position X) of the robot M, but the modified velocity V_{nn}. This mechanical analogy will support the reader's understanding of the proposed solution.

The position drift caused due to the scaling of forces and the required damping injection for a simulated single controller and robot is shown in Fig. 4.19. The desired position of the controller is X_d and the robot position is X. The robot interacts with a wall at X_w. The controller stiffness is 500 N/m and has a damping of 10 Ns/m. The forces from the controller has been scaled by a fixed value $\alpha = 0.5$.
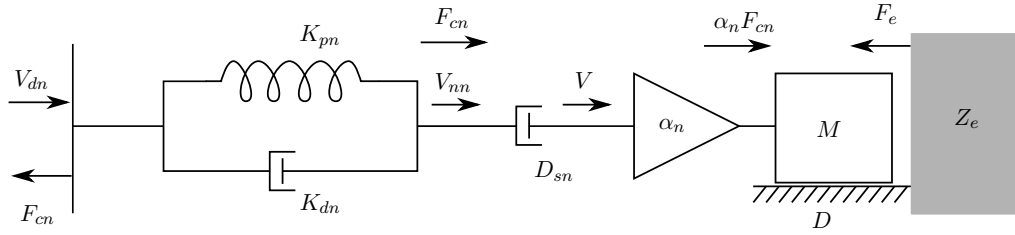
Figure 4.18: Mechanical equivalent of adding D_{sn} in parallel to the controller
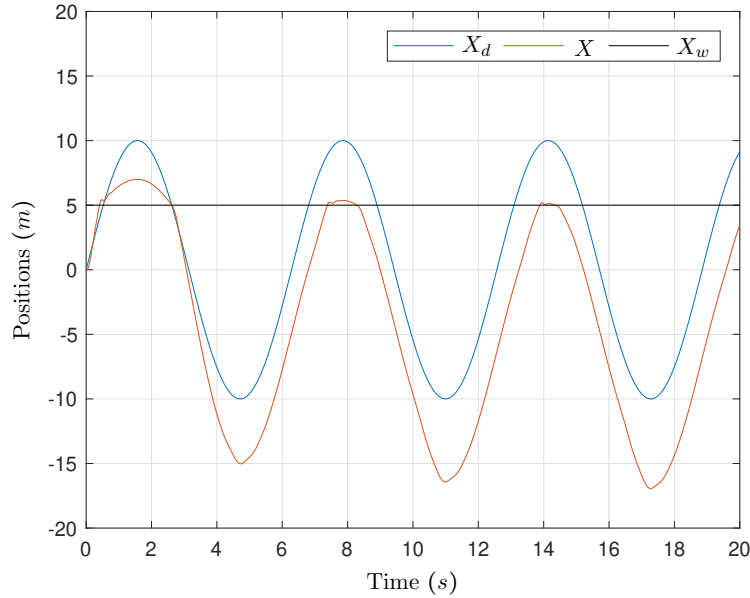

Figure 4.19: Single agent simulation of force scaling showing position drift

To summarize: Using additional damping in the system parallel to the controller and force scaling for adaptive authority allocation leads to position drifts, which affects system performance negatively.

Objectives

The aim of this section is to propose a general multi-agent robot control with adaptive authority allocation without the use of force scaling. This is to reduce the position drifts and at the same time, ensure passivity of the system.

4.4.2 Proposed Method

In this section, the adaptive authority allocation for multi-agent control is framed as multiple adaptive-stiffness controller problem, which does not produce the aforementioned position drifts. The passivity disruption factors, which arise as a result, are removed by limiting the rate at which the AA factors change.

Adaptive Authority Allocation with Adaptive Controllers

When the authority for an agent on the robot has to be reduced, the forces produced by the controller can be scaled down, as was shown in Section 4.3. Also, to increase the

authority, the force scaling can be increased. Instead of scaling the forces, the same effect can be produced by varying the stiffness and damping terms of the controllers accordingly. Consider the robot controlled by two agents in Fig. 4.15. Instead of using the scaling 3-port, the gains of the controller can be modified and the forces can be directly added and commanded to the robot. Let the forces produced by the controllers with unity AA factors be F'_{c1} and F'_{c2}. With the AA factors α_1 and α_2 for each of the controllers, let the output forces from the controllers be F_{c1} and F_{c2}. That is:

$$
\begin{aligned}
F'_{c1} &= K_{p1}(X_{d1} - X) + K_{d1}(V_{d1} - V) \\
F'_{c2} &= K_{p2}(X_{d2} - X) + K_{d2}(V_{d2} - V) \\
F_{c1} + F_{c2} &= \alpha_1 K_{p1}(X_{d1} - X) + \alpha_1 K_{d1}(V_{d1} - V) \\
&+ \alpha_2 K_{p2}(X_{d2} - X) + \alpha_2 K_{d2}(V_{d2} - V) \\
&= \alpha_1 F'_{c1} + \alpha_2 F'_{c2}
\end{aligned}
\tag{4.89}
$$

This idea for multi-agent controller is presented in Fig. 4.20. Note that the final force commanded to the robot is $F_{c1} + F_{c2}$, which already incorporated the gain adaptation.
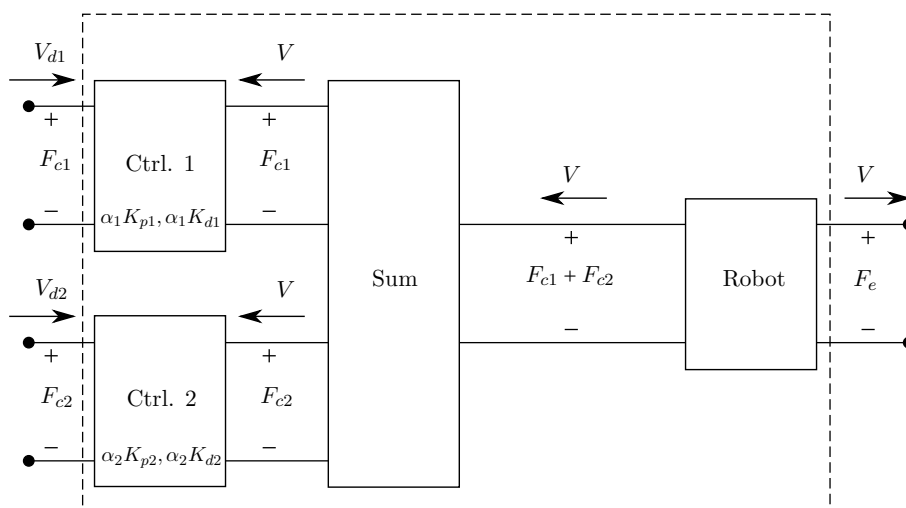

Figure 4.20: Adaptation of controller gains as in (4.89).

The mechanical equivalent of the adaptive gain controllers for a single-DoF system corresponding to the scaling solution from Fig. 4.18 is shown in Fig. 4.21. Note that in this case, the robot is connected directly to the adaptive spring-damper coupling which does not lead to a velocity *leak* and corresponding position drift.
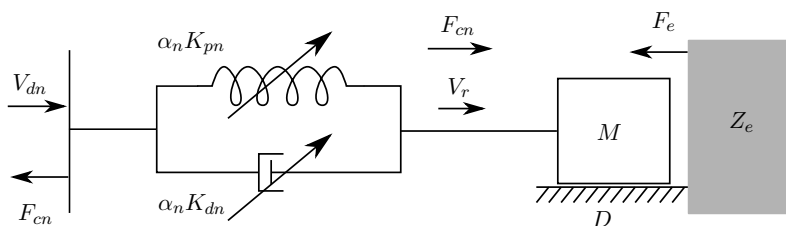

Figure 4.21: Mechanical equivalent of adaptive gain coupling controller

The same system as in Fig. 4.19 is now simulated with a stiffness of 250 N/m and a damping of 5 Ns/m. The effect of $\alpha = 0.5$ is reproduced by reducing the gains to half. The results of the simulation are shown in Fig. 4.22. Note that the position drift has been removed completely.
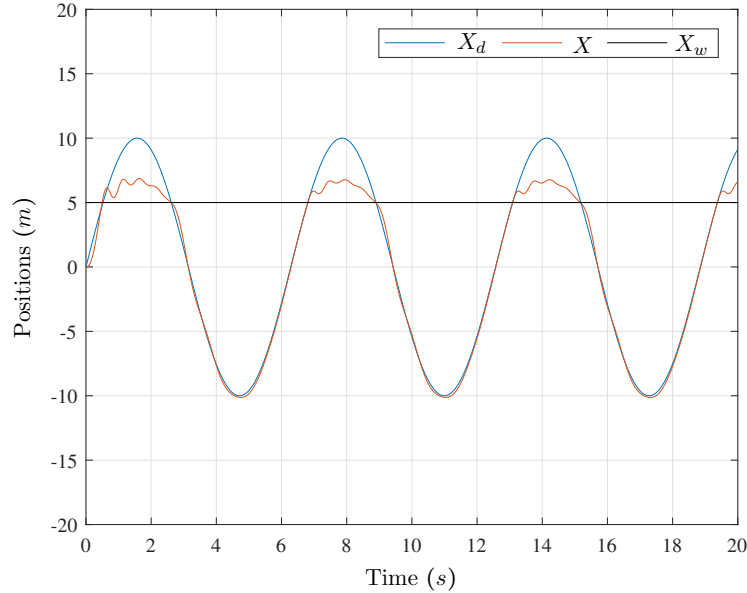

Figure 4.22: Single agent simulation with adaptive gains produces no position drift

The simulations in Fig. 4.19 and Fig. 4.22 had fixed gain reduction. The desired shared control system should enable varying authority allocation as shown in the multi-agent control system proposed in Section 4.3. Now the passivity properties of the multi-agent robot control with adaptive gains will be analyzed.

Passivity of multi-agent control with adaptive stiffness

Let the robot with mass M on a surface with damping D be controlled by n agents, who provide the desired velocity V_{ci} to the respective controller Ctrl. i and $(i = 1, 2, .., n)$. As a result, the robot moves with a velocity V and interacts with the environment, to produce a force F_e. To adapt the authority of each controller, the gains of the controllers are modified with values $\alpha_i(t)$, with $\{\alpha_i(t) \in \mathbb{R} : 0 \leq \alpha_i(t) \leq 1\}$. For brevity, the time dependency of the gains α_i will not be mentioned in the analysis. Note that for this analysis and the following proposed method, only the stiffness is varied by the gain α_i and the damping coefficients are left unchanged. The reason for this will be explained later. The equations of motion of the robot and the controller forces are:

$$
\begin{aligned}
M\dot{V} &= \sum_{i=1}^{n} F_{ci} - F_e - DV, \\
F_{ci} &= \alpha_i K_{pi}(X_{ci} - X) + K_{di}(V_{ci} - V).
\end{aligned}
\tag{4.90}
$$

To analyze the passivity of this system, consider the total energy of the system S_{ag}:

$$
S_{ag} = \frac{1}{2}MV^2 + \sum_{i=1}^{n} \frac{1}{2}\alpha_i K_{pi}(X_{ci} - X)^2,
\tag{4.91}
$$

which is the sum of the kinetic energy of the robot and the potential energies stored in the controllers. From (4.90) and (4.91), the time derivative of S_{ag} can be derived as:

$$
\begin{aligned}
\dot{S}_{ag} &= VM\dot{V} + \sum_{i=1}^{n} \alpha_i K_{pi}(X_{ci} - X)(V_{ci} - V) + \sum_{i=1}^{n} \frac{1}{2}\dot{\alpha}_i K_{pi}(X_{ci} - X)^2, \\
&= \underbrace{\sum_{i=1}^{n} F_{ci}V_{ci} - F_eV - \sum_{i=1}^{n} K_{di}(V_{ci} - V)^2 - DV^2}_{\text{Passive}} + \underbrace{\sum_{i=1}^{n} \frac{1}{2}\dot{\alpha}_i K_{pi}(X_{ci} - X)^2}_{\text{Sign-indefinite}}, \quad (4.92)
\end{aligned}
$$

which makes the system non-passive according to Def. 2.2 due to the sign-indefinite terms appearing from the change in α_i. Note that with K_{pi} and $(X_{ci} - X)^2$ being positive, the system violates the passivity property only when $\dot{\alpha}_i > 0$. This means, only when the control authority of an agent is increasing, the system becomes non-passive.

The violation of passivity for a single-agent controller with time-varying gains has been shown in the following simulations. In Fig. 4.23, the stiffness gain is fixed at $\alpha_1 = 0.5$ as in Fig. 4.22 and as a result, the system is still passive as seen with the negative value of $P_s = \dot{S}_{ag} - F_cV_c - F_eV$ in the bottom plot.

The disruption of passivity for time-varying α_1 gain is shown in Fig. 4.24. The gain for the stiffness is varied in a linear manner going from 1 to 0 with a slope $\dot{\alpha}_1 = -1$ and then rising from 0 to 1 with a slope $\dot{\alpha}_1 = 1$. In both cases, although there is no position drift, the disruption of passivity is seen on the bottom plot with $P_s = \dot{S}_{ag} - F_cV_c - F_eV > 0$ when $\dot{\alpha}_1 > 0$, as per (4.92).

To still ensure passivity of the system with varying controller gains, a novel method is proposed here which limits the gradient of the gain based on the available damping in the system.
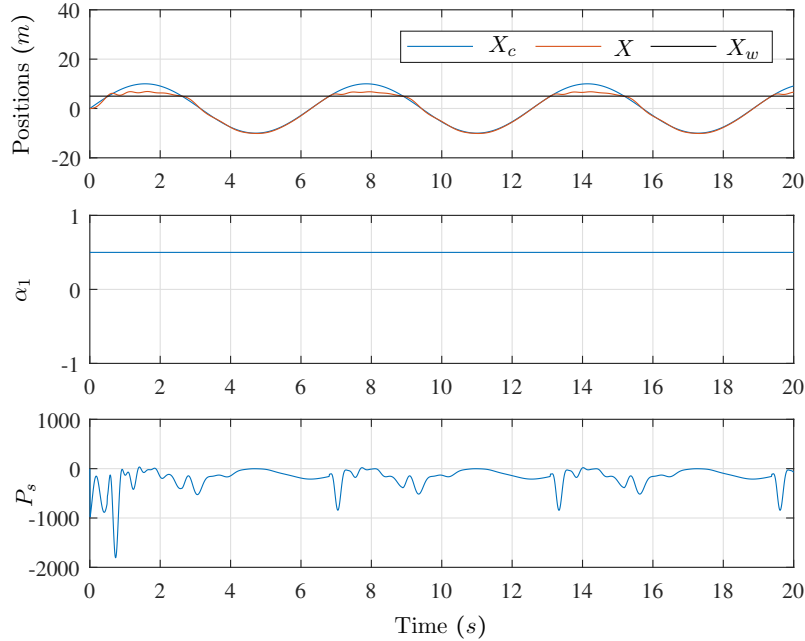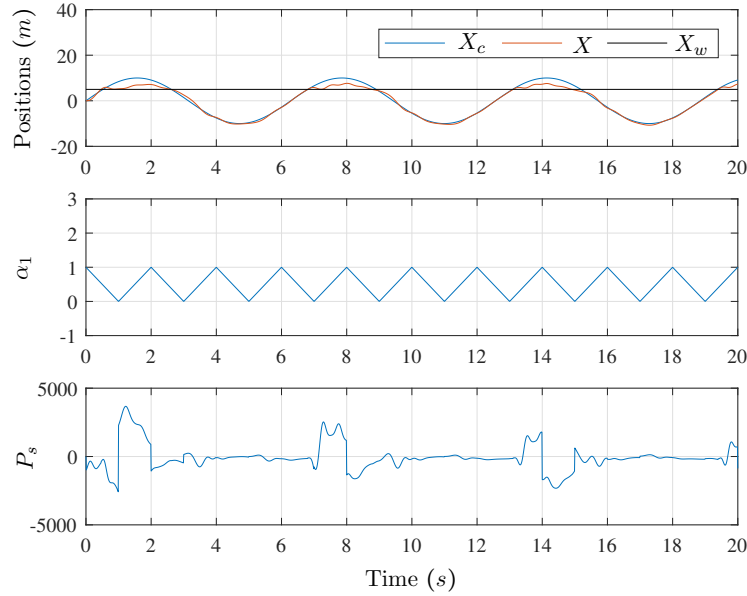

Figure 4.23: Single agent simulation with fixed stiffness produces no position drift and the system is passive

Figure 4.24: Single agent simulation with adaptive gain $\dot{\alpha}_1 = 1$

Gain-Gradient Limitation for Passivity

As derived in (4.92), the sign-indefinite power term P_{si} for each agent i, which violates the passivity is given by:

$$P_{si} = \frac{1}{2}\dot{\alpha}_i K_{pi}(X_{ci} - X)^2, \tag{4.93}$$

and it violates passivity only when $\dot{\alpha}_i > 0$. The passivity preserving term P_{pi} from damping in each controller i is given by:

$$P_{pi} = K_{di}(V_{ci} - V)^2, \tag{4.94}$$

which can dissipate a power $P_{pi} = K_{di}(V_{ci} - V)^2$. So, if the sign-indefinite power P_{si} is limited by this value when P_{si} is positive, then the system will still be passive. This condition is given by:

$$\frac{1}{2}\dot{\alpha}_i K_{pi}(X_{ci} - X)^2 \leq K_{di}(V_{ci} - V)^2,$$
$$\dot{\alpha}_i \leq \frac{2K_{di}(V_{ci} - V)^2}{K_{pi}(X_{ci} - X)^2} \tag{4.95}$$

So, the final gain gradient $\dot{\alpha}_i'$ that can be applied to ensure passivity, is given by:

$$\dot{\alpha}_i' = \begin{cases} \min(\dot{\alpha}_i, \frac{2K_{di}(V_{ci}-V)^2}{K_{pi}(X_{ci}-X)^2}) & \text{if } \dot{\alpha}_i > 0, \\ \dot{\alpha}_i & \text{else,} \end{cases} \tag{4.96}$$

If the damping gain of the controller would also be scaled by the value α_i, the condition for gain-gradient limitation would have been $\dot{\alpha}_i \leq \frac{2\alpha_i K_{di}(V_{ci}-V)^2}{K_{pi}(X_{ci}-X)^2}$. This means that once α_i has become zero, it would be stuck there since the allowed increase would be

$\frac{2\alpha_i K_{di}(V_{ci}-V)^2}{K_{pi}(X_{ci}-X)^2}) = 0$. This is the reason why only the stiffness gains of the controllers are adapted.

The proposed method to limit the gradient of α_1 for a single controller is shown in Fig. 4.25. As in Fig. 4.24, the gain is commanded with a gradient of $\dot{\alpha}_1 = -1, +1$, for the same system. Note that during reduction of α_1, the system is passive and therefore, its value can be reduced as desired. But during the increasing phase, the gradient of this gain is limited and as a result, the system remains passive.
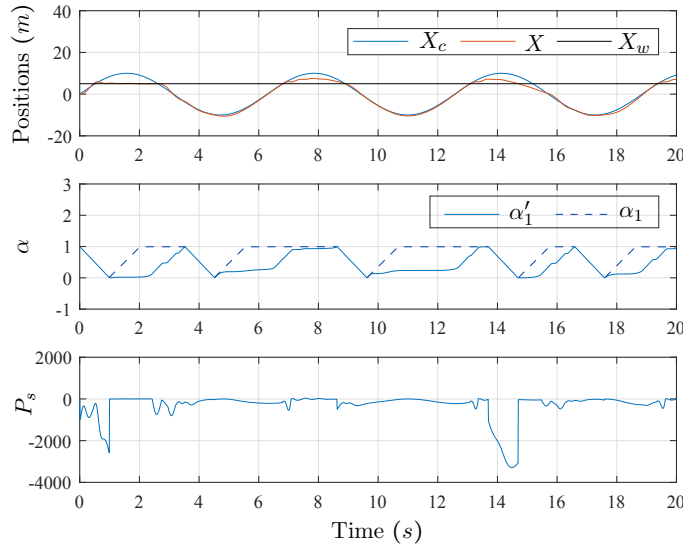

Figure 4.25: Single agent simulation with adaptive gain $\dot{\alpha}_1 = -1, +1$. Gain-gradient limitation makes the system passive.

Now, the simulation for multi-agent control will be considered. The same robot from the previous simulations is controlled by two controllers with desired positions X_{c1} and X_{c2}. The stiffness of the two controllers are modified by the gains α_1 and α_2. Without the proposed method of limiting the gain gradients, the system goes highly non-passive as seen in Fig. 4.26.

The proposed method is applied individually on each of the controllers and the gain-gradients are limited as per (4.96) and the results are presented in Fig. 4.27. Note that now, with the proposed method, the system is always passive.

4.4.3 Experiments and Results

The proposed adaptive-stiffness multi-agent controller is applied on an LWR as shown in Fig. 4.28, which is controlled by two agents and their controllers:

- Agent 1: An impedance controller which regulates the position of the robot's end effector to a desired set-point in the Cartesian space. The AA factor for agent 1 is α_1.

- Agent 2: An impedance tracking controller which commands the robot end-effector to move on circular trajectories in the Cartesian $X - Y$ plane with a diameter of 15 cm and frequency of 1 Hz. The AA factor for agent 2 is α_2.
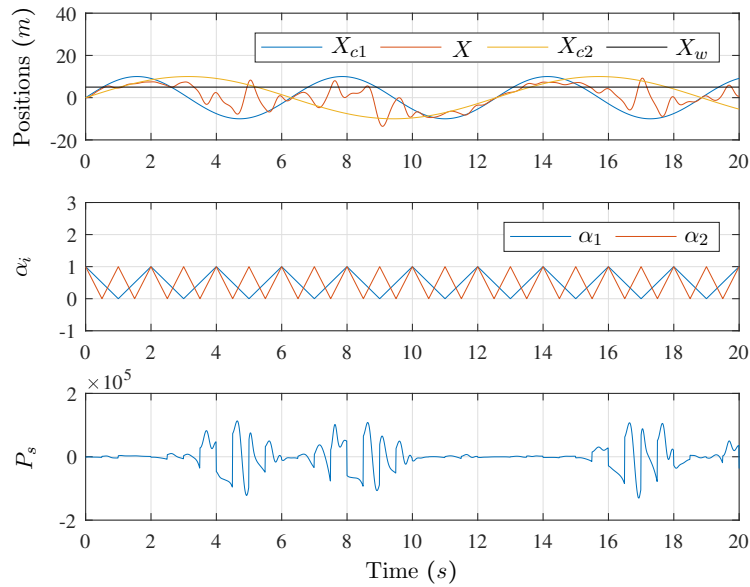
Figure 4.26: Two-agent simulation with adaptive gains $\dot{\alpha}_1 = 1$ and $\dot{\alpha}_2 = 2$. System is non-passive
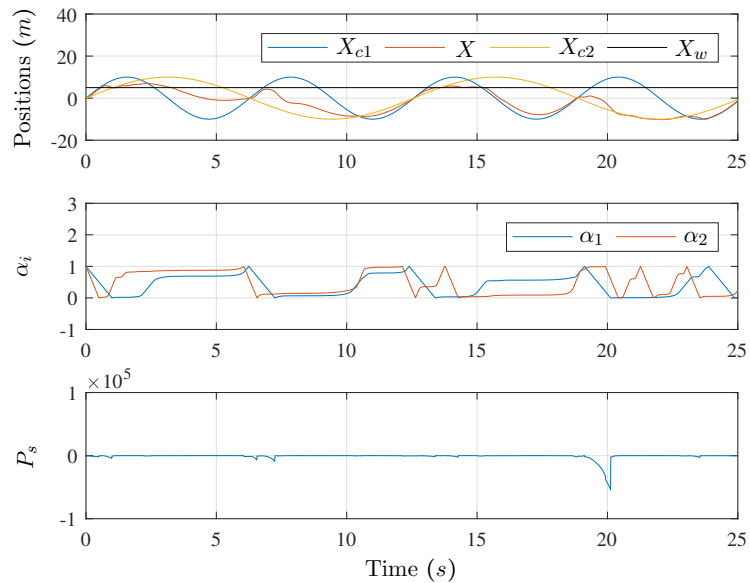

Figure 4.27: Two-agent simulation with adaptive gains $\dot{\alpha}_1 = 1/ms$ and $\dot{\alpha}_2 = 2/ms$. System is ensured passive by limiting the gain gradients.

For both controllers, initial proportional gains of $\boldsymbol{K}_{pt} = diag[500, 500, 500]$ N/m and $\boldsymbol{K}_{pr} = diag[10, 10, 10]$ Nm/rad were chosen for translations and rotations, respectively. The damping gains were $\boldsymbol{K}_{dt} = diag[10, 10, 10]$ Ns/m and $\boldsymbol{K}_{dr} = diag[1, 1, 1]$ Nms/rad for translations and rotations, respectively. The gains α_1 was modified in linear manner from 1 to 0 and then, from 0 to 1. α_2 was assigned a constant value of 1, to clearly identify the performance improvement produced by the proposed method. The wrenches produced by the two controllers were added and commanded to the robot. The desired trajectories
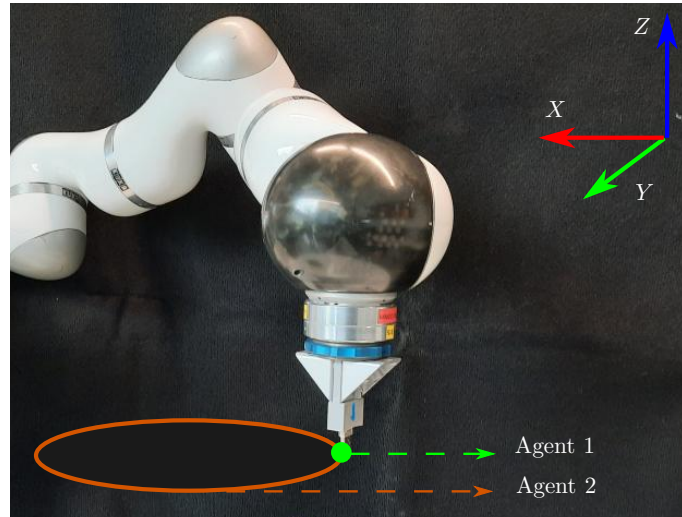
Figure 4.28: Multi-agent end-effector control of LWR

and the robot position are shown in the top row of Fig. 4.29 to Fig. 4.32. The change in the gain α_1 is shown in all the figures in the middle plot, while in all the figures, the last row shows the passivity condition. To show the benefit of the gain-gradient limitation method proposed in this section compared to the damping injection from Section 4.3, the motion of the robot end-effector in the Cartesian $X - Y$ plane is presented in these figures on the right corner. The Green • shows the desired point for the first agent and the Red circle shows the trajectory commanded by the second agent. Note that a position drift is caused when the AA factor α_1 of agent 1 is first reduced (when agent 2 moves the robot) and then increased, but the robot does not pass through the desired • of the first agent.
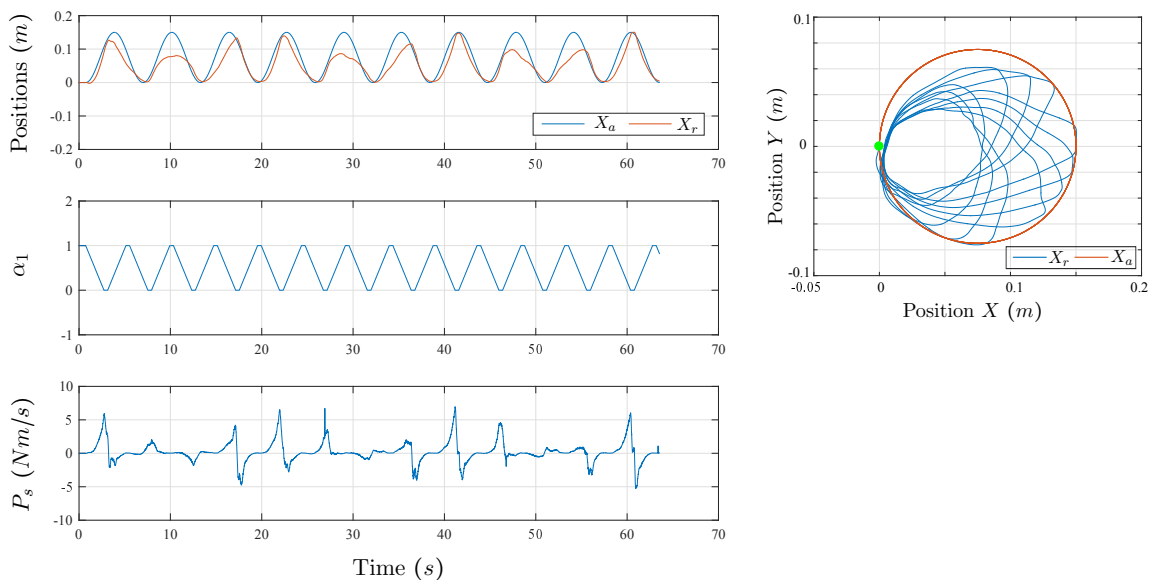
Figure 4.29: Hardware experiment with force scaling from Section 4.3 and damping injection deactivated, which disrupts passivity. The $X - Y$ motion shows no position drift due to the absence of damping

111

Figure 4.30: Hardware experiment with force scaling from Section 4.3 and damping injection activated, which produces passive behavior. But the $X-Y$ motion shows position drift due to the damping to ensure passivity

Figure 4.31: Hardware experiment with stiffness scaling from Section 4.4 and gain-gradient limitation deactivated, which disrupts passivity. The $X-Y$ motion shows no position drift due to the adaptive stiffness approach
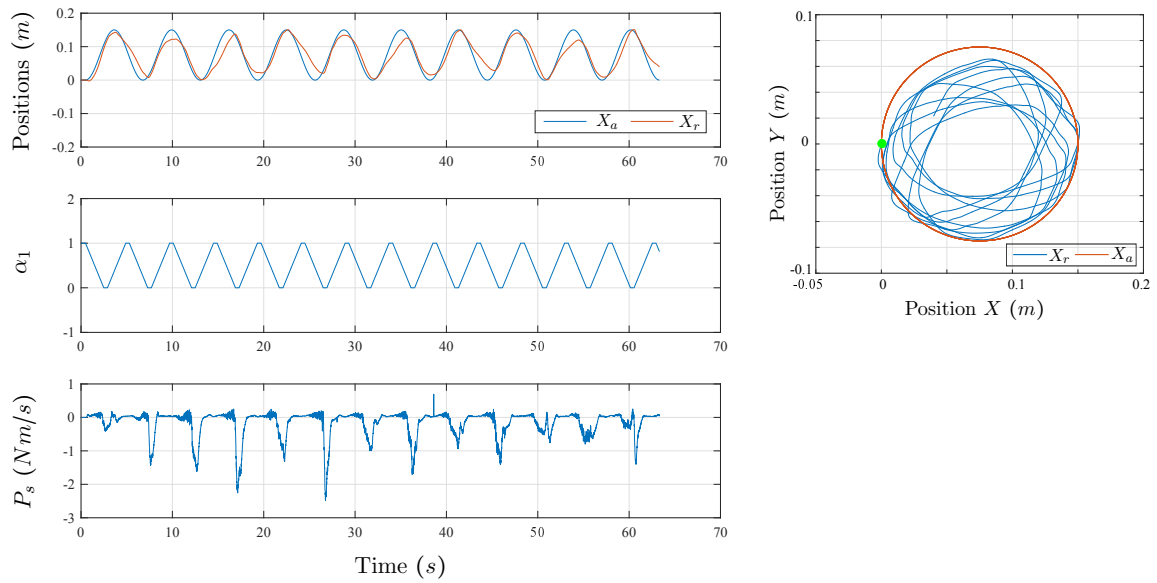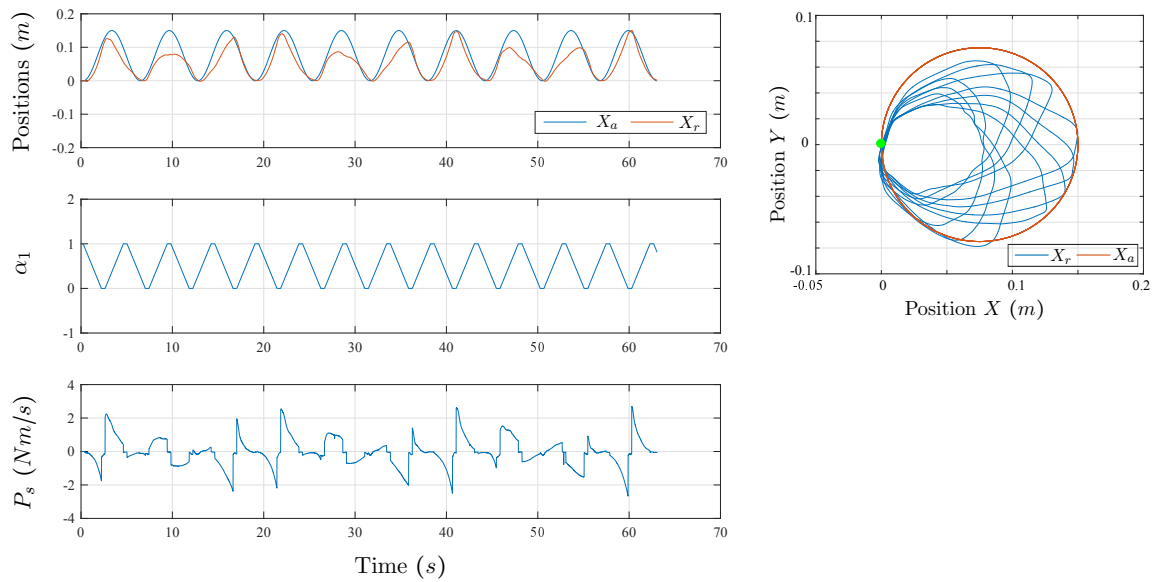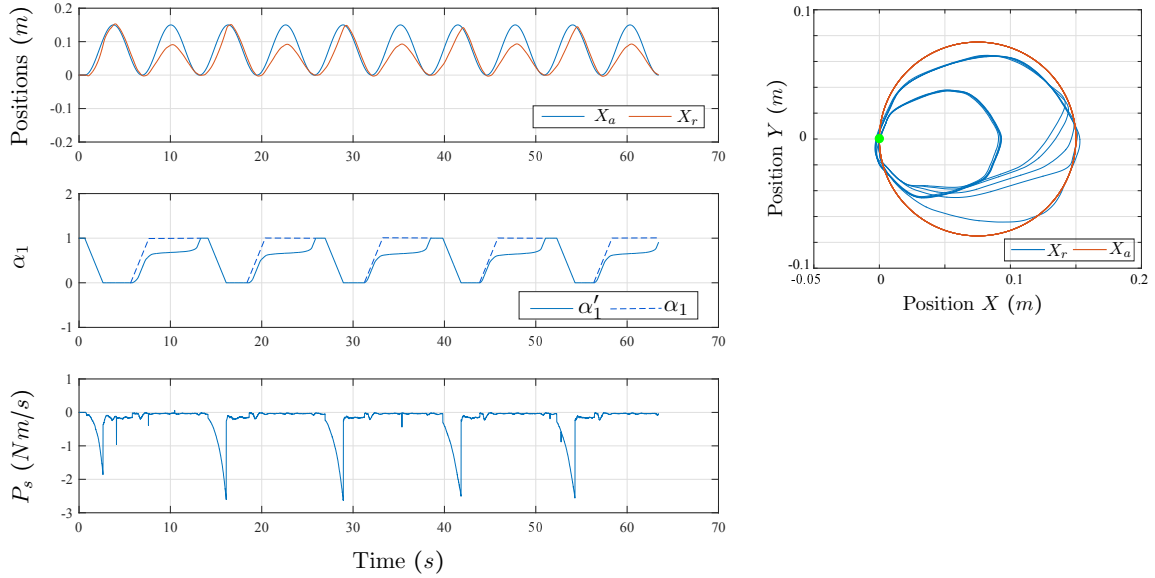
Figure 4.32: Hardware experiment with stiffness scaling from Section 4.4 and gain-gradient method activated, which produces passive behavior. The $X-Y$ motion shows no position drift due to the gain-gradient limitation method to ensure passivity. But the gain modification is slower than desired.

4.4.4 Discussion

The experimental validation of passivity is shown in the last row in figures Fig. 4.29 to Fig. 4.32, where it can be seen that passivity is violated without the proposed methods, that is, $P_s \nleq 0$ in Fig. 4.29 and Fig. 4.31. On the other hand, with the proposed methods, passivity is ensured in Fig. 4.30 and Fig. 4.32. As shown in the $X-Y$ motion plots, compared to the damping injection method in Fig. 4.30, the proposed gain-gradient method removes the position drift which was the main objective for this section.

However, the gain-gradient method that ensures passivity, limits the rate of increase in AA factors, which might be problematic in case the control authority should be distributed in a rapid manner. However, unlike in other application of variable stiffness controllers, the increase in the values of AA factors for arbitration in shared might not be time-sensitive in most cases.

On the other hand, the damping injection of the force scaling method from Section 4.3 does not have any limitation for the rate of increase in AA factors. So, the choice of the method depends on the task at hand. If one of the agents is a human operator who gets visual feedback and can compensate for the position drifts, the method from Section 4.3 might be a good solution. For autonomous control systems, which are more sensitive against position drifts, the adaptive stiffness method from this section might be a possible solution.

Limitations

Limitation 4.4.1:
The gain-gradient control for ensuring passivity of the adaptive stiffness method proposed in this section limits the rate of increase of AA factors.

Objective Achievement

In terms of removing the position drift caused by the damping injection from previous section while maintaining passivity of the multi-agent robot control with adaptive authority allocation, the objective has been achieved with the adaptive stiffness and gain-gradient limitation methods.

4.5 Summary

Chapter 4 first introduced the concept of unity-sum arbitration and used it to allocate authorities between a teleoperation system and ACS in a system-driven approach. The novel system-driven authority allocation from Section 4.2 depends on real sensor measurement quality, which had not been researched earlier. This method can be applied not only in robotics, but also in other fields of shared control, for example, autonomous vehicles with human intervention capabilities. The user-study analysis showed improved performance for the USB insertion task with shared control, compared to pure teleoperation. The task completion times, objective evaluation and subjective measurement of effort showed better results. However, the unity-sum arbitration process resulted in operators not having the freedom to intervene as and when desired. This posed a new question: Is the unity-sum arbitration necessary? How is the passivity of the adaptive shared control system dependent on the AA factors? To answer these questions and to ensure stability of the adaptive shared control system, the passivity properties of a general multi-agent control with force scaling was analyzed in Section 4.3. The passivity disrupting terms were identified and compensated with damping injection, which resulted in position drifts. To reduce the position drifts, the adaptive authority allocation problem was formulated as an adaptive stiffness problem in Section 4.4. A novel gain-gradient limitation method ensured passivity of the system. The benefits of the adaptive stiffness method compared to the force scaling method were validated with simulations and hardware experiments. For the gain-gradient passivity approach, the limitation is that the AA factors can be increased only at a limited rate, which might not be a serious issue in shared control, where arbitration process is not time sensitive in most cases. Combining the damping injection from Section 4.3 with the gain-gradient method from Section 4.4 in task-specific optimized manner is a possible future extension of this chapter. The main take-aways from this chapter are:

1. Unity-sum arbitration is not a necessity to ensure stability of adaptive shared control. This gives more flexibility to modify the AA factors.

2. The system-driven adaptive shared control method can be applied not only in robotics, but also in other fields of human-machine interaction.

3. With the multi-agent control system designed as a multi-port system with adaptive AA factors, different kinds of agents (regulation, tracking, teleoperation) and any form of arbitration method (system-driven or human-driven) can be incorporated for shared control.

In the next chapter, the multi-agent framework from this chapter and the transparent teleoperation system from Chapter 3 will be combined in a modular manner to produce the final outcome of this thesis, namely, the stable and transparent framework for adaptive shared control.

Stable and Transparent Shared Control Framework

5.1 Introduction

The goal of this thesis was to develop a stable and transparent framework for adaptive shared control. To reach this goal, Chapter 3 developed methods to improve the transparency of the teleoperation *part* of shared control, while maintaining system stability. Chapter 4 presented the passive combination of multiple control agents whose authority on the robot was adaptable. This chapter presents the culmination of all the research in this thesis. As summarized in Fig. 5.1, the transparent teleoperation system will be combined with ACS in a stable manner giving rise to the *Stable and transparent framework for adaptive shared control.*
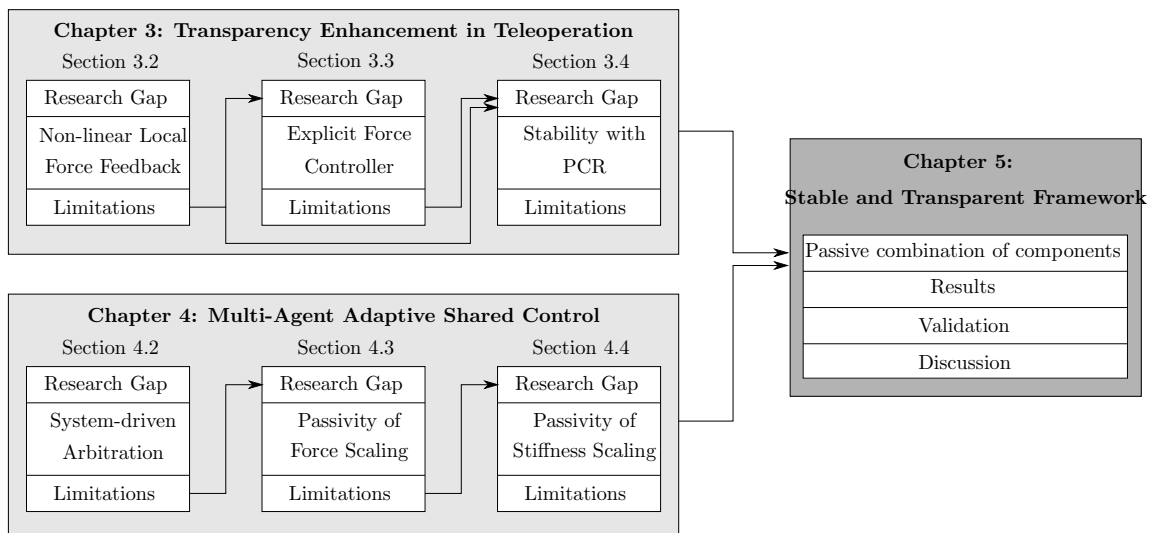

Figure 5.1: Overview of Chapter 5

5.2 Passivity of Components

This section presents individual components of the adaptive shared control framework and their passivity properties. Finally the components will be combined together to ensure finite-gain stability of the overall framework.

1. Transparent Teleoperation System

This part of the shared control includes the haptic device, the passivated feedback controller for delayed communication channel and the position controller. The feedback controller of the designer's choice is made passive using PCR as presented in Section 3.4. The haptic device is OSP due to the inherent, physical damping as presented in Table 2.1. The concept is summarized in Fig. 5.2. As a reminder to the readers, the PCR concept for a time-delayed teleoperation system, which is highlighted within the dashed box in Fig. 5.2 is from Fig. 3.34. The resulting, combined two-port named 'TP System' is overall passive since, it is a feedback interconnection of an OSP (haptic device) and a passive system (feedback controller, communication channel and position controller), as per Lemma 3. Note that in Section 3.4, the entire teleoperation system was proven to be OSP because it also included the remote robot in the entire port-network, which also has inherent damping. Here, the port TP System is stopped after the position controller of the robot, which makes the system only passive and not specifically OSP. The OSP of the entire framework will be shown later.
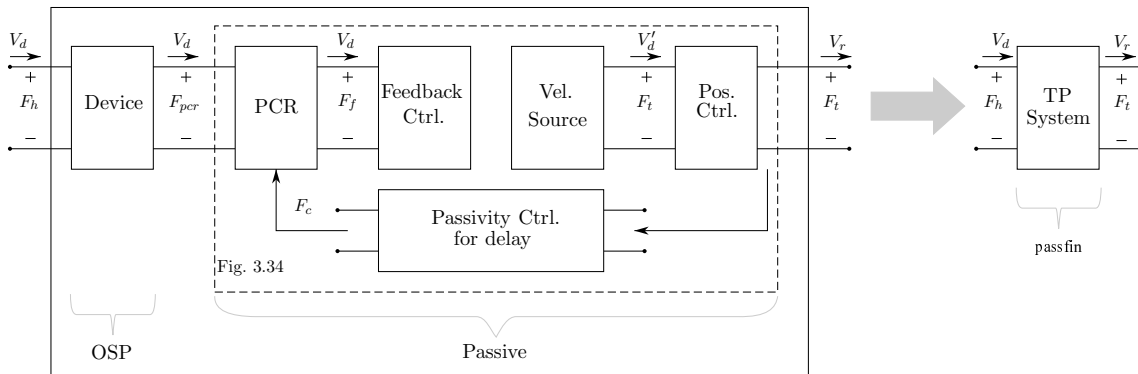

Figure 5.2: Passivity of the teleoperation system with PCR

2. Automatic Control System

The automatic control system (ACS) either regulates the position of the robot to a desired set-point or tracks a desired trajectory. In case of regulation (for example, a virtual wall), there is no external input to the ACS. The internal input is the velocity V_r of the robot and the output is the force F_a produced to move the robot to the desired point, or limit the robot to a region as in the case of virtual walls. The passivity of ACS for regulation is shown in Fig. 5.3 on the left side.

However, in case of tracking, as described in Section 4.3, the ACS has an external input like a desired velocity V_c or position X_c. Then, as shown on the right side of Fig. 5.3, there is a power input to the system from outside, namely $F_a V_c$, which has to be considered for the passivity analysis. In both cases, for an ACS implemented as spring-damper coupling (with spring stiffness K_{pa} and damping K_{da}), the storage function S_a can be the potential

energy stored in the ACS spring (stiffness term K_{pa}), that is, $S_a = \frac{K_{pa}(X_c - X_r)^2}{2}$ with X_r being the position of the robot. The passivity of the system is shown by calculating the time-derivative of S_a,

$$
\begin{aligned}
\dot{S}_a &= K_p(X_c - X_r)(V_c - V_r), \\
&= [F_a - K_{da}(V_c - V_r)](V_c - V_r), \\
&= V_c F_a - V_r F_a - K_{da}(V_c - V_r)^2,
\end{aligned}
\tag{5.97}
$$

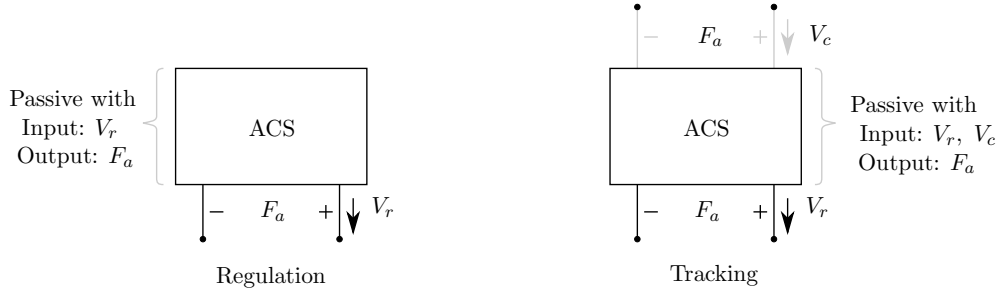which is passive for input $(V_c, -V_r)$ and output (F_a, F_a).

Figure 5.3: Passivity of ACS

Note that the ACS for tracking is a component in the overall shared control scheme which gets input (V_c) from the outside world and produces an output F_a. The other components that have energy exchange with the outside world are the haptic device (input F_h and output V_d), and the remote robot (input $-F_e$ and output V_r). The viscous damping in the haptic device and the remote robot ensure OSP for these devices, which dissipates damping powers $D_d V_d^2$ and $D_r V_r^2$, respectively. In order to ensure OSP of the overall shared control scheme, the last component which interacts with the outside world, namely, the ACS for tracking should have a power dissipation proportional to its output F_a. This can be achieved by adding a constant damping D_{op} parallel to the ACS at the output port of its interaction with the outside world. This modification is shown in Fig. 5.4.
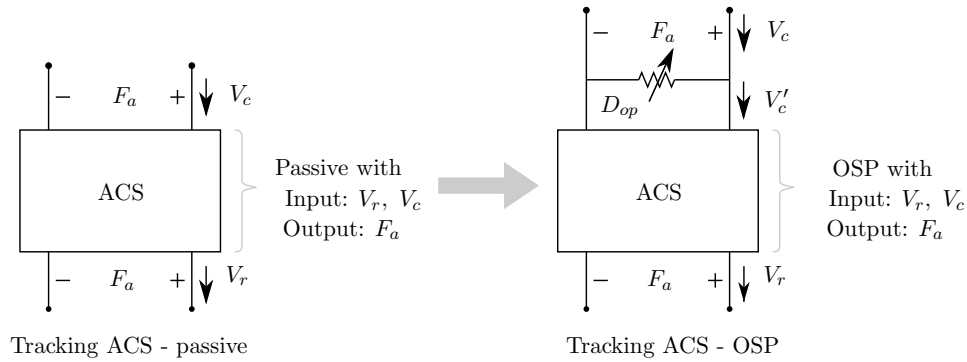

Figure 5.4: Passivity and OSP of ACS

Note that with the additional damping D_{op}, the velocity (and resulting position) commanded to ACS controller will be modified as $V_c' = V_c - \frac{F_a}{D_{op}}$ which results in a desired position of X_c'. The time derivative of the storage function $S_a' = \frac{K_{pa}(X_c' - X_r)^2}{2}$ for the ACS

can be computed as:

$$\begin{aligned}
\dot{S}_a' &= K_p(X_c' - X_r)(V_c' - V_r), \\
&= [F_a - K_{da}(V_c' - V_r)](V_c' - V_r), \\
&= V_c F_a - V_r F_a - \frac{F_a^2}{D_{op}} - K_{da}(V_c' - V_r)^2,
\end{aligned} \tag{5.98}$$

which makes the tracking ACS OSP with input $(V_c, -V_r)$ and output (F_a, F_a). The additional damping D_{op} leads to position drifts and will affect the performance of the tracking ACS. A solution to this issue is to introduce passive drift compensators in the system. An example of such a drift compensator is presented by the author in [BMP$^+$21].

3. Adaptive Authority Allocation

Now, the methods developed in Chapter 4 for combining the forces from the teleoperation system and the ACS, which are both passive individually, will be applied to ensure that the overall system is passive. The force scaling and damping injection from Section 4.3 and, the adaptive stiffness controllers and gain-gradient limitation from Section 4.4 are separately evaluated.

3.a Damping Injection from Section 4.3

As presented in Section 4.3, in a mixed-initiative shared control system with force scaling, the final forces commanded to move the robot is a weighted sum of the forces coming from different agents. In the shared control framework presented here, the two agents are the teleoperation system and the ACS with forces F_t and F_a, respectively as outputs. To combine these two forces in a smooth and passive way, the damping injection method presented in Section 4.3 is first used. The weights α_t for the teleoperation force and α_a for the ACS force can be modified, by keeping the three port passive. The final force commanded to the robot is $F_r = \alpha_t F_t + \alpha_a F_a$. Using the damping injection concept for the scaling from Section 4.3, the final AAA three-port is passive and is shown in Fig. 5.5. As mentioned in Section 4.3, the TP system and the ACS do not receive the actual velocity of the robot V_r, but modified versions of them, V_{rt} and V_{ra}, respectively. This leads to positions drifts which was mentioned as a limitation of the damping injection method.

3.b Gain-Gradient Limitation from Section 4.4

The adaptive gains presented in Section 4.4 are now implemented for the shared control system and is shown in Fig. 5.6. Here, the combination is straightforward since it directly results in a parallel interconnection of passive subsystems, namely, the TP and ACS, which are both made passive by the gain limitation method. Note that both controllers receive the real velocity of the robot V_r and as a result, there will not be any position drift, as it is confirmed by simulations and hardware experiments in Section 4.4.2 and Section 4.4.3, respectively. In this case, the final force commanded to the robot is $F_r = F_t + F_a$.

4. Complete Framework

Now, all these passive components are combined to get the complete framework, which is shown in Fig. 5.7. Note that the concepts of feedback and parallel interconnection of passive systems from Lemma 3 and Lemma 2, respectively are availed here. The regulation
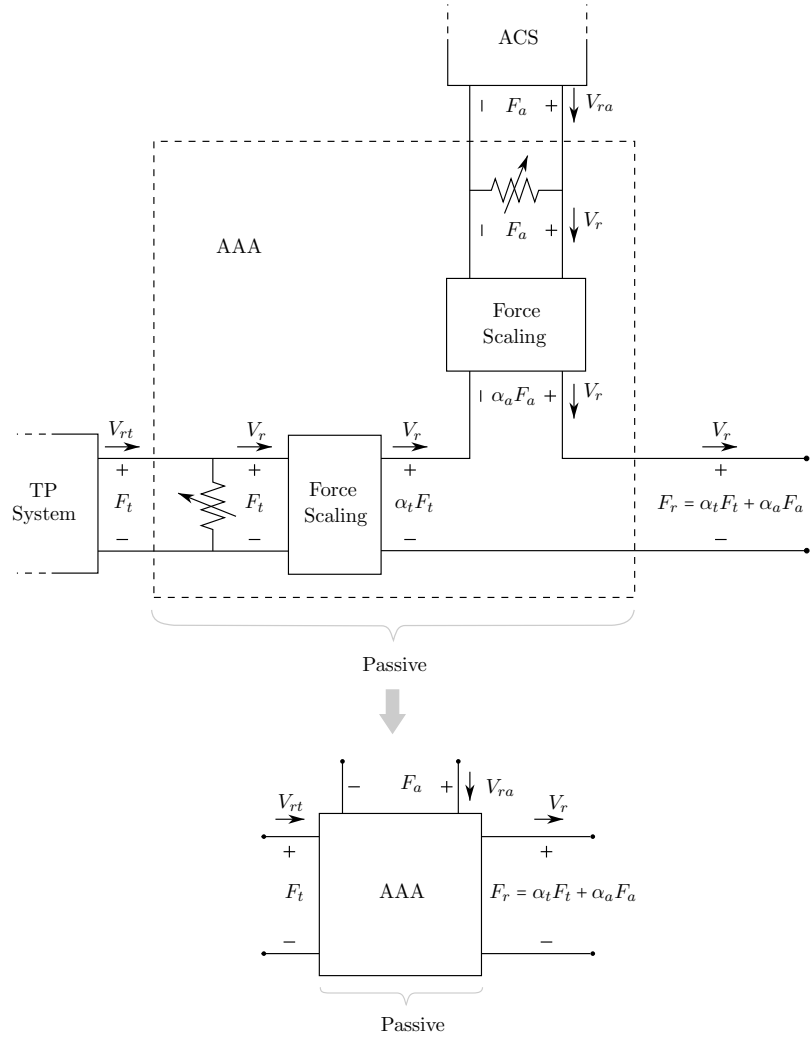
Figure 5.5: Scaling and damping injection from Section 4.3
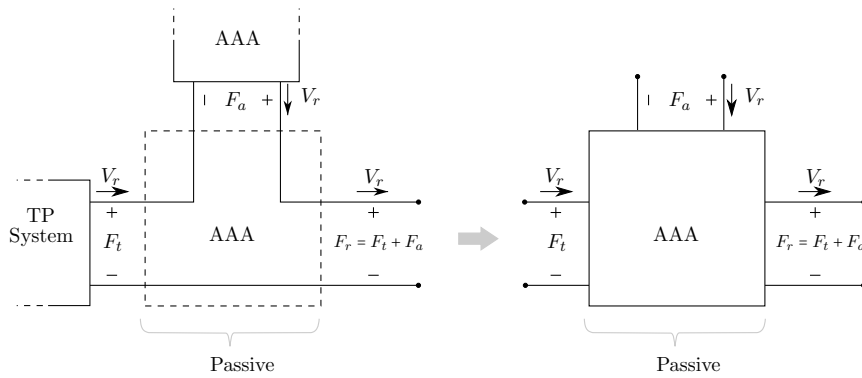

Figure 5.6: Adaptive gains from Section 4.4

case for the ACS is in Black color and the tracking case is specifically given in Gray color. The damping D_{op} is the additional term added to introduce a negative quadratic term of the output F_a to ensure the OSP of the system, for the tracking scenario as described in Section 5.2. Note that the velocity between the TP system (and also the

ACS) and the AAA port is V_r if the adaptive gains from Section 4.4 are used, and the final force commanded to the robot is $F_r = F_t + F_a$. In case the forces are scaled and the damping injection method is used, the velocities from the AAA port will be V_{rt} and V_{ra} to the TP system and ACS, respectively and the force commanded to the robot will be $F_r = \alpha_t F_t + \alpha_a F_a$. In both cases, with passivity proven for each of the subsystems as shown in Fig. 5.7, the overall framework is OPS with inputs: $F_h, -F_e$ and V_c, and outputs: V_d, V_r and F_a and is therefore finite-gain stable.
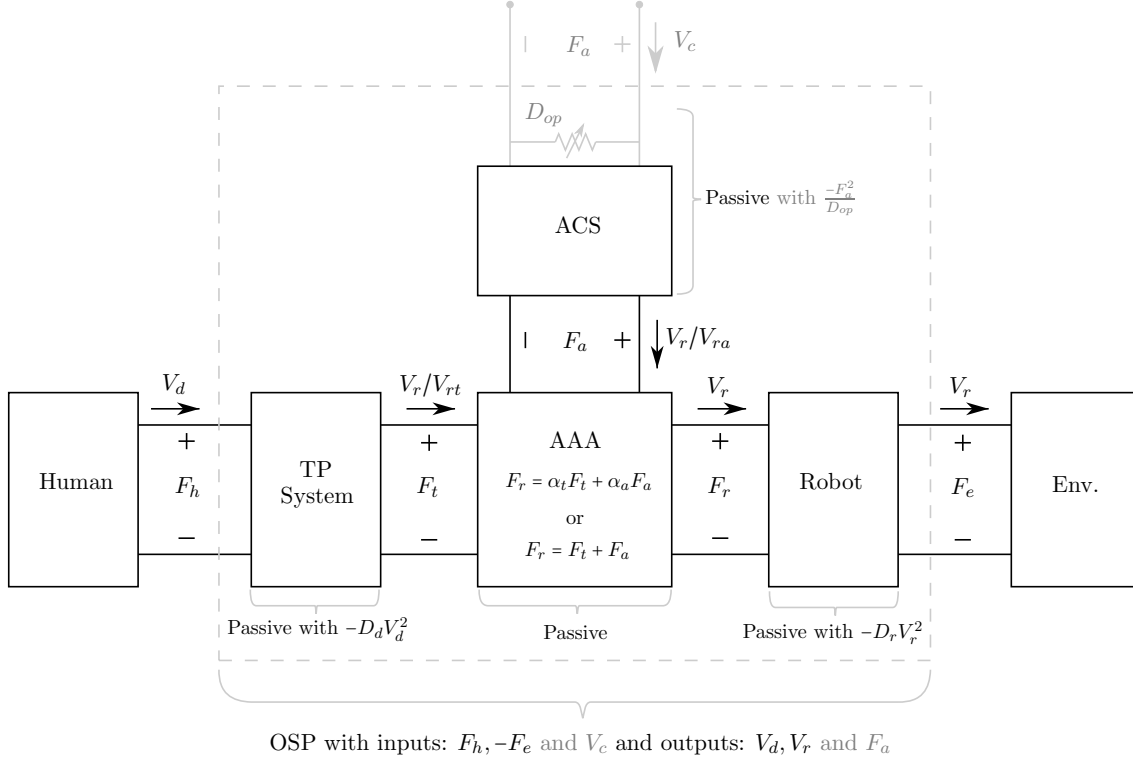

Figure 5.7: Stable and Transparent Framework for Adaptive Shared Control

5.3 Experiments and Results

The proposed shared control framework with the stability methods were implemented on real hardware with LWR-LWR teleoperation and shared control. The ACS is implemented as planar virtual wall, that is, an impedance controller which restricts the

motion of the robot-end effector on a $X - Z$ plane in the Cartesian space as shown in Fig. 5.8a. The system driven shared control method developed in Section 4.2 is availed here and this time, the human operator always has unity authority, that is $\alpha_t = 1 \forall t > 0$. This is opposed to the generally implemented unity-sum condition for AA factors as per Def. 4.1. With this modification, the operators can, as per their desire, take corrective measures whenever necessary. With the initial value of $\alpha_a = 1$, the AA factor for the virtual wall, the operator can move the robot tool on this plane. Virtual forces are produced to support the operator to move the robot in this plane that contains the target, which is a USB female port. First the operator moves the robot tool, a USB male port in this plane from the initial point towards the target. When the robot tool reaches the mid point of the trajectory from the initial pose to the target USB port, a noise is introduced in the
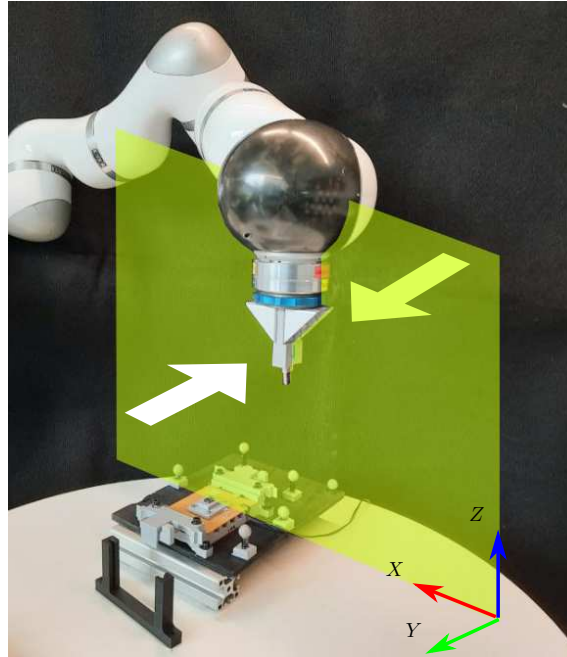
(a) Vertical $X - Z$ plane on which robot is free to move.
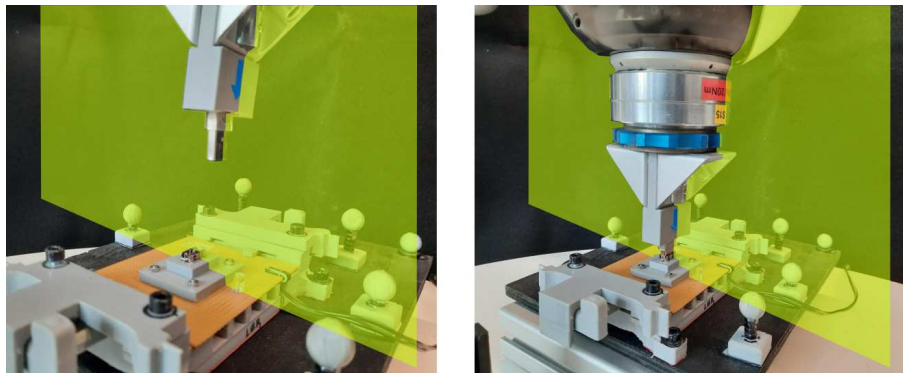
(b) Approach and final insertion

Figure 5.8: Experiment set-up and virtual wall in $X - Z$ plane as ACS

measured target pose, to simulate a scenario similar to the one in Section 4.2. At this point the AA factor of the ACS α_a is reduced by the system-driven approach from Section 4.2. Let this value be α_{as}. The operator, who observes the reduction in α_{as} due to the decrease in confidence of the ACS target pose estimation, can now smoothly reduce the final α_a value used to scale the force from the ACS, F_a. The value of α_a gain commanded by the operator is α_{ah}. Based on the method used for arbitration, the final value of α_a will be chosen. With $\alpha_a = 0$ and $\alpha_t = 1$, the operator has complete authority over the robot to move the robot to the final insertion point. Once the tool moves out the noise region, α_a value is increased by the system and the operator can now give more authority to the ACS by manually increasing α_a and the robot is once again limited to move in the Cartesian $X - Z$ plane. The variation in α_a gain by the system-driven approach and by the operator is shown in Fig. 5.9. With the support from the ACS as the tool is near the target USB

port, the operator can complete the insertion.
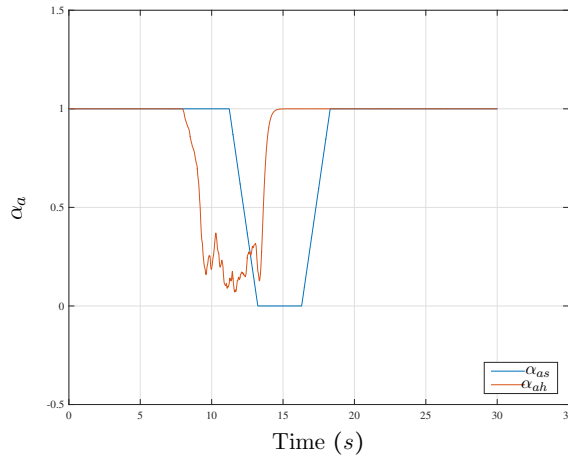
Figure 5.9: Variation of α_a gain: α_{as} by the system driven approach from Section 4.2 and α_{ah} manually

.

Stability

This section presents the passivity and stability properties of the system during the USB insertion task without and with the proposed methods. The final AA gain for the ACS α_a is modified manually as shown in Fig. 5.9. Fig. 5.10 to Fig. 5.13 show the position in the Cartesian Z direction, the active (and deactivated) modification of α_a using the gain-gradient limitation method from Section 4.4 and the overall power P_s of the system in the top, middle and bottom plots, respectively.
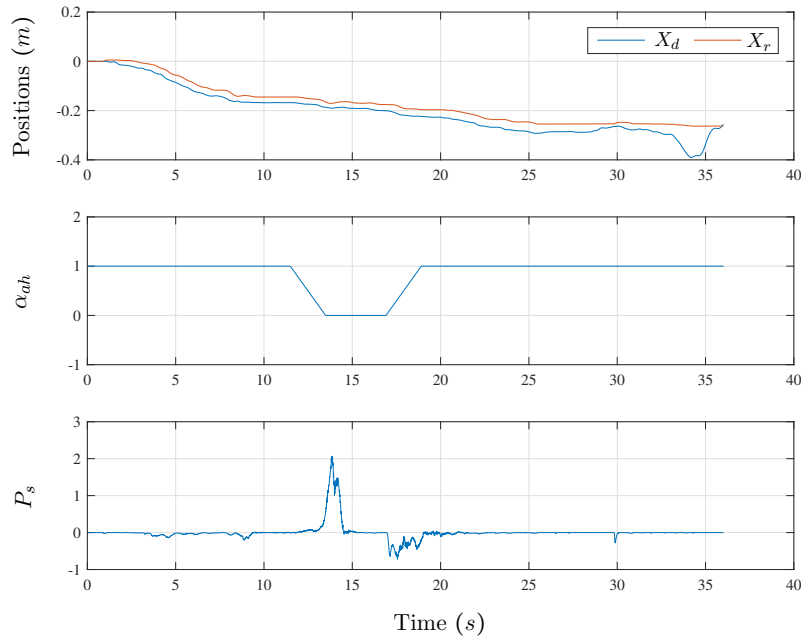
Figure 5.10: Damping injection from Section 4.3 deactivated: Non-passive behavior
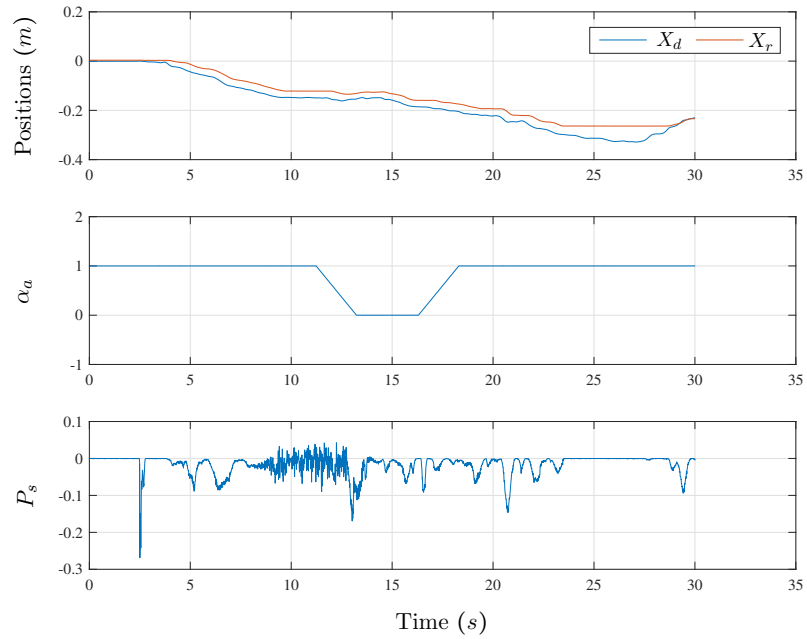
Figure 5.11: Damping injection from Section 4.3 activated: Passive
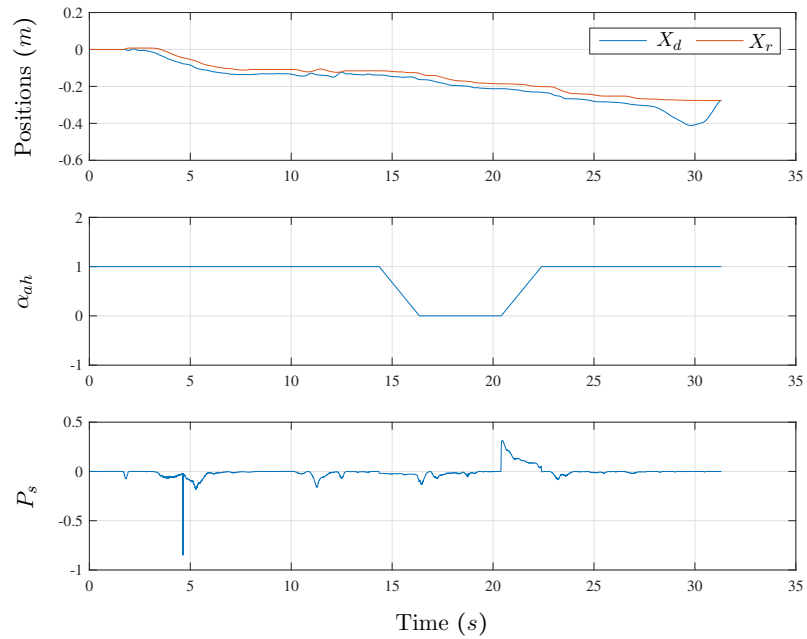
Figure 5.12: Gain-gradient method from Section 4.4 deactivated: Non-passive behavior

In order to demonstrate the position drift caused by the damping injection method from Section 4.3 and its removal by the gain-gradient limitation method from Section 4.4, the motion of the robot end-effector in the Cartesian $X - Z$ plane is shown in Fig. 5.14a and Fig. 5.14b.
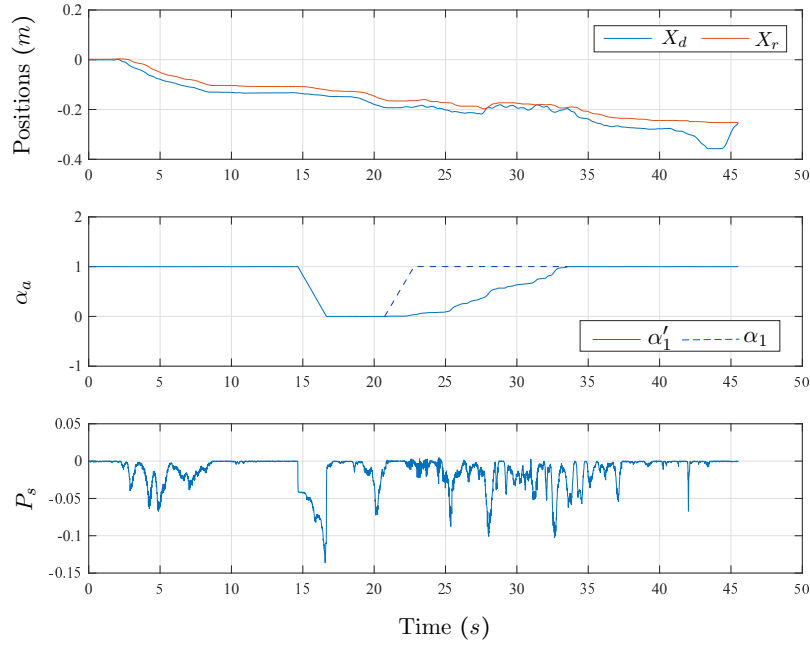
Figure 5.13: Gain-gradient method from Section 4.4 activated: Passive

(a) Position drift with damping injection method

(b) Gain-gradient limitation reduces position drift
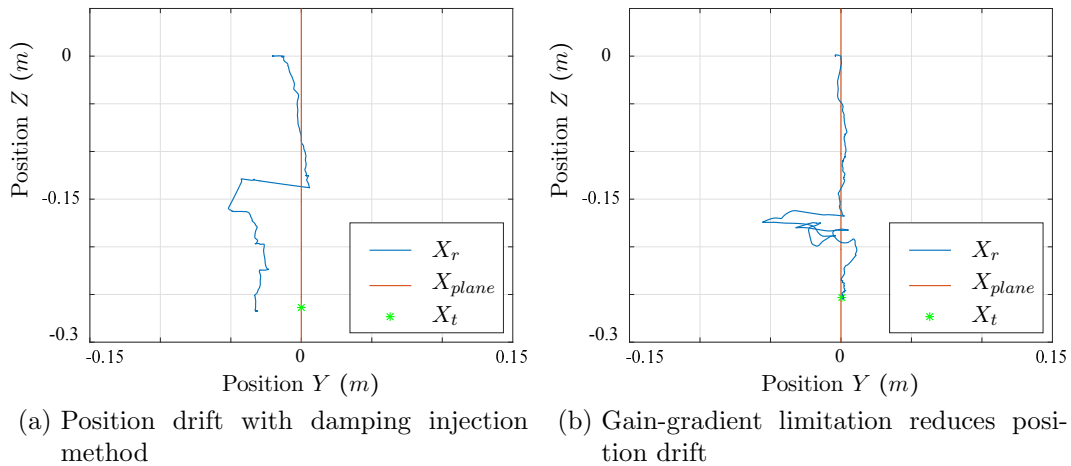
Figure 5.14: Robot motion in Cartesian $Y - Z$ plane

Transparency

Similar to the hardware experiments performed in Section 3.4, the shared control framework with the transparent teleoperation system is presented in Fig. 5.16 to Fig. 5.18 for 3 different delays: $0\ ms$, $200\ ms$ and $600\ ms$, using three different teleoperation architectures. The architectures selected in this chapter are the same as the ones from Section 3.4, namely, position-computed force ($P - F_c$), position measured force $P - F_e$ and with the explicit force controller $P - EFC$. The top plots show the motion of the haptic device (X_d) and the robot (X_r) in Cartesian Z and Y directions. The forces measured at the operator side F_h, the robot side F_e and the virtual forces produces by the ACS F_a are shown in the second plots. Note that the gains α_a and α_t for the ACS and teleoperation are set to 1 for these experiments to show the transparency properties.

Validation Experiment

The application of the developed shared control framework in a stable and transparent manner with adaptive authority allocation is validated with a USB insertion task with high and time-varying delays ($600\ ms$ and variance of $5\ ms$), and is presented in Fig. 5.19. The adaptive stiffness and gain-gradient limitation method from Section 4.4 is used in this experiment due to the reduced position drift, as shown in Fig. 5.14b. The top plot shows the motion of the haptic device (X_d) and robot (X_r) in the Cartesian Z direction. The second plot shows the forces measured at the operator side, robot side and the force produced by the virtual wall. The third and fourth plots show the positions and forces in the Cartesian Y direction. The fifth plot shows the variation of the AA gain for the ACS passivated using the gain-gradient limitation method. The sixth plot demonstrates the passivity of the system and the last plot shows the round-trip delay between the operator and the robot.

Discussion

The stability and transparency properties for the adaptive shared control framework have been validated with the hardware experiments. In Fig. 5.10, the passivity of the shared control system is violated when the gain α_a is reduced for force scaling, as seen from the positive values of P_s between 12 and 15 s of the task execution. On the other hand, the damping injection method from Section 4.3 was activated for the experiment in Fig. 5.11 and as a result, the system was passive. The adaptive stiffness method was implemented for the experiment in Fig. 5.12 without gain-gradient limitation which violates passivity condition when the gain α_a is increased by the operator between 20-23 s. With gain-gradient limitation activated in Fig. 5.13, the system is passive. The position drift introduced by the damping injection method in Fig. 5.14a has been reduced by the adaptive stiffness scaling and gain-gradient method in Fig. 5.14b even while ensuring passivity.

In terms of transparency, the $P-EFC$ method produces lower forces during free motion and also performs better when the robot interacts with the environment and the virtual wall, compared to both $P-F_c$ and $P-F_e$ methods. This behavior is similar to the experiments in Section 3.4 for all delays. The difference can be noted clearly for the 0 ms delay case in Fig. 5.16. With the $P-EFC$ architecture stabilized with the PCR algorithm, the operator can perceive the forces produced by the environment contact, as well as the virtual fixture, which act as haptic guidance. This is a major outcome of the thesis and is presented specially here in Fig. 5.15.
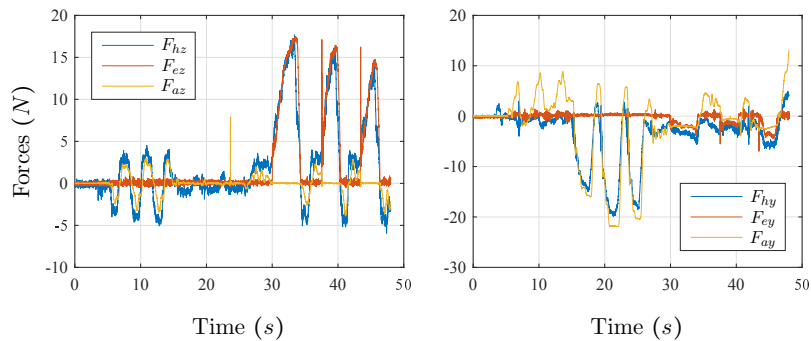
Figure 5.15: Forces in shared control with $P-EFC$ teleoperation. The operator receives transparent feedback of both, contact force F_e and the virtual wall force F_a.

5.4 Summary

This chapter consolidated all the methods developed till now in this thesis. The passive interconnection of the passive components developed in the previous chapters resulted in the final stable and transparent framework for adaptive shared control. The transparent teleoperation from Chapter 3 is combined with the ACS, which is already passive and the authority allocation factors are adapted based on the system-driven method from Section 4.2 for the validation experiments. The reduction of the confidence of the ACS target pose estimation was presented to the operator, who smoothly modified the AA factor of the ACS accordingly. The final AA factor adaptation was ensured to be passive based on the damping injection method from Section 4.3 and gain-gradient limitation from Section 4.4. The USB insertion task performed using the developed framework validated the methods developed in this thesis even for large and time-varying delays. In the next chapter, the different applications of the framework in practical scenarios will be presented. The modular nature of the framework enables different teleoperation architectures and different arbitration techniques.
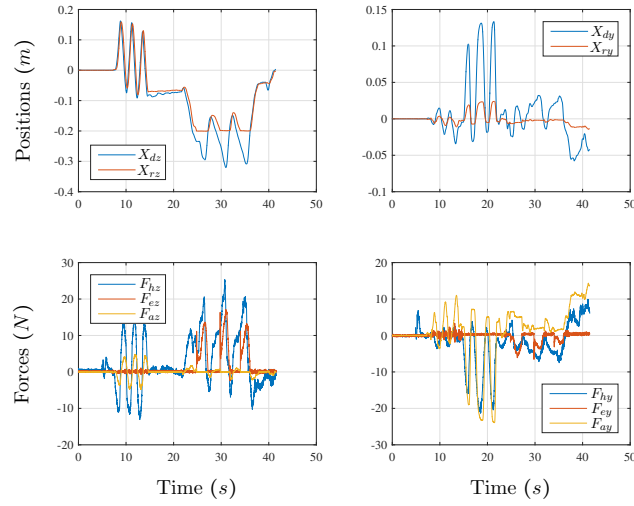
(a) $P - F_c$ architecture
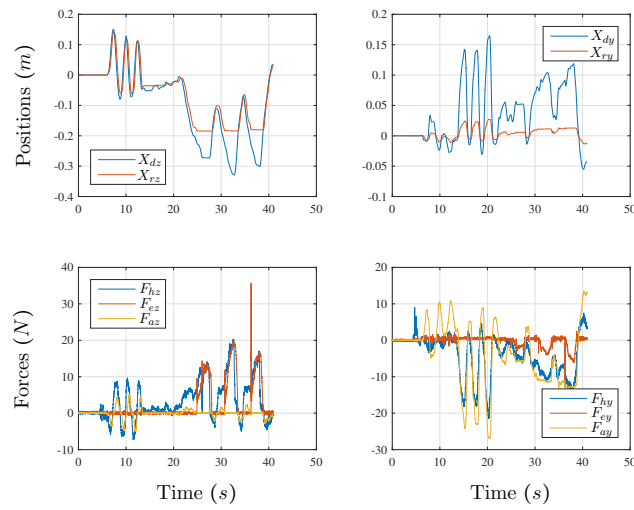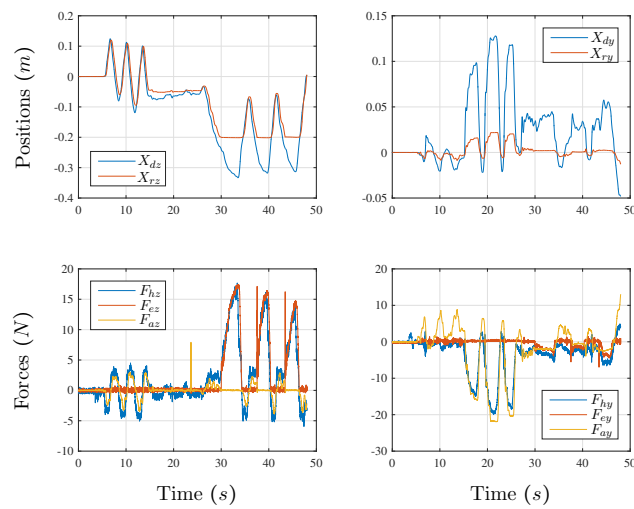
(b) $P - F_e$ architecture

(c) $P - EFC$ architecture

Figure 5.16: Position and forces for all the architectures with 0 delay
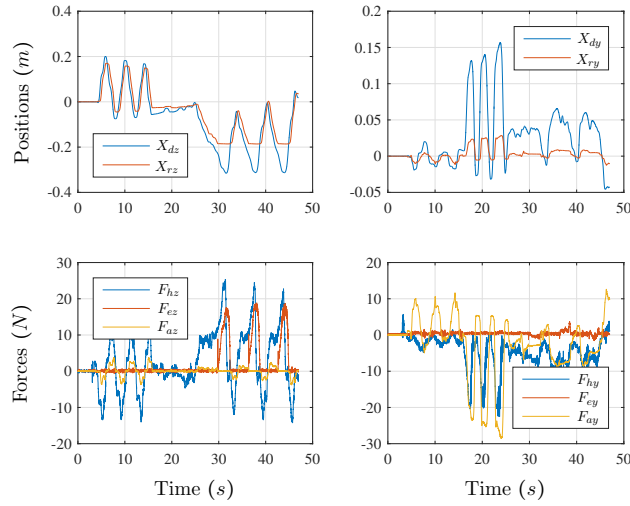
(a) $P - F_c$ architecture
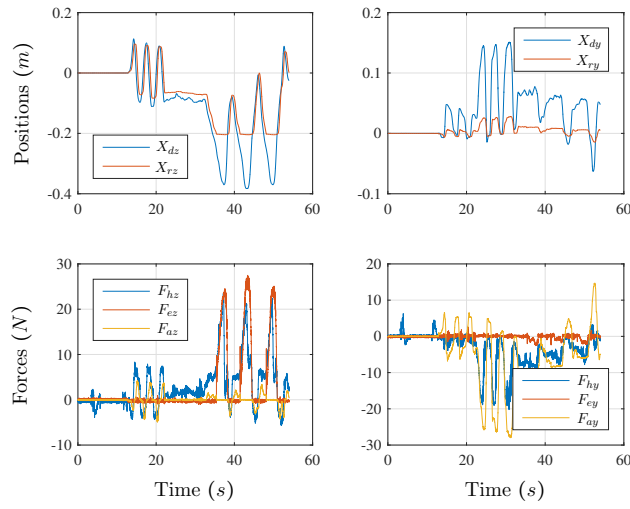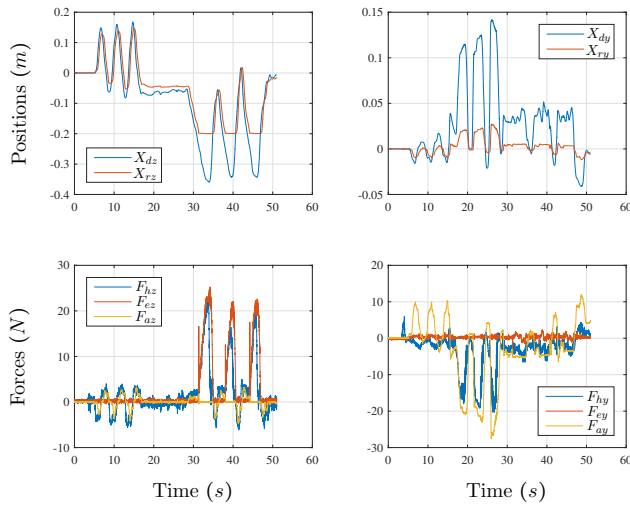
(b) $P - F_e$ architecture

(c) $P - EFC$ architecture

Figure 5.17: Position and forces for all the architectures with 200 ms delay
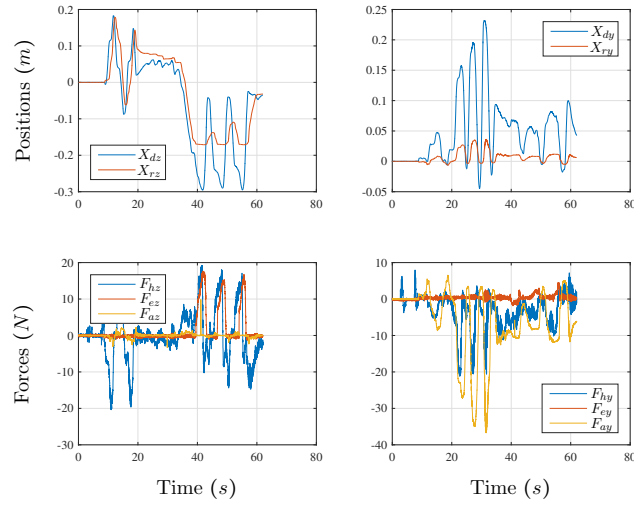
(a) $P - F_c$ architecture
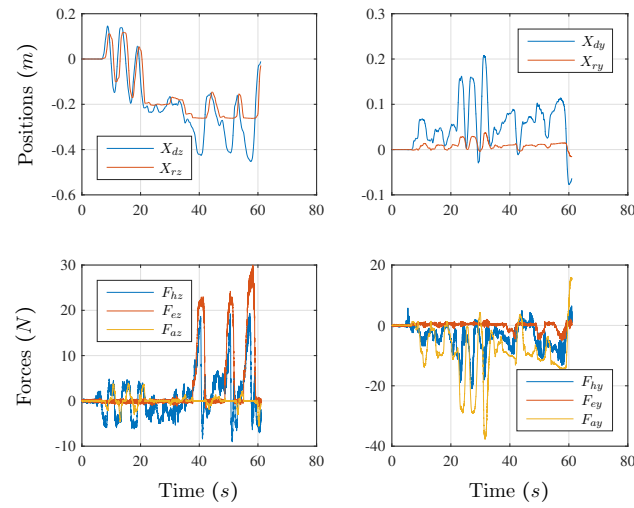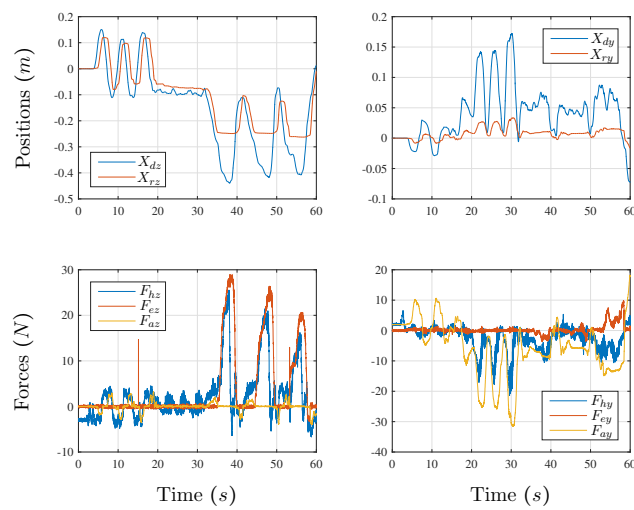
(b) $P - F_e$ architecture

(c) $P - EFC$ architecture

Figure 5.18: Position and forces for all the architectures with 600 ms delay
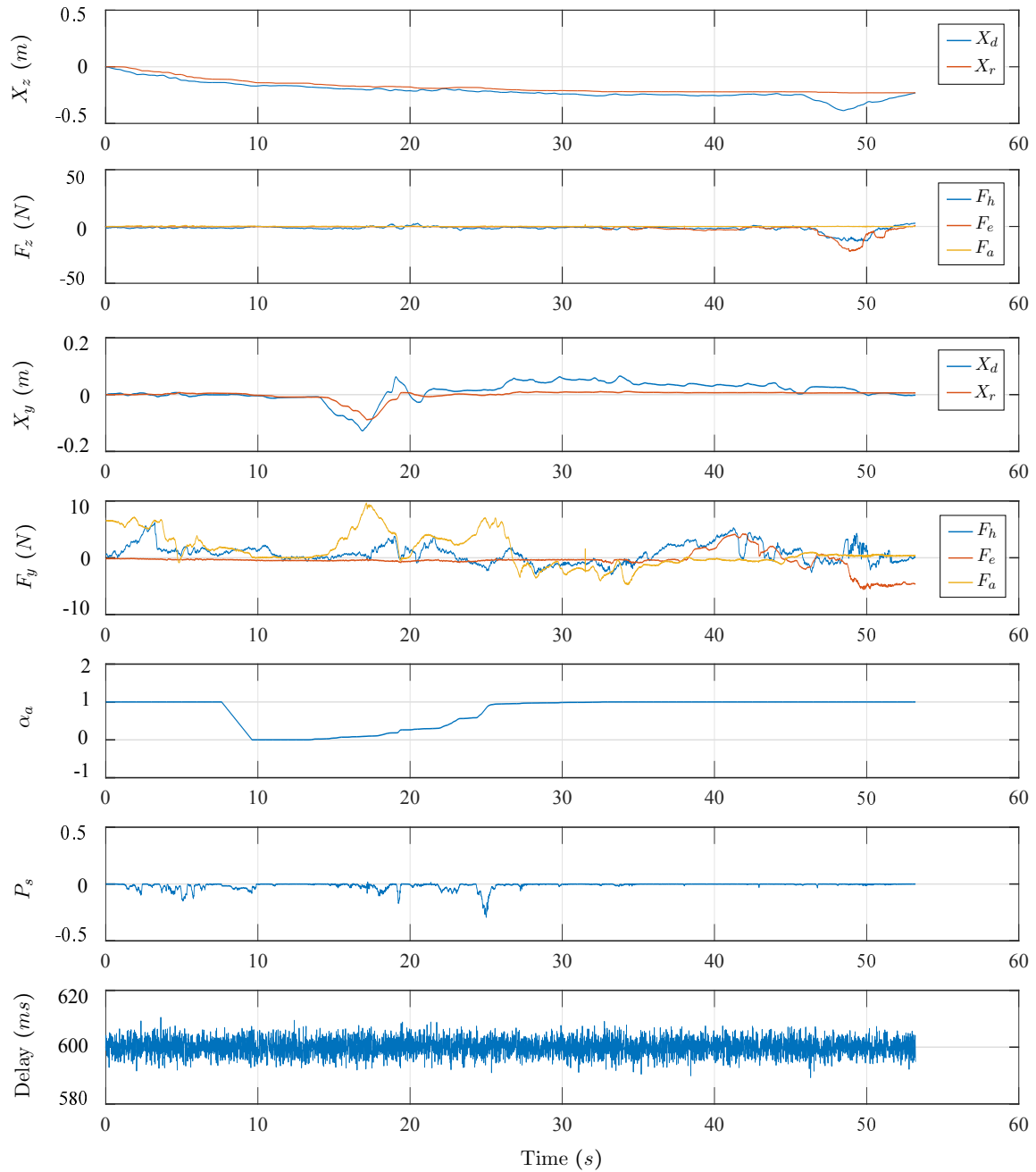
Figure 5.19: USB insertion task with stable and transparent adaptive shared control

Applications

In this chapter, the different applications of the theoretical tools developed in this thesis are presented. Since the work that led to the final shared control framework was incremental, the application scenarios cover different parts of the overall shared control framework. Each of them is highlighted in the final framework presented in the previous chapter. The applications are divided into three sections. Section 6.1 covers the applications in the space domain. Section 6.2 presents an application of the thesis work in terrestrial domain. Finally, the author contributed to multiple other domains in robotics based on the theoretical tools presented in this thesis and they are summarized as secondary contributions in Section 6.3.

6.1 Applications in Space Domain

Robots are mainly conceived for implementing tasks that are dangerous/dull/dirty for humans to perform. Space-exploration is an avenue which presents obvious dangers for humans. Robotic teleoperation can be a fitting solution to tackle challenges in this field. At the same time, the communication time-delays introduced by space communication channels deteriorate the performance of the teleoperated robots. Therefore, shared control comes in handy to let robots perform parts of the tasks possible with available autonomy, while the human operator can intervene as and when the robot fails to complete them.

   This section covers three space application scenarios, where the methods developed in this thesis were used. The first one is the ISS-Earth teleoperation scenario which was tested in the Kontur-2 space mission. The second one is of the on-orbit servicing scenario, simulated with an on-ground, hardware-in-the-loop facility using communication links with geo-stationary relay satellites. The third part covers the in-orbit manufacturing scenario that was also part of the Space-Factory 4.0 project.

6.1.1 ISS-Ground Teleoperation

For future space exploration missions, robots can be the forerunners to inspect new planets and build settlements for the humans that could follow later. Still, due to the existing limitations in autonomous robots, the tasks that can be performed by them on the new planet could be limited. Force feedback teleoperation, being the obvious solution is hindered by the huge time-delays between Earth and the planet (20 minutes with Mars, 2-3 seconds with Moon). A safe solution to avoid this time-delay is to have humans closer to the robots, but not being on the new planet to avoid the risks and costs associated with landing and launching humans. The vision is to have humans orbit the planet and teleoperate the robots on its surface from the spacecraft.

KONTUR-2 was a joint space mission between DLR, the Russian space corporation (ROSKOSMOS), the Russian State Scientific Center for Robotics and Technical Cybernetics (RTC) and RSC Energia for the in-flight verification of force feedback and telepresence technologies. The main objectives of the KONTUR-2 project were the development of a space qualified 2-DoF force feedback joystick (developed by DLR and shown as haptic device in Fig. 6.1), the implementation of telepresence technologies and the investigation of the overall performance when telemanipulating robotic systems on Earth from space with force feedback. The feasibility study of using teleoperation for future planetary explorations with robots on distant planets teleoperated by a human orbiting the planet in a spacecraft (e.g. building habitats on Mars by teleoperated robots) was a desired outcome of the mission. The force feedback joystick was installed in the Russian module of ISS in August 2015 and was in operation until December 2016. In August 2015 the first experiments were conducted successfully, two cosmonauts telemanipulated robots on ground at DLR and RTC from the ISS. The remote robot used for testing the teleoperation performance was the 2-DoF ROKVISS system ([HLR+05], shown as robot in Fig. 6.1). More details on the mission can be found in [RAB+16].
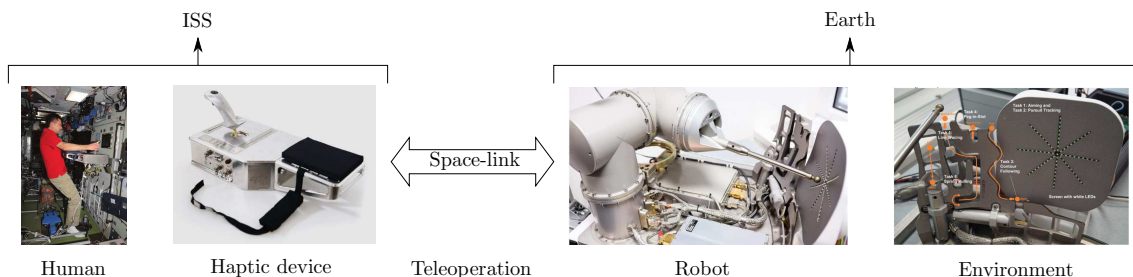
Figure 6.1: Overview of teleoperation system of Kontur-2

The overview of the Kontur-2 space mission is presented in Fig. 6.2. In KONTUR-2, two scenarios had to be considered in the design of the bilateral controller: The operation on-board the ISS and the on-ground cosmonaut training. The first is the nominal mission case, where the cosmonaut controls the robot from the ISS through a S-band link. The second, is a geographically distributed scenario for cosmonaut training purposes. Since the same system needs to operate in both experiments, the requirements for the bilateral controller are clearly strengthened as the two links are characterized by different communication parameters, which are shown in Fig. 6.3.

The contribution to the Kontur-2 project from the author was the implementation of the transparent bilateral controller using the theoretical tools presented in Chapter 2. The conventional 4-channel bilateral controller was modified to a position + measured
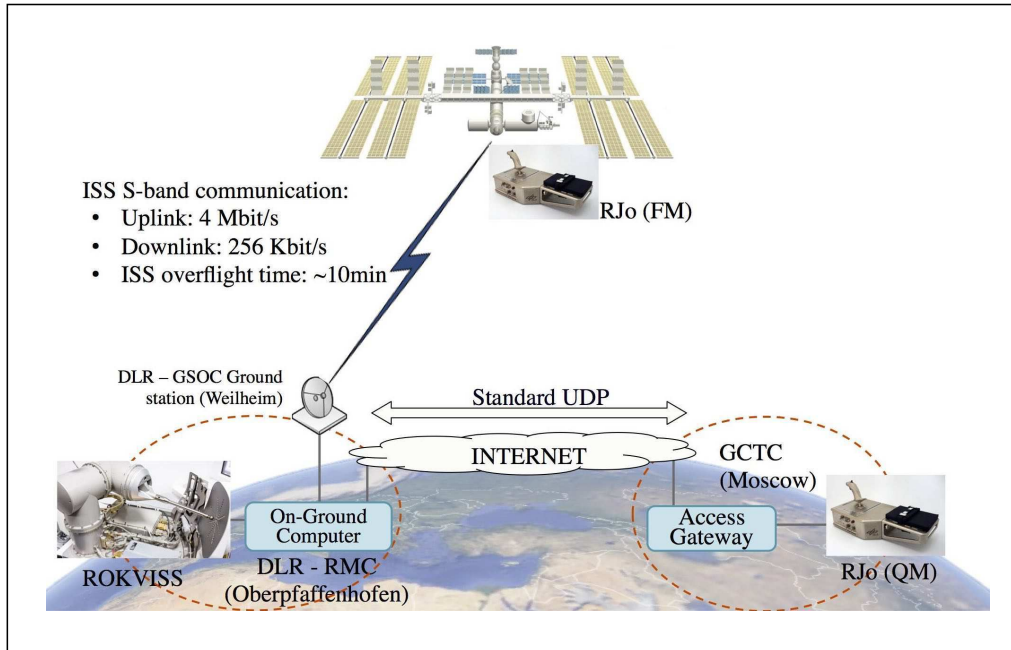
Figure 6.2: Overview of the Kontur-2 space mission
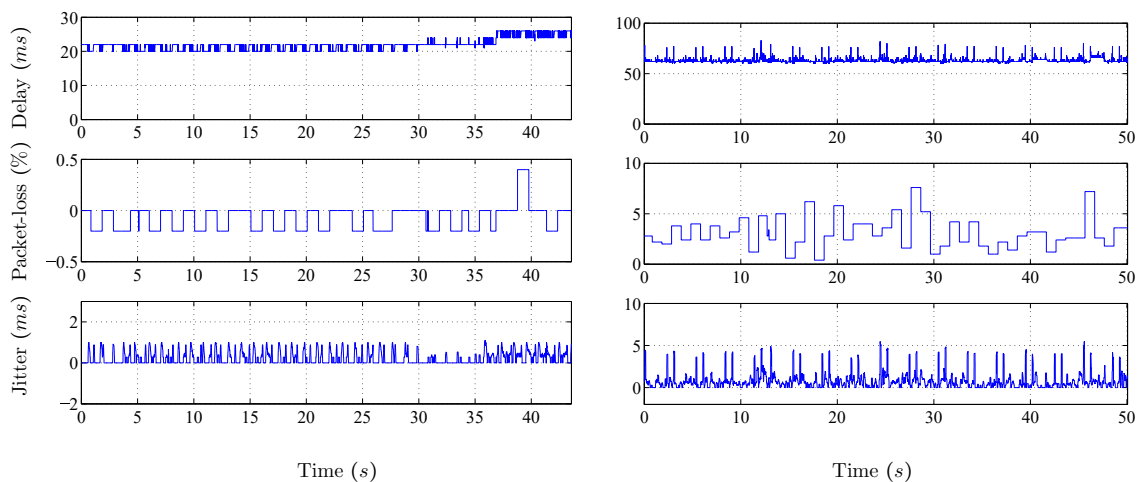
Figure 6.3: Communication parameters for the two scenarios

human force (from haptic device to robot) and computed force + measured environment force (from robot to the haptic device) 4-channel architecture (signal flow diagram in Fig. 6.4) to reduce the spring effects of the feedback position channel [ABR+16]. The robot was fully teleoperated and no autonomous controller was used. The parts of the shared control framework from Fig. 5.7 relevant to the Kontur-2 mission are marked along with the devices, employed bilateral controller (BC) and the communication link features are presented in Table 6.1.

The signal flow diagram of the 4-channel architecture is shown in Fig. 6.4 and the port network of the same is presented in Fig. 6.5. The gains $G_\bullet$ scale the forces $F_\bullet$, so that the system is stable, with optimum performance without delays.

TDPA presented in Chapter 2 was used to remove the destabilizing effects of the com-

Inp. Device	Space Joystick	ACS	Robot	Task
BC	$[V_d, F_h - F_c, F_e]$ 4-channel	–	Rokviss	Aiming
Delay	30, $70ms$			Tracking
Packet loss	0 %, 5 %			Contacts
Part of shared control framework				
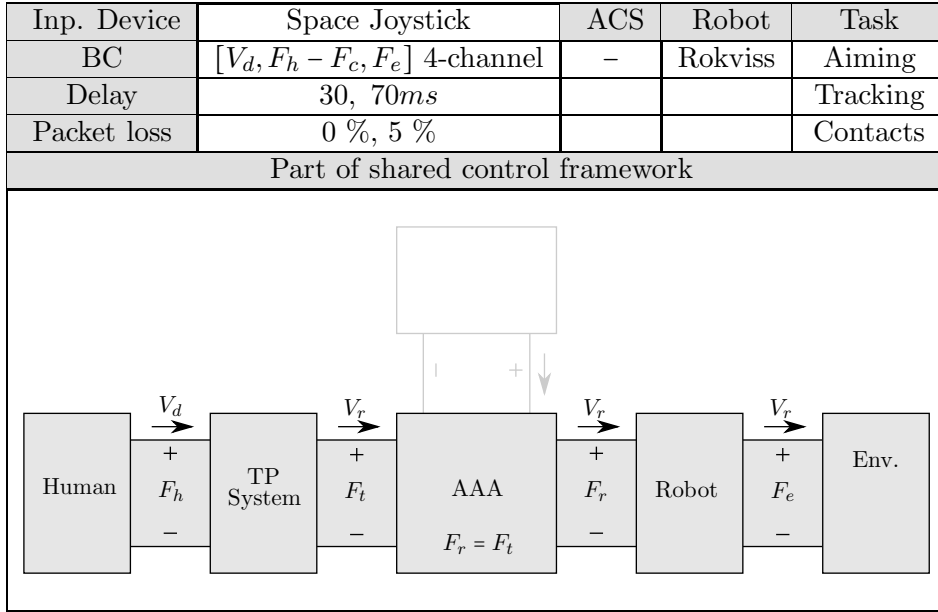
Table 6.1: Scheme of application in Kontur-2
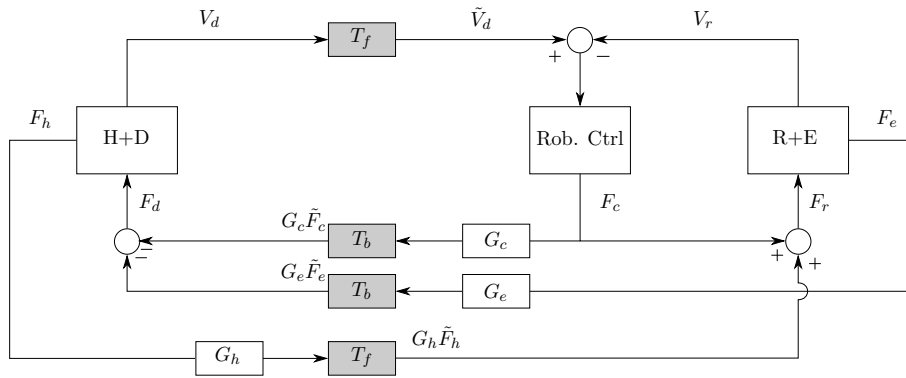
Figure 6.4: Signal flow diagram of the modified 4-channel architecture
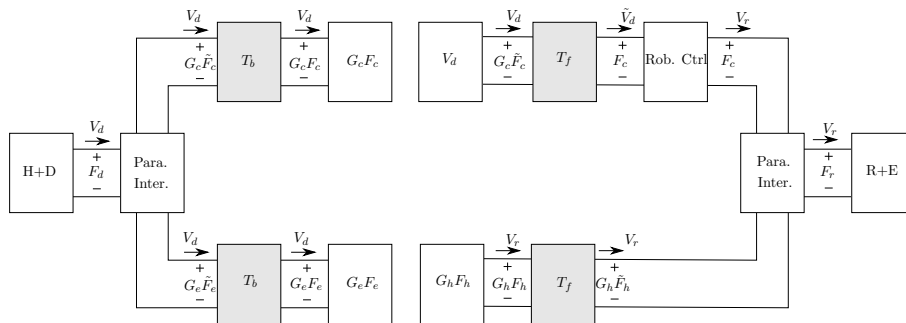
Figure 6.5: Port-network of the 4-channel architecture

munication delays. The basic implementation of the POPCs are shown in Fig. 6.6, where $(\bullet)_p$ represents the passivated signal of $(\bullet)$ for the forces and velocity signals. Readers can find more details of the bilateral controller in [ABR+16].
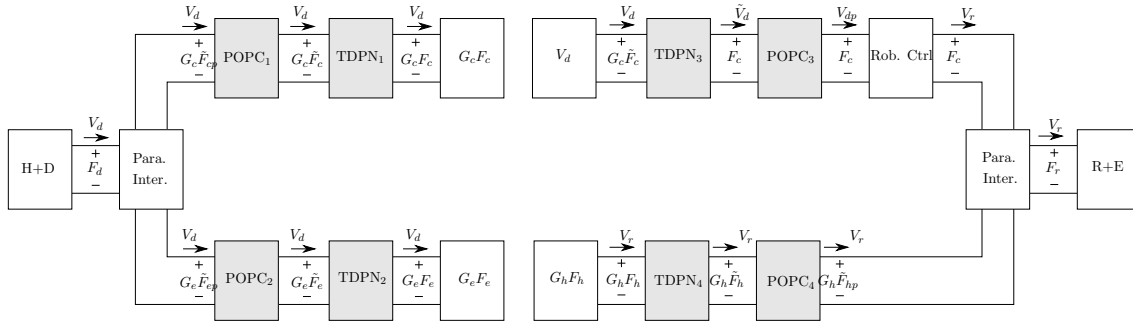
Figure 6.6: Port-network of the 4-channel architecture passivated with POPC

Experiment Results

The ROKVISS robot was teleoperated to interact with a task board, represented as Environment in Fig. 6.1. The cosmonaut had to perform several tasks like aiming, tracking, spring pulling and making hard contacts with the task board. Here the results of the hard contacts and free motions tasks are presented. The results of other tasks can be found in [WSR⁺16].

The first set of experiments were conducted during the cosmonaut training before the launch. The cosmonauts teleoperated the ROKVISS robot in Germany, from the training center at Moscow, through normal internet link. In both cases, the proportional control parameter was chosen to be $K_p = 80 \ Nm/rad$ and the local damper of the haptic device was $D_d = 0.07 \ Nms/rad$. The scaling factors had values of $G_e = 0.006$, $G_c = 0.003$ and $G_h = 40$ respectively, to match the dynamics of both systems. Joystick and ROKVISS are dynamically very different, with maximum torques of $0.2 \ Nm$ and $40 \ Nm$ respectively

As shown in Fig. 6.3, the round-trip was varying around $70 \ ms$ and there were packet loss and jitter due to the UDP communication link. The position of the devices and the forces measured are shown in Fig. 6.7, for both free motion and hard contacts.

(a) During contacts

(b) During free motion
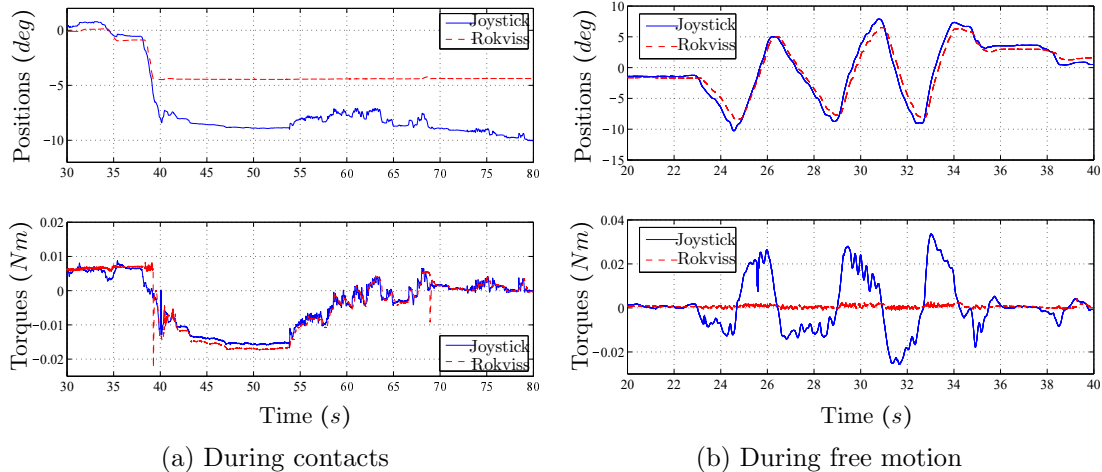
Figure 6.7: Position and forces during training

The real experiments happened during the mission, where the cosmonauts on-board the ISS teleoperated the ROKVISS robot in Germany. The operation window was limited to a maximum of 10 minutes (horizon to horizon passage of ISS) due to the direct S-Bank

link employed. The round-trip delay varied between 20 ms and 30 ms and the packet loss was almost absent. Fig. 6.8 shows the positions and forces of the devices during the mission experiments.

(a) During contacts

(b) During free motion
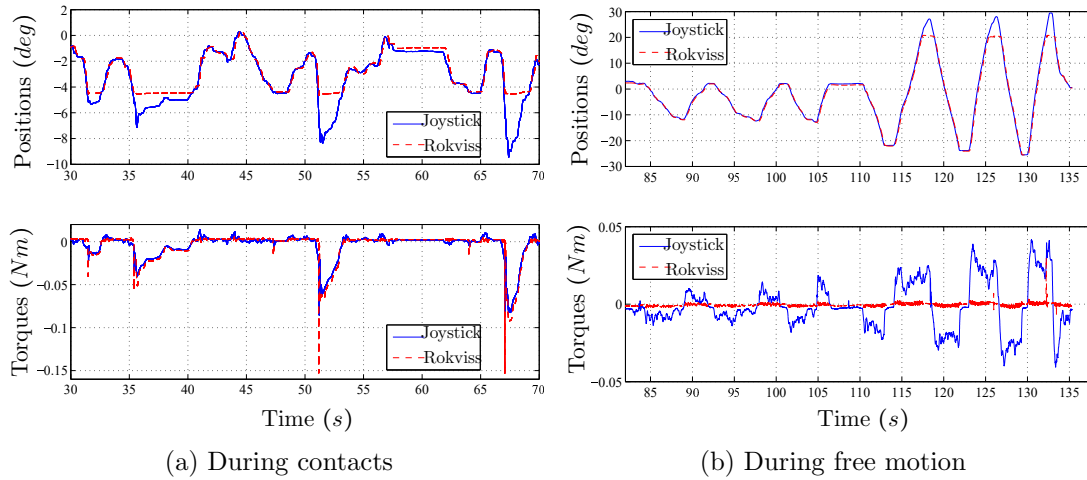
Figure 6.8: Position and forces in real mission

Discussion

As seen the in plots, the position tracking and the force feedback showed high performance. The cosmonauts reported that the tasks were easy to perform with the force feedback joystick. Different telepresence approaches were compared in terms of system and operator performance and the results from terrestrial and space sessions were compared to better understand the effects of microgravity on sensorimotor performance when controlling a telerobotic system. Preliminary analyses revealed that positional accuracy is degraded in microgravity compared to terrestrial conditions [WSR+16]. Yet, these performance losses can partially be compensated by adding extra damping at the joystick, allowing a high telemanipulation performance despite microgravity. After the successful completion of the experimental sessions, a media event was conducted where the two arms of the humanoid robot, Space Justin were controlled in a multilateral way by a cosmonaut in ISS and another operator from Russia, and is shown in Fig. 6.9. The setup availed the same 4-channel architecture with additional haptic augmentation and was published in [PBA+17].

Multilateral setup   robot
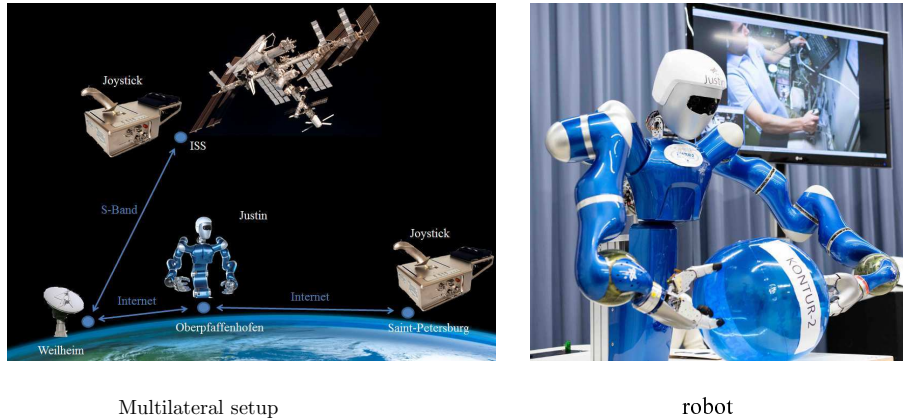
Figure 6.9: ISS-Germany-Russia multilateral setup and robot used in the media event

6.1.2 On-Orbit Servicing

The next space application scenario considered is On-Orbit Servicing (OOS). Space robotic solutions are already taking shape for mitigating the issues due to ever increasing space-debris in the Low Earth Orbit (LEO) [WHS19]. Roughly, a space robot consist of one or more manipulators mounted on a servicer spacecraft. The robot is capable of grasping a free-floating target and docking it onto the servicer, either to de-orbit it or for OOS. Compared to classical robotics, the use of space robots for OOS presents some unique challenges that characterize its complexity and efficiency. Among the most remarkable are: a) controlling the manipulator on a free-floating base, b) addressing impact dynamics, c) reliability of visual sensors in space conditions and d) time-delay between servicer and ground station.

Due to the limitations presented by the visual sensors for full autonomous robot control, teleoperation could promise an imminent solution, in spite of the communication delays between the human operator on ground and the orbital robot. The direct S-Band link used in the Kontur-2 mission enabled transparent force feedback teleoperation due to the very low latency in the communication link, as mentioned in Section 6.1.1. But still, as mentioned in the same section, the available window of operation was limited to a maximum of 10 minutes. This hinders the possibilities for tasks that require more precise and slower execution, as required for OOS. On the other hand, the Ku-Band, which could avail relay satellites in the Geostationary orbits (GEO), enables unlimited operation windows, but increases the delay, packet-loss and jitter [ABDS+16]. To test and validate the possibilities of teleoperation as a solution for OOS in spite of the aforementioned challenges, the OOS-Simulation facility (OOS-Sim, [ADSR+15]) was exploited here. OOS-Sim facility consists of two KUKA-120 industrial robots, on each of which the mock-ups of the satellites are mounted. The mock-up of the servicer satellite is equipped with an LWR used for servicing tasks. The haptic device is another LWR on a separate station. To simulate the relay link through GEO satellites, communication data was recorded through the ASTRA relay satellites and was artificially introduced between the haptic device and the servicer manipulator. The set-up is presented in Fig. 6.10. The target scenario of OOS on LEO satellites through GEO links and the implemented case with the OOS-Sim are shown in Fig. 6.11.

The main questions that needed to be addressed are the following:

1. How are the free floating dynamics and time-delay affecting the control structure of

Human and haptic device   ASTRA link   Orbital robot and client
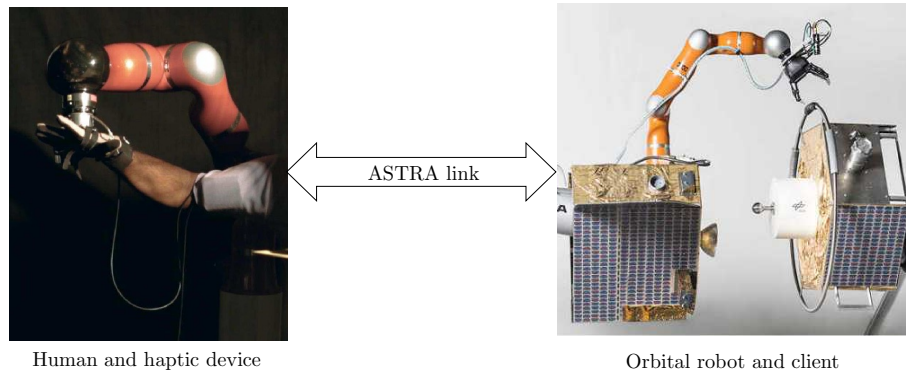
Figure 6.10: The teleoperation system in OOS facility

(a) Target scenario   (b) Implemented scenario
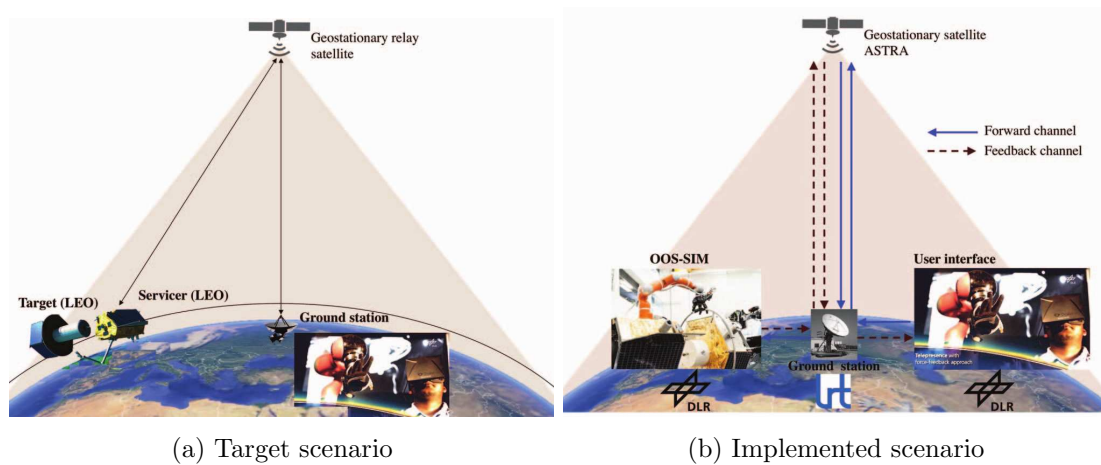
Figure 6.11: Scenarios for On-Orbit Servicing through ASTRA satellite link

the system?

2. Can current space communication infrastructures support real time control requirements established by the bilateral controller (i.e. force-feedback teleoperation)?

3. Can a skilled human operator perform on-orbit servicing tasks through the teleoperation system, probably affected by high latencies and force-feedback distortions?

With the first and second questions answered in other works ([HLR⁺05] and [DSMB⁺19], respectively), the focus of this work was on the third question. To this end, the 4-channel controller used in the Kontur-2 mission and presented in Section 6.1.1 was availed for dealing with the significantly deteriorated communication features, as compared to the Kontur-2 mission.

Communication set-up for the implemented scenario

As shown in the target scenario in Fig. 6.11a, the vision is to teleoperate an orbital robot in the LEO orbit using a GEO relay satellite. To simulate this with the OOS-Sim facility, the signals from the haptic station at DLR were transmitted to LRT ground station in Garching, Germany through normal UDP link, which were then transmitted to the ASTRA relay satellite through Ku-band link. The signals from the ASTRA satellite were relayed

back to LRT and then to the OOS-Sim facility through UDP link. The feedback forces and the visual feedback signals from the facility were reflected back through the same, ground station-ASTRA-Ground station-DLR path. The one-way link characteristics are shown in Fig. 6.12. Note that the two-way link resulted in a delay of 540 ms.
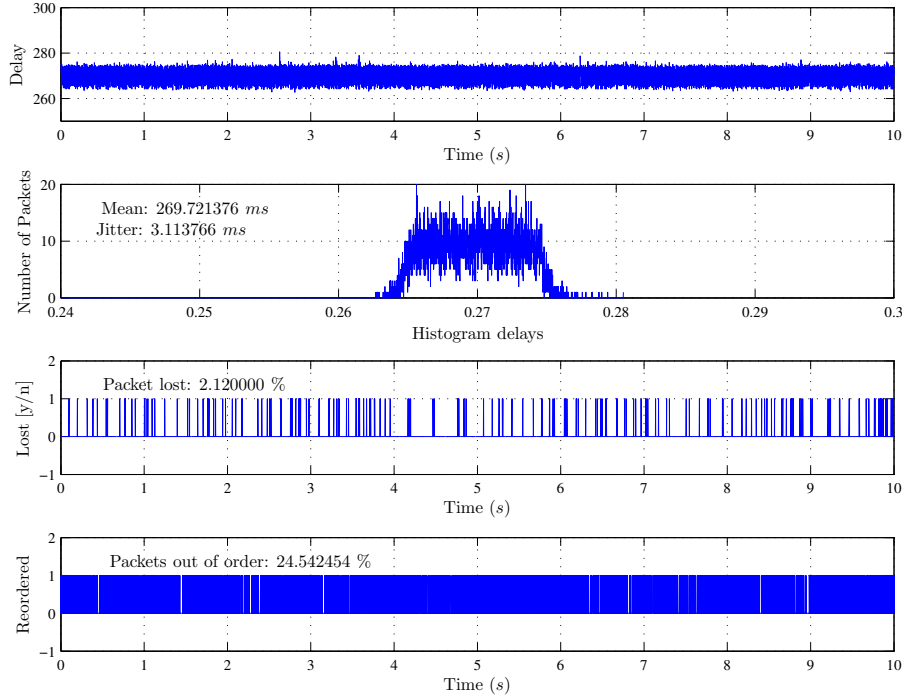
Figure 6.12: One-way communication link features of the relay satellite

Bilateral teleoperation of orbital robot

Since the focus of the research work is on the teleoperation part of the scenario, the dynamics of the simulated satellite and the stability properties related to the control of the free-floating systems will not be addressed here in this thesis. The readers can find complete details of the satellite dynamics and control in the works [DSMB+19] and [ABDS+16]. The bilateral control was the same as shown in Fig. 6.4, which was passivated with TDPA as shown in Fig. 6.6. The teleoperation part in the overall shared control framework is summarized in Table 6.2.

Experiment results

In this section, two experiments are presented that focus on the proof of feasibility of teleoperative grasping and stabilization of a client satellite. In all experiments the ASTRA-link between the haptic device and orbital robot devices are considered twice, which gives a total round-trip delay of around 540 ms. All motions are presented in the inertial frame and zero positions represent the initial positions of the devices. The simulated mass of the client satellite was 280 Kg and it had 3 translational DoF. The mass simulated for the servicer satellite was 740 Kg and its inertia is distributed on its principal axis with components each of 900 Kgm^2.

The first experiment (see Fig. 6.13) presents the 6 DoF position tracking performance

Inp. Device	LWR	ACS	Robot	Task
BC	$[V_d, F_h - F_c, F_e]$ 4-channel	–	LWR on OOS-Sim	Grasping
Delay	540ms			of client
Packet loss	26 %			satellite
Part of shared control framework				
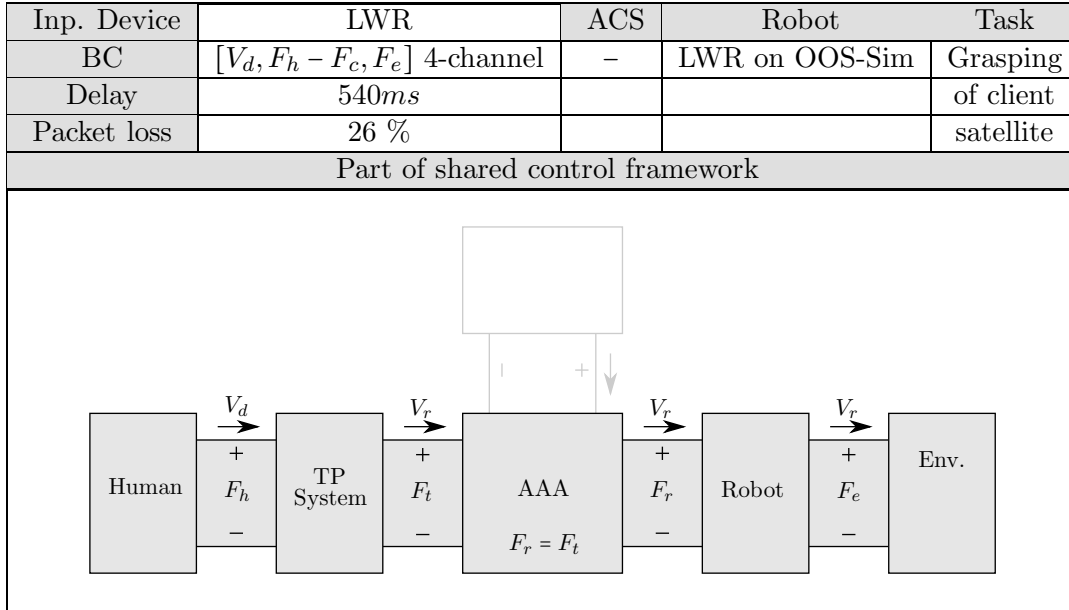
Table 6.2: Scheme of application in OOS

of haptic device and the free-floating orbital robot during free motion without external contacts.
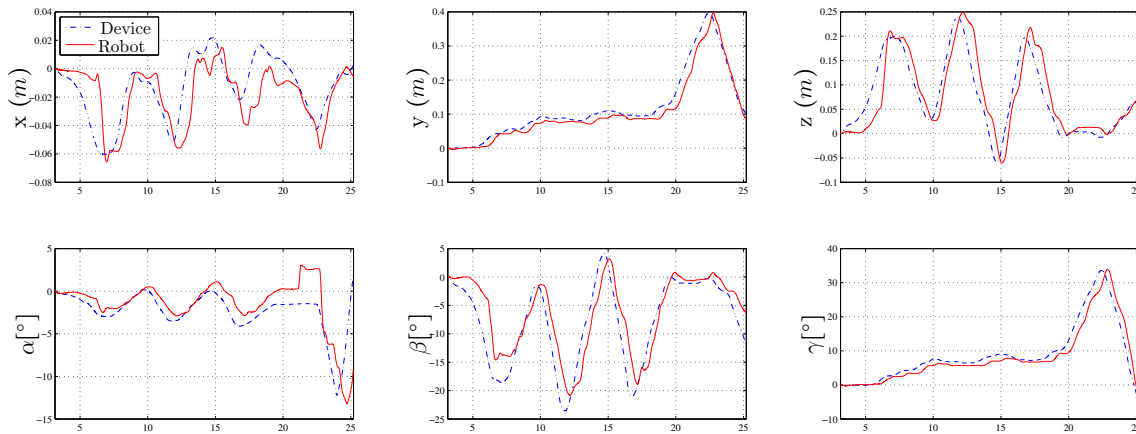
Figure 6.13: Experiment 1: Position and orientation of haptic device and orbital robot in a free motion using the ASTRA-link

Experiment 2 in Fig. 6.14 presents the teleoperative grasping and stabilization procedure with ASTRA-link communication. Both, servicer and client satellite motions are simulated by the industrial robots. The desired final state is a steady coupled system of servicer and client satellite. For the sake of easier interpretation, the motions of servicer manipulator and client are visualized in the 3D plot in Fig. 6.15 (22 $s - 36 s$). The dense points visualize the position of the final state (almost zero relative motion of the satellites).
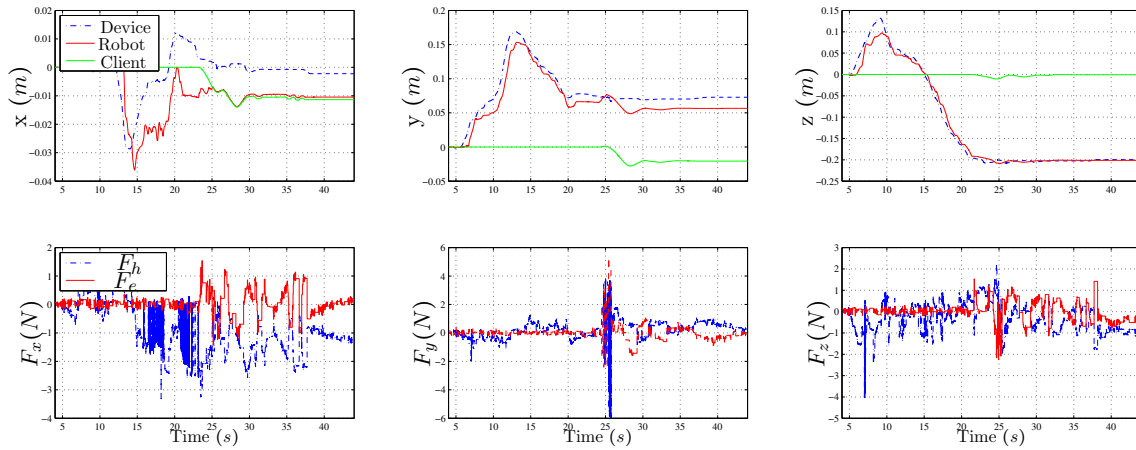
Figure 6.14: Experiment 2: Tracking, grasp and stabilization of the client with force feed-back using the ASTRA-link
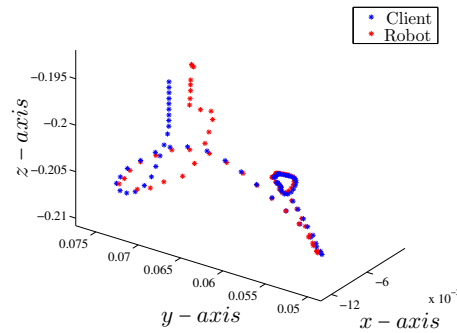
Figure 6.15: Experiment 2: 3D Plot of Grasping and Stabilization

Discussions

Considering that the average round-trip delay is 540 ms, the tracking performance is satisfactory in Fig. 6.13. During time $0\ s - 20\ s$ the human operator at the haptic device commands rotations around the Y-axis and vertical motions to the orbital robot. From time $20\ s - 25\ s$, a translational motion along the Y-axis and rotations around the X and Z-axis is commanded. Despite minor overshoots, even fast motions ($10\ s - 12\ s$) are executed by the orbital robot as demanded. In experiment 2, once the client is grasped, the human operator can act as a damper through impedance matching in order to let the relative motion of the satellite converge to almost zero. That means that the human operator receives good feedback of the oscillatory motions despite the high round-trip delay. Therefore, the operator is able to stabilize the satellites' motion through impedance matching. The haptic device and orbital robot position tracking is satisfactory in free motion and during the stabilization phase. It can be noted that the forces measured at the robot's end-effector, trigger the motion of the client satellite and the operator feels this force after an interval of the round-trip delay. In spite of the minor tracking errors in the first experiment, the operator present in the loop enables proper corrective measures and compensates for the positions drifts. This leads to a successful grasp as proved in the grasping experiment, where the grip can be regarded as perfect since the positions of client and orbital robot match very well as soon as the client is gripped. The results of

the experiments carried out in the OOS-Sim facility verify the feasibility of approaching, grasping and stabilizing of a free-floating satellite using teleoperation with force feedback under large and varying time-delays using the implemented bilateral controller.

Future work planned in the on-orbit servicing scenario is to include adaptive shared control developed in this thesis, for the approach and grasp phases. The ACS uses the camera attached to the end-effector of the manipulator for a vision-based tracking system, which works based on feature detection as shown in Fig. 6.16. When the end-effector reaches close to the grasping point, the estimation of the client pose fails due to the absence of detectable features and measurement degradation due to noise [SADS+15]. A teleoperator can then take corrective measures or complete the task in pure teleoperation mode by reducing the AA factor for the ACS as presented for the aerial scenario in Section 6.2.1.
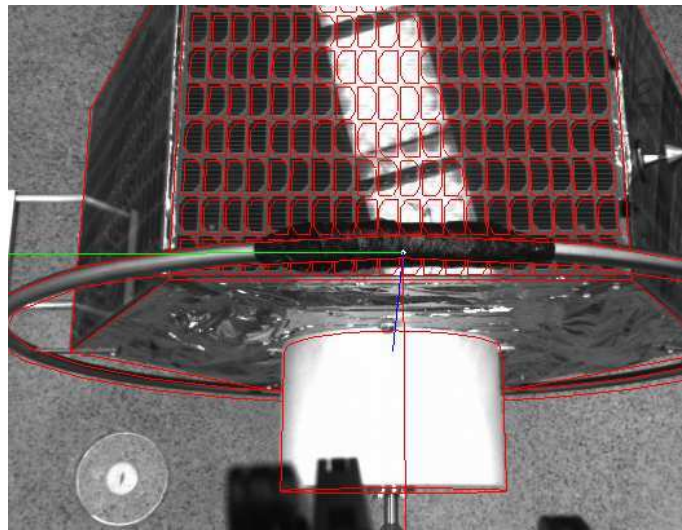
Figure 6.16: Vision-based ACS for on-orbit servicing

6.1.3 In-Orbit Robotic Assembly

With fast-paced advancements in technology, robotic assembly need not be limited to terrestrial applications. To reduce the cost and payload volume of satellites launches [Spa], the assembly of satellites can now be realized in in-orbit factories. Although manufacturing in the international space station (ISS) has been recently tested with 3D printing [MN17], robotic assembly of satellites has not been done yet. Manufacturing in space brings several benefits: structures need not be designed to withstand launch shocks and vibrations, satellites can be repaired and re-purposed in space, and they can be produced on demand [TMO+17], with highly customized production to be made profitable [Dor15]. However, a large number of challenges arise with this concept of in-orbit robotic assembly. Since satellite components are really sensitive, each step during manufacturing and assembly must be tested to avoid inaccuracies [Ue18]. Although autonomous robots are capable of implementing sensitive and complicated tasks [NSSB16, T+02, DSDLR+07], a human supervision in the control loop is preferable to appropriately address unforeseen changes in the environment or robot behavior (see [I+03, T. 8.1]).

To this end, Space Factory 4.0 [WMPH+18], aimed at developing a shared control system which allows for teleoperation of the assembly robot by a human operator, providing force feedback with the support of virtual fixtures (VF, [AHO03, Oka04]). The concept of the Space Factory 4.0 project is presented in Fig. 6.17. A human operator on ground teleoperates a robot in the LEO orbit, via a relay satellite in the GEO orbit, which leads an unlimited window of operation as described in Section 6.1.2. The task for this feasibility project is the assembly of a cube-sat, to be more precise, the insertion of circuit boards with highly sensitive 50-pin connectors, as shown in Fig. 6.18.
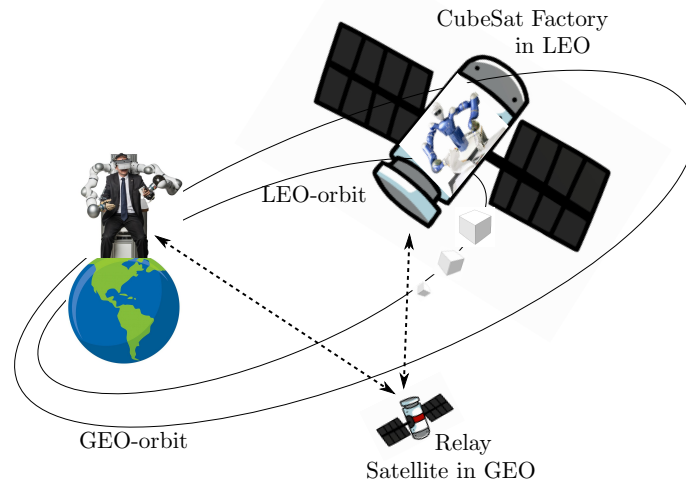
Figure 6.17: Concept of Space Factory 4.0.

Space Factory 4.0 was a joint venture from 2017 to 2019, with partners from a wide array of expertise. The project was funded by the German Aerospace Center (DLR) and the German Federal Ministry for Economic Affairs and Energy (BMWi) and was coordinated by the Technische Universitaet Darmstadt. Robotics and Mechatronics institute of DLR (DLR-RMC) was responsible for the shared control implementation. Other partners were Technical University of Munich (TUM), the Zentrum fuer Telematik (ZfT), OHB Systems, Von Hoerner and Sulger (VHS) and Telespazio VEGA.

Circuit board A
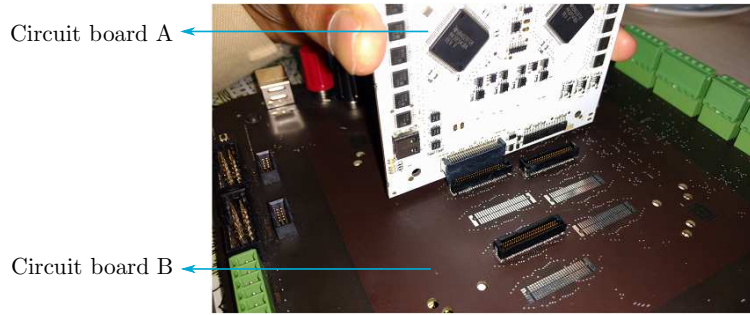
Circuit board B

Figure 6.18: Circuit boards with 50-pin connectors

Shared control for Space Factory 4.0

Insertion of the circuit boards using robotic teleoperation is significantly challenging due to its sensitivity and precision demanded. The male connector was on the circuit board A, and the female connector was on circuit board B as shown in Fig. 6.18. The allowed angular tolerance for a successful insertion was 2 degrees; the allowed position tolerance was 0.7 mm; about 3 N of force in the direction of insertion was required to achieve the connection. To enable the operator to complete the task, the shared control framework used in Space Factory 4.0 project availed virtual fixtures for both translational and rotational guidance. The experimental set-up used in the project is shown in Fig. 6.19.

Camera 1 view   Camera 2 view

Human and haptic device   Robot and task board   Virtual fixtures
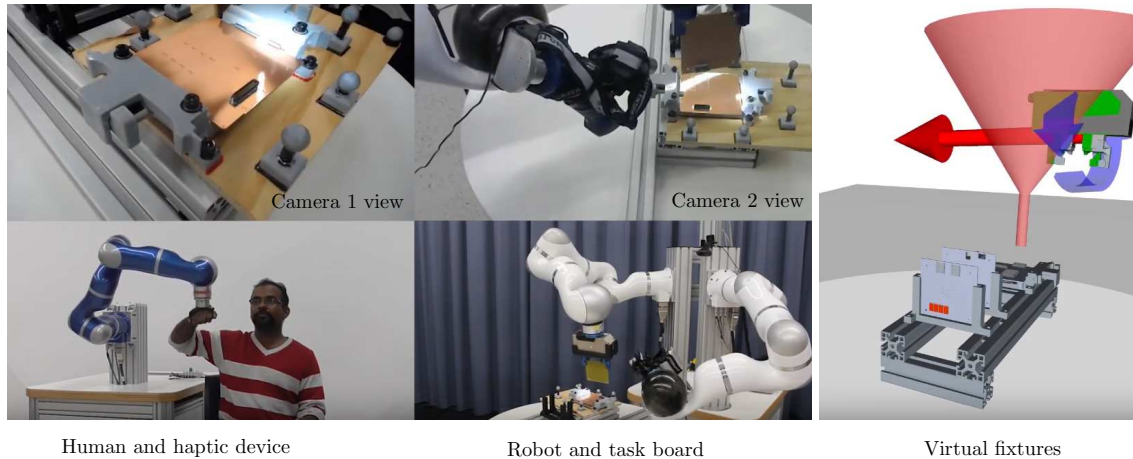
Figure 6.19: The experiment set-up in the Space Factory 4.0 project.

The signal flow diagram of the shared control is presented in Fig. 6.20. The position of the haptic device is commanded to the robot position controller, that produced force F_t. The virtual fixtures guided the robot end-effector to the target pin with the force F_a. The final force commanded to the robot was a weighted sum of the these two forces.

$$F_r = \alpha_t F_t + \alpha_a F_a, \tag{6.99}$$

where α_t and α_a are the AA for the teleoperation force and virtual fixtures forces, respectively. In this project, constant value of 0.5 was assigned to the two AA factors. Since the aim of the project was the feasibility test for such robotic assembly, there was no delay considered in the communication link between the operator and the robot. The feedback controller availed the explicit force controller, which matched the measured human force

F_h to the desired force $F_e + F_a$, that is, the sum of the interaction forces between the robot with the environment, and with the virtual fixtures. The overall system was passivated and stabilized as described in Section 3.3. The shared control framework used in this project is summarized in Table 6.3.
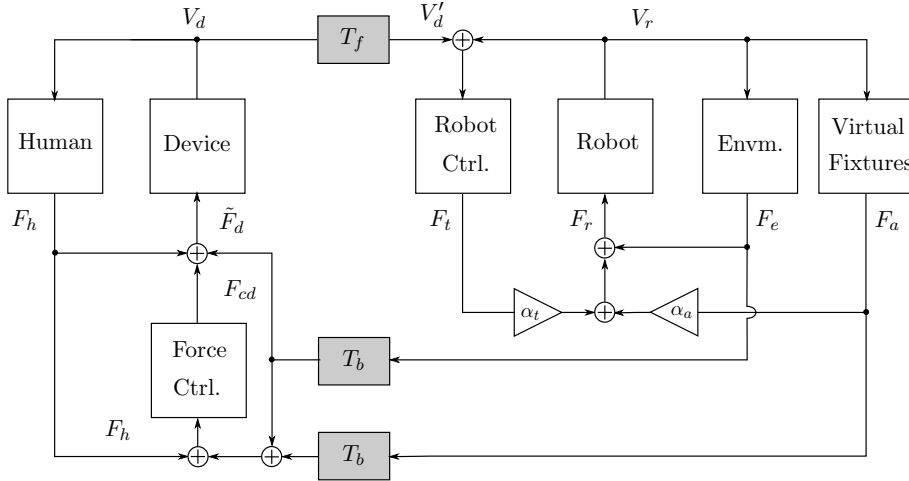
Figure 6.20: Signal-flow diagram of the proposed shared control framework.

Inp. Device	LWR		ACS	Robot	Task
BC	$[V_d - F_a, F_e]$ 3-channel + EFC		Virtual fixtures	LWR	Grasping
Delay	$0ms$				and insertion
Packet loss	0 %				of circuit board
Part of shared control framework					

Table 6.3: Shared control scheme for in-orbit assembly in Space Factory 4.0.

Experiment results

The positions and forces of the operator and robot during the task are shown in Fig. 6.21. The two phases of the task, namely, grasping and insertion are separated in the plot. The positions of the haptic device and the robot are represented by X_d and X_r, respectively. The force perceived by the operator is represented by F_h and the forces sensed by the robot

due to its interaction with the real environment and the virtual fixtures are represented by F_{ea}. It is important to note that the entire task was completed within 80 seconds.
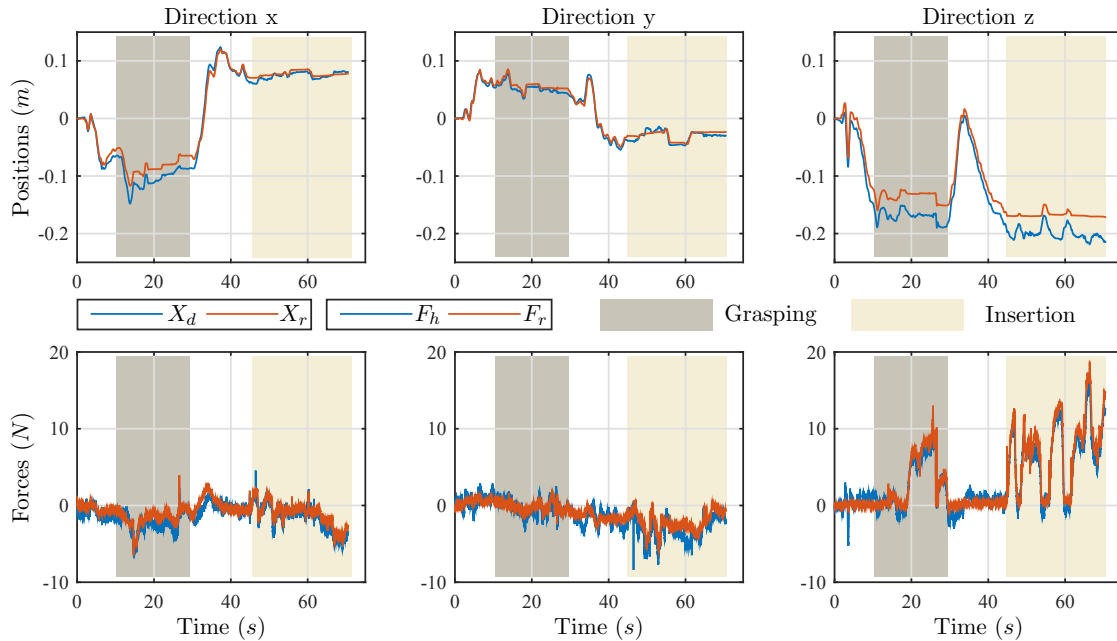
Figure 6.21: Positions and forces during the assembly task.

Discussion

The position controller at the robot side enabled high precision position tracking. This led to accurate grasping and more importantly, the fine placement of the circuit board to the insertion point. It has to be noted that the explicit force controller at the operator side enabled the accurate force tracking of the desired force coming from the robot (very low during free motion and accurate tracking during contacts with the real environment or the virtual fixtures). Accurate feedback of the forces is a requirement in such sensitive tasks, the absence of which could lead to the damage of the pin connectors.

Although communication delay was not considered in this project, the feasibility of the circuit board insertion in the presence of delays looks positive in the light of the experiments presented in Section 3.3 and Chapter 5 using the explicit force controller. If at all the GEO link is used, which presents a delay of around 600 ms might hinder the successful execution of such sensitive tasks, note that the grasping and insertion was completed in less that 80 seconds. This promises that multiple insertions could be completed using direct S-Bank link which provides an operation window of 10 minutes as described in Section 6.1.1.

On-going work in the in-orbit assembly is to adapt the AA factors online with artificial intelligence and machine learning, using the stable and transparent shared control framework developed in this thesis. This is the main focus of the current project *AI-In-Orbit-Factory* [D⁺21].

6.2 Applications in Terrestrial Domain

The teleoperation and shared control framework developed in this thesis are applicable when the distance between the operator and the remote robot are large. Although space is an apt domain for these methods, our research work also focus largely to solve several problems on Earth. Application of robotics to support human workers in hazardous areas is a main objective of our research. The work in this thesis has been applied in industrial inspection and maintenance using aerial manipulators. The suspended aerial manipulator (SAM) was used for this and will be briefly described in Section 6.2.1 followed by the experiments in an industrial mock-up.

6.2.1 Aerial Inspection and Maintenance

The use of aerial manipulators for reaching locations that are dangerous or inaccessible from the ground presents a crucial application scenario for robotics. Aerial manipulation uses aerial robots equipped with arms with specific tools to perform tasks such as assembly or contact inspection. An example of industrial environments is shown in Fig. 6.22, where the pipelines are at high elevations from the ground. As in orbital robots, it is a challenging problem, mainly because of aerodynamic influences and fast reactive dynamics of the aerial vehicle [OHF+18].

Figure 6.22: Example of an hazardous industrial environment (Image source: [OHF+18]).

Due to the challenges associated with aerial manipulation in real-world scenarios, most works in this field were limited to indoor experiments till recently [OTS+21]. Some of these works presented cooperative transport and assembly using several aerial vehicles [MFK11], force application [FNM+14] and drawer opening [KSK15]. The limited payload capabilities allowed for only small and light robotic arms on these aerial systems. Opposed to this, an LWR was attached on a helicopter in the European Union (EU) project ARCAS allowed for much higher payloads and force applications with the environment [KKAS+13]. Although the large rotor blades of the helicopter allowed for these stronger functionalities, the same large rotor size came as a limitation for accessing really narrow structures. So in the EU Horizon 2020 project AEROARMS [OHF+18], a new platform was designed to circumvent these limitations. The DLR's suspended aerial manipulator (SAM), shown in Fig. 6.23, is an octacopter equipped with an LWR [SKB+19]. Instead of attaching a robotic manipulator directly to an aerial carrier, it is mounted on the active platform which is suspended on the carrier by means of a cable. As a result, higher safety can be achieved

because the aerial carrier can keep a distance from the obstacles. For self-stabilization, the SAM is equipped with two actuation systems: winches and propulsion units with 8 rotors. The oscillation damping of the aerial base against winds and reactive dynamics are presented in [SKC+20] and the whole body control and teleoperation is published in the works [CSKO20, CYX+21]. This section only shortly covers the adaptive shared control as an application of the framework developed in this thesis.

Figure 6.23: Suspended aerial manipulator (SAM) platform

Shared Control of SAM

For the outdoor experiments, two tasks were chosen, namely, peg-in-hole and opening of a valve, while the platform self-stabilized the base. The tasks are shown in Fig. 6.24. Both these tasks demanded high accuracy for successful completion. For the peg-in-hole task, the square peg of side 4.5 cm had to be inserted into a square hole of 5.0 cm, which resulted in a desired accuracy of 2.5 mm in translation and less than 7 degrees in rotation for a vertical insertion. A newly designed tool for opening the valve reduced the accuracy requirements to 10 mm in translation and less than 24 degrees in rotation for a vertical insertion. These requirements are graphically presented in Fig. 6.25. The additional challenge for the valve opening was the desired torque application of up to 2.0 Nm in the yaw axis.

The shared control methods developed in this thesis were applied and validated in [LBS+20] for indoor experiments. The virtual fixtures used in the Space Factory from Section 6.1.3 formed the vision-based ACS and produced wrench $\boldsymbol{F_a}$ to restrict the motion of the arm within a cone which directed the tools to the desired targets with the correct orientation. The teleoperation system produced a passive wrench $\boldsymbol{F_t}$ and the weighted sum of wrenches from the two systems were finally commanded to the robot. Since the accuracy of the autonomous controller was highly affected in the field experiments, the authority allocation factor for the virtual fixtures was modified by the operator. When the camera measurements were noisy and the virtual fixtures produced noisy commands, the operator could reduce the virtual fixture AA α_a and complete the task himself. On the other hand, if the camera measurements were not noisy, the operator availed the support
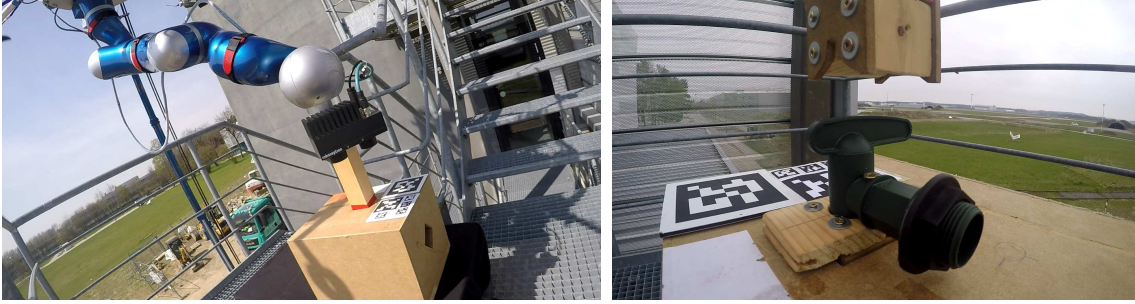
Figure 6.24: Peg-in-hole task (left) and valve opening task (right).
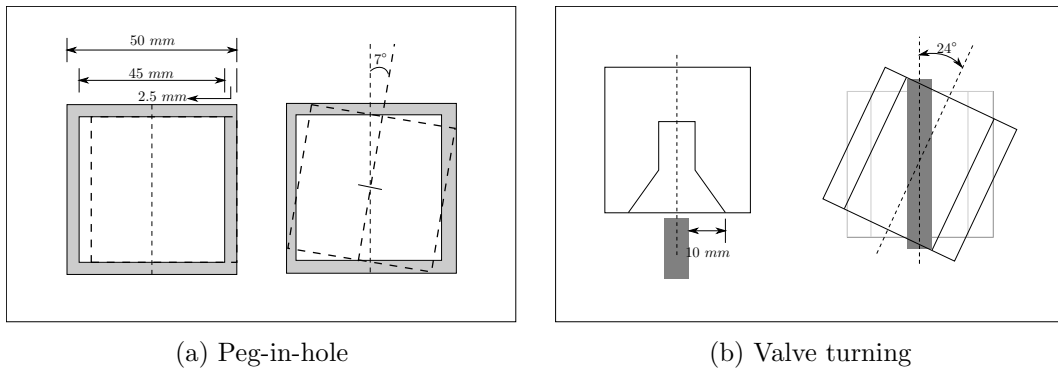
(a) Peg-in-hole

(b) Valve turning

Figure 6.25: Accuracy requirements for tasks

from the virtual fixtures by increasing α_a, which reduced the physical and mental effort demanded from the operator. The part of the shared control framework applied for aerial inspection and maintenance is summarized in Table 6.4. Note that only the adaptive shared control part of the entire control architecture is explained here. More details on the the visual servoing and whole-body control of SAM can be found in [LBS+20] and [CYX+21].

Experiment results

The operator used the Lambda device to teleoperate the SAM LWR and the Kontur-2 joystick presented in Section 6.1.1 to modify the AA factors. The view of the ground control station is shown in Fig. 6.26. The operator screen provided him with the camera views from the SAM platform and also the virtual reality views of the task board and the tools along with the virtual fixtures as shown in Fig. 6.27. The wireless communication link between the haptic device and the SAM platform had a round-trip delay of around 10 ms. A position-computed 2-channel architecture from [CYX+21] was used for the teleoperation controller.

1. Valve opening: During the approach phase, the operator got the support from the virtual fixture to place the tool slot properly on the valve. Here the AA factor for the virtual fixtures was $\alpha_a = 1$. Once the tool was placed exactly on the required spot, the virtual fixture gains were reduced to $\alpha_a = 0$ so that the operator can rotate the tool along the valve axis freely. Else, the torque commanded from the virtual fixtures would act against the teleoperation torque, which would demand a lot of physical effort from the operator. The change in α_a during the different phases of the task is shown in

Inp. Device	Lambda	ACS	Robot	Task
BC	$[V_d, F_c]$ 2-channel	Virtual fixtures	LWR	Peg-in-hole and
Delay	$10ms$		on SAM	valve turning
Packet loss	0 %			
Part of shared control framework				
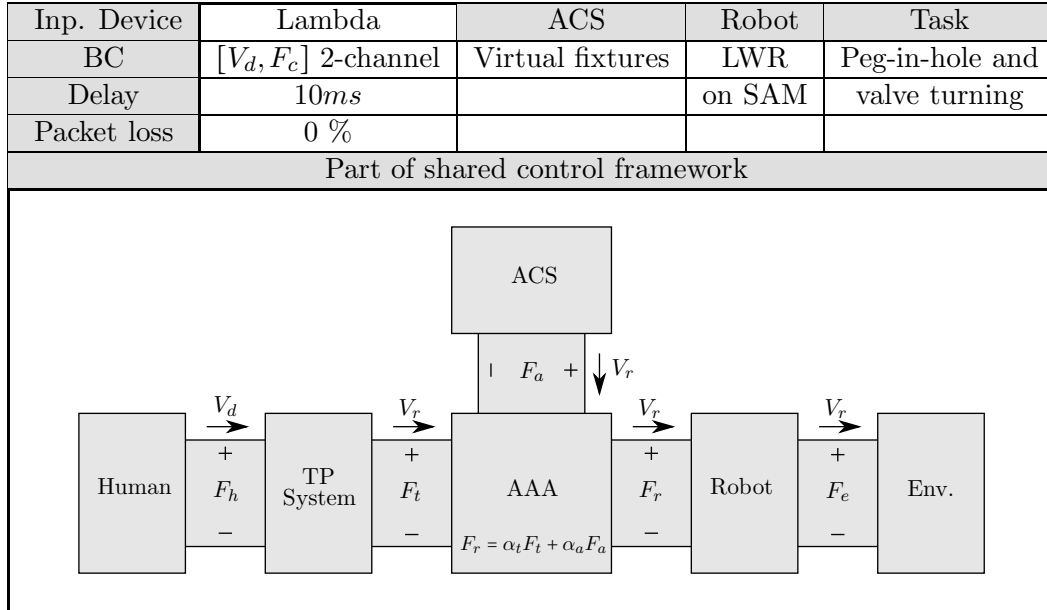
Table 6.4: Shared control scheme for aerial inspection and maintenance
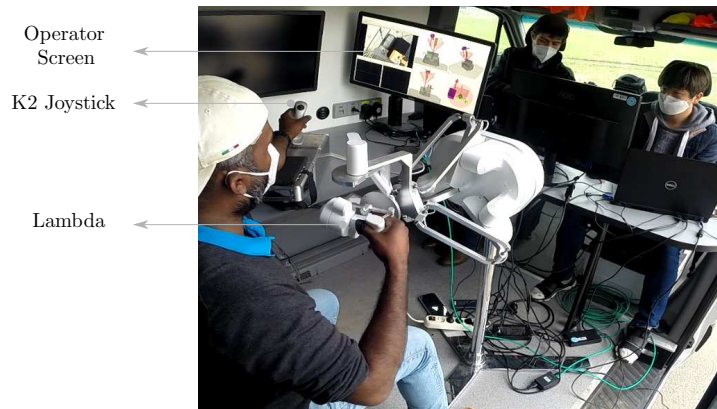
Figure 6.26: View of the control station

Fig. 6.28 in the middle plot. The position of the end-effector and the torques measured during valve opening are shown in Fig. 6.28. Note that on the top plot in Fig. 6.28, the commanded and desired position of the yaw axis of the robot is shown. The robot followed the commanded position, which enabled the successful task completion. The middle plot shows the variation of α_a from 1 to 0, which is done by the operator based on his visual feedback. The bottom plot shows the torque measured at the last joint of the robotic manipulator, which goes up to 2 Nm during the valve opening. To validate the robustness of the adaptive shared controller, the valve opening was implemented 5 times during the field experiments.

2. Peg-in-hole: The adaptation of AA factor of the ACS for the valve opening task was implemented so that the operator can easily turn the valve without the opposing torques from the virtual fixture. On the other hand, for the peg-in-hole task, the need for adaptive shared control is motivated by degradation in camera measurements during real outdoor experiments. When the peg was in the vicinity of the hole, a simulated noise was added
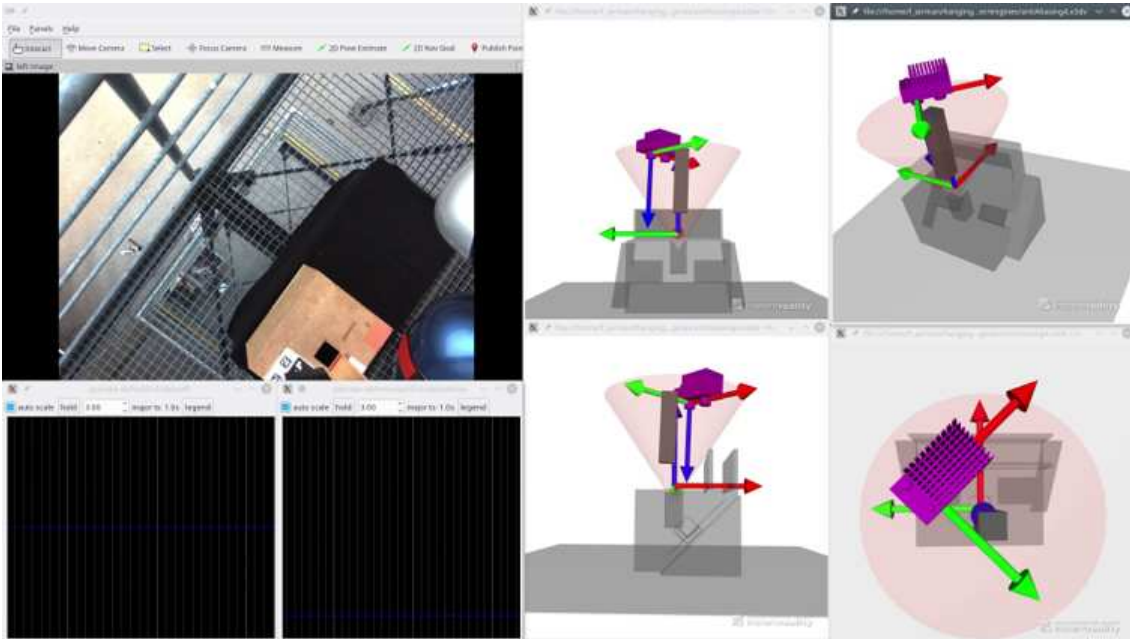
Figure 6.27: View of the operator screen during aerial manipulation
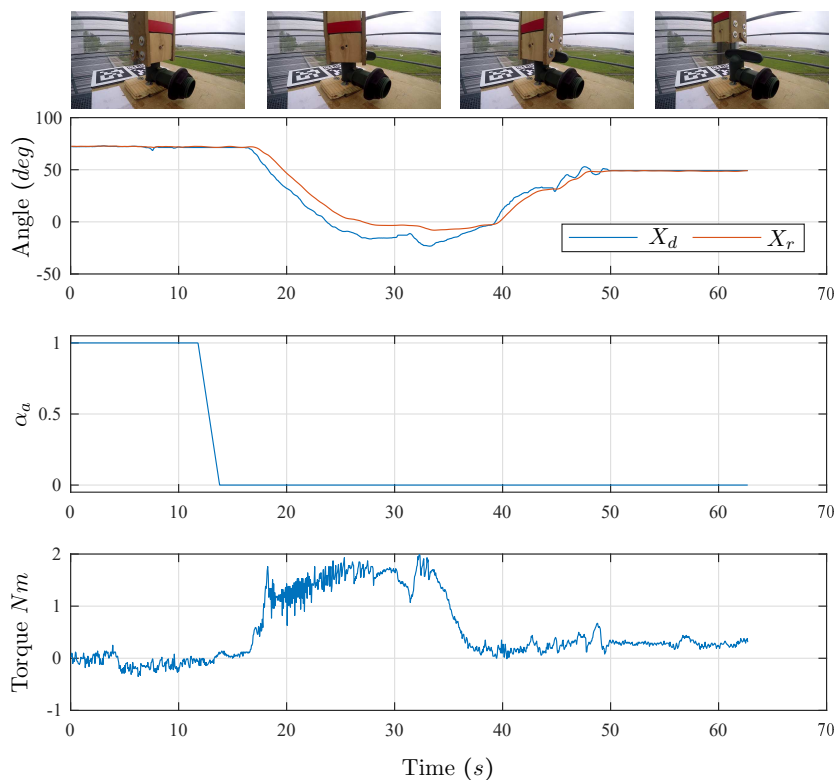
Figure 6.28: Position, torque and α_a for single valve opening

to the camera measurements to reproduce similar noise behaviors for all the experiment runs. Without the adaptation, the camera-based virtual fixtures produced highly noisy forces which made the task execution impossible. When this happens, the operator could reduce the α_a gain for the virtual fixtures and complete the task with pure teleoperation.

The noisy camera measurements and the change in α_a gain are shown in Fig. 6.29.
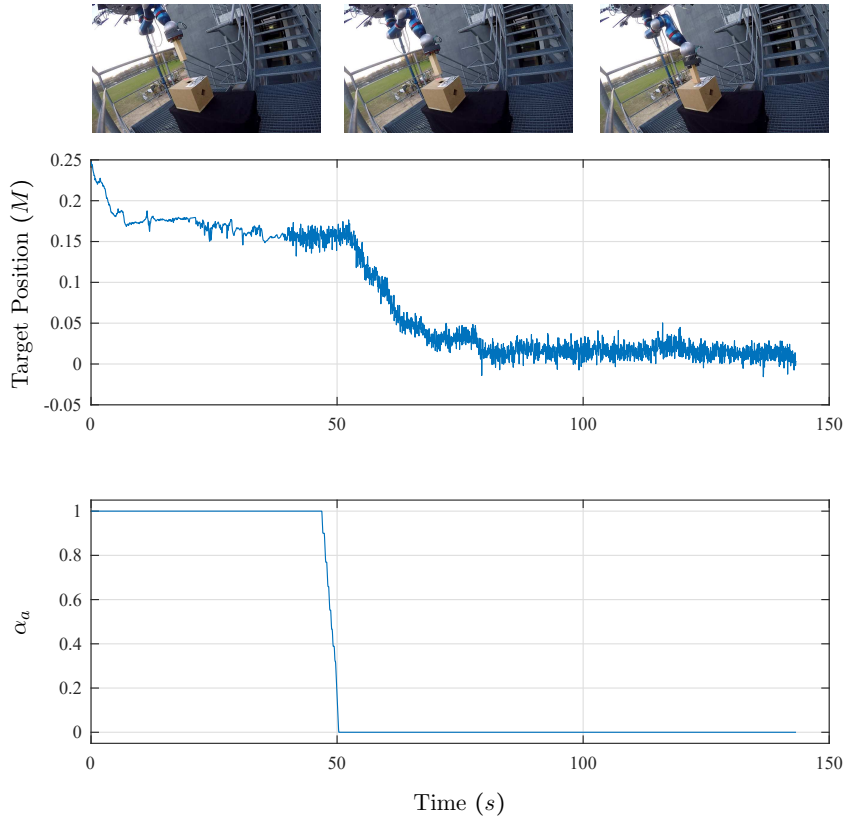
Figure 6.29: Noisy camera measurement and α_a for peg-in-hole

To validate the robustness of the implemented shared control system in real world scenarios, the peg-in-hole task was tested for a total of 24 times. This included 8 runs of pure teleoperation (TP), 8 runs of fixed shared control (FSC, with fixed AA factors) without adding extra noise, and 8 runs with adaptive shared control (ASC), in which the operator reduced α_a value for simulated noisy camera measurements. With all the control approaches, the task was completed successfully in all runs. The runs are shown in Fig. 6.30. The plots show the motion of the peg from a distance of 25 cm above the hole to the point of its first successful insertion.

Discussions

To objectively measure the benefits of the shared control approaches with pure teleoperation, time of completion of the task is used as a performance index. The time for the robot tool to move from 25 cm above to hole to the first insertion was measured for all the runs and their means were calculated for each of the approaches and are summarized in Fig. 6.31. The mean time for fixed shared control was 37 % lower than that for pure teleoperation. This was expected since the operator received support from the virtual fixtures at all points of time. On the other hand, the adaptive shared control approach took 24 % more time, compared to pure teleoperation. This increase in time can be attributed to the time elapsed for the operator to notice the degradation of camera measurements and reduce the α_a gain from 1 to 0. In spite of the larger times needed for the task completion with adaptive shared control, the objective of the task was achieved, which was otherwise
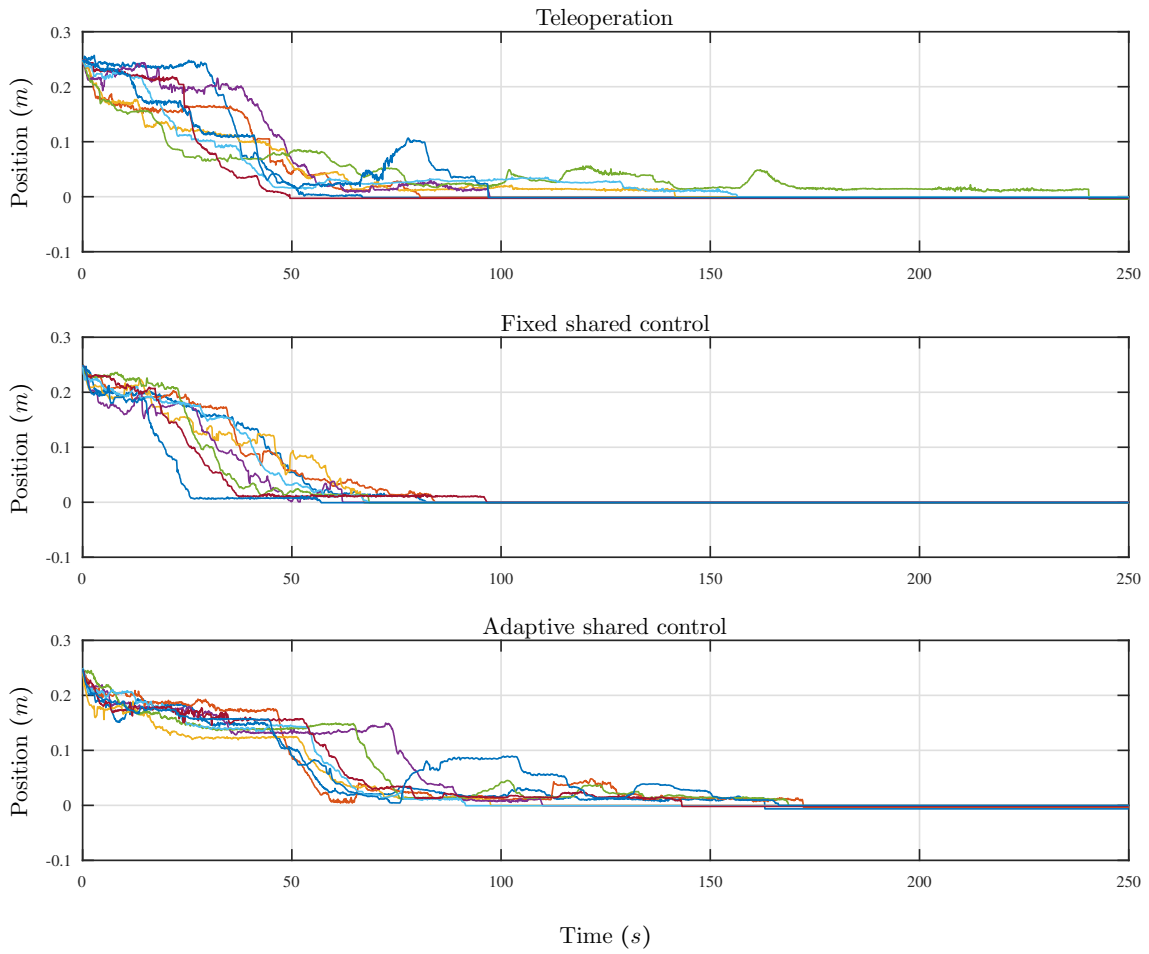
Figure 6.30: Position of tool end for peg-in-hole task

impossible without the possibility for reducing the AA factor of the ACS.
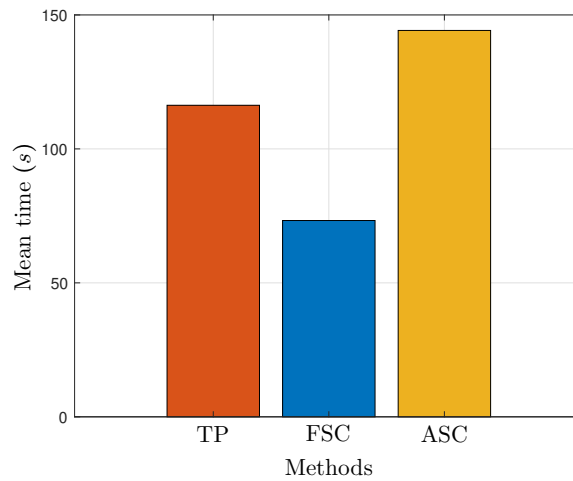
Figure 6.31: Bar graph of mean times for peg-in-hole trials

6.3 Applications of Secondary Contributions

In addition to the aforementioned primary contributions of this thesis, several other secondary contributions were made during the research period. Many of them were used in multiple domains, in practical projects and led to second authorship of several publications. The main contributions in these domains (other than adaptive shared control, which is the main focus of this thesis) are related to ensuring passivity and stability of complex robotic systems using Time Domain Passivity Approach (TDPA). The author would like to highlight some of these secondary contributions in this section.

Whole-body Control of Humanoid Robot

Humanoid robots are applied in a wide area of scenarios, where wheeled robots are not equipped to navigate. The balancing of the whole body and using feet to navigate make it a particularly challenging problem, especially on deformable grounds. One of the secondary contributions made during the research done for this thesis focused on ensuring passivity and stability of the torque-controlled humanoid robot TORO while navigating through deformable grounds, as shown in Fig. 6.32. The author contributed to the derivation of the electrical network representation of the humanoid robot and its interactions with deformable grounds and the application of TDPA to stabilize these interactions. The work was published in [HBRG+18] and also in the thesis [Hen20].

Figure 6.32: Humanoid robot walking

On-ground Simulation of Satellites

As explained in Section 6.1.2, the use of satellites equipped with robotic arms is a promising technology for On-Orbit Servicing (OOS) missions. In order to reduce the risks during real missions, the control algorithms need to be tested on ground, prior to the launch. The hardware-in-the-loop facility OOS-Sim, mentioned in Section 6.1.2 employs two admittance-controlled industrial robots equipped with force-torque sensors to simulate model-based satellite dynamics, interaction dynamics and micro-gravity conditions present in outer space as shown in Fig. 6.33. In such kind of facilities with robotic simulators, delays in the control loop and discretisation effects can violate passivity conditions which can lead to unstable behaviors of the simulated satellites. The author of this thesis

contributed to the passivation techniques for considering delays and discretisation effects for stable simulation of satellite dynamics and their interactions. TDPA was used in these scenarios to ensure stability and this led its application in several projects and multiple publications [DSBS19, DSBG$^+$18].

Figure 6.33: On-ground simulation of satellite dynamics

Partitioned Shared Control for OOS

In addition to the secondary contribution in OOS related to on-ground satellite dynamics simulation, the author also contributed to a partitioned shared control approach in [MBDSO21a]. The developed partitioned shared control approach enabled separate controllers for both, the base of the fully actuated satellite and the robotic manipulator attached to it, as shown in Fig. 6.34. The end-effector of the manipulator was teleoperated with haptic feedback and the base of the satellite regulated itself within a safe region to avoid collisions with the environment (for example, with the target satellites). The method ensured passive and stable interaction with the environment, which enabled prolonged and sliding contacts. The main contribution from the author in this work was in the development and validation of the bilateral controller used for teleoperation.
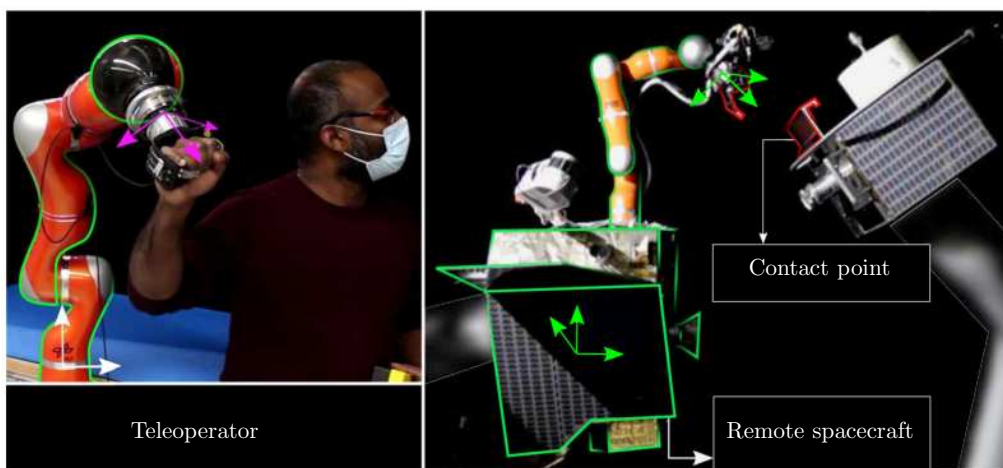
Figure 6.34: Partitioned shared control for OOS

Compliance Control of Helicopter Manipulator

For the EU Project ARCAS, a helicopter equipped with LWR was used for aerial manipulation, as shown in Fig. 6.35. This enabled higher payloads compared to the then existing aerial systems [KKAS+13]. In order to introduce compliance in the overall system (helicopter and manipulator), passivity concepts were used to ensure stable interactions of the manipulator with the environment. The author contributed to the identification of the passivity violating controller terms using electrical network representation and the resulting application of TDPA to ensure stable environment interactions. This work was published in [KBDS+18].

Figure 6.35: Compliance Control of Helicopter Manipulator

Explicit Force Control of Robots

The final domain where the thesis research contributed is in the field of interaction control of robotic manipulators. Explicit force controllers (EFC) in robot enables the application of a desired force F_d on the environment by comparing it with the force F_e measured using a force-torque sensor at the robot end-effector as shown in Fig. 6.36. Although EFC enables precise and high bandwidth control, the system is more vulnerable to instabilities caused by non-collocation in the sensing-actuating loop. A novel method for stabilizing EFC using electrical network and TDPA was developed by the author in [BJA+17] and it was later validated on a redundant manipulator in [JBRK17]. This idea was later used in bilateral controllers with EFC presented in Section 3.3.
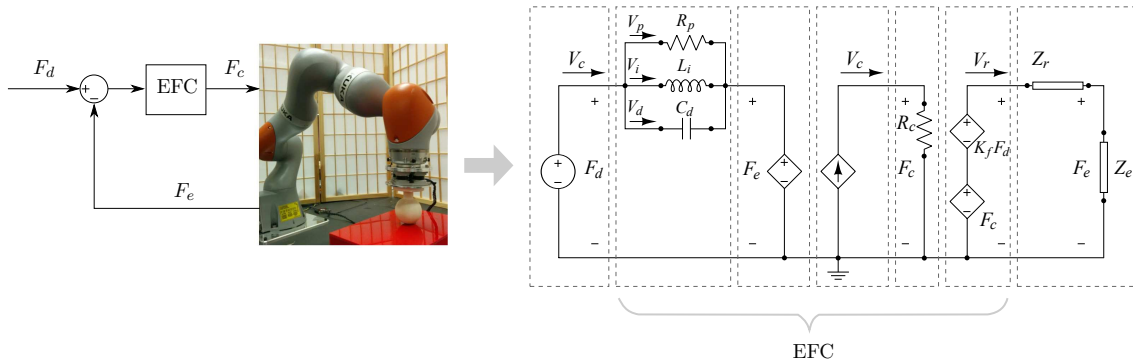
Figure 6.36: Explicit Force Control of Robots with TPDA

Summary

This chapter presented certain practical applications of the work developed during the thesis research. Most of the applications were part of international projects and the methods were validated on real robotic hardware. Plans to extend the work and possibilities of future applications are mentioned. In addition, the major secondary contributions from the author in robotic domains that are not in the main focus of this thesis are shortly summarized.

On-going project *AI-In-Orbit-Factory*, adapts the AA factors using artificial intelligence, thanks to the modular and flexible framework developed during this thesis. Future work includes the application of the adaptive shared control framework for grasping of client satellites for on-orbit servicing, in case the camera-based ACS fails. This is a practical solution for a practical problem which can act as a reliable fall-back approach for space-projects.

Conclusions

In the current age, the scientific endeavors are aimed towards, among others, improvement of human safety and reduction in manufacturing costs, for both terrestrial and interplanetary activities. This is evident in medical, nuclear, industrial and space domains, where inter-alia, robotic technologies play a prominent role. In spite of the rapid progress in artificial intelligence, complete autonomy of robots is still to be achieved. Thus, human-robot collaboration will continue to be of relevance in the foreseeable future.

With this idea in mind, my research improved the synergy between humans and robots with the shared control paradigm. This combines human decision-making and benefits of automatic control systems (like precision and repeatability), while using robots in remote and dangerous environments. The work focused on a specific shared control approach, namely mixed-initiative in which the human operator and autonomous system work together with adaptable control authorities. In past works, focus was laid on the methodologies for authority allocation (AA) and the benefits in terms of task completion time and operator comfort. From a control perspective, the stability of AA and of teleoperation were considered separately without focusing on transparency of the teleoperation system. Like in pure teleoperation, a transparent haptic feedback in shared control has proven to improve operator awareness and performance. There was no unified method to ensure the stability of AA in haptic shared control while enhancing transparency of the stable teleoperation system.

This thesis filled the identified research gaps from a control perspective and developed a framework for adaptive authority allocation (AAA) in shared control ensuring stability of the overall system while enhancing the teleoperation transparency. To this end, the thesis was structured in an incremental flow of theoretical treatment, which was validated by simulations and hardware experiments.

After describing the fundamental theoretical tools, Chapter 3 presented two methods to enhance the transparency of teleoperation systems. The first method is a local force feedback controller with non-linear gain modification, which reduces the perceived inertia of the haptic device. Its model dependency was removed by an explicit force controller stabilized with time domain passivity approach. Finally, the passive coupling reference (PCR) approach was proposed to stabilize arbitrary user-defined feedback controllers in time-delayed teleoperation using existing passivity-based tools.
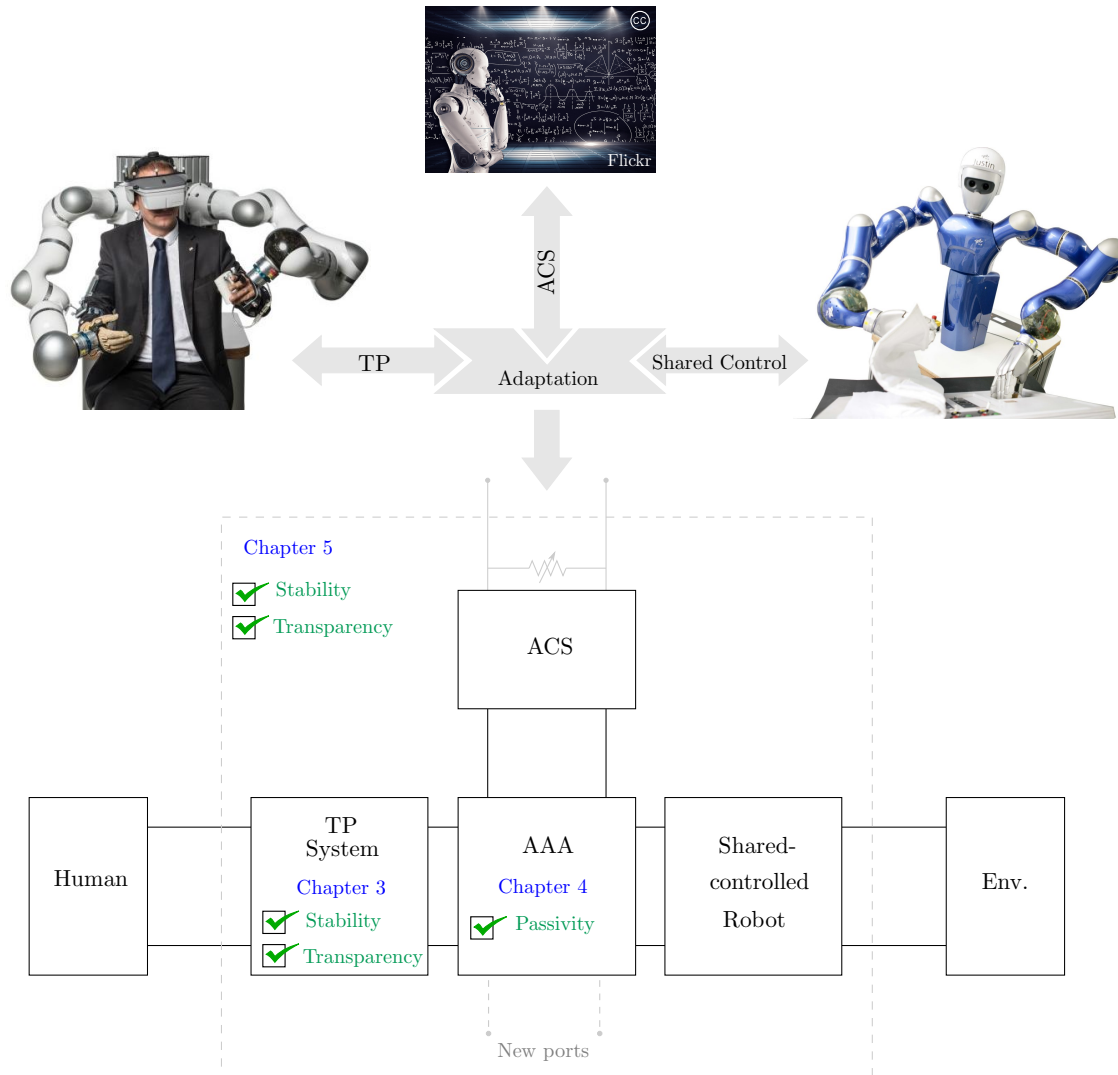
Figure 7.1: Stable and Transparent Framework for Adaptive Shared Control: From vision to completion.

A key challenge of a shared control system is ensuring stability, not just in the presence of time-delays but also with the online adaptation of AA factors, which was addressed in Chapter 4. Therein, a novel system-driven approach (patent-pending) for shared control was proposed, which reduces the authority of the autonomous system when there is degradation in sensor measurements in contrast to existing methods. A user-study validated the benefits of this approach while using the commonly accepted unity-sum arbitration. However the human-intervention capabilities were limited due to the unity-sum constraint.

To avoid this limitation, arbitrary AA factors were considered and two passivity-enforcing methods were proposed for multi-agent control of robots. As a first approach, controller forces were scaled while ensuring passivity with damping injection. The position drifts caused by this damping were later solved by adaptively modulating the controller stiffness and a gain-gradient limitation method was proposed to ensure system passivity. However, gain-gradient limitation was shown to result in slow modification of the AA gains, which is sufficient for time-insensitive tasks.

Chapter 5 presented the unified framework, which combines the transparency enhanced teleoperation from Chapter 3 with passive autonomous controllers in an adaptive manner using the methods proposed in Chapter 4. Although the methods were extensively validated through the analyses and experiments, I have also reported specific limitations throughout the thesis where the proposed methods still have scope for improvement. In particular, combination of PCR using new approaches with improved contact transparency is a current research topic to avoid the force limitations during contacts [PS21]. For the proposed AA adaptation, a task-specific optimization formulation could merge the benefits of both gain-gradient and damping injection methods, by minimizing the position drifts and the AA factor errors.

The overview of unified framework is shown in Fig. 7.1, where the top image recalls the research vision as presented in the introduction of the thesis. This vision was materialized through the unified framework developed in Chapter 5 and shown as the simplified port diagram in Fig. 7.1 (bottom). This framework was validated in practical scenarios through multiple projects in space and terrestrial domains as presented in Chapter 6.

The salient features of the proposed framework, which are of relevance to the robotic community at large, are summarized below:

Transparency:
The teleoperation part of the framework stabilized with the patent-pending PCR algorithm improves transparency and satisfies *guidelines **G2*** and ***G3*** reported in Section 1.1. In other words, the operator receives continuous and transparent feedback, and has the capability to continuously interact the automation. Hence, the PCR algorithm is a key advancement for multiple robotic domains like surgical, internet and space-based telerobotics, where high degree of transparency is the next incremental step for fine manipulation.

Adaptability:
The framework can accommodate different methods of arbitration, which include fixed or adaptive AA factors, and system- and/or human-driven arbitration. Multiple approaches were demonstrated throughout the thesis.

The unconstrained nature of AAA (without unity-sum arbitration) in the framework satisfies *guideline **G1*** and allows a flexible shift of the authority between the operator and autonomous system. Even for the constrained case, the workload on the operator was reduced, which was demonstrated through the user-study, hence satisfying *guideline **G4***.

The adaptability of the framework is relevant not just in the robotics field, but also in other disciplines with human-machine collaboration, like in autonomous vehicles and auto-pilot systems with human-intervention capabilities.

Modularity:
Different forms of ACS and different teleoperation architectures can be integrated into the proposed framework due to its multi-port formulation. This modular structure enables the extension of the framework to multi-lateral robotic scenarios like dual user haptic systems for surgical training. This extension can be implemented by adding new ports to the proposed framework as shown in Fig. 7.1 with the dashed port connected to AAA.

Stability:
The framework was ensured to be stable in spite of large communication delays which was demonstrated in Chapter 5 through the USB insertion task for a 600 ms varying time-delay. This proves the effectiveness of the proposed framework for extremely remote robotic tasks like servicing and assembly in orbit, even while improving transparency.

The passivity tools and analyses that were pursued in this thesis serve as effective methods to stabilize other large-scale robotic systems, by considering their energetic behavior. This was demonstrated through the secondary applications in Chapter 6.

The aforementioned features enable future extension of this research work in a platform-independent way, which is already planned for several projects. Specifically, for the UN-World Food Programme, haptic shared control for telenavigation of Sherp transport system (Fig. 1.3) is envisioned. Other planned projects are surgeon-robot collaboration for minimally invasive surgeries (to increase human-tissue perception) and shared control as a fail-safe for on-orbit servicing and in-orbit assembly tasks.

With the aforementioned contributions, this thesis provides an overarching framework to improve synergy between humans and robots. The flexibility of the framework allows integration of existent teleoperation and shared control approaches, which further promotes synergy within the robotics community.

[AB15]   Jordi Artigas and Ribin Balachandran. Kontroll-netzwerk mit einem hap-tischen eingabemittel: De102014004115 b3. 2015. (Cited on page 22)

[Abb06]   David A Abbink. Neuromuscular analysis of haptic gas pedal feedback during car following. 2006. (Cited on page 15)

[ABDS⁺16] Jordi Artigas, Ribin Balachandran, Marco De Stefano, Michael Panzirsch, Roberto Lampariello, Alin Albu-Schaeffer, Jan Harder, and Juergen Letschnik. Teleoperation for on-orbit servicing missions through the astra geostationary satellite. In *2016 IEEE Aerospace Conference*, pages 1–12. IEEE, 2016. (Cited on pages 21, 22, 23, 77, 137, and 139)

[ABR⁺16]   Jordi Artigas, Ribin Balachandran, Cornelia Riecke, Martin Stelzer, Bern-hard Weber, Jee-Hwan Ryu, and Alin Albu-Schaeffer. Kontur-2: force-feedback teleoperation from the international space station. In *2016 IEEE International Conference on Robotics and Automation (ICRA)*, pages 1166–1173. IEEE, 2016. (Cited on pages 21, 22, 50, 51, 54, 56, 60, 133, and 134)

[ADSR⁺15] J. Artigas, M. De Stefano, W. Rackl, R. Lampariello, B. Brunner, W. Bertl-eff, R. Burger, O. Porges, A. Giordano, C. Borst, and A. Albu-Schaeffer. The oos-sim: An on-ground simulation facility for on-orbit servicing robotic operations. In *Robotics and Automation (ICRA), 2015 IEEE International Conference on*, pages 2854–2860, May 2015. (Cited on page 137)

[AEK05]   Daniel Aarno, Staffan Ekvall, and Danica Kragic. Adaptive virtual fix-tures for machine-assisted teleoperation tasks. In *Proceedings of the 2005 IEEE international conference on robotics and automation*, pages 1139–1144. IEEE, 2005. (Cited on page 16)

[AHO03]   Jake J Abbott, Gregory D Hager, and Allison M Okamura. Steady-hand teleoperation with virtual fixtures. In *The 12th IEEE International Work-shop on Robot and Human Interactive Communication, 2003. Proceedings. ROMAN 2003.*, pages 145–151. IEEE, 2003. (Cited on page 143)

[AM10]   David A Abbink and Mark Mulder. Neuromuscular analysis as a guideline in designing shared control. *Advances in Haptics, Mehrdad Hosseini Zadeh (Ed.), ISBN: 9789533070933*, 2010. (Cited on page 16)

[AMB12]   David A Abbink, Mark Mulder, and Erwin R Boer. Haptic shared control: smoothly shifting control authority? *Cognition, Technology & Work*, 14(1):19–28, 2012. (Cited on pages 14, 15, 16, 18, and 92)

[AMVdH+11] David A Abbink, Mark Mulder, Frans CT Van der Helm, Max Mulder, and Erwin R Boer. Measuring neuromuscular control dynamics during car following with continuous haptic feedback. *IEEE Transactions on Systems, Man, and Cybernetics, Part B (Cybernetics)*, 41(5):1239–1249, 2011. (Cited on page 16)

[ARP10]   Jordi Artigas, Jee-Hwan Ryu, and Carsten Preusche. Time domain passivity control for position-position teleoperation architectures. *Presence: Teleoperators and Virtual Environments*, 19(5):482–497, 2010. (Cited on pages 75 and 76)

[ARPH11]   Jordi Artigas, Jee-Hwan Ryu, Carsten Preusche, and Gerd Hirzinger. Network representation and passivity of delayed teleoperation systems. In *Intelligent Robots and Systems (IROS), 2011 IEEE/RSJ International Conference on*, pages 177–183. IEEE, 2011. (Cited on pages 30, 60, 65, and 66)

[ARS+15]   H Amini, SM Rezaei, Ahmed AD Sarhan, J Akbari, and NA Mardi. Transparency improvement by external force estimation in a time-delayed nonlinear bilateral teleoperation system. *Journal of Dynamic Systems, Measurement, and Control*, 137(5):051013, 2015. (Cited on page 60)

[Art14]   J Artigas. *Time domain passivity control for delayed teleoperation*. PhD thesis, Ph. D. dissertation, UPM-Universidad Politecnica Madrid, Madrid, Spain, 2014. (Cited on page 16)

[ARW+16]   J Artigas, C Riecke, B Weber, M Stelzer, R Balachandran, S Schaetzle, R Bayer, M Steinmetz, J Vogel, B Brunner, et al. Force-feedback teleoperation of on-ground robots from the international space station in the frame of the kontur-2 experiment. In *Proceedings of International Extreme Robotics Conference, St. Petersburg, Russia*, 2016. (Cited on page 24)

[AS08]   Amin Abdossalami and Shahin Sirouspour. Adaptive control of haptic interaction with impedance and admittance type virtual environments. In *Haptic interfaces for virtual environment and teleoperator systems, 2008. haptics 2008. symposium on*, pages 145–152. IEEE, 2008. (Cited on page 49)

[ATB12]   Arash Ajoudani, Nikos Tsagarakis, and Antonio Bicchi. Tele-impedance: Teleoperation with impedance regulation using a body–machine interface. *The International Journal of Robotics Research*, 31(13):1642–1656, 2012. (Cited on page 103)

[BAMR16]   Ribin Balachandran, Jordi Artigas, Usman Mehmood, and Jee-Hwan Ryu. Performance comparison of wave variable transformation and time domain passivity approaches for time-delayed teleoperation: Preliminary results. In *Intelligent Robots and Systems (IROS), 2016 IEEE/RSJ International Conference on*, pages 410–417. IEEE, 2016. (Cited on pages 21, 22, 41, and 44)

[BDSM+21] Ribin Balachandran, Marco De Stefano, Hrishik Mishra, Christian Ott, and Alin Albu-Schaeffer. Passive arbitration in adaptive shared control of robots with variable force and stiffness scaling. *Submitted to Mechatronics*, 2021. (Cited on pages 21 and 22)

[BJA+17] Ribin Balachandran, Mikael Jorda, Jordi Artigas, Jee-Hwan Ryu, and Oussama Khatib. Passivity-based stability in explicit force control of robots. In *Robotics and Automation (ICRA), 2017 IEEE International Conference on*, pages 386–393. IEEE, 2017. (Cited on pages 21, 22, 60, and 156)

[BKOAS18] Ribin Balachandran, Natalia Kozlova, Christian Ott, and Alin Albu-Schaeffer. Non-linear local force feedback for haptic interfaces. In *IFAC Symposium on Robot Control SYROCO*. IFAC, 2018. (Cited on pages 21, 22, and 49)

[BM20] Ribin Balachandran and Hrishik Mishra. Adaptive authority allocation in shared control based on sensor measurement noise (submitted). 2020. (Cited on page 22)

[BMC+20] R. Balachandran, H. Mishra, M. Cappelli, B. Weber, C. Secchi, C. Ott, and A. Albu-Schaeffer. Adaptive authority allocation in shared control of robots using bayesian filters. In *2020 IEEE International Conference on Robotics and Automation (ICRA)*, pages 11298–11304, 2020. (Cited on pages 21, 22, 84, and 93)

[BMP+21] Ribin Balachandran, Hrishik Mishra, Michael Panzirsch, Christian Ott, and Alin Albu-Schaeffer. A finite-gain stable multi-agent robot control framework with adaptive authority allocation. *International Conference on Robotics and Automation (ICRA)*, 2021. (Cited on pages 21, 22, 93, and 118)

[BP21] Ribin Balachandran and Michael Panzirsch. Passive coupling reference approach for user-defined feedback stability in haptics and teleoperation (submitted). 2021. (Cited on page 22)

[BPDS+21] Ribin Balachandran, Michael Panzirsch, Marco De Stefano, Harsimran Singh, Christian Ott, and Alin Albu-Schaeffer. Stabilization of user-defined feedback controllers in teleoperation with passive coupling reference. *IEEE Robotics and Automation Letters*, 6(2):3513–3520, 2021. (Cited on pages 21, 22, and 69)

[BRJ+20] Ribin Balachandran, Jee-Hwan Ryu, Mikael Jorda, Christian Ott, and Alin Albu-Schaeffer. Closing the force loop to enhance transparency in time-delayed teleoperation. In *Robotics and Automation (ICRA), 2020 IEEE International Conference on*. IEEE, 2020. (Cited on pages 21, 22, 60, 69, and 74)

[BS98] G. Beccari and S. Stramigioli. Impedance control as merging mechanism for a behaviour-based architecture. In *Proceedings. 1998 IEEE International Conference on Robotics and Automation (Cat. No.98CH36146)*, volume 2, pages 1429–1434 vol.2, 1998. (Cited on page 93)

[CO14]   Vinay Chawda and Marcia K Oâ€™Malley.   Position synchronization in
           bilateral teleoperation under time-varying communication delays. *Ieee/asme
           transactions on mechatronics*, 20(1):245–253, 2014. (Cited on page 48)

[Col93]   J Edward Colgate.   Robust impedance shaping telemanipulation.   *IEEE
           Transactions on robotics and automation*, 9(4), 1993. (Cited on page 49)

[CS04]   Nikhil Chopra and Mark W Spong. Adaptive coordination control of bilat-
           eral teleoperators with time delay. In *Decision and Control, 2004. CDC.
           43rd IEEE Conference on*, volume 5, pages 4540–4547. IEEE, 2004. (Cited
           on pages 16, 69, 74, 75, and 76)

[CSG93]   Richard Colbaugh, Homayoun Seraji, and Kristin Glass. Direct adaptive
           impedance control of robot manipulators.   *Journal of Robotic Systems*,
           10(2):217–248, 1993. (Cited on page 103)

[CSKO20]   Andre Coelho, Harsimran Singh, Konstantin Kondak, and Christian Ott.
           Whole-body bilateral teleoperation of a redundant aerial manipulator. In
           2020 IEEE International Conference on Robotics and Automation (ICRA),
           pages 9150–9156. IEEE, 2020. (Cited on page 148)

[CSL+21]   Andre Coelho, Yuri S Sarkisov, Jongseok Lee, Ribin Balachandran, Anto-
           nio Franchi, Konstantin Kondak, and Christian Ott. Hierarchical control
           of redundant aerial manipulators with enhanced field of view. In *2021
           International Conference on Unmanned Aircraft Systems (ICUAS)*, pages
           994–1002. IEEE, 2021. (Cited on page 23)

[CSM+18]   Andre Coelho, Harsimran Singh, Tin Muskardin, Ribin Balachandran, and
           Konstantin Kondak. Smoother position-drift compensation for time domain
           passivity approach based teleoperation. In *2018 IEEE/RSJ International
           Conference on Intelligent Robots and Systems (IROS)*, pages 5525–5532.
           IEEE, 2018. (Cited on pages 24 and 101)

[CSO14]   Nick Colonnese, Sean M Sketch, and Allison M Okamura. Closed-loop stiff-
           ness and damping accuracy of impedance-type haptic displays. In *Haptics
           Symposium (HAPTICS), 2014 IEEE*, 2014. (Cited on pages 40 and 41)

[CYX+21]   Andre Coelho, Sarkisov Yuri, Wu Xuwei, Mishra Hrishik, Singh Harsimran,
           Alexander Dietrich, Antonio Franchi, Kondak Konstantin, and Christian
           Ott. Whole-body teleoperation and shared control of redundant robots
           with applications to aerial manipulation. *Journal of Intelligent & Robotic
           Systems*, 102(1), 2021. (Cited on pages 148 and 149)

[CZ01]   Gordon Cheng and Alexander Zelinsky. Supervised autonomy: A framework
           for human-robot systems development. *Autonomous Robots*, 10(3):251–266,
           2001. (Cited on page 13)

[D+21]   Thomas Dasbach et al. Ai-in-orbit-factory: Ai approaches for adaptive
           robotic in-orbit manufacturing of modular satellites.   2021.   (Cited on
           page 146)

[DLM05]   Alessandro De Luca and Raffaella Mattone. Sensorless robot collision detection and hybrid force/motion control. In *Robotics and Automation, 2005. ICRA 2005. Proceedings of the 2005 IEEE International Conference on*, pages 999–1004. IEEE, 2005. (Cited on page 72)

[DO20]   A. Dietrich and C. Ott. Hierarchical impedance-based tracking control of kinematically redundant robots. *IEEE Transactions on Robotics*, 36(1):204–221, 2020. (Cited on page 93)

[Dor15]   Wolfgang Dorst. *Umsetzungsstrategie Industrie 4.0: Ergebnisbericht der Plattform Industrie 4.0*. Bitkom Research GmbH, 2015. (Cited on page 143)

[DS13]   Anca D Dragan and Siddhartha S Srinivasa. A policy-blending formalism for shared control. *The International Journal of Robotics Research*, 32(7):790–805, 2013. (Cited on pages 16 and 84)

[DSAS16]   Marco De Stefano, Jordi Artigas, and Cristian Secchi. An optimized passivity-based method for simulating satellite dynamics on a position controlled robot in presence of latencies. In *2016 IEEE/RSJ International Conference on Intelligent Robots and Systems (IROS)*, pages 5419–5426. IEEE, 2016. (Cited on page 77)

[DSBG+18]   Marco De Stefano, Ribin Balachandran, Alessandro M Giordano, Christian Ott, and Cristian Secchi. An energy-based approach for the multi-rate control of a manipulator on an actuated base. In *2018 IEEE International Conference on Robotics and Automation (ICRA)*, pages 1072–1077. IEEE, 2018. (Cited on pages 23 and 154)

[DSBS19]   Marco De Stefano, Ribin Balachandran, and Cristian Secchi. A passivity-based approach for simulating satellite dynamics with robots: Discrete-time integration and time-delay compensation. *IEEE Transactions on Robotics*, 36(1):189–203, 2019. (Cited on pages 23, 35, and 154)

[DSDLR+07] Joris De Schutter, Tinne De Laet, Johan Rutgeerts, Wilm Decré, Ruben Smits, Erwin Aertbeliën, Kasper Claes, and Herman Bruyninckx. Constraint-based task specification and estimation for sensor-based robot systems in the presence of geometric uncertainty. *The International Journal of Robotics Research*, 26(5):433–455, 2007. (Cited on page 143)

[DSMB+19]   Marco De Stefano, Hrishik Mishra, Ribin Balachandran, Roberto Lampariello, Christian Ott, and Cristian Secchi. Multi-rate tracking control for a space robot on a controlled satellite: A passivity-based strategy. *IEEE Robotics and Automation Letters*, 4(2):1319–1326, 2019. (Cited on pages 23, 138, and 139)

[EK09]   P. Evrard and A. Kheddar. Homotopy-based controller for physical human-robot interaction. In *RO-MAN 2009 - The 18th IEEE International Symposium on Robot and Human Interactive Communication*, pages 1–6, 2009. (Cited on page 93)

[ERER20]   Issam El Rassi and Jean-Michel El Rassi. A review of haptic feedback in tele-operated robotic surgery. *Journal of medical engineering & technology*, 44(5):247–254, 2020. (Cited on page 17)

[ES86]   Steven D Eppinger and Warren P Seering. On dynamic models of robot force control. 1986. (Cited on page 60)

[FNM+14]   Matteo Fumagalli, Roberto Naldi, Alessandro Macchelli, Francesco Forte, Arvid QL Keemink, Stefano Stramigioli, Raffaella Carloni, and Lorenzo Marconi. Developing an aerial manipulator prototype: Physical interaction with the environment. *IEEE robotics & automation magazine*, 21(3):41–50, 2014. (Cited on page 147)

[For20]   The World Economic Forum. The future of jobs report 2020. 2020. (Cited on page 13)

[FPBS15]   Federica Ferraguti, Nicola Preda, Marcello Bonfe, and Cristian Secchi. Bilateral teleoperation of a dual arms surgical robot with passive virtual fixtures generation. In *2015 IEEE/RSJ International Conference on Intelligent Robots and Systems (IROS)*, pages 4223–4228. IEEE, 2015. (Cited on page 16)

[FSF13]   Federica Ferraguti, Cristian Secchi, and Cesare Fantuzzi. A tank-based approach to impedance control with variable stiffness. In *2013 IEEE international conference on robotics and automation*, pages 4948–4953. IEEE, 2013. (Cited on page 103)

[FSM+11]   Michel Franken, Stefano Stramigioli, Sarthak Misra, Cristian Secchi, and Alessandro Macchelli. Bilateral telemanipulation with time delays: A two-layer approach combining passivity and transparency. *Robotics, IEEE Transactions on*, 27(4):741–756, 2011. (Cited on pages 16 and 69)

[FTLS+19] Federica Ferraguti, Chiara Talignani Landi, Lorenzo Sabattini, Marcello Bonfè, Cesare Fantuzzi, and Cristian Secchi. A variable admittance control strategy for stable physical human–robot interaction. *The International Journal of Robotics Research*, 38(6):747–765, 2019. (Cited on page 103)

[GG05]   Paul G Griffiths and R Brent Gillespie. Sharing control between humans and automation using haptic interface: primary and secondary task performance benefits. *Human factors*, 47(3):574–590, 2005. (Cited on pages 15 and 16)

[GRS09]   Jorge Juan Gil, Angel Rubio, and Joan Savall. Decreasing the apparent inertia of an impedance haptic device by using force feedforward. *IEEE Transactions on Control Systems Technology*, 2009. (Cited on page 49)

[GWS08]   Kenneth Goodrich, Ralph Williams, and Paul Schutte. Piloted evaluation of the h-mode, a variable autonomy control system, in motion-based simulation. In *AIAA Atmospheric Flight Mechanics Conference and Exhibit*, page 6554, 2008. (Cited on page 15)

[HBRG+18] Bernd Henze, Ribin Balachandran, Maximo A Roa-Garzon, Christian Ott, and Alin Albu-Schäffer. Passivity analysis and control of humanoid robots on movable ground. *IEEE Robotics and Automation Letters*, 3(4):3457–3464, 2018. (Cited on pages 23, 35, and 154)

[HCFS]   Takeshi Hatanaka, Nikhil Chopra, Masayuki Fujita, and Mark W Spong. Foundation: Passivity, stability and passivity-based motion control. In *Passivity-Based Control and Estimation in Networked Robotics*. Springer. (Cited on page 16)

[Hen20]   Bernd Henze. *Whole-Body Control for Multi-Contact Balancing of Humanoid Robots*. PhD thesis, Technische Universitaet Muenchen, 2020. (Cited on page 154)

[Her16]   Katharina Hertkorn. *Shared grasping: A combination of telepresence and grasp planning*. KIT Scientific Publishing, 2016. (Cited on page 15)

[HHK⁺11] Thomas Hulin, Katharina Hertkorn, Philipp Kremer, Simon Schätzle, Jordi Artigas, Mikel Sagardia, Franziska Zacharias, and Carsten Preusche. The dlr bimanual haptic device with optimized workspace. In *Robotics and Automation (ICRA), 2011 IEEE International Conference on*, pages 3441–3442. IEEE, 2011. (Cited on page 47)

[HL11]   Ke Huang and Dongjun Lee. Hybrid virtual-proxy based control framework for passive bilateral teleoperation over the internet. In *2011 IEEE/RSJ International Conference on Intelligent Robots and Systems*, pages 149–156. IEEE, 2011. (Cited on page 69)

[HLL⁺18] Lingyan Hu, Jianhua Li, Xiaoping Liu, Pengwen Xiong, and Shengxing He. The maximum output force controller and its application to a virtual surgery system. *International Journal of Advanced Robotic Systems*, 2018. (Cited on page 69)

[HLR⁺05] G Hirzinger, K Landzettel, D Reintsema, C Preusche, A Albu-Schäffer, B Rebele, and M Turk. Rokviss-robotics component verification on iss. In *Proc. 8th Int. Symp. Artif. Intell. Robot. Autom. Space (iSAIRAS)(Munich 2005) p. Session2B*, 2005. (Cited on pages 132 and 138)

[Hog85]   Neville Hogan. Impedance Control: An Approach to Manipulation: Part Iâ€"Theory. *Journal of Dynamic Systems, Measurement, and Control*, 107(1):1–7, 03 1985. (Cited on page 93)

[HPS⁺21] Thomas Hulin, Michael Panzirsch, Harsimran Singh, Ribin Balachandran, Andre Coelho, Aaron Pereira, Bernhard M Weber, Nicolai Bechtel, Cornelia Riecke, Bernhard Brunner, et al. Model-augmented haptic telemanipulation: Concept, retrospective overview and current use-cases. *Frontiers in Robotics and AI*, 8:76, 2021. (Cited on page 23)

[HR02]   Blake Hannaford and Jee-Hwan Ryu. Time-domain passivity control of haptic interfaces. *Robotics and Automation, IEEE Transactions on*, 18(1):1–10, 2002. (Cited on pages 16, 35, and 64)

[HS88]   Sandra G Hart and Lowell E Staveland. Development of nasa-tlx (task load index): Results of empirical and theoretical research. *Advances in psychology*, 52:139–183, 1988. (Cited on page 90)

[HS06]   Peter F Hokayem and Mark W Spong. Bilateral teleoperation: An historical survey. *Automatica*, 42(12):2035–2057, 2006. (Cited on pages 14, 16, and 47)

[HZS99]   K Hastrudi-Zaad and SE Salcudean. On the use of local force feedback for transparent teleoperation. In *Robotics and Automation, 1999. Proceedings. 1999 IEEE International Conference on*, volume 3, pages 1863–1869. IEEE, 1999. (Cited on pages 49 and 50)

[HZS02]   Keyvan Hashtrudi-Zaad and Septimiu E Salcudean. Transparency in time-delayed systems and the effect of local force feedback for transparent teleoperation. *IEEE Transactions on Robotics and Automation*, 18(1):108–114, 2002. (Cited on page 49)

[I$^+$03]   Toshiyuki Inagaki et al. Adaptive automation: Sharing and trading of control. *Handbook of cognitive task design*, 8:147–169, 2003. (Cited on pages 14, 15, and 143)

[IK12]   Takumi Ishii and Seiichiro Katsura. Bilateral control with local force feedback for delay-free teleoperation. In *Advanced Motion Control (AMC), 2012 12th IEEE International Workshop on*, pages 1–6. IEEE, 2012. (Cited on page 49)

[JBRK17]   Mikael Jorda, Ribin Balachandran, Jee-Hwan Ryu, and Oussama Khatib. New passivity observers for improved robot force control. In *Intelligent Robots and Systems (IROS), 2017 IEEE/RSJ International Conference on*, pages 2177–2184. IEEE, 2017. (Cited on pages 22, 60, and 156)

[JSK$^+$18]   Aghil Jafari, Harsimran Singh, Harsha Karunanayaka, Jee-Hwan Ryu, Jj Chong, and Appolinaire C Etoundi. Lyapunov observer/controller for stable haptic interaction. In *2018 IEEE/ASME International Conference on Advanced Intelligent Mechatronics (AIM)*, pages 1–6. IEEE, 2018. (Cited on page 69)

[KBDS$^+$18]   Min Jun Kim, Ribin Balachandran, Marco De Stefano, Konstantin Kondak, and Christian Ott. Passive compliance control of aerial manipulators. In *2018 IEEE/RSJ International Conference on Intelligent Robots and Systems (IROS)*, pages 4177–4184. IEEE, 2018. (Cited on pages 23 and 156)

[KBR14]   Jong-Phil Kim, Sang-Yun Baek, and Jeha Ryu. A force bounding approach for multi-degree-of-freedom haptic interaction. *IEEE/ASME Transactions on Mechatronics*, 20(3):1193–1203, 2014. (Cited on page 69)

[KFG$^+$20]   Thomas Krueger, Edmundo Ferreira, Andrei Gherghescu, Lukas Hann, Emiel den Exter, Frank PJ van der Hulst, Levin Gerdes, Aaron Pereira, Harsimran Singh, Michael Panzirsch, et al. Designing and testing a robotic avatar for space-to-ground teleoperation: the developers insights. In *71st International Astronautical Congress*. International Astronautical Federation, 2020. (Cited on page 23)

[KH01]   Yoon Sang Kim and Blake Hannaford. Some practical issues in time domain passivity control of haptic interfaces. In *Intelligent Robots and Systems, 2001. Proceedings. 2001 IEEE/RSJ International Conference on*, volume 3, pages 1744–1750. IEEE, 2001. (Cited on page 56)

[Kha87]   Oussama Khatib. A unified approach for motion and force control of robot manipulators: The operational space formulation. *IEEE Journal on Robotics and Automation*, 3(1):43–53, 1987. (Cited on page 37)

[Kha02]   Hassan K Khalil. Nonlinear systems. *Upper Saddle River*, 2002. (Cited on pages 26, 27, and 28)

[KHZ11]   Behzad Khademian and Keyvan Hashtrudi-Zaad. Shared control architectures for haptic training: Performance and coupled stability analysis. *The International Journal of Robotics Research*, 30(13):1627–1642, 2011. (Cited on page 17)

[KKAS⁺13]   Konstantin Kondak, Kai Krieger, Alin Albu-Schaeffer, Marc Schwarzbach, Maximilian Laiacker, Ivan Maza, Angel Rodriguez-Castano, and Anibal Ollero. Closed-loop behavior of an autonomous helicopter equipped with a robotic arm for aerial manipulation tasks. *International Journal of Advanced Robotic Systems*, 10(2):145, 2013. (Cited on pages 147 and 155)

[KSB12]   Ayse Kucukyilmaz, Tevfik Metin Sezgin, and Cagatay Basdogan. Intention recognition for dynamic role exchange in haptic collaboration. *IEEE transactions on haptics*, 6(1):58–68, 2012. (Cited on pages 16 and 84)

[KSK15]   Suseong Kim, Hoseong Seo, and H Jin Kim. Operating an unknown drawer using an aerial manipulator. In *2015 IEEE International Conference on Robotics and Automation (ICRA)*, pages 5503–5508. IEEE, 2015. (Cited on page 147)

[KTTK98]   Kenji Kaneko, Hiroki Tokashiki, Kazuo Tanie, and Kiyoshi Komoriza. Macro-micro bilateral teleoperation based on operational force feedforward. *IEEE Transactions on Robotics and Automation*, pages 1761–1769, 1998. (Cited on page 49)

[Law93]   Dale A Lawrence. Stability and transparency in bilateral teleoperation. *Robotics and Automation, IEEE Transactions on*, 9(5):624–637, 1993. (Cited on pages 14, 39, 40, 42, and 88)

[LBS⁺20]   Jongseok Lee, Ribin Balachandran, Yuri S Sarkisov, Marco De Stefano, Andre Coelho, Kashmira Shinde, Min Jun Kim, Rudolph Triebel, and Konstantin Kondak. Visual-inertial telepresence for aerial manipulation. In *2020 IEEE International Conference on Robotics and Automation (ICRA)*, pages 1222–1229. IEEE, 2020. (Cited on pages 21, 22, 93, 148, and 149)

[LC11]   Yen-Chen Liu and Nikhil Chopra. Semi-autonomous teleoperation in task space with redundant slave robot under communication delays. In *2011 IEEE/RSJ International Conference on Intelligent Robots and Systems*, pages 679–684. IEEE, 2011. (Cited on page 16)

[LCS02]   Regelio Lozano, Nikhil Chopra, and Mark W Spong. Passivation of force reflecting bilateral teleoperators with time varying delay. In *Proceedings of the 8. Mechatronics Forum*, pages 954–962. Citeseer, 2002. (Cited on pages 16 and 69)

Bibliography

[LEM82]   Markley F.L. Lefferts E.J. and Shuster M.D. Kalman Filtering for Space-craft Attitude Estimation. 5(5):417–429, 1982. (Cited on page 87)

[LH10]   Dongjun Lee and Ke Huang. Passive-set-position-modulation framework for interactive robotic systems. *Robotics, IEEE Transactions on*, 26(2):354–369, 2010. (Cited on page 69)

[LHPO09]   Yanfang Li, Joel C Huegel, Volkan Patoglu, and Marcia K O'Malley. Progressive shared control for training in virtual environments. In *World Haptics 2009-Third Joint EuroHaptics conference and Symposium on Haptic Interfaces for Virtual Environment and Teleoperator Systems*, pages 332–337. IEEE, 2009. (Cited on page 16)

[Li98]   Perry Y Li. Passive control of bilateral teleoperated manipulators. In *Proceedings of the 1998 American Control Conference. ACC (IEEE Cat. No. 98CH36207)*, volume 6, pages 3838–3842. IEEE, 1998. (Cited on page 69)

[LK07]   S. G. Loizou and V. Kumar. Mixed initiative control of autonomous vehicles. In *Proceedings 2007 IEEE International Conference on Robotics and Automation*, pages 1431–1436, 2007. (Cited on page 93)

[LL09]   Kyungno Lee and Doo Yong Lee. Adjusting output-limiter for stable haptic rendering in virtual environments. *IEEE transactions on control systems technology*, 2009. (Cited on page 69)

[LMBO18]   Dylan P Losey, Craig G McDonald, Edoardo Battaglia, and Marcia K O'Malley. A review of intent detection, arbitration, and communication aspects of shared control for physical human–robot interaction. *Applied Mechanics Reviews*, 70(1), 2018. (Cited on pages 15 and 16)

[LPO09]   Yanfang Li, Volkan Patoglu, and Marcia K O'Malley. Negative efficacy of fixed gain error reducing shared control for training in virtual environments. *ACM Transactions on Applied Perception (TAP)*, 6(1):1–21, 2009. (Cited on pages 15 and 16)

[LS13]   Zhijun Li and Chun-Yi Su. Neural-adaptive control of single-master–multiple-slaves teleoperation for coordinated multiple mobile manipulators with time-varying communication delays and input uncertainties. *IEEE transactions on neural networks and learning systems*, 24(9):1400–1413, 2013. (Cited on page 93)

[LTH14]   Jian Li, Mahdi Tavakoli, and Qi Huang. Absolute stability of multi-dof multilateral haptic systems. *IEEE Transactions on Control Systems Technology*, 22(6):2319–2328, 2014. (Cited on page 17)

[MBDSO21a] Hrishik Mishra, Ribin Balachandran, Marco De Stefano, and Christian Ott. A compliant partitioned shared control strategy for an orbital robot. *IEEE Robotics and Automation Letters*, 6(4):7317–7324, 2021. (Cited on pages 23 and 155)

[MBDSO21b] Hrishik Mishra, Ribin Balachandran, Marco De Stefano, and Christian Ott. A partitioned shared control strategy for interaction-oriented end-effector tasks using an orbital robot. 2021. (Cited on page 16)

[MCD17]   Rebecca McWilliam, Daniela Constantinescu, and Daniela Damian. Passive haptic deformation using force bounding. In *The 5th International Conference on Control, Mechatronics and Automation*, 2017. (Cited on page 69)

[Meh70]   R. K. Mehra. Approaches to adaptive filtering. In *1970 IEEE Symposium on Adaptive Processes (9th) Decision and Control*, pages 141–141, Dec 1970. (Cited on page 87)

[MF16]   Adnan Munawar and Gregory Fischer. A surgical robot teleoperation framework for providing haptic feedback incorporating virtual environment-based guidance. *Frontiers in Robotics and AI*, 3:47, 2016. (Cited on pages 16 and 17)

[MFK11]   Nathan Michael, Jonathan Fink, and Vijay Kumar. Cooperative manipulation and transportation with aerial robots. *Autonomous Robots*, 30(1):73–86, 2011. (Cited on page 147)

[MH17a]   Selma Musić and Sandra Hirche. Control sharing in human-robot team interaction. *Annual Reviews in Control*, 44:342–354, 2017. (Cited on pages 17 and 85)

[MH17b]   Selma MusiÄ‡ and Sandra Hirche. Control sharing in human-robot team interaction. *Annual Reviews in Control*, 44:342 – 354, 2017. (Cited on page 15)

[MN17]   M. Snyder M. Napoli, J. Kugler. The additive manufacturing facility: One year on the iss national lab. *Proceedings of the ISS Research and Development Conference*, 2017. (Cited on page 143)

[MO04]   Panadda Marayong and Allison M Okamura. Speed-accuracy characteristics of human-machine cooperative manipulation using virtual fixtures with variable admittance. *Human Factors*, 46(3):518–532, 2004. (Cited on page 15)

[MRP⁺21]   Youssef Michel, Rahaf Rahal, Claudio Pacchierotti, Paolo Robuffo Giordano, and Dongheui Lee. Bilateral teleoperation with adaptive impedance control for contact tasks. *IEEE Robotics and Automation Letters*, 6(3):5429–5436, 2021. (Cited on page 103)

[Mur17]   Richard M Murray. *A mathematical introduction to robotic manipulation*. CRC press, 2017. (Cited on page 86)

[NBO11]   Emmanuel Nuño, Luis Basañez, and Romeo Ortega. Passivity-based control for bilateral teleoperation: A tutorial. *Automatica*, 47, 2011. (Cited on page 69)

[Nic20]   Davide Nicolis. A general framework for shared control in robot teleoperation with force and visual feedback. *Special Topics in Information Technology*, page 119, 2020. (Cited on page 17)

[NS91]   G Niemeyer and J-JE Slotine. Stable adaptive teleoperation. *Oceanic Engineering, IEEE Journal of*, 16(1):152–162, 1991. (Cited on page 50)

[NS97]   Günter Niemeyer and J-JE Slotine. Using wave variables for system analysis and robot control. 2:1619–1625, 1997. (Cited on pages 16, 34, 35, 42, 69, 74, 75, and 76)

[NSSB16]   Korbinian Nottensteiner, Mikel Sagardia, Andreas Stemmer, and Christoph Borst. Narrow passage sampling in the observation of robotic assembly tasks. In *2016 IEEE International Conference on Robotics and Automation (ICRA)*, pages 130–137. IEEE, 2016. (Cited on page 143)

[OGD15]   Parker Owan, Joseph Garbini, and Santosh Devasia. Uncertainty-based arbitration of human-machine shared control. *arXiv preprint arXiv:1511.05996*, 2015. (Cited on pages 16 and 84)

[OGGL06]   Marcia K Oâ€™Malley, Abhishek Gupta, Matthew Gen, and Yanfang Li. Shared control in haptic systems for performance enhancement and training. 2006. (Cited on page 16)

[OHF⁺18]   Anibal Ollero, Guillermo Heredia, Antonio Franchi, Gianluca Antonelli, Konstantin Kondak, Alberto Sanfeliu, Antidio Viguria, J Ramiro Martinez-de Dios, Francesco Pierri, Juan Cortés, et al. The aeroarms project: Aerial robots with advanced manipulation capabilities for inspection and maintenance. *IEEE Robotics & Automation Magazine*, 25(4):12–23, 2018. (Cited on pages 23 and 147)

[Oka04]   Allison M Okamura. Methods for haptic feedback in teleoperated robot-assisted surgery. *Industrial Robot: An International Journal*, 2004. (Cited on page 143)

[OP14]   Roberto Oboe and Davide Pilastro. Non-linear adaptive impedance controller for rehabilitation purposes. In *2014 IEEE 13th International Workshop on Advanced Motion Control (AMC)*, pages 272–277. IEEE, 2014. (Cited on page 103)

[OPNSR13]   Romeo Ortega, Julio Antonio Loría Perez, Per Johan Nicklasson, and Hebertt J Sira-Ramirez. *Passivity-based control of Euler-Lagrange systems: mechanical, electrical and electromechanical applications.* Springer Science & Business Media, 2013. (Cited on page 27)

[OTS⁺21]   Anibal Ollero, Marco Tognon, Alejandro Suarez, Dongjun Lee, and Antonio Franchi. Past, present, and future of aerial robotic manipulators. *IEEE Transactions on Robotics*, 2021. (Cited on page 147)

[Ott08]   Christian Ott. *Cartesian impedance control of redundant and flexible-joint robots.* Springer, 2008. (Cited on page 37)

[Pan18]   Michael Panzirsch. *Passivity-based multilateral control for delayed teleoperation.* PhD thesis, Universidad Politécnica de Madrid, 2018. (Cited on pages 16 and 17)

[PB19]   Michael Panzirsch and Ribin Balachandran. Time domain control for passive variable motion and force scaling in delayed teleoperation. *IFAC-PapersOnLine*, 52(18):31–36, 2019. (Cited on pages 23 and 94)

[PBA15]   Michael Panzirsch, Ribin Balachandran, and Jordi Artigas. Cartesian task allocation for cooperative, multilateral teleoperation under time delay. In *Robotics and Automation (ICRA), 2015 IEEE International Conference on*, pages 312–317. IEEE, 2015. (Cited on pages 16, 17, 23, and 93)

[PBA⁺17]   Michael Panzirsch, Ribin Balachandran, Jordi Artigas, Cornelia Riecke, Manuel Ferre, and Alin Albu-Schaeffer. Haptic intention augmentation for cooperative teleoperation. In *2017 IEEE International Conference on Robotics and Automation (ICRA)*, pages 5335–5341. IEEE, 2017. (Cited on pages 23, 93, and 136)

[PBW⁺18]   Michael Panzirsch, Ribin Balachandran, Bernhard Weber, Manuel Ferre, and Jordi Artigas. Haptic augmentation for teleoperation through virtual grasping points. *IEEE transactions on haptics*, 11(3):400–416, 2018. (Cited on page 23)

[PdV⁺07]   J. Philips, J. del R. Millan, G. Vanacker, E. Lew, F. Galan, P. W. Ferrez, H. Van Brussel, and M. Nuttin. Adaptive shared control of a brain-actuated simulated wheelchair. In *2007 IEEE 10th International Conference on Rehabilitation Robotics*, pages 408–414, June 2007. (Cited on page 15)

[Pea13]   Michael Panzirsch et al. Multilateral control for delayed teleoperation. In *2013 16th International Conference on Advanced Robotics (ICAR)*. IEEE, 2013. (Cited on page 69)

[Pea19]   Michael Panzirsch et al. Reducing the conservatism of the time domain passivity approach through consideration of energy reflection in delayed coupled network systems. *Mechatronics*, 2019. (Cited on pages 74, 75, and 76)

[PHA⁺16]   Michael Panzirsch, Thomas Hulin, Jordi Artigas, Christian Ott, and Manuel Ferre. Integrating measured force feedback in passive multilateral teleoperation. In *International Conference on Human Haptic Sensing and Touch Enabled Computer Applications*, pages 316–326. Springer, 2016. (Cited on pages 42, 50, 69, and 73)

[PHK⁺06]   Helena Pongrac, Peter Hinterseer, Julius Kammerl, Eckehard Steinbach, Berthold Färber, UDB Muenchen, and TU Muenchen. Limitations of human 3d force discrimination. *Human-Centered Robotics Systems*, 2006. (Cited on page 78)

[PJTKLP10]   Robert Platt Jr, Russ Tedrake, Leslie Kaelbling, and Tomas Lozano-Perez. Belief space planning assuming maximum likelihood observations. *Proceedings of the Robotics: Science and Systems*, 2010. (Cited on pages 16 and 84)

[PK06]   Jaeheung Park and Oussama Khatib. A haptic teleoperation approach based on contact force control. *The International Journal of Robotics Research*, 25(5-6):575–591, 2006. (Cited on page 60)

[PR97]   Raja Parasuraman and Victor Riley. Humans and automation: Use, misuse, disuse, abuse. *Human factors*, 39(2):230–253, 1997. (Cited on page 15)

Bibliography

[PRW11]   Robert Platt, Muhammad RAbdallah, and Charles Wampler. Multi-priority cartesian impedance control. *Robotics: Science and Systems VI*, page 145, 2011. (Cited on page 93)

[PS21]   Michael Panzirsch and Harsimran Singh. Position synchronization through the energy-reflection based time domain passivity approach in position-position architectures. *IEEE Robotics and Automation Letters*, 2021. (Cited on pages 48 and 161)

[RAB⁺16]   Cornelia Riecke, Jordi Artigas, Ribin Balachandran, Ralph Bayer, Alexander Beyer, Bernhard Brunner, Johann Buchner, Thomas Gumpert, Robin Gruber, Franz Hacker, et al. Kontur-2 mission: the dlr force feedback joystick for space telemanipulation from the iss. 2016. (Cited on pages 24 and 132)

[Rah20]   Rahaf Rahal. *Shared Control and Authority Distribution for Robotic Teleoperation*. PhD thesis, Univ. Rennes 1, 2020. (Cited on page 17)

[RAP10a]   Jee Hwan Ryu, Jordi Artigas, and Carsten Preusche. A passive bilateral control scheme for a teleoperator with time-varying communication delay. *Mechatronics*, 20(7):812–823, 2010. (Cited on pages 35, 36, and 59)

[RAP10b]   Jee-Hwan Ryu, Jordi Artigas, and Carsten Preusche. A passive bilateral control scheme for a teleoperator with time-varying communication delay. *Mechatronics*, 20(7):812–823, 2010. (Cited on page 69)

[Reb15]   JL Pinto Rebelo. Robust and transparent multi-degree-of-freedom bilateral teleoperation with time-delay. 2015. (Cited on page 16)

[RHVJ19]   Jee-Hwan Ryu, Quang Ha-Van, and Aghil Jafari. Multilateral teleoperation over communication time delay using the time-domain passivity approach. *IEEE Transactions on Control Systems Technology*, 28(6):2705–2712, 2019. (Cited on page 17)

[Ros93]   Louis B Rosenberg. Virtual fixtures: Perceptual tools for telerobotic manipulation. In *Proceedings of IEEE virtual reality annual international symposium*, pages 76–82. IEEE, 1993. (Cited on page 15)

[RPHH05]   Jee-Hwan Ryu, Carsten Preusche, Blake Hannaford, and Gerd Hirzinger. Time domain passivity control with reference energy following. *IEEE Transactions on Control Systems Technology*, 13(5):737–742, 2005. (Cited on page 36)

[RS15]   Joao Rebelo and Andre Schiele. Time domain passivity controller for 4-channel time-delay bilateral teleoperation. *Haptics, IEEE Transactions on*, 8(1):79–89, 2015. (Cited on page 60)

[RWM⁺20]   Cornelia Riecke, Bernhard Weber, Maximilian Maier, Martin Stelzer, Ribin Balachandran, Alexander Kondratiev, Andrey Vasiliev, Aleksei Sergeev, Vladimir Dubinin, and Olga Rudakova. Kontur-3: Human machine interfaces for telenavigation and manipulation of robots from iss. In *2020 IEEE Aerospace Conference*, pages 1–10. IEEE, 2020. (Cited on page 24)

[SADS+15] Phillip Schmidt, Jordi Artigas, Marco De Stefano, Ribin Balachandran, and Christian Ott. Increasing the performance of torque-based visual servoing by applying time domain passivity. *IFAC-PapersOnLine*, 48(19):13–18, 2015. (Cited on pages 24 and 142)

[Sag19] Mikel Sagardia. *Virtual manipulations with force feedback in complex interaction scenarios.* PhD thesis, Technische Universität München, 2019. (Cited on pages 47 and 48)

[Sär13] Simo Särkkä. *Bayesian Filtering and Smoothing.* Cambridge University Press, New York, NY, USA, 2013. (Cited on pages 86 and 87)

[SBE16] Phillip W. Schmidt, Ribin Balachandran, and Jordi Artigas Esclusa. Shared control for robotic on-orbit servicing. 2016. (Cited on page 23)

[Sce96] Mark W Scerbo. Theoretical perspectives on adaptive automation. *Automation and human performance: Theory and applications*, pages 37–63, 1996. (Cited on pages 16 and 84)

[SCN+21] Mario Selvaggio, Marco Cognetti, Stefanos Nikolaidis, Serena Ivaldi, and Bruno Siciliano. Autonomy in physical human-robot interaction: a brief survey. *IEEE Robotics and Automation Letters*, 2021. (Cited on pages 15, 16, 17, and 85)

[Sea19] Harsimran Singh and et al. Preserving the physical coupling in teleoperation despite time delay through observer-based gradient control. *IFAC-PapersOnLine*, 2019. (Cited on page 75)

[Sea20] Harsimran Singh and et al. Proxy-based approach for position synchronization of delayed robot coupling without sacrificing performance. *IEEE Robotics and Automation Letters*, 2020. (Cited on page 48)

[SFF+18] Mario Selvaggio, Giuseppe Andrea Fontanelli, Fanny Ficuciello, Luigi Villani, and Bruno Siciliano. Passive virtual fixtures adaptation in minimally invasive robotic surgery. *IEEE Robotics and Automation Letters*, 3(4):3129–3136, 2018. (Cited on page 17)

[SGFS19] Mario Selvaggio, P Robuffo Giordano, F Ficuciellol, and Bruno Siciliano. Passive task-prioritized shared-control teleoperation with haptic guidance. In *2019 International Conference on Robotics and Automation (ICRA)*, pages 430–436. IEEE, 2019. (Cited on pages 16 and 17)

[SH13] S. Sã¤rkkÃ¤ and J. Hartikainen. Non-linear noise adaptive kalman filtering via variational bayes. In *2013 IEEE International Workshop on Machine Learning for Signal Processing (MLSP)*, pages 1–6, Sep. 2013. (Cited on page 87)

[SKB+19] Yuri S Sarkisov, Min Jun Kim, Davide Bicego, Dzmitry Tsetserukou, Christian Ott, Antonio Franchi, and Konstantin Kondak. Development of sam: cable-suspended aerial manipulator. In *2019 International Conference on Robotics and Automation (ICRA)*, pages 5323–5329. IEEE, 2019. (Cited on page 147)

[SKC⁺20]   Yuri S Sarkisov, Min Jun Kim, Andre Coelho, Dzmitry Tsetserukou, Christian Ott, and Konstantin Kondak. Optimal oscillation damping control of cable-suspended aerial manipulator with a single imu sensor. In *2020 IEEE International Conference on Robotics and Automation (ICRA)*, pages 5349–5355. IEEE, 2020. (Cited on page 148)

[SN17]   Akhlaghi S. and Yhou N. Adaptive Adjustment of Noise Covariance in Kalman Filter for Dynamic State Estimation. pages 1–5, 2017. (Cited on page 87)

[Spa]   Spaceflight industries â€" launch pricinginformation. *http://spaceflight.com/schedulepricing/pricing.* (Cited on page 143)

[SRCG06]   Joshua P Switkes, Eric J Rossetter, Ian A Coe, and J Christian Gerdes. Handwheel force feedback for lanekeeping assistance: Combined dynamics and stability. 2006. (Cited on page 17)

[SSNK20]   Jayant Singh, Aravinda Ramakrishnan Srinivasan, Gerhard Neumann, and Ayse Kucukyilmaz. Haptic-guided teleoperation of a 7-dof collaborative robot arm with an identical twin master. *IEEE transactions on haptics*, 13(1):246–252, 2020. (Cited on page 48)

[SSVO10]   Bruno Siciliano, Lorenzo Sciavicco, Luigi Villani, and Giuseppe Oriolo. *Robotics: modelling, planning and control.* Springer, 2010. (Cited on pages 38 and 77)

[SV12]   Bruno Siciliano and Luigi Villani. *Robot force control*, volume 540. Springer Science & Business Media, 2012. (Cited on page 60)

[T⁺02]   Sebastian Thrun et al. Robotic mapping: A survey. *Exploring artificial intelligence in the new millennium*, 1(1-35):1, 2002. (Cited on page 143)

[THH⁺11]   Andreas Tobergte, Patrick Helmer, Ulrich Hagn, Patrice Rouiller, Sophie Thielmann, Sébastien Grange, Alin Albu-Schäffer, François Conti, and Gerd Hirzinger. The sigma. 7 haptic interface for mirosurge: A new bi-manual surgical console. In *Intelligent Robots and Systems (IROS), 2011 IEEE/RSJ International Conference on*, pages 3023–3030. IEEE, 2011. (Cited on pages 47, 48, and 49)

[TMO⁺17]   Alejandro E Trujillo, Matthew T Moraguez, Andrew Owens, Samuel I Wald, and Olivier De Weck. Feasibility analysis of commercial in-space manufacturing applications. In *AIAA SPACE and Astronautics Forum and Exposition*, page 5360, 2017. (Cited on page 143)

[TN04]   Neal A Tanner and Günter Niemeyer. Practical limitations of wave variable controllers in teleoperation. In *Robotics, Automation and Mechatronics, 2004 IEEE Conference on*, volume 1, pages 25–30. IEEE, 2004. (Cited on page 35)

[TN05]   Neal A Tanner and Günter Niemeyer. Improving perception in time-delayed telerobotics. *The International Journal of Robotics Research*, 24(8):631–644, 2005. (Cited on page 42)

[Tra15] Pete Trautman. Assistive planning in complex, dynamic environments: a probabilistic approach. In *2015 IEEE International Conference on Systems, Man, and Cybernetics*, pages 3072–3078. IEEE, 2015. (Cited on pages 16 and 84)

[TSMO18] Tetsuya Tashiro, Tomoyuki Shimono, Takahiro Mizoguchi, and Kouhei Ohnishi. Time delay compensation for force controller in bilateral teleoperation system under time delay. In *2018 IEEE 15th International Workshop on Advanced Motion Control (AMC)*, pages 649–654. IEEE, 2018. (Cited on page 60)

[UB] Marc Ueberle and Martin Buss. Design, control, and evaluation of a new 6 dof haptic device. *IEEE Transactions on Robotics and Automation*. (Cited on page 49)

[Ue18] Unisec-europe.eu. Cubesat electrical interface â€" university space engineering consortium. In *http://unisec-europe.eu/standards/bus/*, 2018. (Cited on page 143)

[UWFP20] DLR UN World Food Program. The ahead project: Autonomous humanitarian emergency aid devices. 2020. (Cited on page 17)

[VOAK+13] J Van Oosterhout, DA Abbink, JF Koning, H Boessenkool, JGW Wildenbeest, and CJM Heemskerk. Haptic shared control improves hot cell remote handling despite controller inaccuracies. *Fusion Engineering and Design*, 88(9-10):2119–2122, 2013. (Cited on page 15)

[VT87] Michael A Vidulich and Pamela S Tsang. Absolute magnitude estimation and relative judgement approaches to subjective workload assessment. In *Proceedings of the Human Factors Society Annual Meeting*, volume 31, pages 1057–1061. SAGE Publications Sage CA: Los Angeles, CA, 1987. (Cited on page 90)

[VV65] Mac E Van Valkenburg. Introduction to modern network synthesis. 1965. (Cited on page 94)

[WAH+12] Jeroen GW Wildenbeest, David A Abbink, Cock JM Heemskerk, Frans CT Van Der Helm, and Henri Boessenkool. The impact of haptic feedback quality on the performance of teleoperated assembly tasks. *IEEE Transactions on Haptics*, 6(2):242–252, 2012. (Cited on page 15)

[WBR+19] Bernhard Weber, Ribin Balachandran, Cornelia Riecke, Freek Stulp, and Martin Stelzer. Teleoperating robots from the international space station: Microgravity effects on performance with force feedback. In *2019 IEEE/RSJ International Conference on Intelligent Robots and Systems (IROS)*, pages 8144–8150. IEEE, 2019. (Cited on page 23)

[WHS19] Markus Wilde, Jan Harder, and Enrico Stoll. On-orbit servicing and active debris removal: enabling a paradigm shift in spaceflight. *Frontiers in Robotics and AI*, 6:136, 2019. (Cited on page 137)

[WL12]   Huanran Wang and Xiaoping P Liu. Stability analysis of haptic shared control and its application on a mobile assistive robot. In *2012 IEEE International Workshop on Haptic Audio Visual Environments and Games (HAVE 2012) Proceedings*, pages 44–49. IEEE, 2012. (Cited on page 17)

[WMPH+18]   Thiago Weber Martins, Aaron Pereira, Thomas Hulin, Oliver Ruf, Stefan Kugler, Alessandro Giordano, Ribin Balachandrand, Fabian Benedikt, John Lewis, Reiner Anderl, et al. Space factory 4.0-new processes for the robotic assembly of modular satellites on an in-orbit platform based on industrie 4.0 approach. 2018. (Cited on pages 17, 24, 93, and 143)

[WSR+16]   Bernhard Weber, Simon Schätzle, Cornelia Riecke, Bernhard Brunner, Sergey Tarassenko, Jordi Artigas, Ribin Balachandran, and Alin Albu-Schäffer. Weight and weightlessness effects on sensorimotor performance during manual tracking. In *International Conference on Human Haptic Sensing and Touch Enabled Computer Applications*, pages 111–121. Springer, 2016. (Cited on pages 24, 135, and 136)

[YY94]   Yasuyoshi Yokokohji and Tsuneo Yoshikawa. Bilateral control of master-slave manipulators for ideal kinesthetic coupling-formulation and experiment. *Robotics and Automation, IEEE Transactions on*, 10(5):605–620, 1994. (Cited on pages 14, 39, and 40)

[ZHC18]   Martijn JA Zeestraten, Ioannis Havoutis, and Sylvain Calinon. Programming by demonstration for shared control with an application in teleoperation. *IEEE Robotics and Automation Letters*, 3(3):1848–1855, 2018. (Cited on page 16)